Insights into Glacial Terminations from a South Atlantic Perspective

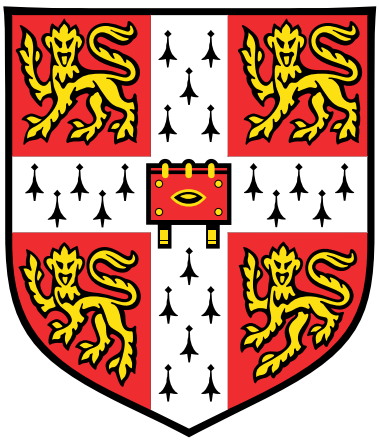

Jenny Roberts

Department of Earth Sciences

University of Cambridge

This dissertation is submitted for the degree of

Doctor of Philosophy

Trinity College

2016

“How inappropriate to call this planet Earth when it is quite clearly Ocean...”
Arthur C. Clarke

Declaration

I hereby declare that except where specific reference is made to the work of others, the contents of this dissertation are original and have not been submitted in whole or in part for consideration for any other degree or qualification in this, or any other university. This dissertation is my own work and contains nothing which is the outcome of work done in collaboration with others, except as specified in the text and Acknowledgements. This dissertation does not exceed 275 numbered pages of which not more than 225 pages are text, appendices, illustrations and bibliography.

Jenny Roberts
2016

Acknowledgements

I would like to thank my supervisors David Hodell, Vicky Peck and Sev Kender for providing me with the opportunity to work on such a fascinating topic and for their guidance and support throughout this Ph.D. Thanks also to the captain, crew and science parties of the RRS *James Clark Ross* and R/V *Marion Dufresne* for the acquisition of the marine sediment cores that formed the basis of the work presented here.

Throughout the last 3 years I have benefitted immensely from discussion with a large number of people that are too numerous to acknowledge in a single page. However I mention a few key people here; thanks to Nick McCave, Julia Gottschalk, Luke Skinner, Aleksey Sadekov and Harry Elderfield from the Department of Earth Sciences, Dominic Hodgson, Steve Roberts, Claire Allen, C.-D. Hillenbrand, Louise Sime and Max Holloway from the British Antarctic Survey, Erin McClymont from Durham, Laura Robinson and Pete Spooner from Bristol, and Claire Waelbroeck and Natalia Vázquez Riveiros from LSCE. Additionally, I would like to thank the following people for their technical support and expertise: Linda Booth, Caroline Daunt, John Nicolson, Simon Crowhurst, Ian Mather, James Rolfe, Mervyn Greaves, Salima Souanef-Ureta, Martin West, Amanda Hayton and Melanie Leng.

During my Ph.D. I was lucky to be involved in two oceanographic research expeditions that provided me with the opportunity to visit some beautiful and remote parts of the world, and gain first-hand experience of marine sediment core acquisition. My thanks go to the P.I.s on both of these cruises, and to the other members of the crew, for making these cruises so enjoyable and providing me with some unforgettable memories.

I feel very fortunate to have been done this Ph.D. dissertation surrounded by such a caring group of friends and family. Thanks to you all for the excellent trips in search of mountains, and bring on 'Sufferfest2016'!

Abstract

The last two glacial terminations represent the most recent, and best documented, periods of Earth warming in the geological record. During these terminations atmospheric CO_2 rose by approximately 100 ppm and global mean temperatures increased by 4-6^{o}C. Whilst the driver for these deglaciations ultimately derives from changes in the insolation forcing at the edge of the atmosphere, feedbacks within the Earth's climate system act to amplify these small external forcings tipping the Earth from a cold glacial climate state to a warm interglacial climate state. A key question in Quaternary climate science is understanding which feedbacks are important in regulating global climate on glacial-interglacial timescales. On this topic, the Southern Ocean has long been considered to be an important player in regulating atmospheric CO_2 on glacial-interglacial timescales. This thesis investigates some of the hypothesised drivers of changes in atmospheric CO_2 on glacial-interglacial timescales by generating high-resolution multi-proxy records from the Southern Ocean spanning the last two glacial terminations. In particular, I focus on changes in the structure, circulation and biological productivity within the sub-Antarctic zone.

A change in the deep ocean density structure has been hypothesised to have resulted in the release of CO_2 from the deep ocean. Centennially-resolved records from the sub-Antarctic are used to reconstruct deep and intermediate water density for the first time. I demonstrate that timing of the major breakdown in the density gradient of the ocean significantly lagged the breakdown in the chemical gradient, suggesting that changes in the deep ocean density structure were not the major driver of the deglacial rise in atmospheric CO_2 .

Changes in the density structure of the Southern Ocean likely had significant implications for global circulation. In particular, the flow of low salinity water through the Drake Passage is thought to be important in setting the strength and geometry of Atlantic Overturning Circulation. Drake Passage through-flow speed was reconstructed from two sites in the central and northern margin of the Antarctic Circumpolar Current downstream of the Drake Passage. These records suggest a very different structure of Antarctic Circumpolar flow through the Drake Passage during glacial periods, and evidence significant changes in ocean temperature as a result of pronounced reductions in Drake Passage through-flow.

The strength of the biological pump has long been identified as an important player in regulating atmospheric CO_2 . In particular, a strong glacial increase in sub-Antarctic productivity has been observed at open ocean sites in the South Atlantic and Indian Ocean. However, the glacial-interglacial changes in productivity in sub-Antarctic shelf settings are less well-documented. The new high-resolution records presented here from the sub-Antarctic southwest Atlantic suggest a significant change in the $CaCO_3$:C_{org} ratio that likely has implications for the surface ocean's ability to uptake CO_2 .

Contents

List of Figures

List of Tables

Abbreviations

AABW	Antarctic Bottom Water
AAIW	Antarctic Intermediate Water
AASW	Antarctic Surface Water
ACC	Antarctic Circumpolar Current
ALK	Alkalinity
BFAR	Benthic Foraminifera Accumulation Rate
DCA	Detrended Correspondence Analysis
DIC	Dissolved Inorganic Carbon
EDC	EPICA Dome C
EDML	EPICA Dronning Maud Land
GC	Gravity core
GCM	General Circulation Model
IRD	Ice-Rafted Debris
ISW	Ice Shelf Water
LGM	Last Glacial Maximum
MAR	Mass Accumulation Rate
MIS	Marine Isotope Stage
PF	Polar Front
PIS	Patagonian Ice Sheet
SACCF	Southern Antarctic Circumpolar Front
SAF	Sub-Antarctic Front
SAMW	Sub-Antarctic Mode Water
SFSD	South Falkland Slope Drift
$\overline{SS}$	Sortable silt mean grain size
SST	Sea Surface Temperature
SWW	Southern Westerly Winds
T-I	Termination I
T-II	Termination II
TOC	Total Organic Carbon
(U/L) CDW	(Upper/Lower) Circumpolar Deep Water
WAIS	West Antarctic Ice Sheet
XRF	X-ray Fluorescence

Chapter 1

Introduction

1.1 Motivation

In this introduction, I discuss some of the motivations for studying palaeoclimate, and in particular changes in past climate across glacial terminations. I will then summarise the structure of the thesis and the scientific questions addressed in each chapter.

1.1.1 Why study palaeoclimate?

A widely cited reason for studying palaeoclimate is that data-based reconstructions of past climate can better inform models and thus improve projections of future climate change. Modern human activity affects Earth's climate through the emission of radiatively important gases (IPCC, 2014). The concentration of atmospheric CO_2 is currently higher than at any time in the past 15 million years (Pagani et al., 2005) and is continuing to increase. With an ever expanding human population, and no deceleration in fossil fuel consumption, we are heading into a climatically uncertain future. It is therefore increasingly important to develop an understanding of the climate system in order to make reliable predictions about the future, both short- and long-term.

Records of past changes in Earth climate can be used to inform our understanding of, and response to, future climate change. However, instrumental records of past climate through satellite observation, sea level measurements and meteorological records, have only been widely available for about the last 100 years, and prior to the advent of satellites in the 1960s were biased toward heavily populated regions in the Northern hemisphere. Additionally, the range of climate variability in instrumental records is relatively small compared to the future climate scenarios based on model predictions (Figure 1.1). It is therefore necessary to have an alternative means to assess climate variability in the past.

Proxy data-based reconstructions of past climate from ice cores, marine sediment cores, lake sediment cores and speleothems can provide a globally distributed and temporally continuous window into past climates. Using these records, it is possible to look back through 4.6 billion years of Earth history to find appropriate analogues to understand some of the tipping points in the Earth climate system that may be relevant for modern anthropogenic climate change. Collectively, these records of past climate changes have been used to develop an understanding of climate sensitivity (the expected temperature change for a doubling of atmospheric CO_2) and in some instances (e.g.

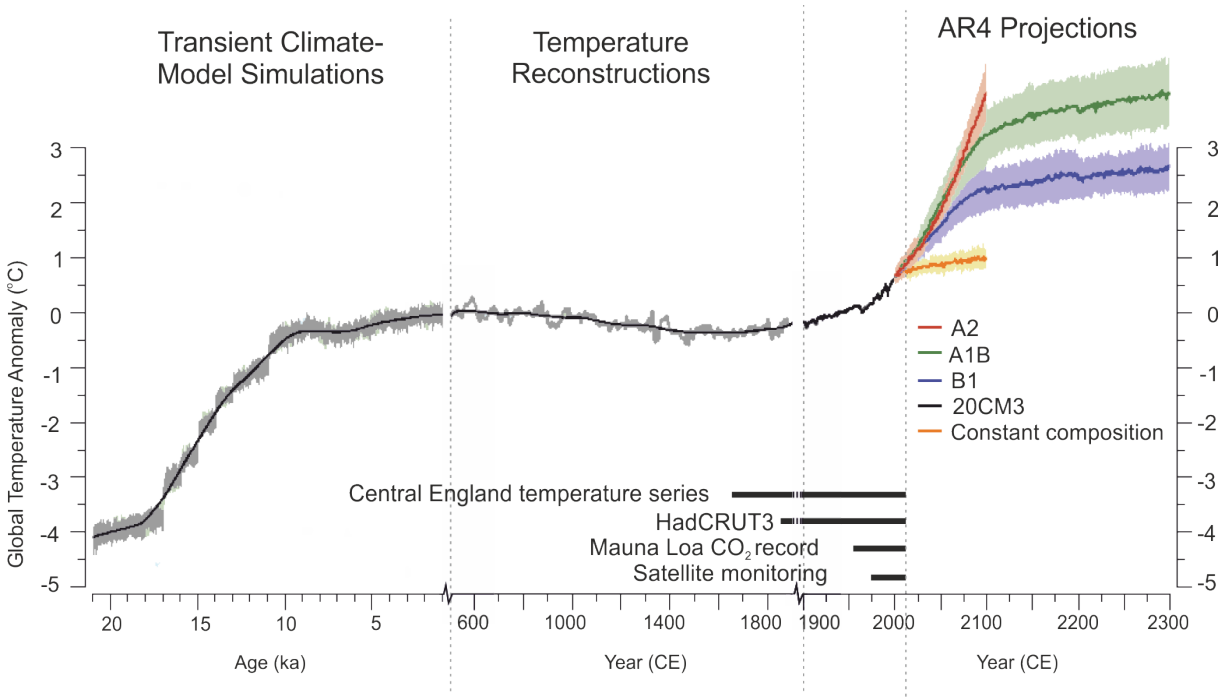

Figure 1.1: Global temperature change over the last glacial termination and the range of projections of future climate change (IPCC, 2014). Instrumental records are only available across a very short period of time (note the variable scale on the x-axis) and record an interval of relatively stable climate.

Hopcroft and Valdes 2014) to directly tune general circulation model output to improve model projections of future climate change.

Finally, studies of past climate have revealed that even before human intervention, Earth's climate was not stable. There have been periods of Earth history in which the Earth was completely glaciated for several millions of years, termed *Snowball Earth* (Harland, 1964), and then abruptly switched to a 'greenhouse' climate with levels of atmospheric CO_2 far exceeding the highest modelled estimates of future anthropogenic CO_2 emissions (Hoffman, 1998). Understanding the natural variability of Earth's climate system provides context to the human-induced changes in the climate system that are occurring today.

1.1.2 Glacial terminations

Instrumental measurements of changes in Earth climate over the last millennium show that Earth's climate has been relatively stable in comparison to predictions of future emission scenarios (Figure 1.1). In contrast, the geological record offers the opportunity to look back to periods in Earth history when significant increases in atmospheric pCO_2 and warming occurred, and make predictions of the potential response of the climate to changes in radiative forcing.

However, a major difficulty of using the geological record to reconstruct past climate is that the uncertainties in the record increase with age. Difficulties in accurately dating events and discontinuities in the geological archive typically become increasingly significant further back in the geological record. Therefore, in order to reconstruct climatic response to a CO_2 forcing, it is ad-

vantageous to study the youngest cases of climatic warming.

Over the last 2.6 million years, an interval of Earth history known as the Pleistocene, Earth's climate has fluctuated between cold 'glacial' periods and warm 'interglacial' periods. Since the mid-Pleistocene transition (1.25-0.7 Ma), these glacial-interglacial cycles have been paced at approximately 100,000 years (Imbrie et al. 1993; Petit et al. 1999; Figure 1.2). The pattern of glacial-interglacial cycles is not symmetric, rather it follows a 'saw-toothed' pattern with a long interval of cooling to a glacial maximum followed by a relatively short (~10 kyr) warming interval, called a 'glacial termination' (Broecker and van Donk, 1970). During these glacial terminations, atmospheric CO_2 increases by 80-100 ppm (Ahn and Brook, 2008; Monnin et al., 2004; Petit et al., 1999), and global mean temperatures rise by ~4°C (Past Interglacials Working Group of PAGES, 2016; Shakun et al., 2012). The large coverage of high-resolution proxy data records from across glacial terminations provides a useful test-bed for assessing the sensitivity of palaeoclimate models, and thus can be used to improve model projection of future climate change.

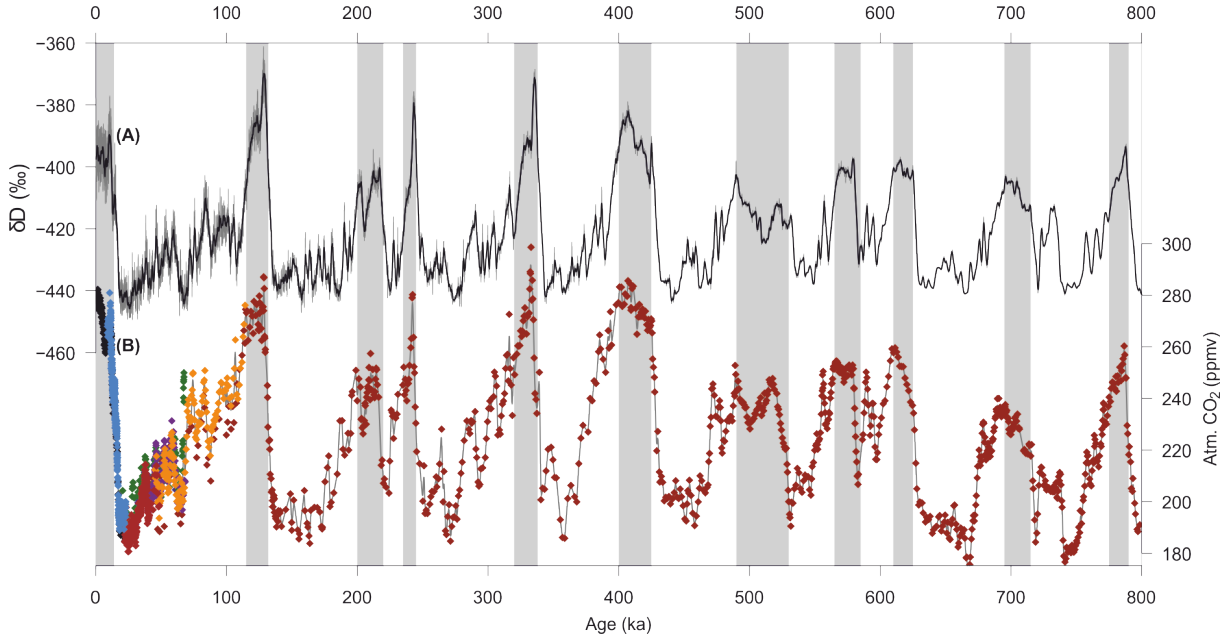

Figure 1.2: Late Pleistocene glacial-interglacial cycles as recorded in Antarctic ice cores. (A) Antarctic temperature proxy, EPICA Dome C (EDC) δD (‰) (Jouzel et al., 2007); (B) Composite of atmospheric CO_2 records from Antarctic ice cores: EDC (black, Monnin et al. 2004); Taylor Dome (dark blue, Indermühle et al. 2000); Byrd (green; Ahn and Brook 2008); Vostok (red, Petit et al. 1999); TALos Dome Ice Core (TALDICE) (purple, Bereiter et al. 2012); EPICA Dronning Maud Land (EDML) (orange, Lüthi et al. 2010); Siple (brown, Ahn and Brook 2014); West Antarctic Ice Sheet (WAIS) Divide (pale blue, Marcott et al. 2014).

1.1.3 Drivers of glacial terminations

The underlying driver of Pleistocene glacial-interglacial cycles is changes in the incoming solar radation, controlled by slight perturbations of Earth's orbit around the Sun. There are three orbital parameters which affect the incoming insolation; eccentricity (the ellipticity of Earth's orbit),

precession (the relationship between equinoxes and aphelion/perihelion) and obliquity (the tilt of Earth's axis). These three orbital parameters have characteristic cyclicity of 100,000 years, 23,000 years and 41,000 years respectively (Milankovitch, 1930). However, despite the similarity in the pacing of the Late Pleistocene glacial-interglacial cycles to the eccentricity cycle, the absolute variation in insolation that is attributed to the eccentricity cycle is very small, and insufficient to account for the dramatic glacial-interglacial changes observed. Thus rapid, non-linear feedbacks internal to the Earth system must act to amplify small variations in the incoming solar forcing.

The strong correlation of atmospheric pCO_2 and global temperature (Jouzel et al., 2007; Petit et al., 1999) suggests that variations in atmospheric CO_2, and its effect on the radiative budget of the Earth, likely played an important role in amplifying the variations in the external astronomical forcing (de Noblet et al., 1996; Khodri et al., 2001). However, in spite of the importance of CO_2 as an amplifier in the climate system, our understanding of glacial-interglacial variations in atmospheric pCO_2 remains incomplete.

The glacial-interglacial variations in atmospheric CO_2 suggest that CO_2 is exchanged with another reservoir of CO_2. The deep ocean stores 60 times more CO_2 than in the pre-industrial atmosphere and has a mixing time on the order of 1000 years, and is thus the primary reservoir of exchangeable CO_2 on glacial-interglacial timescales (Broecker and Peng, 1974; Sigman and Boyle, 2000). Understanding how ocean carbon storage has changed over glacial-interglacial timescales is critical in constraining the CO_2 feedback driving glacial terminations.

1.1.4 Oceanic pumps

There are three oceanic processes, termed oceanic pumps, responsible for modulating the balance of CO_2 stored in the ocean interior and the atmosphere on glacial-interglacial timescales: (i) the solubility pump (Broecker and Peng, 1987), (ii) the carbonate pump (Sigman and Boyle, 2000), and (iii) the biological pump (Knox and McElroy, 1984; Sarmiento and Toggweiler, 1984; Siegenthaler and Wenk, 1984).

The solubility pump theory is based on the solubility of CO_2 in seawater at different temperatures and salinities (Broecker and Peng, 1987). During glacial times a colder glacial ocean has the potential to take up more CO_2 from the atmosphere. However, it is also more saline (due to the accumulation of freshwater in continental ice sheets). This increase in salinity has the reverse effect to temperature, resulting in the release in the CO_2 from the surface ocean. Broecker and Peng (1987) suggest however, that this salinity effect may be compensated in the surface ocean by the export of salt to depth through the formation of sea ice associated brines. They propose that a freshening of surface waters results in greater capacity of the ocean to store CO_2, resulting in the net reduction in atmospheric pCO_2. In summary, a cooling coupled with an increase in sea ice associated brines could result in the net uptake of CO_2 during glacial periods.

The ocean carbonate system exerts a significant impact on the concentration of atmospheric CO_2 through its regulation of the partial pressure of aqueous CO_2 in the surface ocean. The partial pressure of aqueous CO_2 is controlled by the speciation of carbon between the different species of dissolved inorganic carbon; aqueous CO_2 ($CO_{2\ (aq)}$), bicarbonate (HCO_3^-) and carbonate (CO_3^{2-}):

$$CO_2(aq) + H_2O \rightleftharpoons HCO_3^- + H^+ \rightleftharpoons CO_3^{2-} + 2H^+ \tag{1.1}$$

It is possible to decrease the partial pressure of aqueous CO_2 by shifting the balance of equilibrium away from CO_2. Dissolved inorganic carbon (DIC) and alkalinity (ALK) can be used to track the balance of equilibrium:

$$ALK = \left[HCO_3^-\right] + 2\left[CO_3^{2-}\right] \tag{1.2}$$

$$DIC = \left[CO_2(aq)\right] + \left[HCO_3^-\right] + \left[CO_3^{2-}\right] \tag{1.3}$$

An increase in the ALK:DIC ratio describes an increase in the concentration of carbonate ion relative to aqueous CO_2, i.e. a shift in the equilibrium balance away from CO_2. It is possible to change the ALK:DIC ratio through various processes, such as carbonate formation/dissolution or photosynthesis/respiration.

The marine carbonate pump involves the production of calcium carbonate ($CaCO_3$) by marine organisms and its subsequent transport to depth. In the surface ocean, the formation of calcium carbonate ($2HCO_3^- + Ca^{2+} \rightarrow CaCO_3 + CO_2 + H_2O$) has the effect of decreasing the ALK:DIC ratio, which pushes the equilibrium balance towards CO_2. This imbalance is corrected by the outgassing of atmospheric CO_2 from the surface ocean.

In contrast the biological pump (sometimes referred to as the soft-tissue pump) refers to the formation of organic matter through photosynthesis, and its subsequent export to the deep ocean:

$$106CO_2 + 16NO_3^- + HPO_4^{2-} + 139H_2O \rightarrow C_{106}H_{261}O_{109}N_{16}P + 138O_2 + 18OH^- \tag{1.4}$$

This reaction results in a strong decrease in DIC relative to ALK. This increase in the ALK:DIC ratio shifts the equilibrium away from CO_2 resulting in the net uptake of CO_2 from the atmosphere by the surface ocean. The relative production of organic carbon versus carbonate in the surface ocean is therefore important in determining whether the surface ocean acts as a net carbon source or sink.

In summary, the three oceanic pumps can be used to conceptually understand glacial-interglacial changes in atmospheric CO_2. During glacial periods, the cooling of surface waters coupled with the increase in production of sea ice can result in the uptake of CO_2 by the surface ocean through the solubility pump. Additionally, a change in the production of organic carbon relative to carbonate can result in CO_2 uptake through a decrease in the carbonate pump and an increase in the biological/soft-tissue pump.

1.1.5 The Southern Ocean's role in glacial-interglacial CO_2 change

The Southern Ocean has long been identified as a region of climatic importance (Knox and McElroy, 1984; Sarmiento and Toggweiler, 1984; Siegenthaler and Wenk, 1984). Here, the upwelling of deep water and the formation of Antarctic Bottom Water (AABW) and Antarctic Intermediate Water (AAIW) provides a two-way exchange of CO_2 between the deep ocean and the atmosphere. Processes within the Southern Ocean have been suggested to have decreased atmospheric CO_2 during glaciations by influencing the three oceanic CO_2 pumps. These Southern Ocean processes

include; (i) increased sub-Antarctic productivity through iron fertilisation (Martin, 1990); (ii) decreased air-sea gas exchange via increased surface ocean stratification (François et al., 1997); (iii) decreased vertical mixing through changes in the deep ocean density (Toggweiler, 1999), or through changes in the South-Westerly Winds (SWWs) which drive upwelling of deep water (Toggweiler et al., 2006).

In the Southern Ocean, wind-driven upwelling brings carbon- and nutrient rich deep water to the surface (Marshall and Speer, 2012; Russell et al., 2006). However, despite the high concentration of macronutrients, productivity in the modern Southern Ocean remains relatively suppressed because of the limitation of light and micronutrients such as iron (de Baar et al., 1995). This high-nutrient low-chlorophyll signature of the Southern Ocean suggests a large untapped potential of the Southern Ocean for drawing down CO_2 through an increase in the efficiency of the biological pump (Martin, 1990). Evidence of increased productivity in the sub-Antarctic (Kohfeld et al., 2013, and references therein) appear to support the idea of an increase in the efficiency of the biological pump during glacial times.

An alternative explanation involves supressing the Southern Ocean 'CO_2 leak' during glacial periods by invoking physical stratification of the surface ocean. The presence of sea ice and its associated meltwater lenses can provide a density barrier preventing upwelled CO_2-rich deep water from outgassing to the atmosphere. Nitrogen isotopes measured on particulate organic matter suggest a significant decrease in the vertical supply of nitrate to the euphotic zone during the Last Glacial Maximum (LGM), which has been taken as evidence of increased stratification of the upper water column (François et al., 1997). Supporting evidence for this hypothesis comes from sea-ice associated diatoms assemblages that suggest a significant expansion of Antarctic sea ice during glacial times (Allen et al., 2011; Collins et al., 2012; Gersonde et al., 2005; Shemesh et al., 2002) providing a potential mechanism for shallow stratification. Thus, a decrease in air-sea gas exchange in the Southern Ocean could also play a role in reducing atmospheric CO_2 during glacial times.

Alternatively, the Southern Ocean CO_2 leak can be 'plugged' deeper in the water column. Deep ocean density stratification has been suggested to be important in trapping CO_2-rich deep water in the abyssal ocean (Toggweiler, 1999) during glacial periods. Reconstructions of deep water temperature and salinity from porewaters suggest that the Last Glacial Maximum (LGM) deep Southern Ocean was significantly more dense than it is today (Adkins et al., 2002), and therefore had the potential to sequester CO_2. A wealth of geochemical proxy data provides supporting evidence for a poorly mixed interior ocean during glacials. These records evidence a discrete chemical divide at 2500 m (Hodell et al., 2003b) separating poorly ventilated (Skinner et al., 2010) highly respired (Boyle, 1988; Hodell et al., 2003b) deep water from well ventilated (Burke and Robinson, 2012; de Pol-Holz et al., 2010) intermediate water.

Besides deep ocean density stratification, the interaction between the deep ocean and atmosphere can also be reduced through a decrease in rate of upwelling. Wind-driven upwelling south of the Polar Front (PF) ventilates the modern deep ocean. During glacial times, it is hypothesised that a migration of the SWWs results in a decrease in upwelling across the Antarctic Circumpolar Current (ACC) and thus a reduction in the CO_2 outgassing from the Southern Ocean (Toggweiler et al., 2006). The position of the SWWs during glacial periods is notoriously difficult to constrain. Land-based proxy records of precipitation changes in southern South America and the sub-Antarctic islands suggest a general decrease in precipitation during glacial periods which has been

interpreted to reflect the equatorward migration of the Southern Westerly Winds (SWWs) (Kohfeld et al., 2013). However, modelling studies (Sime et al., 2013) suggest that this pattern of precipitation could also be reconciled with a poleward migration, arguing that precipitation proxies alone are ambiguous and cannot be used as evidence of a northward migration. Regardless of direction, a change in the influence of the SWWs on the ACC could be an important factor in regulating the atmospheric CO_2 on glacial-interglacial timescales.

In summary, there are multiple mechanisms within the Southern Ocean which have been proposed to reduce the Southern Ocean CO_2 leak during glacial times. These mechanisms include an increase in surface productivity and an increase in both shallow and deep ocean stratification. There is proxy evidence that has been used to provide support for each scenario. One difficulty with many of these proxy records (e.g. Adkins et al. 2002; Gersonde et al. 2005; McCave et al. 2014) is that they typically compare snapshots of LGM conditions relative to the modern, or have low temporal resolution (e.g. Allen et al. 2011; François et al. 1997; Kumar et al. 1995) such that it is difficult to resolve time dependent changes across the glacial termination. Therefore, it is often challenging to determine the significance of each of these proposed mechanisms in terms of driving changes in atmospheric CO_2. Furthermore, the vast majority of the proxy data reconstructions of changes in the Southern Ocean focus on the last glacial termination, which typically contains the most complete and highest resolution sequences of changes across deglaciations. However, the penultimate deglaciation (135-125 ka), which spans the transition to the Last Interglacial - a time when global temperatures were typically warmer than the average interglacial (Past Interglacials Working Group of PAGES, 2016) - is an important time interval to study with respect to future climate change. Reconstructions of changes in Southern Ocean circulation, productivity and stratification across this transition can potentially provide information about the important feedbacks in the climate system in a warmer climatic state.

1.1.6 The southwest Atlantic

Whilst the deep ocean has been identified as an important sink of CO_2, the sluggish ventilation of deep water masses (François et al., 1997; Goldstein et al., 2001; Sikes et al., 2000) suggests that the more dynamic circulation of intermediate waters may play an important role in destabilising the climate at glacial terminations. Numerical and conceptual models have increasingly highlighted the active role that Southern Hemisphere intermediate water masses play in driving climate variability (Seidov, 2001; Weaver et al., 2003). In particular, the interplay of AAIW and North Atlantic Deep Water (NADW) has often been cited as a key factor in regulating ocean overturning circulation (Pahnke et al., 2008; Rickaby and Elderfield, 2005).

AAIW primarily forms in the southeast Pacific (Talley, 1999) where winter cooling of Sub-Antarctic Mode Water (SAMW) results in the densest classes of SAMW subducting to form AAIW (Rintoul and England 2002; Sloyan and Rintoul 2001; Talley 1999; Figure 1.3). AAIW enters the Atlantic basin through the Drake Passage (the so-called 'cold water route') where it is modified by precipitation and mixing with Antarctic Surface Waters (AASW) before subducting and spreading into the South Atlantic sub-tropical gyre through eddy mixing out of the Falkland Current (Talley 1999; Figure 1.3). Today, the volumetric contribution of water passing through this 'cold-water route' is equal to the amount of water that enters the Atlantic from the Indian Ocean – the so-called

'warm-water route' (Speich et al., 2001). The southwest Atlantic therefore presents an important site to study the AAIW end-member as it enters the Atlantic Basin.

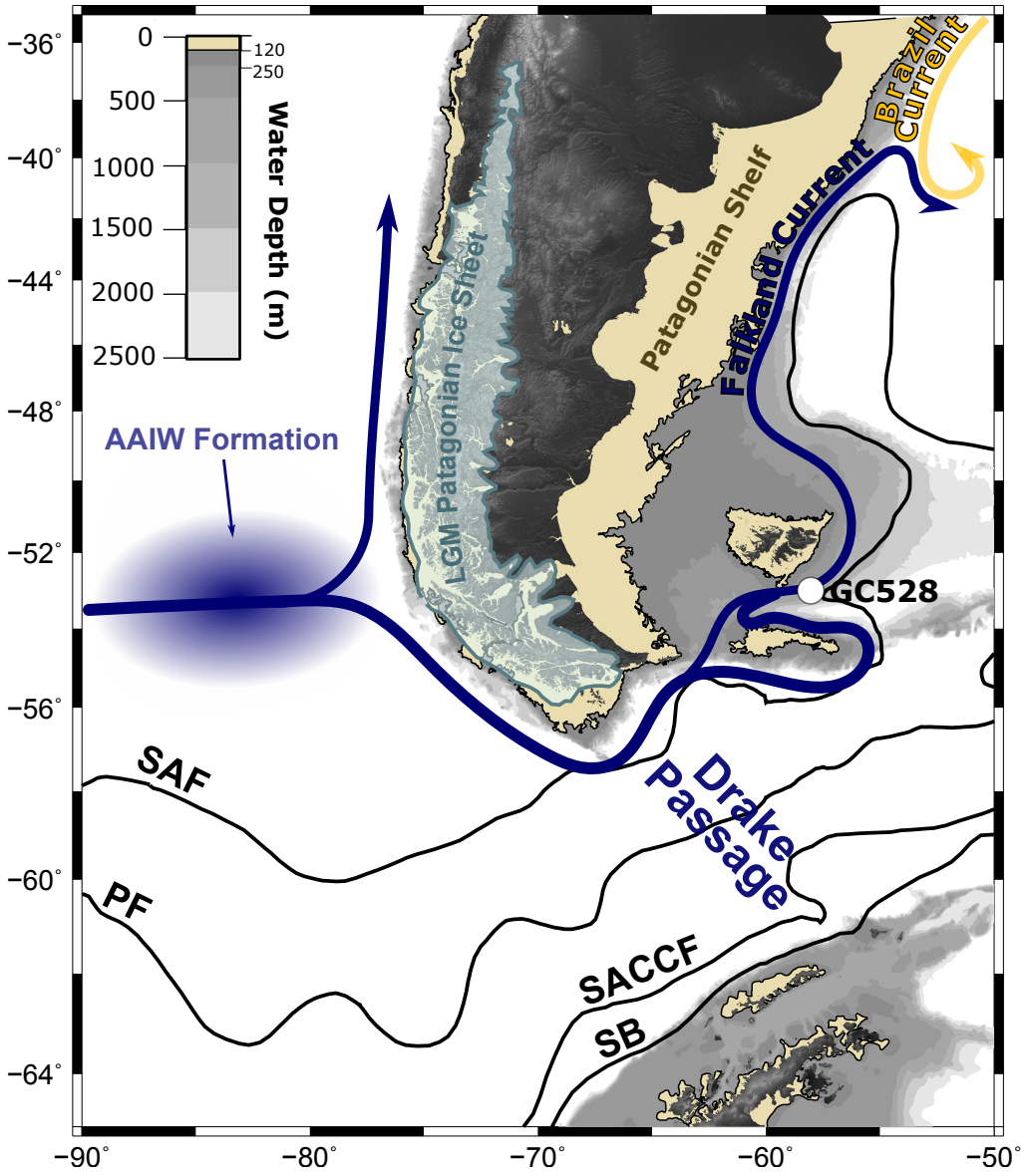

Figure 1.3: Map of the Drake Passage and southern South America showing the main route of Antarctic Intermediate Water (AAIW; blue) into the Atlantic Basin. The main oceanic fronts are shown as black lines; the Sub-Antarctic Front (SAF), the Polar Front (PF), the Southern ACC Front (SACCF) and the Southern Boundary Front (SB).

Ocean dynamics in the southwest Atlantic and the Drake Passage may have been influenced by the Patagonian Ice Sheet (PIS) over glacial terminations. During the Last Glacial Maximum (LGM) the PIS was the largest southern hemisphere continental icesheet, apart from Antarctica. Terrestrial and sub-marine mapping of glacial landforms suggests that the western PIS was marine-terminating at the LGM (DaSilva et al., 1997) whilst the eastern PIS was dominated by gently sloping ice tongues which spread east down the Strait of Magellan from an ice cap centred over the crest of the Andes (McCulloch et al. 2000; Figure 1.3). The deglaciation of the PIS contributed a

significant flux of freshwater into the South Pacific - a location critical to the formation of AAIW. Modelling studies (Weaver et al., 2003) have shown that freshwater 'hosing' in the region of the Drake Passage has the potential to significantly impact overturning circulation. However, proxy data of changes in AAIW export into the Atlantic over the termination remains sparse.

Finally, the Patagonian continental shelf in the southwest Atlantic represents one of the most expansive continental shelves in the world. Productivity on the shelf accounts for the sequestration of 0.3-0.6 $PgCa^{-1}$(Takahashi et al., 2002), 15-30% of the modern net oceanic CO_2 uptake. Glacial-interglacial changes in the strength of the biological pump in this region currently represents a major source of uncertainty in the global carbon budget.

In summary, the southwest Atlantic represents an important, yet under-studied, region of the ocean that has the potential to strongly affect global climate. Variations in the PIS, Antarctic sea ice and the SWWs all have the potential to influence the structure of the surface ocean and the export of AAIW through the Drake Passage, with consequences for global overturning circulation. Additionally, changes in the strength of the biological pump over the Patagonian Shelf may play an important role in the ocean's ability to uptake CO_2. This thesis addresses these gaps in the current knowledge through proxy-based reconstructions of changes in the water masses in the southwest Atlantic over the last two glacial terminations.

1.2 Thesis outline

In this thesis, I present a number of studies in which I reconstruct the changes in the carbonate, solubility and biological pumps over glacial terminations, and discuss how these changes relate to variations in atmospheric CO_2. Proxy records from two marine sediment cores from intermediate water depth (600 m) in the southwest Atlantic form the basis of this thesis, supplemented by records generated from other cores in the South Atlantic and Southern Ocean.

Chapter 2 describes the main methods used in the generation of proxy records from GC528 and GC642. The justification for choosing a particular proxy is explained within each science chapter.

Chapter 3 describes the age models underpinning the two main core sites. I discuss the merits and failings of using stratigraphic alignment to determine the age model in each of these cores. I demonstrate that because of the shallow nature of the core site, the oxygen isotope record may not be responding to a 'global' change and thus tuning of the benthic oxygen isotope record to the global benthic stack (LR04; Lisiecki and Raymo 2005) is not appropriate. Instead, I suggest the correlation of sea surface temperature records to Antarctic temperature records provides a more robust age model across Termination II. I explain that whilst it is possible to achieve good age constraints across the two glacial terminations, the age models in other sections of the core are relatively unconstrained. Based on the difficult in reconstructing age models outside of glacial terminations, the subsequent science chapters focus solely on the terminations.

In Chapter 4, I address the hypothesis that changes in deep ocean density stratification are linked to the deglacial rise in atmospheric pCO_2. I make the first reconstruction of the evolution of deep (3700m) and intermediate (600m) water density over the last deglaciation. These reconstructions of the physical density gradient of the South Atlantic are compared to changes in the chemical ($\delta^{13}C$, ^{14}C) gradient and variations in atmospheric pCO_2 over the last deglaciation. I show evidence of a

clear difference in the timing of the breakdown in the physical gradient relative to the breakdown in the chemical divide and the rise in atmospheric pCO_2. I argue that deep ocean density destratification (in the South Atlantic) is not responsible for the rise in atmospheric pCO_2 over the last deglaciation.

Chapter 5 discusses the relationship between ACC flow velocity and its density structure in the Drake Passage region over the last two glacial terminations. I show evidence of changes in ACC bottom current flow related to changes in the deep ocean density (reconstructed in Chapter 4). I provide evidence of millennial-scale reductions in Drake Passage through-flow linked to the expansion of Antarctic sea ice, and explore the potential effects that this reduction had on Atlantic Meridional Overturning Circulation.

In Chapter 6, I explore how changes in the strength of the biological pump in highly productive shelf regions in the sub-Antarctic may have impacted the ocean's ability to uptake CO_2 from the atmosphere. I find evidence of significant glacial-interglacial changes in the C_{org}:$CaCO_3$ ratio over the last two glacial terminations which imply a major reduction in ocean CO_2 uptake in these regions during interglacial periods. I argue that the deglacial change in the biological pump in these highly productive sub-Antarctic shelf regions represents an important component of the global carbon cycle.

In Chapter 7, I summarise the main findings in each of the science chapters and discuss the wider implications of this work for understanding climate change across glacial terminations. I assess the relative importance of the different oceanic pumps in regulating climate over deglaciations and discuss the remaining gaps in the state of knowledge.

Chapter 2

Materials and Methods

This chapter introduces the two marine sediment cores that will form the basis of this thesis. The second half of the chapter describes the main methodologies which have used to generate proxy records from these cores. I leave the justification for the use of each proxy to the science chapters (Chapters 3-6).

2.1 Material

Two marine sediment cores (GC528 and GC642) are used throughout this thesis to reconstruct climate variability in the southwest Atlantic over the last two glacial terminations. Additional cores which supplement the analysis carried out on GC528 and GC642 are used to develop a more regional understanding of oceanic changes occurring across glacial terminations. In this section, I discuss the decision behind the acquisition of the two main cores (GC528 and GC642) and the basic interpretation of the sedimentary sequence at both sites.

Table 2.1: Locations and coring information for sites GC528 and GC642.

Core	**Latitude (^{o}N)**	**Longitude (^{o}E)**	**Depth (mbsl)**	**Cruise**	**Date recovered**	**Recovery (m)**
GC528	-53^o 00.78'	-58^o 02.43'	598	JR244	Jan 2011	7.14
GC642	-53^o 00.02'	-58^o 04.64'	578	JR257	Mar 2012	7.35

Figure 2.1: Map and seismic reflection profile of the South Falkland Slope Drift. (A) Low- and (B) High- resolution map of the southwest Atlantic showing the location of the site GC528/GC642 on the South Falkland Slope Drift. Main jets of the Falkland Current (blue arrows); Sub-Antarctic Front (SAF; green line); estimated thickness of drift (Koenitz et al. 2008; coloured contours); GC528 (dark blue dot); GC642 (light blue dot); (C) Salinity (purple) and oxygen (blue) concentration profile taken from the Falkland Trough shows the position of GC528/GC642 relative to main water masses in the region; (D) Seismic reflection profile SGFI93_107 and interpretation of the major stratigraphic units within the SFSD (Koenitz et al., 2008).

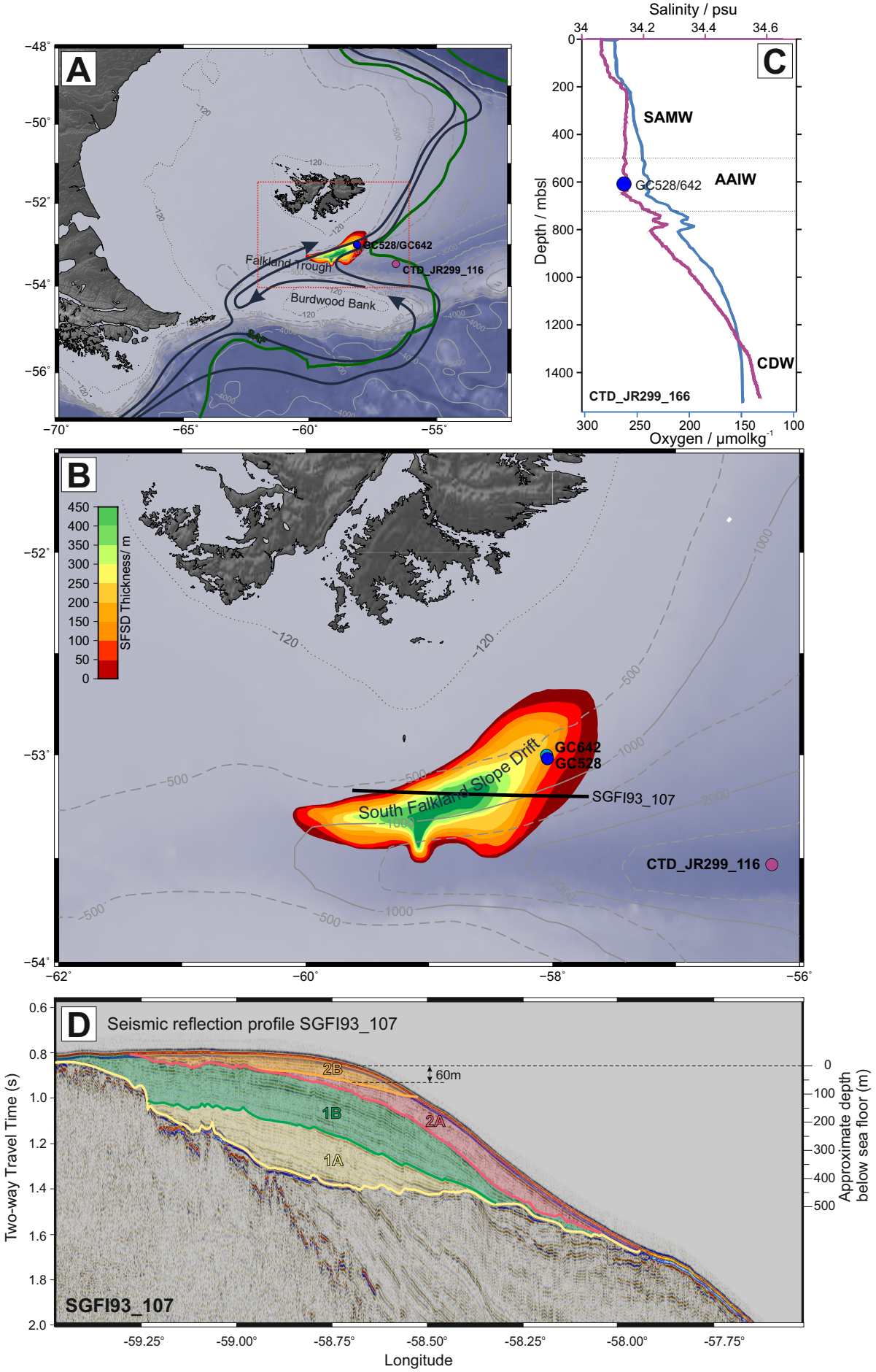
A
GC528/GC642
CTD_JR299_116
Falkland Trough
Burdwood Bank
−48˚
−50˚
−52˚
−54˚
−56˚
−70˚
−65˚
−60˚
−55˚
C
Salinity / psu
34
34.2
34.4
34.6
SAMW
AAIW
CDW
GC528/642
CTD_JR299_166
Depth / mbsl
Oxygen / µmolkg-1
B
SFSD Thickness/ m
South Falkland Slope Drift
GC642
GC528
SGFI93_107
CTD_JR299_116
−52˚
−53˚
−54˚
−62˚
−60˚
−58˚
−56˚
D
Seismic reflection profile SGFI93_107
2B
1B
1A
2A
60m
SGFI93_107
Two-way Travel Time (s)
Approximate depth below sea floor (m)
Longitude
-59.25°
-59.00°
-58.75°
-58.50°
-58.25°
-58.00°
-57.75°

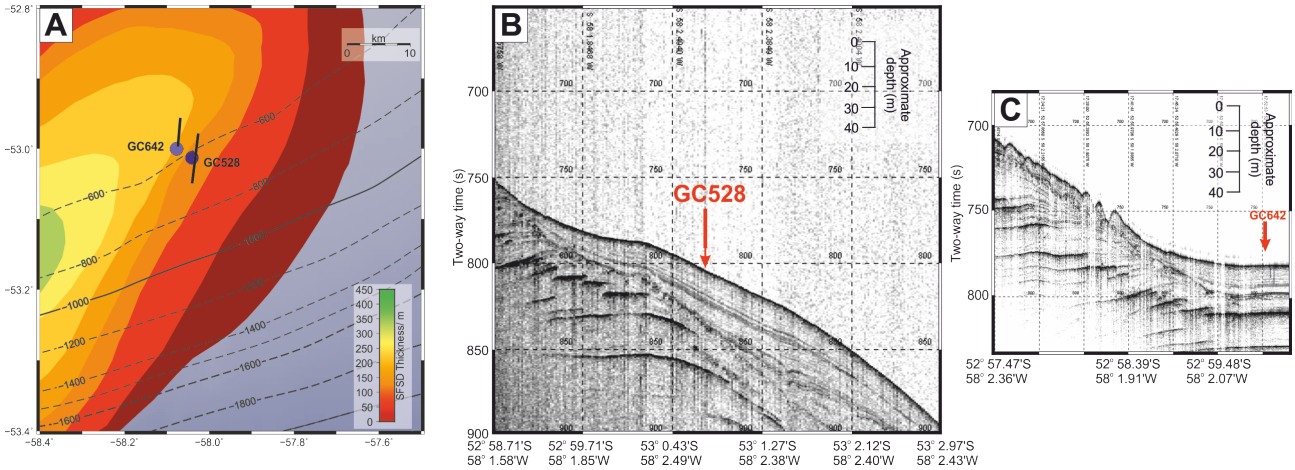

Figure 2.2: TOPAS sub-bottom profiles of site location GC528 and GC642. (A) Map of region showing the two cores GC528 (dark blue) and GC642 (light blue) in relation to the SFSD (thickness as coloured contours) and bathymetry (grey contours); (B) TOPAS sub-bottom profile of site GC528; (C) TOPAS sub-bottom profile of site GC642.

2.1.1 Sediment core acquisition

Gravity cores (GC) 528 and 642 (Figure 2.1; Table 2.1) were collected on British Antarctic Survey (BAS) cruises JR244 (January 2011) and JR257 (March 2012) on the RRS *James Clark Ross*. The two cores are located on the upper flanks of the South Falkland Slope Drift (SFSD), a large contourite deposit on the Falkland Margin. The SFSD is strongly influenced by sub-Antarctic Front (SAF), the most northerly ACC jet, as it emerges from Drake Passage. Deposited between 400 to 2000 m water depth (Figure 2.1), the SFSD is ideally situated to monitor orbital scale variability in the export of AAIW beneath the SAF throughout the Quaternary. High-resolution seismic reflection profiles taken across the SFSD reveal four main sedimentary units, totalling up to 450 m thick, likely deposited since the deep opening of Drake Passage in the Early Miocene (Figure 2.1D; Koenitz et al. 2008). The uppermost unit (2B), which at its most expanded is approximately 60 m thick, is a continuous sedimentary sequence thought to date back 4.7 Myr (Koenitz et al., 2008).

Site selection: The Kongsberg EM122 multibeam echosounder was used in conjunction with the Kongsberg TOPAS PS18 parametric sub-bottom profiler to map out new areas of sea-floor bathymetry and to survey the geology of the shallow sub-surface. The main use of the EM122 was to obtain detailed swath bathymetry in areas proposed for coring in order to identify geological features that would provide a context for recovered sediments. The TOPAS profiler was used to survey and subsequently pin-point suitable sites for deploying the BAS gravity corer (Figure 2.2). The aim was to find suitable sedimentary sequences which appeared to be continuous and showed no evidence of disturbances or hiatuses in the top 20 m of sediment.

Gravity core setup: The BAS gravity corer utilises a combination of 3 m- and 6 m-long steel barrels, the top end of which is nailed to a bomb weight. Inside the barrels are pre-marked core liners taped together for deployments >6 m and with arrows pointing up and labelled. The gravity corer was typically veered into the seabed at 54 m/min. GC528 was collected with a gravity core

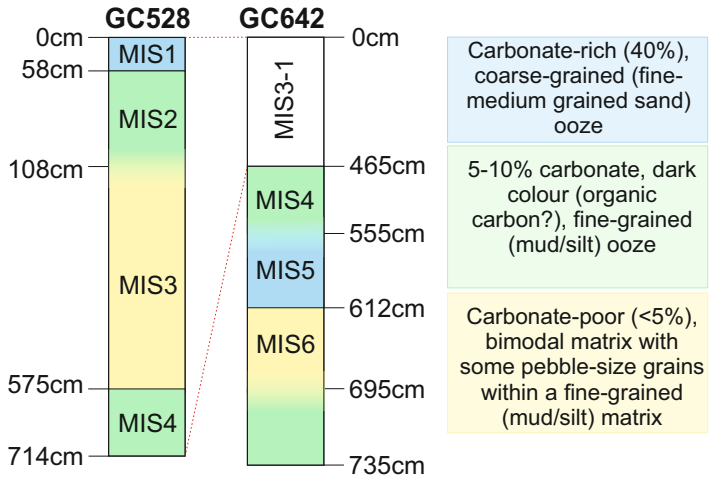

Figure 2.3: Summary of main features of the sedimentary log of GC528 and GC642.

rigged with a 9 m-long barrel; 7.17 m of sediment were recovered. Based on sedimentation rates (1.3 cm/kyr) published by Koenitz et al. (2008), which rely on the correlation of the base on the main stratigraphic units to significant climatic/circulation events, the base on core GC528 was expected to date back to 500 ka. However, upon opening the core it was apparent (Section 2.1.2) that the core spans a maximum of 80 ka. The following year, a larger gravity corer was deployed (14 m-long barrel) in a more condensed sequence of the contourite in the attempt to recover a longer sequence of time. Despite the longer core barrel, the recovery of GC642 was restricted to 7.37 m, however observations of sedimentological variations (Section 2.1.2) reveal that core is markedly older and likely spans the Last Interglacial (125 ka).

2.1.2 Lithology and core description

The cores were split using a router and guiding system. The working half of the cores was logged as soon as possible after splitting, before oxidation and water losses could significantly modify the colour of the sediments. Images of each section of the core were taken using a digital Colour Line Scan Camera. Colour quantification (L*a*b*) was performed on the high-resolution (70 µm) images to establish a stratigraphic sequence within the core.

The top of core GC528 is comprised of carbonate-rich (40%) sand; both benthic and planktonic foraminifera were identified within this section of the core (Figures 2.3). At 58 cm there is an abrupt transition to a finer, darker sediment type bearing significantly less carbonate, and a greater concentration of organic matter. This organic-rich unit is present between 58-107 cm after which there is a gradual transition to a slightly coarser unit which contains very little biogenic carbonate, and some pebble-sized grains. This coarser unit is present between 107-575 cm, below which a darker organic-rich, carbonate-bearing (<10%) sediment (similar to the unit in between 58-107 cm) is present. Based on the variations in sediment type, I suggest that the top 0-58 cm dates to MIS1, the dark organic-rich sediment between 58-108 cm and 575-714 cm refers to MIS2 and MIS4 respectively, and the expansive carbonate-poor interval between 58-107 cm spans MIS3.

All sections of gravity core GC642 were split and logged, however only the lower 276 cm

of the core (which contains the most variability in the sedimentary sequence) is described here. The top of section 6 (465 cm core depth) contains a relatively dark organic-rich sediment. This unit is present until 555 cm at which point a gradual transition to carbonate-rich (>30%) sediment occurs. This interval is very similar to the interval between 0-58 cm in GC528, and likely dates back to the Last Interglacial (MIS5). The inferred interglacial unit is present between 555-612 cm after which an abrupt transition to carbonate-poor sediment occurs. The carbonate-poor sediment (which might be MIS6) continues until 695 cm. Between 695 cm and the base of the core 735 cm, a gradual transition to more organic-rich, carbonate-bearing (<10%) mud occurs. I suggest that the carbonate-rich sand between 555-612 cm was deposited during an interglacial period, however whether it spans all of MIS5, or solely the climatic optimum of the Last Interglacial, i.e. MIS5e, remains ambiguous and requires further age constraints (see Chapter 3).

2.2 Methods

In this section, I detail all the methods used in the following science chapters. I describe in detail how each proxy was obtained, the process of preparing samples and extracting the data. I leave the justification for the use of each proxy to the science chapters themselves. The analyses performed on the two cores can be grouped based on the size fraction that they were measured from (Figure 2.4).

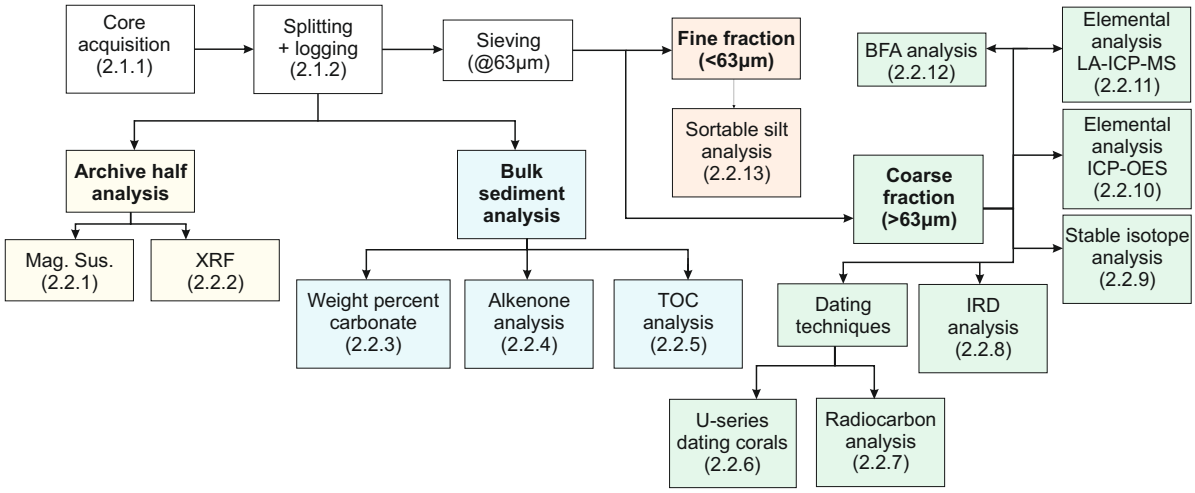

Figure 2.4: Flow diagram showing the main analytical techniques used in this thesis. The numbers in brackets refers to the section in the text.

2.2.1 Magnetic susceptibility

High resolution (1 cm) magnetic susceptibility records were generated on cores GC528 and GC642 using a multi-sensor core logger - standard (MSCL-S) at the British Oceanographic Sediment Core Research Facility (BOSCORF), Southampton. Magnetic susceptibility is the degree of magnetisation of a material in response to an applied magnetic field. It is measured by passing a low intensity (approx. 80 A/m RMS) non-saturating, alternating magnetic field (0.565 kHz) close to

the core. Any material in the vicinity of the sensor that has a magnetic susceptibility will cause a change in the oscillator frequency. This pulsed frequency information is converted into magnetic susceptibility values. The MSCL-S is calibrated at the manufacturers and thus all magnetic susceptibility sensors supplied should record exactly the same value for any given sample. Magnetic susceptibility values are expressed in non-dimensional SI units.

2.2.2 X-ray Fluorescence (XRF)

Variations in the elemental composition of the sediment were determined using XRF analysis. XRF analysers determine the chemistry of a sample by measuring the fluorescent x-ray emitted from a sample when it is excited by a primary x-ray source. This method is non-destructive and allows for very high resolution (2.5 mm) records of elemental concentrations downcore. The split core surface was carefully scraped clean and covered with a 4 µm thin Ultralene film to avoid contamination and prevent desiccation (Richter et al., 2006). XRF analysis was carried out using an Avaatech XRF core scanner at the Godwin Laboratory for Palaeoclimate Research. Each section was scanned three times: at 10 kilovolts (kV) to measure Al to Fe (including Si and Ca), at 30 kV to measure Pb to Fe (including Sr and Zn), and at 50 kV to measure Rb through Ba. Quantitative assessment of the spectra was determined by running the measurements through the advanced spectrum interpretation software package WinAxil. In order to account for heterogeneity of the sediment (e.g. variable water content and grain-size distribution), irregularities of the split core surface and spatial variations in thickness of the pore-water film, log-ratios were used to express downcore variability in the elemental concentrations (Weltje and Tjallingii, 2008).

2.2.3 Weight percentage carbonate

Percent carbonate ($CaCO_3$) was determined by coulometric titration on a UIC model 5011 Coulometer and Carbonate Carbon System 140 (Engleman et al. 1985); acidifying dried bulk sediment with 10 % phosphoric acid. Precision is estimated to be ±1.0% (1σ, n=120) based on replicate analysis of reagent-grade $CaCO_3$ (100%).

2.2.4 Alkenone analysis

Sea surface temperatures (SSTs) were inferred from the derivation of the U^K_{37} index (Prahl and Wakeham, 1987) from alkenone analysis of cores GC528 and GC642.

Lipids were extracted from ~3 g of homogenised, freeze-dried sediment using a CEM microwave system with 12 mL of Dichloromethane (DCM):MeOH (3:1, v/v). Internal standards were added for quantification (5α-cholestane, dotriacontane and tetracontane). The microwave temperature programme heated samples to 70 °C over 5 min, held at 70 °C for 5 min and then cooled down over 30 min (Kornilova and Rosell-Melé, 2003). The supernatant was then decanted into vials, and the extracts were dried under a gentle stream of nitrogen. The total lipid extract was separated using silica column chromatography, with the alkenone-containing fraction recovered using 100% DCM.

The relative abundances of di-, tri-, and tetra-unsaturated C_{37} alkenones were measured using two different methods: gas-chromatograph fitted with a flame ionisation detector (GC-FID) and

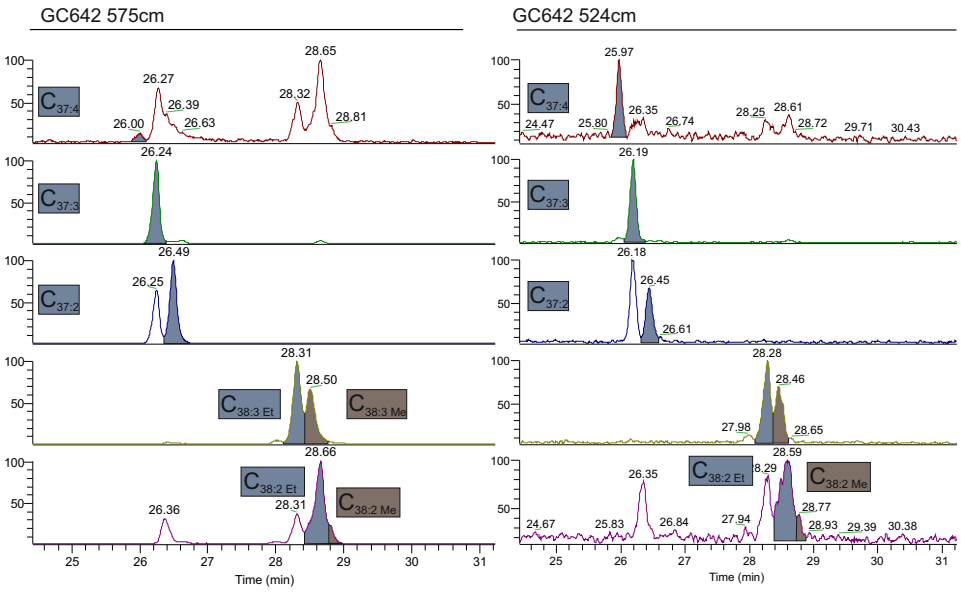

Figure 2.5: Example chromatograms from the core GC642. The peaks related to the di-, tri-, and tetra unsaturated ketones with 37 carbon atoms are highlighted, as are the di- and tri- unsaturated ketones with 38 carbon atoms. (Left) GC642 575 cm, an interglacial sample; (Right) GC642 524 cm, a glacial sample.

gas-chromatography with chemical ionisation mass spectrometry (GC-CIMS). The advantage of GC-CIMS is that it is possible to target specific compounds using the relative retention times compared with those of known standards. This provides precise relative abundances of specific target compounds. In contrast, GC-FID provides quantitative information about the abundance of C_{37} alkenones relative to an internal standard, and thus can provide information about the total concentration of C_{37} alkenones in a given sample. The samples in this thesis have been measured both by GC-FID and GC-CIMS, this work was carried out at the University of Durham.

GC-FID method: Separation was achieved using a 30 m HP-5MS fused silica column (0.25 mm i.d., 0.25 µm 5% phenyl methyl siloxane) and using He as the carrier gas. Following injection, the oven temperature was programmed as: 60–200°C at 20°C/min, 200-320°C at 6°C/min, held at 320°C for 35 min.

GC-CIMS method: Alkenones were measured on a Trace Ultra gas chromatograph directly coupled to a Thermo DSQ single quadrupole mass spectrometer, fitted with a programmed temperature vapourising (PTV) injector. Alkenones were separated using a 30m x 0.25 mm i.d., Restek RXi-5ms column (0.25µm 5% diphenyl-95% dimethyl polysiloxane coating). Helium was employed as the carrier gas (2 ml min^{-1}). The injector was held at 120°C and splitless mode (1.2 min) during injection, and then immediately temperature programmed from 120°C to 310° at 10°C s^{-1}, then held for 0.6 min. The oven was programmed to hold at 200°C for 1 min, then increased to 310°C at 6 °C min^{-1}, and held at 310°C for 12 min. The mass spectrometer was operated in positive chemical ionisation mode (PICI), using high-purity anhydrous ammonia (N6.0, BOC) introduced to the ion source through the CI gas inlet. Selected ion monitoring was performed, targeting the 8 ions corresponding to the $[M + NH4]^+$ adducts of the target C_{37} and C_{38} alkenones and the internal

standard (nonadecanone), each with a SIM width of 1 m/z and a dwell time of 30 ms. The target m/z were: 300 (nonadecanone), 544 ($C_{37:4}$), 546 ($C_{37:3}$), 548 ($C_{37:2}$), 560 ($C_{38:3Et}$ and $C_{38:3Me}$), 562 ($C_{38:2Et}$ and $C_{38:2Me}$), 564 and 578 (C_{36} alkyl alkenoates) (Rosell-Mele et al., 1995).

The principle compound groups analysed in this thesis, the long chained alkenones, have distinctive patterns in the GC chromatograms. Compound quantification was achieved by integrating the areas under the compound-specific peaks using the software Xcalibur (Figure 2.5). The U^K_{37} index is based on the relative concentrations of di-, tri-, and tetra unsaturated ketones with 37 carbon atoms Prahl and Wakeham (1987):

$$U^K_{37} = \frac{C_{37:2} - C_{37:4}}{C_{37:2} + C_{37:3} + C_{37:4}} \tag{2.1}$$

Sea surface temperatures were estimated based on the U^K_{37}-SST calibration of (Prahl et al., 1988):

$$SST = \frac{U^K_{37} - 0.093}{0.03} \tag{2.2}$$

The U^K_{37} index was used to derive SSTs rather than the more commonly used $U^{K'}_{37}$ because previous studies from the sub-Antarctic found better agreement of the temporal trend of the U^K_{37}-SST records with other surface proxy records (Ho et al., 2012).

Throughout the alkenone analysis, the relative abundance of ΣC_{37}:ΣC_{38} alkenones was monitored. The abundance of C_{37} and C_{38} alkenones within a sediment sample has been linked to shifts in the dominant alkenone-producing haptophyte population (McClymont et al., 2005). *E.huxleyi* typically produces alkenones with ΣC_{37}:ΣC_{38} in the range 0.9-2.26, whereas *G.oceanica* (the second most dominant alkenone-producing haptophyte) produces alkenones ΣC_{37}:ΣC_{38} in the range 0.59-0.81 (Volkman et al., 1995).

In Chapter 6, I use the total alkenone concentration as a proxy for productivity. Quantification was achieved by comparing integrated peak areas to those of the internal standard 5a-cholestane. The peak areas of the C_{37} alkenones with di-, tri-, and tetra unsaturations were used to calculate the total alkenone concentration:

$$[C_{37}] = \frac{M_s A_{C_{37}}}{M_x A_s} \tag{2.3}$$

where $[C_{37}]$ is the concentration of C_{37} alkenone, M_s is the mass of standard added to the sample, $A_{C_{37}}$ is the total area of alkenone on the chromatograph, M_x is the mass of sediment extracted and A_s is the area of the standard on the chromatogram.

2.2.5 Total Organic Carbon analysis

Samples (<5 cm^3) of wet mud were sampled from the cores at a 5 cm resolution for organic carbon analysis (Total Organic Carbon, TOC, and stable carbon isotopic composition of the organic carbon fraction, $\delta^{13}C_{TOC}$). Initially the carbonate fraction was removed by acidifying 3–6 g of sample in 100 ml of 5% HCl. After 24 hr, the solution was diluted using 400 ml of deionised water and left to settle. Three further rinses in deionised water were made to ensure a suitable dilution of the remaining acid. The sample was then dried at 50°C. The dry sample was ground and homogenised

before being weighed out for TOC analysis. TOC analysis was performed by combustion in an online system comprising a Costech ECS4010 elemental analyser (EA) coupled with a VG Triple-Trap and a VG Optima dual-inlet mass spectrometer at the NERC Isotope Geosciences Laboratory (NIGL). Each analytical run contained 10 replicates of the internal NIGL standard BROC2 and 2 replicates of the external standard SOILB. $\delta^{13}C_{\mathrm{TOC}}$ is reported relative to the VPDB standard, with a precision of 0.1‰ (1 S.D.).

2.2.6 Coral U-series dating

Uranium-series dating was carried on a several solitary deep-sea corals found in GC528. U-series dating is based on the principle that carbonate materials incorporate U and Th isotopes in isotopic disequilibrium (Ivanovich, 1994). By measuring the time-dependent activity ratios (^{230}Th/^{238}U), (^{234}U/^{238}U) and (^{232}Th/^{238}U), sample ages can be calculated by solving the decay equation for t:

$$\left(\frac{^{230}Th}{^{238}U}\right) - \left(\frac{^{232}Th}{^{238}U}\right)\left(\frac{^{230}Th}{^{232}Th}\right)_i \left(e^{-\lambda_{230}t}\right) = 1 - e^{-\lambda_{230}t} + \left(\frac{\delta_{234}U_m}{1000}\right)\left(\frac{\lambda_{230}}{\lambda_{230}-\lambda_{234}}\right)\left\{1 - e^{-(\lambda_{230}-\lambda_{234})t}\right\} \quad (2.4)$$

where parentheses denote isotope activity ratios, λ_n is the decay constant of isotope n, t is the sample age, (^{230}Th/^{232}Th)$_{\mathrm{i}}$ is the initial Th activity ratio in the carbonate, and $\delta^{234}U_m$ is the measured ^{234}U/^{238}U activity ratio in permil notation:

$$\delta^{234}U_m = \left(\left(\frac{^{234}U}{^{238}U}\right)_{measured} - 1\right) * 1000 \quad (2.5)$$

The corals were dated using laser ablation (LA) multi-collector ICP-MS (Spooner et al., 2016) in the Bristol Isotope Group (BIG) facilities. Samples (>0.05 g) were cut with a diamond blade, polished flat using P1200 grade sandpaper and rinsed with 18.2 MΩ water. A reusable, pressure-sensitive adhesive (Blu-tac) was used to fix the samples and standards onto the stage. LA analyses were carried using a Photon Machine Analyte G2 193 nm laser attached to a Thermo Finnigan Neptune MC-ICPMS, set up as detailed in Spooner et al. (2016). Samples were ablated along a straight line on the sample surface rather than ablating a single spot. This 'line scan' method maintains a steadier signal intensity and inter-element fractionation compared to spot analyses. The activity ratios (^{230}Th/^{238}U) and (^{232}Th/^{238}U) were determined to an accuracy of 10% and 50% respectively. Samples were bracketed between standards to monitor long-term drift.

In order to solve equation 2.4, the initial activity ratio of ^{230}Th/^{232}Th and the present $\delta^{234}U$ (which was not measured) need to be assumed. Previous studies of cold-water corals suggest a relatively constant $\delta^{234}U_i$, within 10‰ of modern seawater values (Robinson et al., 2014). Therefore, closed-system behaviour is a reasonable first-order assumption for deep-sea corals, and thus the measured ^{234}U/^{238}U activity ratio ($\delta^{234}U_m$) is equivalent to the exponential decay of ^{234}U from an initial

seawater value ($\delta^{234}U_i$) :

$$\delta^{234}U_m = \delta^{234}U_i e^{-\lambda_{234}t} \tag{2.6}$$

I assume the initial activity ratio of ^{234}U/^{238}U is equivalent to seawater, i.e. $\delta^{234}U_i$ =148±10 (Robinson et al., 2005). An initial activity ratio of ^{230}Th/^{232}Th for the sediment is assumed to be in the range 14.8±14.8 (Cheng et al., 2000). A discussion of the errors associated with U-series dating can be found in Section 3.1.3.

2.2.7 Radiocarbon dating

Radiocarbon dating of carbonate in GC528 was carried out in two separate laboratories; some of the samples were picked and sent off to BetaAnalytic for graphitising and AMS ^{14}C dating, whilst other samples (22 of the 28 samples measured) were graphitised in the Godwin Laboratory for Palaeoclimate Research, University of Cambridge and subsequently analysed at the ^{14}Chrono Centre at the University of Belfast by Accelerator Mass Spectrometry. Here, I describe the graphitisation method used in the Godwin Laboratory, and I compare the radiocarbon results produced by both techniques to conclude that no systematic inter-laboratory offset is observed in the ^{14}C ages produced by either method.

Sample preparation: Samples (2-6 mg) of monospecific *Uvigerina bifurcata* were picked from the >125 μm size fraction. For some samples it was necessary to combine benthic foraminifera from two adjacent samples in order to have enough material to date accurately. All samples were crushed between glass plates, transferred to plastic lock-cap vials and cleaned according to a protocol similar to that developed for Mg/Ca analysis (Barker et al., 2003). Clays and particulate carbonate material were removed by repeated rinses in deionised water (Barker et al., 2003) before being transferred to glass vials for drying and graphitisation.

Graphitisation (Godwin Laboratory for Palaeoclimate Research): Samples were graphitised in the Godwin Laboratory for Palaeoclimate Research, University of Cambridge using the hydrogen and iron catalyst method (Vogel et al., 1984). The experimental setup and procedure have been developed (Freeman et al., 2016) to increase the accuracy for running small samples of foraminiferal carbonate. CO_2 is produced by reacting the sample with phosphoric acid in an evacuated vial at 80°C. The CO_2 is then introduced into the line and water vapour removed using an ethanol cold trap at –80°C. The CO_2 is transferred into a reactor and hydrogen added to give the desired H_2:CO_2 ratio. Each reactor is then heated at 650°C for at least 2.5 hr, until the reactor pressure reaches a minimum indicating that graphite has been produced. The graphite is then removed and pressed into cathode targets to be sent to the AMS laboratory (^{14}Chrono Centre at the University of Belfast) along with background and standards.

Comparison of BetaAnalytic and Godwin graphitisation setup: The graphitisation process used by BetaAnalytic is slightly different to that used by the Godwin Laboratory. Graphite is produced by hydrogen reduction of the CO_2 sample over a cobalt catalyst, as opposed to an iron

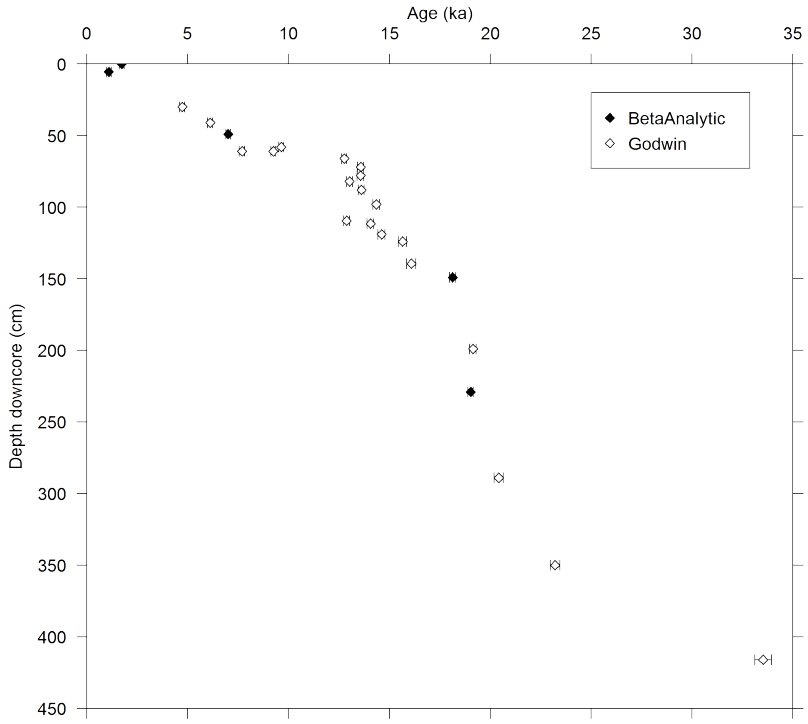

Figure 2.6: BetaAnalytic (black) versus Godwin Laboratory for Palaeoclimate Research (white) ^{14}C ages for core GC528.

catalyst. Additionally the CO_2 trapped for graphitisation is produced via the combustion of the sample at 800°C under a 100% oxygen atmosphere, as opposed to through the addition of concentrated acid. There is therefore the potential that variations in the methods could lead to small fractionation effects that could compromise the use of the radiocarbon data in placing downcore age constraints. The radiocarbon dates produced by the two laboratories are shown in Figure 2.6. There is no apparent systematic offset in the ages of the radiocarbon samples run at BetaAnalytic compared to those produced from graphitisation at the Godwin Laboratory for Palaeoclimate Research. This does not imply that methodological differences do not result in variable fractionation, however it shows that any offset produced by the difference in method is significantly smaller than the natural variability and errors associated with the AMS ^{14}C dating procedure.

Radiocarbon calibration and reservoir correction: Carbon-14 ages were converted to calendar ages using the Marine13 dataset (Reimer et al., 2013). The atmosphere-deep ocean offset (i.e. the 'reservoir age') was taken from paired U-Th/^{14}C ages in corals (Burke and Robinson, 2012). There is millennial-scale resolution of coral U-Th/^{14}C ages between 16-0 ka (Burke and Robinson, 2012), however prior to 16 ka, there are no coral U-Th/^{14}C ages. The ^{14}C-reservoir ages after 16 ka are similar to those estimated from foraminifer ^{14}C from intermediate water depths on the Chilean margin (de Pol-Holz et al., 2010). This record suggests that prior to 16 ka, there was no significant change in the ^{14}C-reservoir age of intermediate water. Therefore, I assume a constant reservoir age

of 1.36±0.4 kyr (the age of the oldest U-Th/^{14}C dated coral analysed by Burke and Robinson 2012) prior to 16 ka for the radiocarbon dates in GC528.

2.2.8 Ice-rafted debris (IRD) analysis

Terrigenous grains from the carbonate-free fraction over a threshold size were visually counted as a proxy for ice-rafted debris (IRD). I used two threshold sizes, >300 μm and >600 μm. Both records have the same temporal trends, however in this thesis I only display the >300 μm - which is the closest size fraction to >250 μm (a pre-existing record which is later compared to GC528). Grains of volcanic glass were not counted as they have the potential to be carried to sites GC526/642 in volcanic ash clouds. However, grains of other volcanic origin were counted as these were likely ice rafted from the Chilean margin (where the lithology is dominantly igneous). IRD counts are reported as grains/gram.

2.2.9 Stable isotope analysis

Stable isotopes of oxygen and carbon were measured on select species of benthic and planktonic foraminifera from GC528 and GC642. Stable isotope determination was carried out at the Godwin Laboratory for Palaeoclimate Research, University of Cambridge, using a VG SIRA mass spectrometer for samples >100 μg, and a Thermo Kiel device connected to a Thermo MAT 253 isotope ratio mass spectrometer for samples weighing between 20-100 μg. Results are reported with reference to the international Vienna Peedee Belemnite (VPDB) standard with an analytical precision of ±0.08‰ for $\delta^{18}O$ and ±0.06‰ for $\delta^{13}C$. The stable isotopic records of *Uvigerina bifurcata* (125-212 μm), *Angulogerina angulosa* (63-125 μm), *Cassidulina carinata* (63-125 μm), *Oridorsalis umbonatus* (125-212 μm) and *Neogloboquadrina pachyderma sinistral* (63-125 μm) from cores GC528 and GC642 are discussed in this thesis.

2.2.10 Elemental analysis of *Uvigerina bifurcata* via ICP-OES

Samples (100-300 μg) of the benthic foraminifera *Uvigerina bifurcata* from the 125-212 μm size fraction were picked from cores GC528 over the glacial termination. Samples were weighed prior to cleaning in order to monitor the recovery of carbonate throughout the cleaning procedure. Samples were crushed between glass plates, transferred to pre-cleaned plastic lock-cap vials and cleaned according to a protocol similar to that developed for Mg/Ca analysis (Barker et al., 2003). Clays and particulate carbonate material were removed by repeated rinses in deionised water, at this point an aliquot of the sample was removed for stable isotope analysis. The remaining sample was oxidatively cleaned of organic matter in 2% H_2O_2 (buffered by NaOH) maintained at 90°C. After the oxidative step, samples were visually checked under a miscrocope for silicates and other contaminants that had not been removed in the previous cleaning steps. Following a weak acid leach and a final set of rinses in deionised water, the samples were transferred to new pre-cleaned vials for dissolution.

Cleaned foraminifera samples were dissolved in 0.1 M HNO_3 and analysed using inductively coupled plasma optical emission spectrometry (ICP-OES) following de Villiers et al. (2002). The

samples were monitored for contamination by through assessment of the concentrations of Mn, Fe, Al and Zn. Mg/Ca ratios were determined following redilution to a constant calcium concentration (100 ppm) to overcome the Ca matrix effect on Mg/Ca ratios (de Villiers et al., 2002). Long-term instrumental precision of the Mg/Ca ratio data determined by replicate analyses of a standard solution was ± 0.46%, translating into an uncertainty of 0.06°C.

2.2.11 Elemental analysis of *N. pachyderma (sin)* via LA-ICP-MS

In core GC528, *Neogloboquadrina pachyderma (sinistral)* was the most continuous planktonic species present throughout the glacial period, however, due to the small size fraction of the *N. pachyderma (sin)* (63-125 μm), a laser ablation technique was chosen to generate the Mg/Ca record over the more typical solution method. The advantage of using laser ablation was that it allowed measurements to be made from 5-10 individuals, whose cumulative mass yielded less than 50 μg of $CaCO_3$ (too small for measurement using the conventional solution technique). Care was taken to select only adult *N. pachyderma (sin)* in order to prevent bias in the record from variations in the phase of lifecycle. Typically 15-20 individuals were measured per sample, however in samples containing fewer than 10 individuals adjacent samples were combined to bring the total number to between 15-20 individuals. Organics were removed from the samples using a 10% buffered H_2O_2 solution and ultrasonicated 10-20 seconds. Samples were then rinsed in methanol before being mounted for laser ablation.

N. pachyderma Mg/Ca was determined using laser ablation inductively coupled plasma mass spectrometry (LA-ICP-MS). Analyte G2 (Teledyne Photon Machines Inc), ArF excimer laser (l = 193 nm) coupled to an Thermo i-CapQ ICPMS at the Department of Earth Science, University of Cambridge was used to measure depth profiles through test walls (Eggins et al., 2003; Sadekov et al., 2008). The horizontal and vertical resolution of the technique was optimized by ablating small-diameter spots (15x15 μm) at four laser pulses per second and 2 J/cm^2 laser fluence. Between three and four profiles were generated for each foraminiferal shell. The ICP-MS is optimised using NIST610 reference glass material for maximum sensitivity across Li-Sr mass range and maintaining ThO/Th < 0.5 % and Th/U ratio ~1. The isotopes ^{11}B, ^{24}Mg, ^{43}Ca, ^{44}Ca, ^{55}Mn, ^{63}Cu, ^{66}Zn, ^{88}Sr, ^{138}Ba and ^{27}Al were measured during each depth profile analysis, which required only 30-50 seconds to acquire. Data reduction involved initial screening of spectra for outliers, subtraction of the mean background intensities (measured with the laser turned off) from the analysed isotope intensities, internal standardisation to ^{43}Ca, and external standardisation using the NIST-SRM610 glass reference material. In-house eBlue and NIST-SRM612 were used to monitor long term standards reproducibility which was Sr/Ca = 0.253 ± 0.00331 (1 S.D.) mmol/mol, Mg/Ca = 3.670 ± 0.066 (1 S.D.) mmol/mol.

The final Mg/Ca of a sample was based on the average Mg/Ca value of all the shells measured in an individual sample which itself was an average of the number of spots measured on the individual. A single sample is therefore the average of approximately 70 individual measurements.

Near-surface temperatures were determined using the *N. pachyderma*-specific temperature calibration of Elderfield and Ganssen (2000): $Mg/Ca = 0.5e^{0.1T}$. This calibration was selected as it produced the closest match between the core top temperatures and modern thermocline temperatures at site GC528.

2.2.12 Benthic foraminifera census counts

Census counts of benthic foraminifera from the >63 μm size fraction were used to determine down-core changes in the benthic foraminifera assemblage. To keep results comparable with down-core data, I analysed the species composition of only calcareous foraminiferal assemblages. Agglutinated foraminifera easily disintegrate after death and thus result in variable and typically very low down-core abundances of tests or test fragments, depending on diagenetic processes in sediment and sample processing conditions (Brodniewicz, 1965; Schröder, 1988).

At least 300 individuals were counted per sample where possible. Samples containing significantly more than 500 individuals were split to reduce the number of individuals counted and to prevent the introduction of bias which might incur if, for example, only the first 300 individuals observed were counted.

Specimens of the dominant species downcore were imaged using a scanning electron microscope (SEM) to aid taxonomic identification. Additionally, very high resolution images were taken to assess the relative impact of dissolution on the shell walls.

The major changes in benthic foraminifera assemblage were determined through a multivariate statistical approach, detrended correspondence analysis (DCA), using the program PAST. The advantage of using DCA over standard correspondence analysis is that it suppresses 'edge effects' on the dataset, and thus will weight every point in the succession equally. The benthic foraminifera census counts were reduced prior to DCA; samples containing fewer than 50 individuals were not included, and species which constituted less than 1% of total counts in any of the samples were also removed.

2.2.13 Sortable silt analysis

Sample preparation: The sample (~20g) was wet sieved through a 63 μm sieve. The sand fraction (>63 μm) was taken for foraminiferal and IRD analysis. The fine fraction was left to settle for a minimum of 2 weeks before the supernatant water was siphoned off. The remaining fine fraction was dried in an oven at 50°C for one week, before being weighed.

The entire fine fraction sample was then transferred into a Nalgene bottle and the carbonate fraction removed using 1M acetic acid. The samples were agitated for 24 hours, and left to settle. The supernatant liquid was siphoned off and a second acid rinse applied to ensure that all carbonate was removed from the sediment. The sample was then flushed twice with deionised water, leaving the sample to settle in between each rinse.

The samples were then treated using 2M sodium carbonate (Na_2CO_3) solution at 85°C to remove the biogenic silica from the sample. The samples were transferred to a hot water bath kept at a constant temperature of 80°C for a minimum of 6 hr, every 2 hr the sample was disaggregated in an ultrasonic bath for 2 min. Smear slides were used at regular intervals to monitor the dissolution of biogenic silica. After treatment in the hot water bath, samples were left to settle for an hour before the supernatant was removed. The samples were then rinsed 3 times with deionised water, settling in between each rinse. Samples were topped up with 0.2% solution of sodium hexametaphosphate (Calgon) before being place on a spinning carousel for disaggregation.

Grain size analysis: A detailed grain size analysis of the silt fraction (10-63 μm) was performed using a Coulter Counter (Multisizer 3) (Bianchi et al., 1999). The set-up was adapted following Moffa-Sanchez et al. (2015) that provides better precision; with an increased stirrer speed, ultrasonication for a minimum of 3 minutes prior to analysis, and aliquots taken from a specific depth within the Nalgene bottle. The error in the sortable silt mean based on replicate runs was 0.5 μm (1 S.D, n = 3).

2.3 Summary

The methods that were employed in this thesis are summarised below:

1. Sediment cores GC528 and GC642 were split and logged prior to sampling. The archive half of the cores was analysed for downcore elemental variations using an Avaatech XRF core scanner, and magnetic susceptibility measurements were made using a MSCL-S.

2. Sediment core samples (50 cm^3) were taken from GC528 at 1 cm resolution and from GC642 at 2 cm resolution. A small quantity of sediment was taken for weight percent $CaCO_3$ determination, total organic carbon analyses and alkenone analysis. The remaining sediment was disaggregated in deionised water and wet sieved at 63 μm.

3. Detailed benthic foraminifera census counts were carried out on the coarse fraction (>63 μm). Over 300 individuals were counted from samples at ~500 year resolution over the last glacial termination (25-0 ka) and the Last Interglacial period (130-110 ka).

4. Foraminifera from the coarse fraction (>63 μm) were picked for stable isotope analysis. In this thesis I include the stable isotope data generated on *U. bifurcata*, *A. angulosa*, *C. carinata*, *O. umbonatus* and *N. pachyderma (sin)*.

5. Samples of *U. bifurcata* (2-6mg, 125-212 μm) were selected for radiocarbon dating. Uranium-series dating of individual coral samples from core GC528 was measured via LA-ICP-MS.

6. Samples of *U. bifurcata* (100-300 mg, 125-212 μm) were picked and cleaned following Barker et al. (2003) for elemental analysis via ICP-OES (de Villiers et al., 2002).

7. Samples of *N. pachyderma* (15-20 individuals/sample, 63-125 μm) were picked and cleaned in a 10% buffered H_2O_2 solution. The elemental concentration was determined via LA-ICP-MS (Eggins et al., 2003). The data was manually clipped based on evidence of contamination and external crusts.

8. Terrigenous grains from the >300 μm were counted as a proxy for IRD. Grains of volcanic glass were not included in these counts.

9. Carbonate and biogenic silica was digested from the fine fraction. Grain size of the sortable silt fraction (10-63 μm) was determined using a Coulter Counter (Multisizer 3).

10. Weight percent $CaCO_3$ was determined by acidifying dried bulk sediment with 10 % phosphoric acid and measuring the CO_2 released by coulometric titration.

11. Total organic carbon (TOC) weight percent and $\delta^{13}C$ was determined by acidifying bulk sediment with 5% hydrochloric acid. TOC analysis was performed by combustion in an online system comprising a Costech ECS4010 EA and a VG Optima MS.

12. Alkenones were extracted from freeze-dried homogenised samples using a CEM microwave system. Column chemistry was used to separate the alkenone-containing fraction from the total lipid extract and subsequently analysed using gas chromatography.

Chapter 3

Age Models

3.1 GC528 Age Model

The age model for core GC528 is based on reservoir-corrected radiocarbon dating of benthic foraminifera from discrete stratigraphic intervals. Beyond the limit of radiocarbon dating (40 ka) other techniques for dating the core including oxygen isotope stratigraphy, coral U-series dating and stratigraphic alignment of proxy data to Antarctic records were explored, however these methods were unable to place satisfactory age constraints on the core. In the following discussion, I describe the various techniques that were used to place age constraints on core GC528 and then discuss the Bayesian statistical approach employed to generate the final age model.

3.1.1 Radiocarbon dates

The age model for GC528 was generated using 28 radiocarbon dates of monospecific samples of *Uvigerina bifurcata* (>125 μm fraction, 2-6 mg). The graphitisation method is detailed in Section 2.2.7. Six of the 28 samples were graphitised and analysed by BetaAnalytic, no inter-lab offset between samples was found.

Carbon-14 ages were converted to calendar ages using the Marine13 dataset (Reimer et al., 2013). Constraints on reservoir age of the bottom water younger than 16 ka were taken from paired U-Th/^{14}C ages in corals (Burke and Robinson, 2012). Prior to 16 ka, a constant reservoir age of 1.36±0.4 kyr (the age of the oldest U-Th/^{14}C dated coral analysed by Burke and Robinson 2012) was applied downcore. The radiocarbon data and calendar ages are tabulated in Appendix A.1.

The oldest sample (39400 ^{14}C kyr) is close to the dating limit of radiocarbon, and has the greatest potential to be biased by contamination of modern radioacarbon. It is therefore useful to consider alternative methods for dating the basal sections of the core.

3.1.2 Correlation to other proxy records

In this section I explore the potential to correlate proxy records from GC528 with other globally-distributed proxy records in order to place age constraints on the basal sections of GC528.

Oxygen isotope stratigraphy: Downcore benthic oxygen isotope measurements can be compared to a global stack of benthic oxygen isotopes, e.g. Imbrie et al. 1989; Lisiecki and Raymo 2005. This approach makes the assumption that all oxygen isotope changes occur synchronously within the global ocean. Typically this method has been applied to deep water sites where this assumption is perhaps more valid.

The correlation of GC528 *U. bifurcata* $\delta^{18}O$ to the LR04 benthic stack is shown in Figure 3.1a. Despite having a similar Holocene value, the glacial and deglacial records show is a clear offset between the benthic $\delta^{18}O$ record at GC528 and the global stack, with GC528 $\delta^{18}O$ generally more positive suggesting colder (or more saline) conditions. This offset cannot be attributed to biological fractionation, as biological fractionation should result in a uniform offset between the two records (e.g. Woodruff et al. 1980). Therefore, I suggest that the large deglacial amplitude of the benthic $\delta^{18}O$ record at GC528 indicates a larger warming across the deglaciation or a stronger freshening that the global average. Similarly, this may also imply that the timing of changes in the southwest Atlantic are different from the global average, thus leading me to question the validity of correlating such a shallow site with the global benthic stack. Furthermore, there is little variability across MIS3 which makes tuning difficult.

Magnetic susceptibility: In the Scotia Sea, Weber et al. (2012) demonstrated that the magnetic susceptibility records of marine sediment cores could be correlated to the Antarctic ice core record EDML non-sea salt Ca^{2+} (Fischer et al., 2007). The EDML nss-Ca^{2+} record has been interpreted to reflect the signal of Patagonian dust (Pugh et al., 2009) that stimulated productivity leading to changes in bacterial magnetite (Yamazaki and Ikehara, 2012). Core GC528 lies immediately downwind of Patagonia and thus the magnetic susceptibility record should respond strongly to variations in Patagonian dust.

The correlation between EDML non-sea salt Ca^{2+} and the magnetic susceptibility record from GC528 is shown in Figure 3.1b. Although the magnetic susceptibility in GC528 is significantly higher during MIS 2, which is consistent with the idea of dust-stimulated productivity blooms, the correlation between the two records is not strong. In addition, the magnetic susceptibility record from GC528 'flat-lines' during MIS 3 which makes correlation to EDML non-sea salt Ca^{2+} in this interval impossible. The lack of variability in this section of the core also raises suspicion that the magnetic susceptibility record has been affected by some post-depositional process which acted to homogenise the record.

Bulk organic carbon isotopes: A variety of laboratory and field studies with global coverage have shown that the carbon isotopic composition of the bulk organic fraction of marine phytoplankton generally decreases as the concentration of aqueous CO_2 within the surface water increases (Degens, 1969; Rau et al., 1992). It may therefore be possible to correlate the bulk organic carbon $\delta^{13}C$ from GC528 with Antarctic ice core records of pCO_2 (Figure 3.1c).

Although there are caveats with this approach, including the potential for contamination by terrestrial organic carbon and disequilibrium of the surface water with respect to the atmosphere (see Kienast et al. 2001 for details), it appears that positive excursions in bulk organic carbon $\delta^{13}C$ during MIS3 do correlate to increases in atmospheric pCO_2. However, I emphasise that

the justification for this approach of stratigraphic alignment is very tenuous, and without other independent age constraints, it should be treated skeptically.

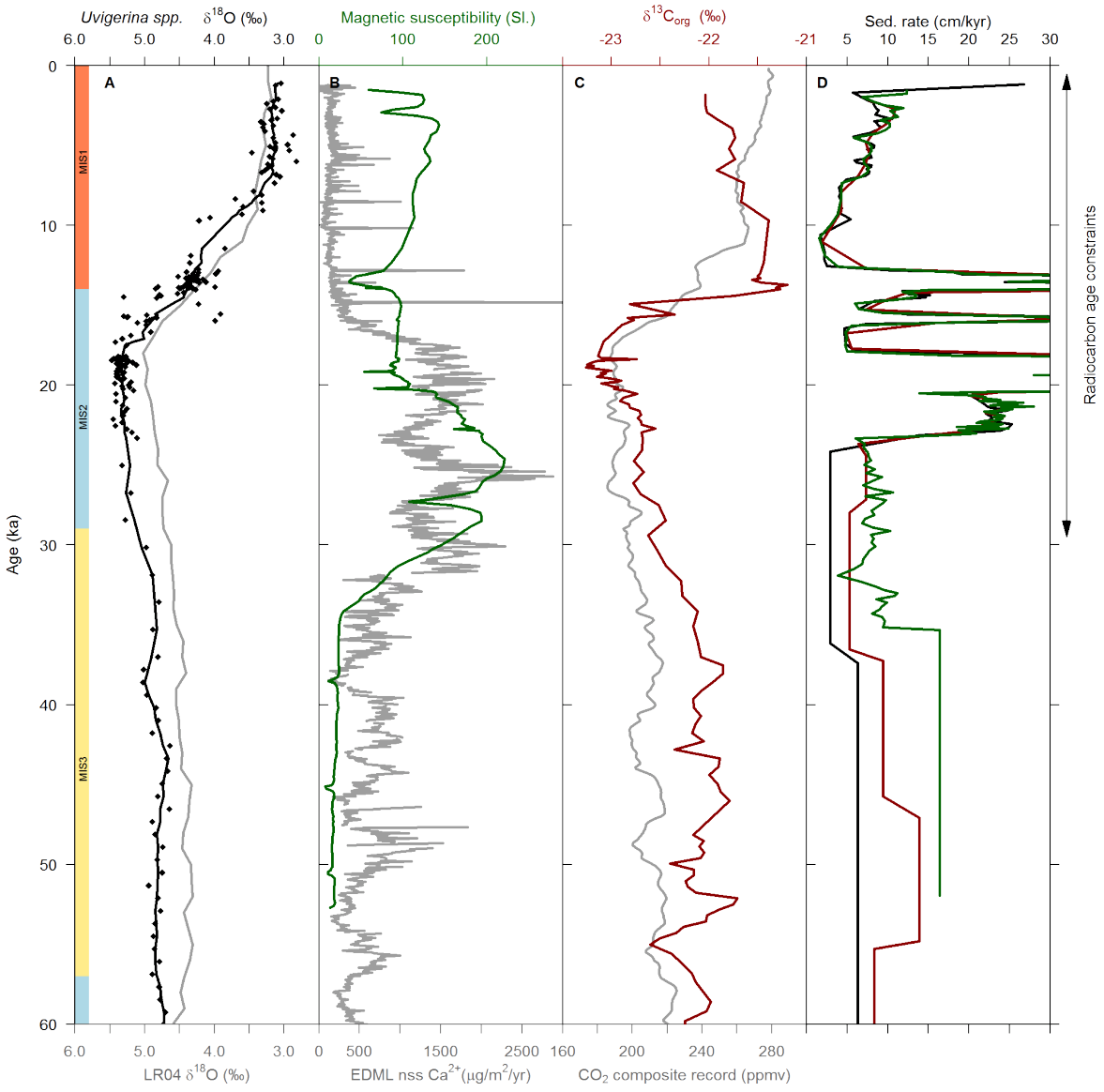

Figure 3.1: Alignment of GC528 proxy records with global proxy records. (A) Benthic oxygen isotope stratigraphic correlation with the global benthic stack, LR04 (grey curve, Lisiecki and Raymo 2005); (B) Comparison of the magnetic susceptibility record from GC528 and the Antarctic dust record, EDML Ca^{2+} (grey curve, Fischer et al. 2007); (C) Alignment of bulk organic carbon $\delta^{13}C$ with composite CO_2 stack (grey curve, Schilt et al. 2010); (D) Comparison of the different sedimentation rates produced by each alignment (Oxygen isotope stratigraphy, black; Magnetic susceptibility alignment, green; Bulk organic carbon $\delta^{13}C$ alignment, red).

In summary, various different approaches of stratigraphic alignment were trialled in order to place age constraints on the basal sections of core GC528, where there are large errors associated with radiocarbon analysis (>30 kyr). However, despite a number of different approaches being trialled (oxygen isotope stratigraphy, tuning of magnetic susceptibility to Antarctic dust, and the

tuning of bulk organic carbon $\delta^{13}C$ to atmospheric CO_2 concentrations), the age model of the core older than MIS2 cannot be well constrained. There is a lack of variability in the core over MIS3 which makes alignment difficult, and additionally, it appears that some records have diagenetically altered, making the correlation based on these records questionable. It is therefore necessary to find other means of placing age constraints on the core which do not rely on stratigraphic alignment.

3.1.3 Coral U-series dating

Several solitary deep sea corals (*Balanophyllia sp.*) were found within core GC528 at several depths (Figure 3.2), as well as a number of intervals with a significant proportion of coral fragments. The advantage of dating corals is that they can be dated both using U-series dating as well as ^{14}C dating. By using both of these approaches on a single specimen, it is possible to determine the absolute age of the coral (from U-series dating), and also the ^{14}C reservoir age of the water mass in which the coral grew.

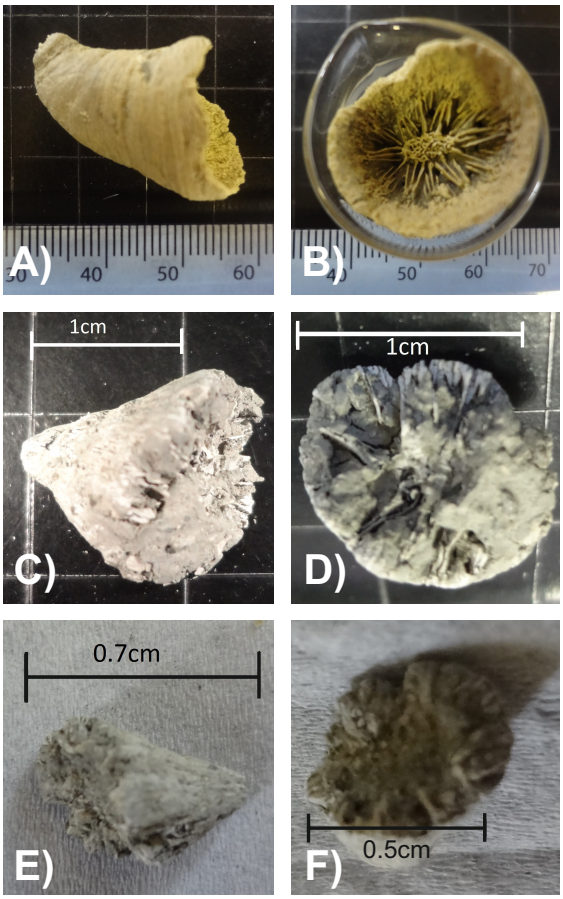

Figure 3.2: Examples of corals found within core GC528.

Recent developments in laser ablation multi-collector ICP-MS (Spooner et al., 2016) have enabled rapid dating of deep-sea corals at moderate precision. The key advantage of this technique is that is allows many corals to be screened in a short period of time, typically 50 samples can be dated in 12 hours. The age uncertainties (2σ) range from <0.8 kyr at 0-10 ka, 1.5 kyr at 20 ka

and 15 kyr at 125 ka, the main source of error derives from heterogeneity in the standard material. Three of the coral specimens found in the core were dated via this method, the results are shown in Table 3.1.

Table 3.1: U-series measurements on corals taken from core GC528. This work was carried out at the University of Bristol in collaboration with Pete Spooner.

Coral depth (cm)	**[^{230}Th/^{238}U]**	**Error**	**[^{232}Th/^{238}U]**	**Error**
32	0.058734778	0.05873	0.000127	0.00006
58	0.116978355	0.00943	0.000975	0.00048
416	0.413120524	0.02987	0.058806	0.02940

As discussed in Section 2.2.6, in order to calculate the absolute age of the coral using U-series dating, an initial atom ratio of ^{230}Th/^{232}Th for the sediment and the initial activity ratio of ^{234}U/^{238}U of seawater must be assumed. I assume an initial activity ratio of ^{230}Th/^{232}Th for the sediment of 14.8±14.8 (Cheng et al., 2000), and the initial activity ratio of ^{234}U/^{238}U ($\delta^{234}U$) of 148±10 (Robinson et al., 2005). Even using these relatively clean values for [^{230}Th/^{232}Th] and $\delta^{234}U$, the choice of initial [^{230}Th/^{232}Th] and $\delta^{234}U$ can have a significant effect on the calculated age of the coral due to the non-linearity of the U/Th age equation (Figure 3.3). The coral ages and their associated errors are shown in Table 3.2.

Table 3.2: Difference in ages produced by U-series and radiocarbon dating.

Coral depth (cm)	**U-series coral age (ka)**	**Error**	**Radiocarbon coral age (ka)**	**Error**	**Radiocarbon foram. age (ka)**	**Error**
32	8.91	0.17	6.33	0.03	5.69	0.06
58	17.20	0.72	12.51	0.05	10.60	0.06
416	45.82	72.53	37.22	0.54	34.83	0.40

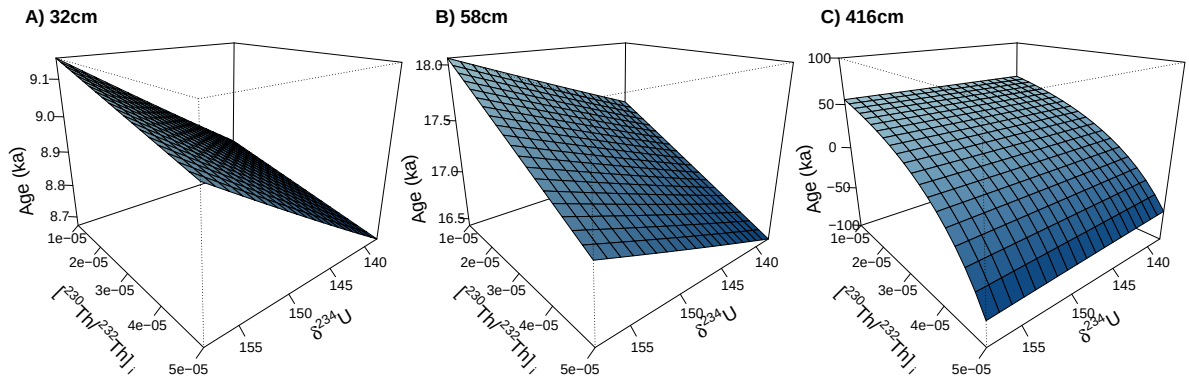

Figure 3.3: Sensitivity of coral age to small variations in initial [^{230}Th/^{232}Th] and $\delta^{234}U$ for the three corals; (A) 32 cm; (B) 58 cm; (C) 416 cm.

The U-Th age of each coral is significantly older than the radiocarbon calendar age of the coral. This is opposite to what one would expect – typically the radiocarbon age of the coral should be

older than the U-Th age as the radiocarbon age has an associated reservoir effect. There are a number of possible reasons for this discrepancy, such as, heterogeneity in the standard biasing the age of the U-series age (Spooner et al., 2016), or a lack of accuracy produced by the LA-ICP-MS method relative to the conventional TIMS or solution MC-ICPMS methods (Eggins et al., 2005). However, the most likely explanation is the assumption that the $[^{230}Th/^{232}Th]_i$ is equivalent to seawater (Cheng et al., 2000). Incorporation of Th-rich sediment into the skeleton of the coral during growth, or the failure to thoroughly clean the coral skeleton before ablation will result in a greater amount of ^{230}Th in the signal than has been produced simply through in-situ radioactive decay. This will bias U-series ages to look artificially older.

One approach which may alleviate this problem is to use radiocarbon dates on the corals to try to estimate the $[^{230}Th/^{232}Th]_i$. By attempting to match the U-series age to the radiocarbon calendar age on one of the corals it may be possible to use the calculated $[^{230}Th/^{232}Th]_i$ to make estimates of the ages on the other two corals. This method was trialled using the coral at 32 cm, and produced an initial Th activity ratio, $[^{230}Th/^{232}Th]_i$=145. However, when this activity ratio was applied to the coral at 58 cm, it produced a negative age. This suggests that the $[^{230}Th/^{232}Th]_i$ was not constant between all the corals which may reflect changes in the $[^{230}Th/^{232}Th]$ of seawater during growth of the corals or, more likely, variable encrusting of sediment onto the coral which was not removed during the cleaning process.

Comparison of the radiocarbon age of the coral with that of benthic foraminifera from the same stratigraphic depth (Table 3.2) shows that the corals are consistently older than the surrounding sediment. This suggests that the corals have 'migrated' upwards in the core relative to finer grained sediment of the same age, or they have been remobilised after death. This interpretation raises the question of whether it is appropriate to use corals as dating markers within marine sediment cores.

In summary, it appears that corals from core GC528 have been heavily contaminated by detrital thorium from the surrounding sediment. This contamination results in significant uncertainty in the U-series age estimates of corals from GC528. Additionally, the discrepancy between coral radiocarbon ages and the radiocarbon ages of benthic foraminifera from the same stratigraphic depth suggests that the corals have migrated upwards relative to the sediment. Therefore, even if the corals could be cleaned sufficiently to remove all detrital thorium, these corals would not provide useful age constraints.

3.1.4 Age-depth Modelling

Based on the above discussion, I suggest that only radiocarbon dating can provide meaningful age constraints on the core GC528. As radiocarbon dating has errors associated with the dating technique, the ^{14}C calibration and the reservoir correction, I use a Bayesian statistical approach to produce the best-fit age model for the core between 0-35 ka. The advantage of using Bayesian statistics is that it can quantitatively assess outlying radiocarbon measurements and stratigraphic markers, enabling a more rigorous assessment of the age constraints. Two programs often used for age-depth modelling are Bchron (Parnell et al., 2008) and Bacon (Blaauw and Christen, 2011). Both programs are based on a Markov chain Monte Carlo fitting algorithm to construct the age-depth model; these two programs take the probability distribution of the given radiocarbon dates and run thousands of iterations of potential age-depth models through the data to produce the most

probable age-depth model for the core. Much of the intricacy of the mathematics used within each program is encoded within the package in a fairly non-transparent way. The two age-depth models produced by Bacon and Bchron are compared in order to assess the robust features of the age model.

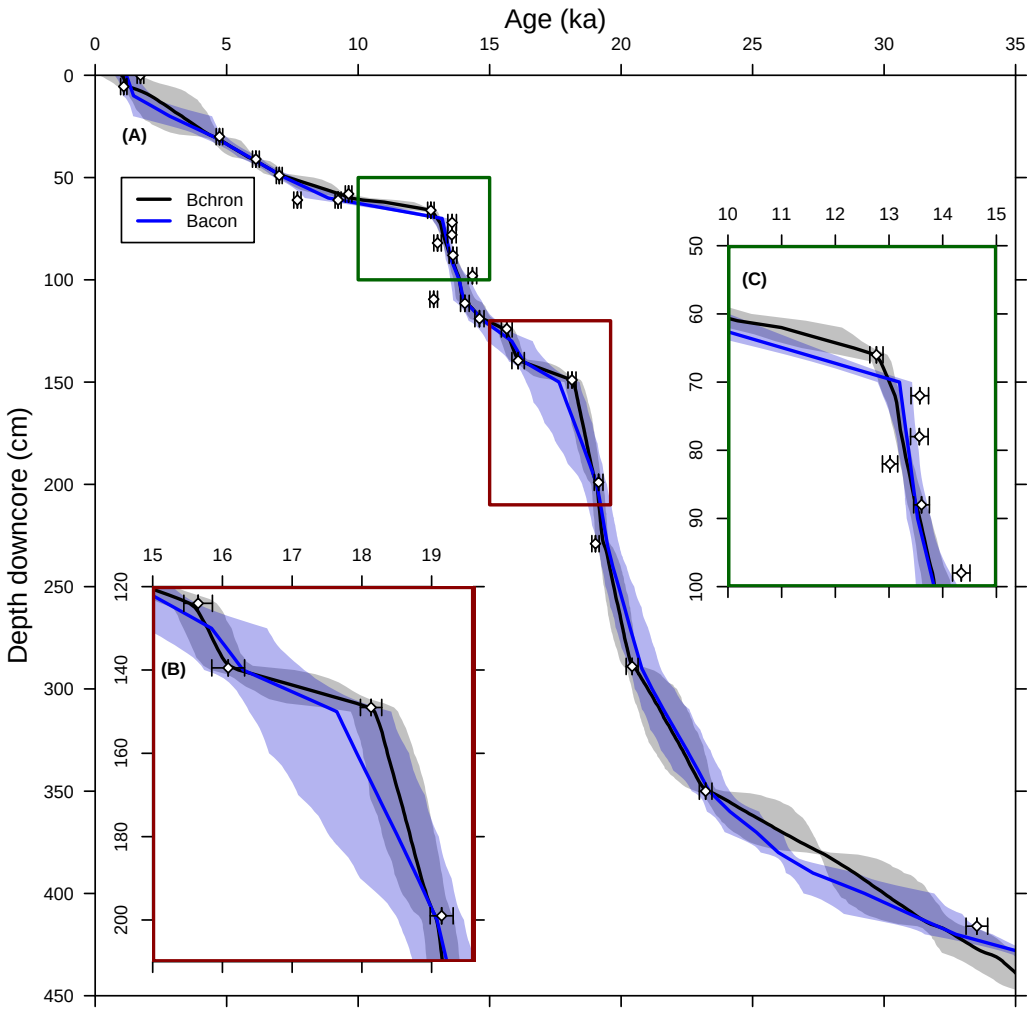

Figure 3.4: Comparison between the age-depth models produced by Bchron (Parnell et al., 2008) and Bacon (Blaauw and Christen, 2011). (A) 0-450 cm of core GC528; (B) 120-210 cm; (C) 50-100 cm.

In general, there is good agreement between the best-fit solutions produced by the two programs, however there are significant differences in the model output at the onset of the deglaciation (150-200 cm; Figure 3.4b). The two models produce differences of up to 500 years during this interval, which has significant implications when considering the timing of deglaciation.

The differences in the age model produced are primarily due to the fact that the Bacon has a strong memory effect, i.e. the age-depth model at any particular point within the core depends heavily on up-core and down-core sedimentation rates, whereas Bchron has no memory effect and therefore can produce very different sedimentation rates in two adjacent sections of core. There is

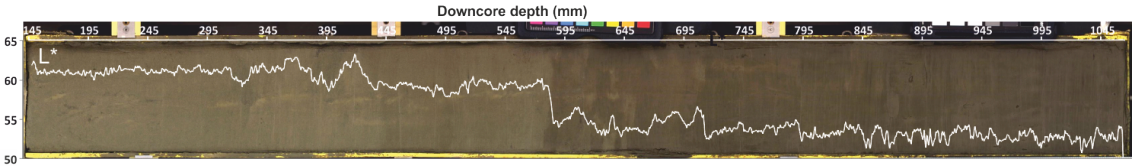

Figure 3.5: Sedimentological evidence for a discontinuity at 59cm within core GC528. A discrete shift in the L* ('whiteness') ratio can be observed.

clearly a balance that must be struck between choosing an age model that fits all radiocarbon data or choosing an age model that assumes that some data is anomalous, thus producing a smoother age-depth model which is perhaps a more representative of the 'real-world'. In the first scenario, an assumption is made that all radiocarbon dates and stratigraphic tiepoints are accurate and there has been no re-working in the core. Whereas the second scenario assumes that the core faithfully records a continuous deposition history, i.e. there are no rapid changes in sedimentation rate. In sections of the core where there is a high density of radiocarbon dates (e.g. 59 cm; Figure 3.4c) both models produce very similar age-depth models which clearly show that rapid changes in sedimentation rate have occurred within the core. Furthermore, there is sedimentological evidence of compositional changes within the core (Figure 3.5) that highlight the potential for hiatuses in the depositional history of the core, suggesting that two adjacent sections may have significantly different sedimentation rates. Based on the likelihood that there are discontinuities in GC528, the Bchron age model is used as the final age model for GC528; I interpret the Bacon age model as being 'over-smoothed'.

3.2 GC642 Age Model

The initial estimation of the age of GC642 during the sedimentary logging of the core suggests that the basal sections of GC642 is older than GC528 (Section 2.1.2). In the following discussion, I use various different proxy records measured on both core GC528 and GC642 to re-affirm that core GC642 is older than GC528. Owing to the large errors associated with the age model in the basal sections of GC528, alignment between the two cores cannot be used to provide an accurate estimation of the age of GC642. Instead a combination of biostratigraphic markers and chronostratigraphic tiepoints are used to date the core over the interval spanning the penultimate deglaciation and the Last Interglacial period (140-100 ka).

3.2.1 Correlation of GC642 and GC528

The two cores were correlated using a variety of different proxies measured downcore, including bulk organic carbon $\delta^{13}C$, XRF elemental data, foraminiferal isotopic composition and bulk magnetic susceptibility. It is possible to get a convincing correlation between the two cores based on a single proxy, but as I demonstrate here, there are slight differences between alignments depending on which proxy record is considered.

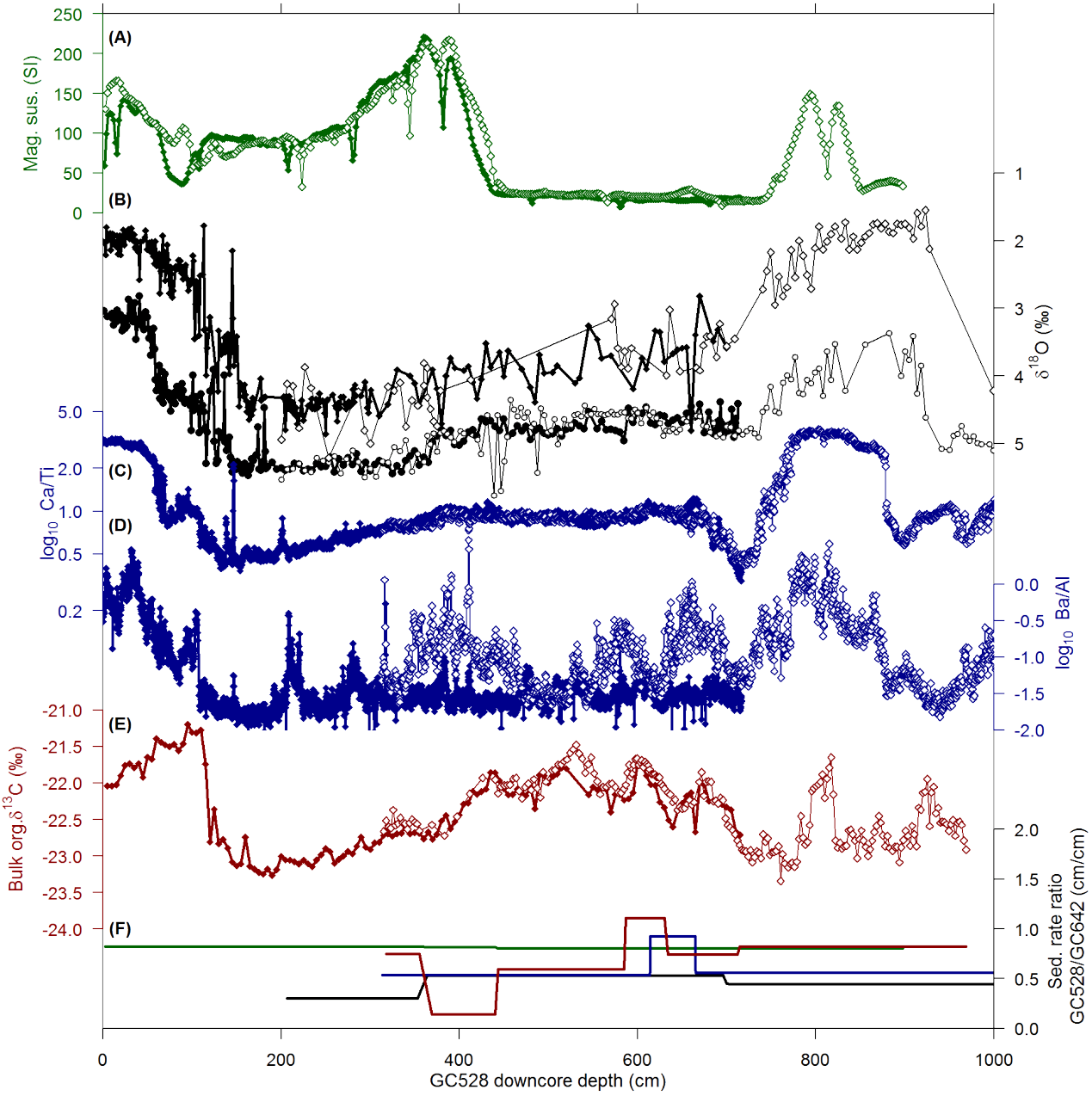

Figure 3.6: Alignment of GC642 (open symbols) to GC528 (closed symbols) based on different proxy records; (A) Magnetic susceptibility; (B) Planktonic (diamonds) and benthic $\delta^{18}O$ (circles) measurements; (C) XRF Ca/Ti; (D) XRF Ba/Al; (E) Bulk organic carbon $\delta^{13}C$; (F) Comparison of the difference in sedimentation rate between GC528 and GC642 based on the different proxy alignments (Magnetic susceptibility, green; benthic $\delta^{18}O$, black; XRF Ca/Ti, blue; Bulk organic carbon $\delta^{13}C$, red).

Magnetic Susceptibility: The magnetic susceptibility of the two cores showed a consistent pattern between the top 600 cm of GC528 and the top 400 cm of GC642 (Figure 3.6a). In the Southern Ocean, the magnetic susceptibility of the sediment can be largely attributed to the presence of biogenic magnetite (Yamazaki and Ikehara, 2012). Glacial-interglacial increases in productivity should be regionally consistent, and thus, it is in theory possible to correlate the two cores based on downcore magnetic susceptibility. However, as I discussed earlier, the base of GC528 appears to 'flat-line'. I interpret this to be evidence of post-depositional overprinting of the original magnetic susceptibility record. This overprinting could be relatively localised in origin, and therefore correlating the two cores based on the interval in which the magnetic susceptibility record drops to near-zero values might be a poor assumption.

Oxygen isotope stratigraphy: Oxygen isotope stratigraphy is often used to place age constraints on marine sediment cores. This approach assumes that changes in the oxygen isotopic composition of the bottom water occur everywhere synchronously. Here, I align cores GC528 and GC642 based on the oxygen isotopic record of the benthic species *U. bifurcata*. The glacial section in both cores is highly expanded and there is very little variation in the benthic oxygen isotopic composition (Figure 3.6b), however there are a few distinctive markers, such as the MIS3/4 transition, which may be correlatable between the two cores.

Justification of the benthic oxygen isotopic alignment can be provided by applying the same alignment to the planktonic oxygen isotopic records from the two sites (Figure 3.6b). Planktonic $\delta^{18}O$ has the potential to display greater variability than the benthic $\delta^{18}O$ record, as changes in sea surface temperatures will influence planktonic $\delta^{18}O$ values. Unfortunately, in GC528 and GC642 there are very few planktonic foraminifera in the glacial intervals and as a result the *N. pachyderma (sin)* $\delta^{18}O$ record was produced from discrete samples in which 2-3 individuals were measured. The large scatter observed in the *N. pachyderma* $\delta^{18}O$ record therefore likely reflects individual shell variability rather than regional changes in sea surface temperature or seawater $\delta^{18}O$. Furthermore, significant gaps in the GC642 *N. pachyderma (sin)* $\delta^{18}O$ record, where there are no *N. pachyderma (sin)* present, prevent a thorough assessment of the validity of the oxygen isotope stratigraphic alignment.

X-ray Fluorescence: X-ray fluorescence (XRF) is used to measure the elemental concentrations at extremely high resolution (2.5 mm) within the two sediment cores. Comparison of elements which have the potential to show glacial-interglacial variability can provide a useful method for correlating cores.

Here, I look at the Ca/Ti down core ratio. This ratio can be used to determine the relative influence of marine versus terrestrial sediment exported to the seafloor. Calcium is present in the core largely though the deposition of biogenic carbonate, e.g. coccolithophores and foraminifera. In contrast titanium is largely a product of terrestrial weathering. There is a strong glacial-interglacial signal in Ca/Ti in the two cores (Figure 3.6c) suggesting significant variations in productivity and/or terrestrial sediment deposition. The alignment of the Ca/Ti ratio of GC528 and GC642 shows good correlation (Figure 3.6c). This is in stark contrast to other elemental ratios, such as Ba/Al. Barium is an element that has been observed to reflect the influences of biological cycling (Francois et al., 1995), whilst aluminium is associated with the deposition of terrestrial sediment, in particular

Patagonian dust (Dammshäuser et al., 2011). However, unlike the Ca/Ti ratio, the Ba/Al ratio between the two cores is an order of magnitude different in some sections of the core (Figure 3.6d). This suggests highly localised patterns of productivity and/or terrestrial sedimentation, or, more likely, provides evidence of diagenetic processes within the sediment which act to focus or degrade elemental signals within the cores. The same pattern is observed in other elements, such as Cu, Mn, Zr. It appears that unless the variations in the elemental concentration is extreme, as is the case for Ca, then post-depositional processes acting within the sediment can eradicate original signal.

Bulk Organic Carbon Isotopes: The bulk organic carbon $\delta^{13}C$ reflects changes in the source of organic matter to the sediment, such as variations in marine productivity versus terrestrial fluxes of organic matter, or changes in the type of marine organic matter being exported to the sediment. There is likely to be a significant degree of spatial variability in this signal, related to regional upwelling and patterns of productivity; however, the two core sites are sufficiently close that they should display similar down core records of bulk organic carbon $\delta^{13}C$. I find good correlation in the bulk organic $\delta^{13}C$ at the two sites (Figure 3.6e), and sufficient variability to allow the cores to be correlated to a good degree of precision.

Comparison of the different alignments: There are significant differences between the different proxy alignments (Figure 3.6f). I evaluate these differences quantitatively by looking at variations in sedimentation rate. The $\delta^{18}O$ and XRF alignments suggest that the sedimentation rate of GC642 is approximately half that of GC528. However, the bulk organic carbon $\delta^{13}C$ and magnetic susceptibility alignments suggest that the sedimentation rates of GC642 are roughly equivalent to GC528 (Figure 3.6f). The age of the base of GC642 based on the $\delta^{13}C$ and magnetic susceptibility alignments is ~80 ka, whereas it is ~200 ka based on the $\delta^{18}O$ and XRF alignments.

Summary: I trialled using the alignment of several different proxy records to correlate the two cores (GC528 and GC642). There is some overlap between GC528 and GC642 that can be used to correlate the two records and clearly demonstrates that the base of GC642 is older than the base of GC528. However, the lack of variability in the region of overlap of the two cores coupled with the potential issue of post-depositional overprinting of some records makes accurate alignment of the two cores difficult. In the next section I explore other methods for placing age constraints on GC642.

3.2.2 Biostratigraphy

Biostratigraphy has proved useful in placing broad age constraints on marine sediment cores globally. Typically, in the Southern Ocean, the presence or absence of specific diatoms would be used to determine the relative age of the samples within a core (e.g. Zielinski and Gersonde 2002). However, in GC528 and GC642, the preservation of diatoms is extremely poor throughout the core, and thus diatom stratigraphy cannot be used to provide age constraints. Instead, the presence or absence of specific species of coccolithophore (e.g. Pujos and Giraudeau 1993) can be used to place some age constraint on the core GC642. Smear slides from specific intervals within GC642 were

Table 3.3: Nano-fossil observations from core GC642. This work was carried out by Jeremy Young (University College London).

Depth (cm)	Nano-fossil observations	Age constraints
589	Abundant *G. muellerae* + frequent *E. huxleyi* + frequent *Coccolithus pelagicus spp. braarudii*	Interglacial – MIS5 (e?)
609	Abundant *G. muellerae* + rare *G. aperta*, frequent *E. huxleyi*, common small *Calcidiscus leptoporus*, frequent *Coccolithus pelagicus ssp. braarudii*, frequent *Helicosphaera carteri*, rare *Syracosphaera sp.*	Interglacial – MIS5 (e?)
649	Barren, non-calcareous	Glacial
676	Barren, non-calcareous	Glacial
706	Rare *Coccolithus pelagicus ssp. Braarudii* + very rare *E. huxleyi*	Interglacial – MIS7?
726	Barren, non-calcareous	Glacial

prepared and sent off to Jeremy Young (University College London) for nano-fossil identification. A summary of the nano-fossil assemblages is shown in Table 3.3.

In all the carbonate-bearing samples there is a dominance of *Gephyrocapsa* over *Emiliania huxleyi*. This is opposite to the pattern observed in the modern ocean. The increase in *E. huxleyi* relative to *Gephyrocapsa* has been dated to MIS2/3 (e.g. Flores et al. 1999, 1997; Thierstein et al. 1977; Wells and Okada 1997). However in the South Atlantic, this reversal may have occurred even earlier, between MIS 5e and MIS 5a (Pujos and Giraudeau, 1993). Assuming that core GC642 follows the South Atlantic trend, the samples at 589 cm and 609 cm are likely older than MIS5a.

The samples at 589 cm and 609 cm both show a dominance of *G. muellerae*. During the mid-Brunhes period (MIS13-9) calcareous nanofossil assemblages globally were dominated by *G. caribbeanica* (as opposed to *G. muellerae*) (e.g. Baumann and Freitag 2004; Bollmann et al. 1998). This suggests that samples 589 cm and 609 cm are younger than MIS9. In the Cape Basin, Flores et al. (1999) show that the *Gephyrocapsa* assemblage is dominated by *G. oceanica* during MIS 7. Therefore, I suggest that samples 589 cm and 609 cm likely date back to MIS5.

All calcareous samples contain *E.huxleyi*. The earliest occurrence of *E.huxleyi* in the sub-Antarctic was at 300 ka, i.e. MIS 8/9 (Lupi, 2009). Based on this, I suggest that the sample at 706 cm must be no older than MIS8/9.

Calcidiscus leptoporus is the dominant subordinate species during peak interglacial times (Holocene and substage 5e) (Wells and Okada, 1997). The presence of *C. leptoporus* in sample 609 cm is suggestive that this is from a peak interglacial period.

In summary, the assemblage from 589 cm and 609 cm is indicative of interglacial conditions, specifically from MIS5. This interpretation is based on the premise that in the Holocene *E. huxleyi* would be the dominant species, and in MIS9 *E. huxleyi* would be very rare. In addition, the *Gephyrocapsa* assemblage during MIS7 would likely be more diverse, with *G. oceanica* dominating over *G. muellerae*. The presence of *C. leptoporus* suggests peak interglacial conditions at 609 cm, most likely MIS5e.

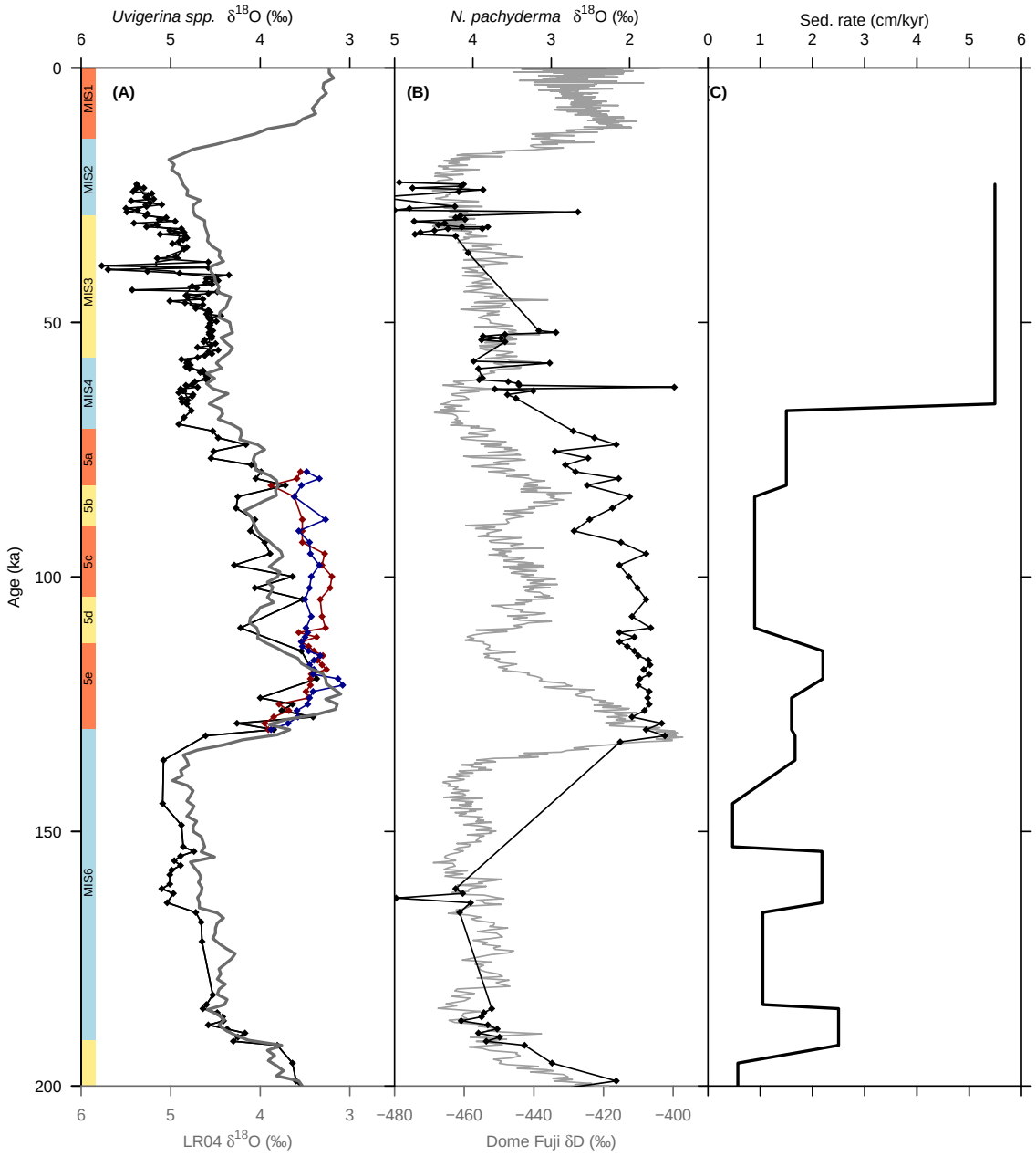

Figure 3.7: Oxygen isotope age model for GC642 based on the tuning of benthic (*Uvigerina bifurcata*) $\delta^{18}O$ record to LR04 (Lisiecki and Raymo, 2005). (A) Benthic oxygen isotope records from GC642; *Uvigerina bifurcata*, black; *Angulogerina angulosa*, red; *Cassidulina carinata*, blue; LR04, grey (Lisiecki and Raymo, 2005); (B) Planktonic (*Neogloboquadrina pachderma sinistral*) $\delta^{18}O$ record - age constraints based on the tuning of the benthic (*Uvigerina bifurcata*) $\delta^{18}O$ record to LR04. An Antarctic temperature record (Dome Fuji δD ; Uemura et al. 2012) is shown in grey for comparison; (C) Sedimentation rate based on the benthic oxygen isotope age model.

3.2.3 Chronostratigraphy

Age models for marine sediment cores are often generated by correlating some proxy measurement within the core to a 'global' signal, for example stacked benthic oxygen isotope records or Antarctic ice core records. Two different approaches were trialled to place age constraints onto core GC642:

1) Oxygen isotope stratigraphy (e.g. Lisiecki and Raymo 2005)

2) Alkenone-derived sea surface temperature correlated to hemispheric temperature records (e.g. Capron et al. 2014; Martínez-Garcia et al. 2009)

Oxygen isotope stratigraphy: A chronology for GC642 is developed by correlating the benthic *U. bifurcata* $\delta^{18}O$ record to the LR04 global benthic stack (Figure 3.7a; Lisiecki and Raymo 2005).

Whilst there is generally good correlation between the benthic oxygen isotopic record in core GC642 and the global benthic oxygen isotope stack (Lisiecki and Raymo, 2005), over the Last Interglacial period (130-80 ka) *U. bifurcata* is less abundant. The low resolution benthic oxygen isotope record over this interval reflects this dearth of *U. bifurcata*. An attempt was made to improve the resolution by measuring oxygen isotopes on other more abundant species, *Angulogerina angulosa* and *Cassidulina carinata*, during this interval (Figure 3.7a). However, the lack of *A. angulosa* or *C. carinata* over the major climatic transitions (e.g. MIS6-5 and MIS5-4) prevents the placement of additional age constraints on the core.

The sedimentation rates produced by the benthic $\delta^{18}O$ age model are relatively consistent, with slightly slower sedimentation rates (<1 cm/kyr) during the glacial periods and faster sedimentation rates (1-2 cm/kyr) during the interglacial period (Figure 3.7c). This pattern of sedimentation is opposite to that observed in GC528 (Figure 3.4).

Other published age models from the South Atlantic justify the benthic oxygen isotope stratigraphic alignment by demonstrating that planktonic oxygen isotopes on the same age model correlate well with Antarctic ice core temperature data (e.g. Hodell et al. 2003a). The Dome Fuji ice core δD record (Uemura et al., 2012) is compared to the planktonic $\delta^{18}O$ record from GC642. The Dome Fuji ice core record was chosen for comparison because it is one of the only Antarctic records spanning back to MIS 6 that is located near the Atlantic sector of the Southern Ocean, and therefore is assumed to be the closest match to temperature variability occurring in the southwest Atlantic. In core GC642 there is a lack of planktonic foraminifera over key climatic transitions, in particular MIS6-5e, which prevents verification of the benthic oxygen isotope age model in this part of the record (Figure 3.7b). However, there is sufficient resolution over the MIS5e-5d transition; the planktonic $\delta^{18}O$ record does not appear to respond to the decrease in Antarctic temperatures. I suggest that based on this evidence, the age model based on the alignment of the benthic oxygen isotope record to the global benthic stack is ambiguous – at least in this section of the core.

Alkenone-SST stratigraphy: One alternative to using benthic oxygen isotope records to generate age control points is to use SST records and correlate them to well-dated Antarctic temperature records, e.g. Capron et al. (2014); Martínez-Garcia et al. (2009). The alkenone-derived sea surface temperature record at GC642 shows strong correlation with the Dome Fuji Antarctic temperature record (Figure 3.8c). The alkenone-derived sea surface temperature record appears to capture the MIS5e temperature 'over-shoot' at the onset of the interglacial period.

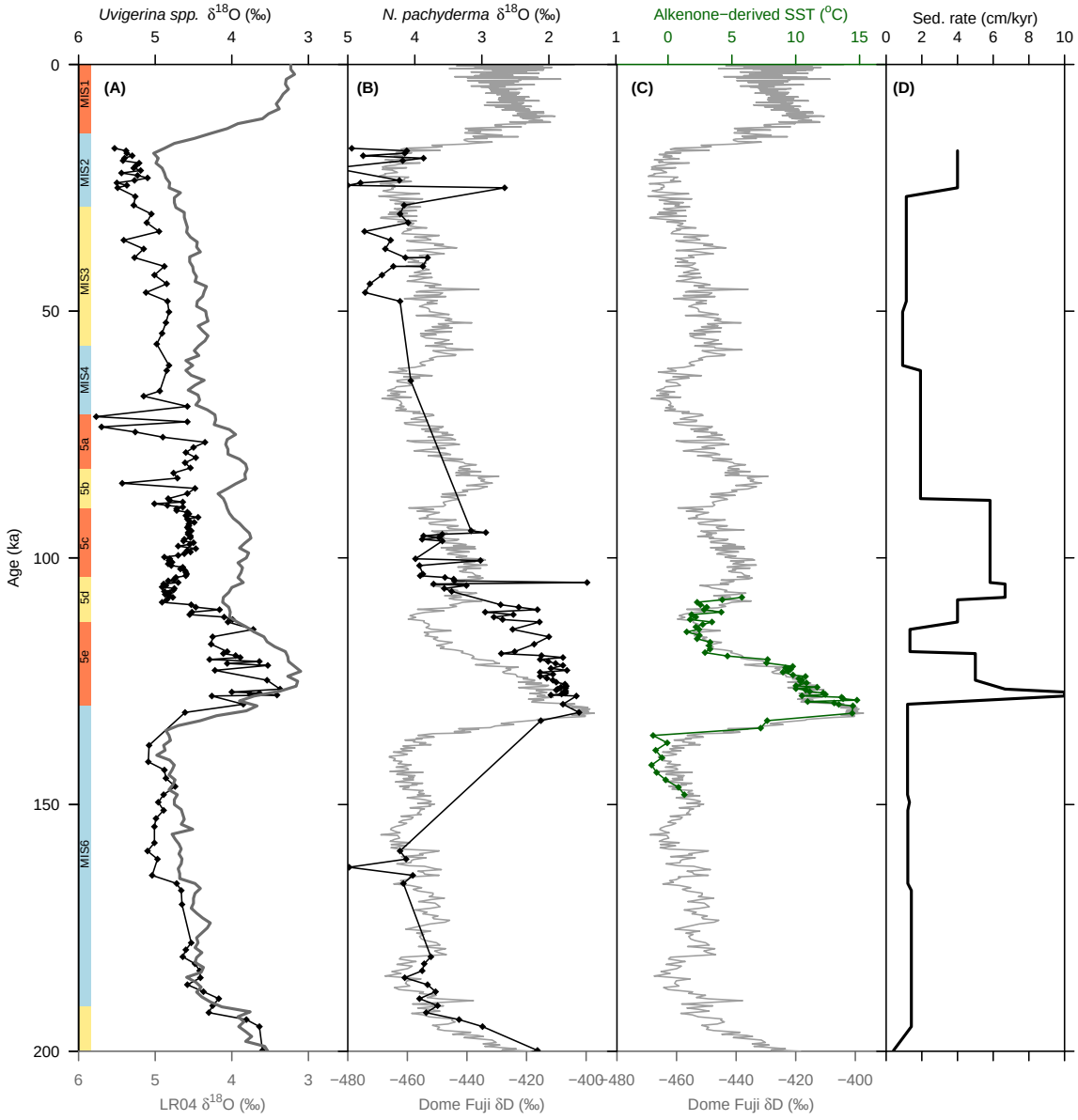

Figure 3.8: Alkenone-SST age model for GC642 based on the tuning of the alkenone-derived SST record to Antarctic temperatures (Uemura et al., 2012). (A) *Uvigerina bifurcata* oxygen isotope record from GC642 tuned to alkenone-based age model. Additional tie points are used for sections of the core in which alkenone-SST estimates are unavailable. LR04, grey (Lisiecki and Raymo, 2005); (B) Planktonic (*Neogloboquadrina pachderma sinistral*) $\delta^{18}O$ record - age constraints based alkenone-SST age model. An Antarctic temperature record (Dome Fuji δD ; Uemura et al. 2012) is shown in grey for comparison; (C) Alkenone-SSTs tuned to Antarctic temperatures (Dome Fuji δD ; Uemura et al. 2012); (D) Sedimentation rate based on the alkenone-SST age model.

Similarly to the benthic $\delta^{18}O$ age model, the alkenone-SST alignment suggests that sedimentation rates in GC642 are higher during the interglacial period than the glacial (Figure 3.8c). However, the glacial-interglacial variability in sedimentation rates are much more pronounced, with glacial sedimentation rates averaging between 1-4 cm/kyr, in comparison to the interglacial period in which sedimentation rates are as high as 7 cm/kyr.

The benthic *U. bifurcata* oxygen isotope record is mapped onto this alkenone-based age model and compared with the LR04 benthic stack (Lisiecki and Raymo, 2005) (Figure 3.8a). Additional tiepoints (Table A.5) in sections of the core in which alkenone data is lacking are included to produce a fairly convincing correlation between the benthic oxygen isotope record in GC528 and the LR04 stack. There is a constant offset between the two records of 0.8‰, suggesting that the intermediate water over site GC528 is typically colder (or more saline) than the global mean.

Applying the same age model to the planktonic oxygen isotope record is perhaps less convincing (Figure 3.8b). Unlike the alkenone-SST record, the planktonic oxygen isotope records does not capture the MIS 5e-5d transition. This potentially suggests that the sub-surface dwelling planktonic foraminifera experience different temperature changes to the surface alkenone signal. The decoupling of the alkenone and planktonic temperature signals is explored further in Chapter 5.

Comparison of the two age models:

The age models produced by the oxygen isotopic alignment of GC642 to the global benthic oxygen isotope stack and the alignment of the alkenone-SST record to Antarctic temperatures are applied to the records of magnetic susceptibility (Figure 3.9 and 3.10a), planktonic and benthic $\delta^{18}O$ (Figure 3.9 and 3.10b), XRF data (Figure 3.9 and 3.10c-d) and bulk organic carbon $\delta^{13}C$ (Figure 3.9 and 3.10e) from cores GC528 and GC642. As I have discussed earlier, the age control on the core GC528 prior to 25 ka is poorly constrained, and therefore in the following discussion I apply the radiocarbon age model on GC528 for the interval between 25-0 ka, but in the interval prior to 25 ka GC528 is correlated to GC642 through the alignment of the bulk organic carbon $\delta^{13}C$ records and then an age model for GC642 (based on alkenones or benthic $\delta^{18}O$) is applied.

The benthic oxygen isotope-based age model for GC642 suggests that similarly to site GC528, magnetic susceptibility achieves a maximum during the glacial periods (Figure 3.9a). It is interesting that the glacial period MIS4 is not accompanied by a similar magnetic susceptibility maximum. In contrast, the XRF Ca/Ti record clearly identifies MIS4 as a reduction in the Ca/Ti ratio (Figure 3.9c). The planktonic oxygen isotope record suggests a progressive cooling between MIS5a to MIS2 (MIS3 is not apparent in this record; Figure 3.9b). The planktonic $\delta^{18}O$ values during the Last Interglacial (MIS5) are lower than the Holocene, but interestingly, the benthic $\delta^{18}O$ record shows the opposite trend with higher $\delta^{18}O$ values during MIS5. Potentially, this is an artefact of the low resolution of *Uvigerina bifurcata* samples during MIS5. Comparison of the bulk organic carbon $\delta^{13}C$ shows a marked increase across both Termination I and II (Figure 3.9e). Similarly, during MIS3, the $\delta^{13}C$ of bulk organic carbon is also elevated; however, unlike across the major glacial terminations, the transition between MIS4 and MIS3 much less abrupt. Surprisingly, there is no significant change in $\delta^{13}C$ of bulk organic carbon at the onset of MIS5c and MIS5a across these intervals bulk organic carbon $\delta^{13}C$ remains at glacial values.

In contrast to the benthic oxygen isotope stratigraphic age model, the age model produced by alkenone alignment suggests that MIS5e is significantly different to the following warm sub-stages (MI5a and MIS5c; Figure 3.10). The planktonic and benthic $\delta^{18}O$ values during MIS5e are significantly lower than the rest of the interglacial period, and the Ca/Ti ratio is significantly higher. This age model produces a large difference in the timing of the increase in magnetic susceptibility during the last glacial period between the two cores; the magnetic susceptibility record of GC642

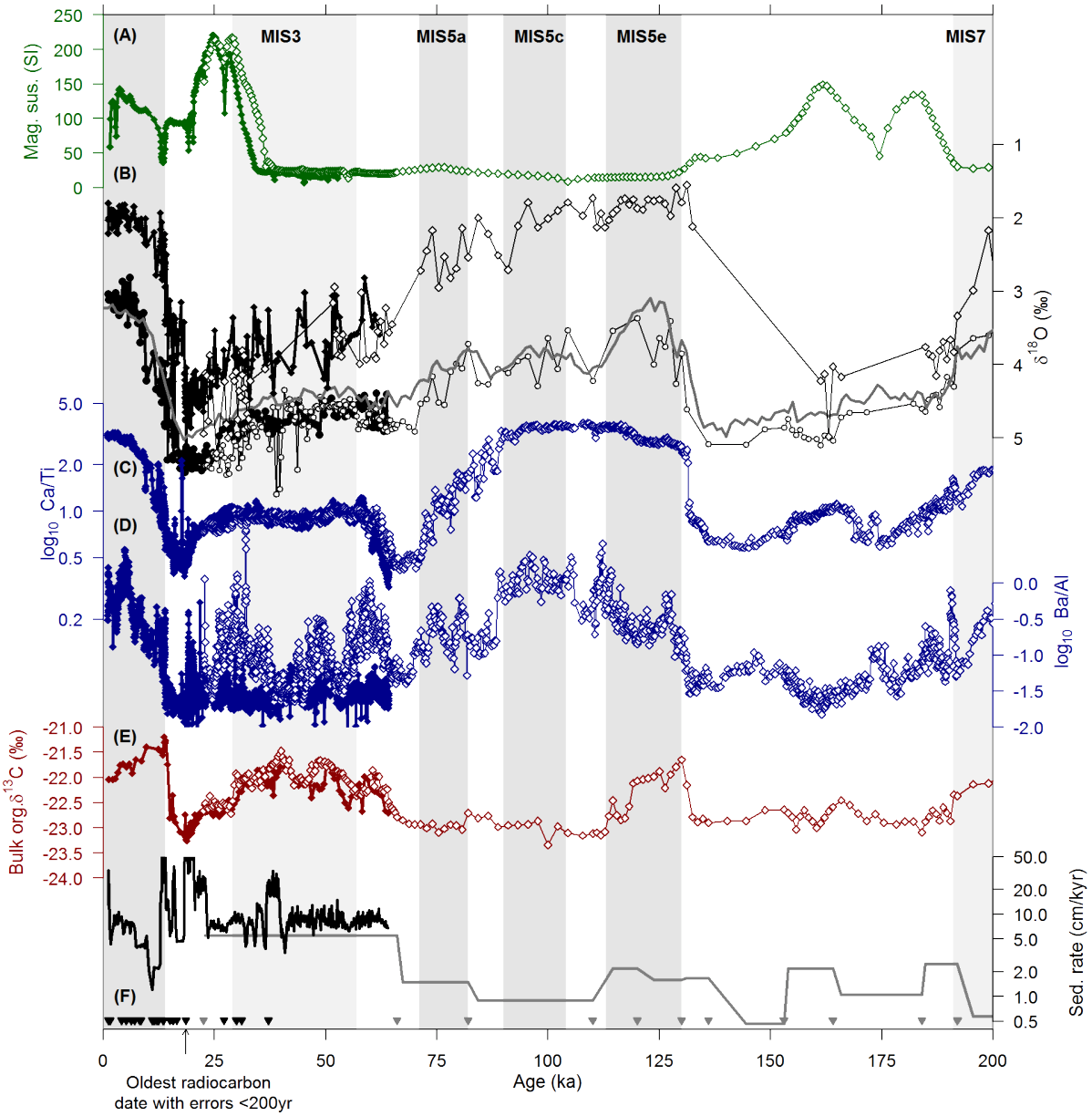

Figure 3.9: Proxy record from GC642 (open symbols) fitted on the oxygen isotope age model. These records are shown in comparison to GC528 (closed symbols) in which the age model is based on radiocarbon in the interval 25-0 ka. Prior to 25 ka, the age model for GC528 is poorly constrained; however, in order to make a comparison between the two cores, oxygen isotope stratigraphy is used to place age constraints on the oldest sections of GC528. (A) Magnetic susceptibility; (B) Planktonic (diamonds) and benthic $\delta^{18}O$ (circles) measurements from GC528 and GC642. The LR04 stack is shown as a solid grey line; (C) XRF Ca/Ti; (D) XRF Ba/Al; (E) Bulk organic carbon $\delta^{13}C$; (F) Sedimentation rates for GC528 (black) and GC642 (grey). Radiocarbon dates from GC528 shown as black arrows. The tiepoints used in the age model for GC642 shown as grey arrows.

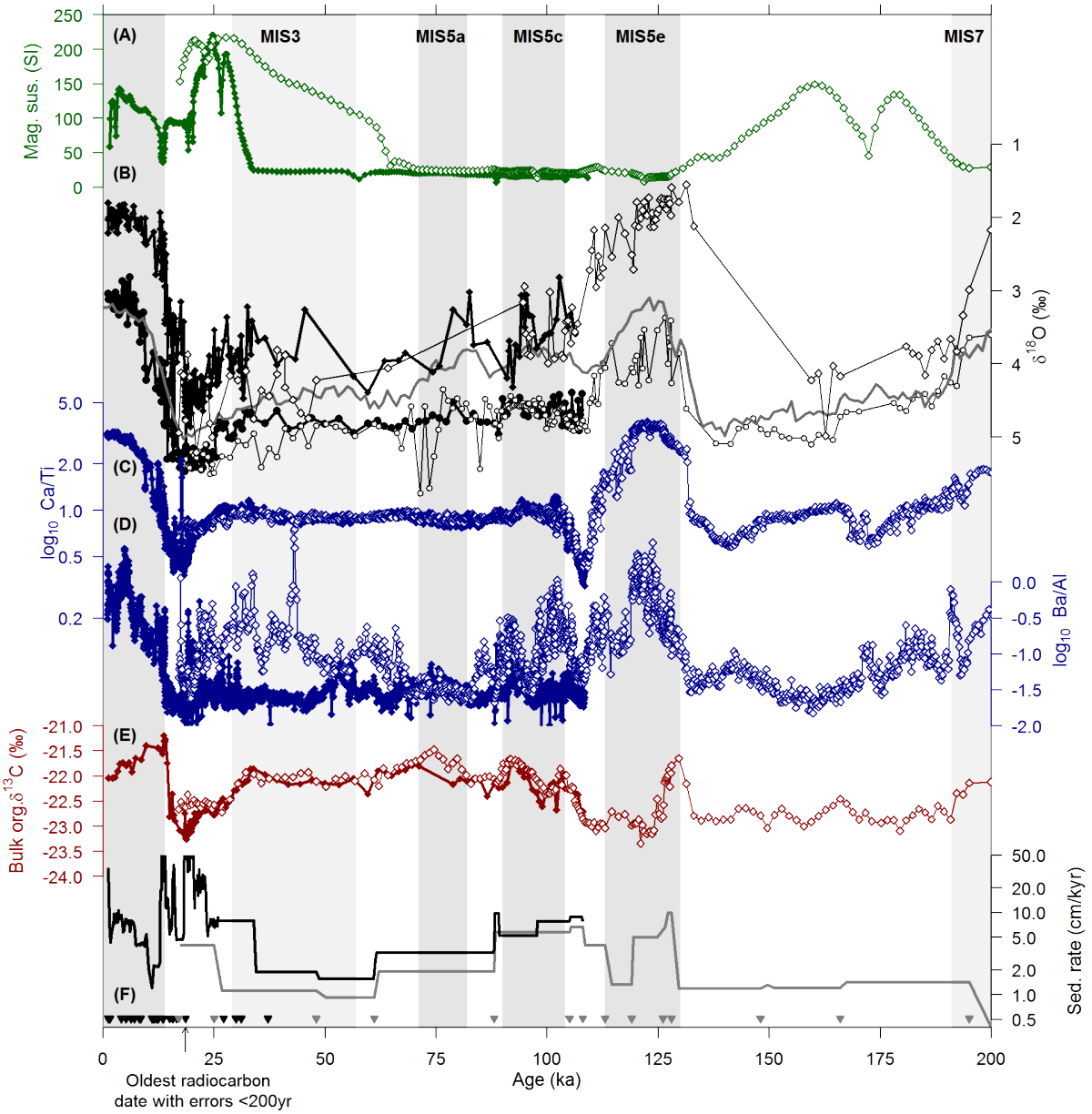

Figure 3.10: Proxy record from GC642 (open symbols) fitted on the alkenone-benthic $\delta^{18}O$ age model. These records are shown in comparison to GC528 (closed symbols) in which the age model is based on radiocarbon in the interval 25-0 ka. Prior to 25 ka, the age model for GC528 is poorly constrained; however, in order to make a comparison between the two cores, oxygen isotope stratigraphy is used to place age constraints on the oldest sections of GC528. (A) Magnetic susceptibility; (B) Planktonic (diamonds) and benthic $\delta^{18}O$ (circles) measurements from GC528 and GC642. The LR04 stack is shown as a solid grey line; (C) XRF Ca/Ti; (D) XRF Ba/Al; (E) Bulk organic carbon $\delta^{13}C$; (F) Sedimentation rates for GC528 (black) and GC642 (grey). Radiocarbon dates from GC528 shown as black arrows. The tiepoints used in the age model for GC642 shown as grey arrows.

based on this alignment suggests that magnetic susceptibility is high across MIS4-2, in contrast the magnetic susceptibility record of GC528 increases abruptly across the MIS3-2 transition. As I discuss earlier, the magnetic susceptibility record in marine sediment cores can be strongly influenced by diagenetic processes, which can be a highly localised.

The choice of the final age model ultimately is determined by the decision of which proxy records are most robust. Many marine sediment cores have age models that are based on the alignment of benthic oxygen isotopes to a global stack. Whilst this is a fairly good assumption for deep ocean sites (where most of the benthic $\delta^{18}O$ change is related to variations in ice volume), in shallower sites, variations in ocean temperature may also be important in controlling benthic $\delta^{18}O$. The timing and magnitude of these temperature variations may vary significantly between different sectors of the ocean. Indeed across the last deglaciation, the deglacial amplitude in benthic $\delta^{18}O$ in core GC528 is 0.5‰ greater than the global LR04 stack (Lisiecki and Raymo, 2005). Thus, an offset in the benthic $\delta^{18}O$ from the global LR04 stack (as observed in the alkenone-based age model) is not improbable. Furthermore, it has been shown (Stern and Lisiecki, 2014) that the expression of the onset of the last deglaciation in the intermediate south Atlantic occurred significantly earlier than other regions of the ocean globally, leading the deep south Atlantic by nearly 1000 years. As a result of these difficulties, I would suggest caution should be taken when using benthic $\delta^{18}O$ to generate an age model at this site. Frustratingly, the alkenone-based age model also has its problems; in particular, the alkenone-based sea surface temperature record across the last deglaciation does not resemble Antarctic δD. In contrast, the similarity between the alkenone-based SST record and Antarctic δD across the Last Interglacial is striking. Based on this similarity, I have opted for this age model over the benthic $\delta^{18}O$ age model; however, I emphasise that there remains a significant amount of certainty with the age model, and ideally I would want there to be other independent age constraints on this core to validate the final choice of age model.

3.3 Summary

In this section I have demonstrated through the correlation of GC528 and GC642 proxy records that core GC642 spans a greater period of time than GC528. This was reinforced through the identification of specific species of coccolithophores that can be used as biostratigraphic markers; suggesting that the cores spans back at least as far as MIS7.

The final choice of age model for core GC642 has proven highly problematic; difficulties in correlating the two cores in the depth domain (Figure 3.6) suggest that some proxies are more regional synchronous whereas others may be responding to more localised signals. Furthermore, the tuning of the alkenone and benthic $\delta^{18}O$ to global stacks produces vastly different age models, in particular it is difficult to determine whether the minimum in $\delta^{18}O$ in GC642 corresponds to the entirety of MIS5 (Figure 3.9) or only the Interglacial climatic optimum MIS5e (Figure 3.10). Both alignments agree on the timing of the MIS6-5 transition within the core. Therefore, in the following chapters, I will focus mainly on the climatic transitions surrounding Termination II, the interval that I have greatest confidence in the age constraints on the core GC642. In Chapters 5 and 6, I report proxy records generated on GC642 that span the interval following the MIS6-5 transition. In these chapters, I used the alkenone-based age model to place stratigraphic constraint

on these proxy records; however, it should be emphasised that as two very different age models are plausible, the age model in this section of the core remains highly uncertain.

Chapter 4

Dynamic changes in the South Atlantic over the last deglaciation

4.1 Introduction

The last glacial termination was accompanied by an 80 ppm rise in atmospheric pCO_2 (Delmas et al., 1980; Neftel et al., 1982), and it is widely believed that this increase in pCO_2 was driven by processes occurring within the Southern Ocean (Knox and McElroy, 1984; Sarmiento and Toggweiler, 1984; Siegenthaler and Wenk, 1984). These Southern Ocean processes are proposed to have released CO_2 from the deep ocean through a combination of decreased nutrient utilisation (Martin, 1990), increased vertical mixing (Toggweiler, 1999) and increased air-sea gas exchange (Stephens and Keeling, 2000).

Geochemical records show evidence for an 'old' (Skinner et al., 2010) respired dissolved inorganic carbon pool in the glacial Southern Ocean below 2500 m (Boyle, 1988; Hodell et al., 2003b) which became better ventilated over the course of the deglaciation (Burke and Robinson, 2012; Skinner et al., 2010), supporting the idea that the deep ocean was isolated from the atmosphere during glacials. Over the deglacial period this chemical stratification between the deep ocean and the overlying intermediate ocean decreased, e.g. Hodell et al. (2003b), implying a change in circulation or ventilation within the Southern Ocean which enabled CO_2 to be upwelled and outgassed to the atmosphere (Toggweiler, 1999). The chemical destratification of the ocean has been attributed either to (i) an increase in air-sea gas exchange, through a decline in the spatial and temporal extent of sea ice (Stephens and Keeling, 2000) and/or a decrease in surface ocean stratification (François et al., 1997); or (ii) a breakdown in the density stratification between the poorly-ventilated deep ocean and the better-ventilated water masses above (Sigman et al., 2010). Evidence supporting either scenario remains elusive.

Porewater $\delta^{18}O$ and salinity profiles from deep ocean sediments have provided the first estimates of the density of the deep ocean during the Last Glacial Maximum (LGM) (Adkins et al., 2002; Malone et al., 2004). These studies found that the glacial deep ocean was highly saline (~37 psu) and had an in-situ density that was 2 kg/m^3 denser than modern deep water (Figure 4.1). These studies lend support to the hypothesis that CO_2 storage within a highly stratified glacial ocean played a significant role in driving lower glacial atmospheric pCO_2. However, porewater

profiles only provide a 'snap-shot' of the physical properties of the deep ocean at the LGM, and do not provide information about the time-dependent changes in the density of deep water over the deglaciation. Thus, from these studies alone, it is impossible to assess whether the destratification of the deep ocean density gradients drove the atmospheric pCO_2 increase over the deglacial period.

Isotope-enabled intermediate complexity models have been used to suggest a mechanistic link between the physical (density) and chemical ($\delta^{13}C$) properties of the ocean over glacial-interglacial timescales (Bouttes et al., 2010; Tagliabue et al., 2009). These models suggest that deep ocean stratification, generated by the formation of dense brines during sea ice growth, is required to reconcile the spatial distribution of seawater $\delta^{13}C$. This result implies that a decrease in spatial extent of Antarctic sea ice over the deglacial period will affect both the density of the deep ocean and its chemical properties synchronously. Testing this hypothesis of a mechanistic link between the physical and chemical properties of the ocean requires observational evidence of the density structure evolution of the Southern Ocean over the entire deglacial period.

In this chapter, I determine the deglacial evolution of the intermediate-deep density gradient in the South Atlantic Ocean by generating temperature and salinity proxy records over the last 20 ka at two sites in the sub-Antarctic Atlantic (Figure 4.1). I compare the evolution of the density gradient with benthic $\delta^{13}C$ and ^{14}C records from the two sites in order to assess the hypothesis of a mechanistic link between the physical and chemical properties of the deglacial ocean.

4.2 Core locations

Developing an understanding of the vertical changes occurring within the ocean typically requires a depth transect of sediment cores that are located within a confined region, where surface signals should be common to all sites. However, due to a lack of cores from intermediate water depths in the Eastern Atlantic/Cape Basin combined with low sedimentation rates at those few available sites (e.g. Catherine et al. 2001; Hodell et al. 2003b) and the dearth of deep sites in the western sub-Antarctic Atlantic, it was necessary to study two rather distal sites. The core locations and in-situ temperature, salinity and density of the sites used are given in Table 4.1 and Figure 4.1.

Table 4.1: Core locations and physical properties (T, S and σ) of the bottom water.

Core	Latitude (°N)	Longitude (°E)	Depth (mbsl)	Temp. (°C)	Salinity (psu)	Density (kg/m^3)
GC528	-53° 00.8'	-58° 02.4'	598	3.93-4.47	34.2	1029.9
MD07-3076Q	-44° 09.2'	-14° 13.7'	3770	1.69-1.99	34.7	1044.9

Core GC528 was retrieved from the slope of the Falkland Plateau, whereas core MD07-3076Q was retrieved from the eastern flank of the mid-Atlantic ridge. Despite the geographic separation of these cores, they underlie roughly equivalent surface circumpolar ocean regimes (sub-Antarctic Zone). The modern sub-Antarctic Atlantic is zonally continuous, in terms of potential density (Figure 4.2). In this study I make the assumption that deglacial changes occurring at either site would occur everywhere synchronously along isopycnals in the sub-Antarctic South Atlantic.

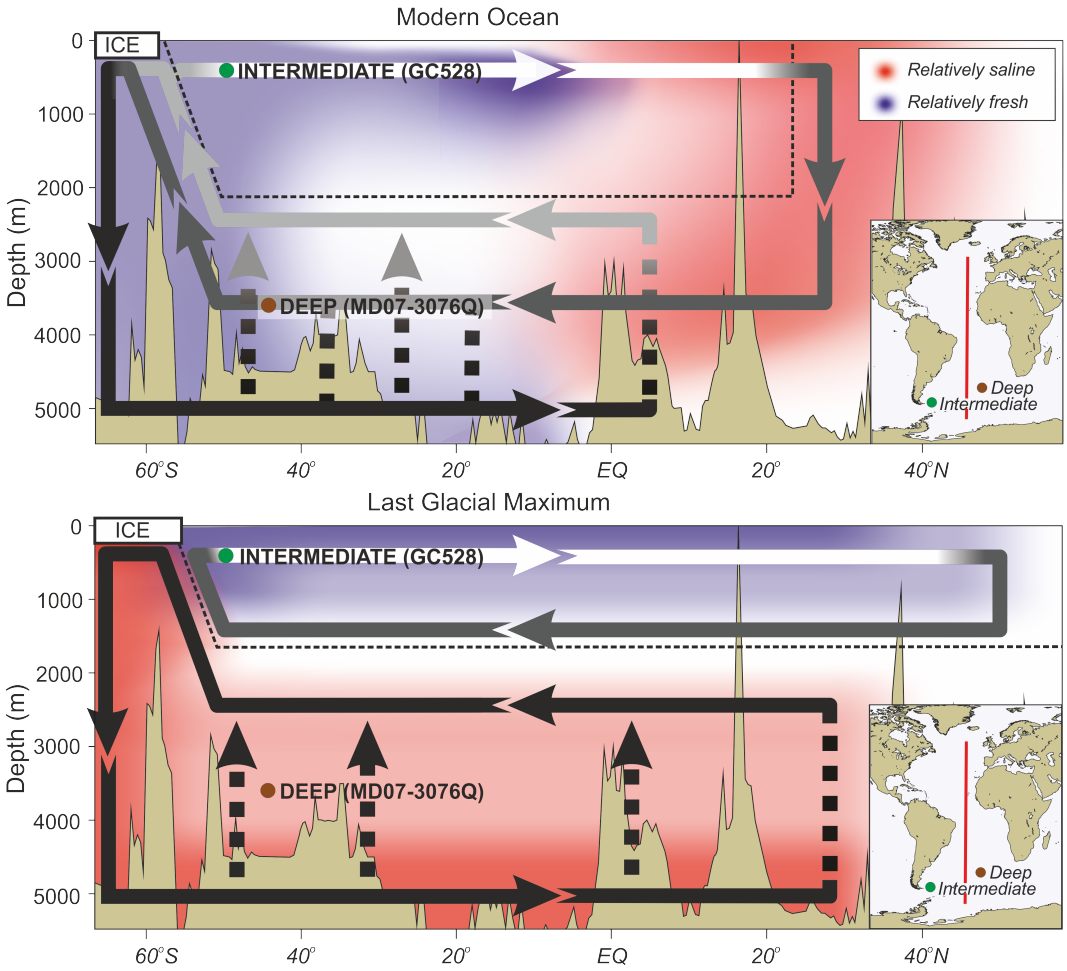

Figure 4.1: Location of intermediate (GC528) and deep (MD07-3076Q) sites overlain on a schematic map of ocean circulation for (Top) modern ocean and (Bottom) LGM, adapted from Ferrari et al. (2014). The grayscale colors indicate the flow path of major water masses. Background colors indicate the relative salinity of water masses.

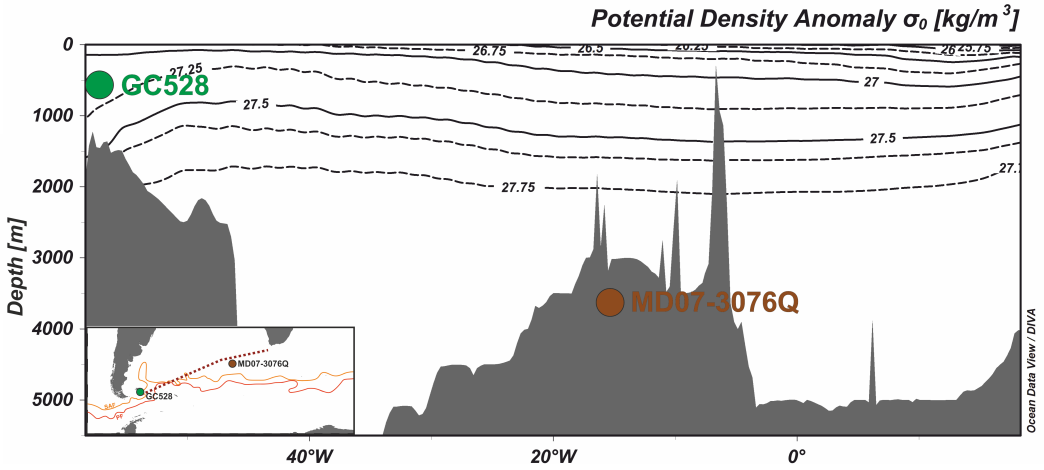

Figure 4.2: West-East transect of the variation in potential density across the sub-Antarctic Atlantic.

4.3 Methods

4.3.1 Age Models

The age model for core GC528 is based on benthic radiocarbon dating and is described fully in Chapter 3. The chronological control of MD07-3076Q is based on radiocarbon measurements and the stratigraphic alignment of sea surface temperature proxies with Antarctic temperature, and is described fully in Gottschalk et al. (2015).

4.3.2 Sample Preparation

In GC528, samples of *Uvigerina bifurcata* (125-212 μm size fraction) were hand-picked, cleaned using the methodology of Barker et al. (2003). From each sample ~100 μg was used for oxygen and carbon stable isotope analysis and ~400 μg was used for trace element geochemistry. All analyses were conducted at the Godwin Laboratory for Palaeoclimate Research, University of Cambridge.

In MD07-3076Q, samples of *Uvigerina spp.* (125-212 μm size fraction) were hand-picked and ~3 whole specimens were used for stable isotope analysis, and 10-15 whole specimens were cleaned for Mg/Ca analysis using the methodology of Barker et al. (2003).

4.3.3 Mg/Ca-derived benthic temperatures

At both core sites, Mg/Ca ratios were measured on the shallow infaunal foraminifera *Uvigerina spp.* This genus was selected because of its down-core abundance, and because its infaunal habitat makes it is relatively insensitive to variations in the carbonate ion concentration of the bottom water (Elderfield et al. 2010; Elmore et al. 2015).

In order to increase the temporal resolution of the Mg/Ca record from MD07-3076Q, additional *Uvigerina spp.* Mg/Ca data was incorporated from samples that had been cleaned using the clay removal and silicate removal steps (Barker et al., 2003) but without a full oxidative cleaning. Comparison of samples which had been both oxidatively cleaned and non-oxidatively cleaned show an average offset of 0.045mmol/mol (Figure 4.3 a-b). The non-oxidatively cleaned samples were corrected by -0.045 mmol/mol, however this does not significantly change the overall temperature trend (Figure 4.3c).

The Mg/Ca elemental ratios were determined by Inductively Coupled Plasma–Optical Emission Spectroscopy (de Villiers et al., 2002). The Mn/Ca ratio was measured to monitor cleaning efficiency and diagenetic effects. There is no relationship between the Mn/Ca ratio and the Mg/Ca ratio (Figure 4.3d), implying that diagenetic coatings do not significantly affect the Mg/Ca ratio measured. Non-oxidatively cleaned samples typically have a higher Mn/Ca ratio than oxidatively cleaned samples however, the concentration of Mn/Ca is so small (up to 0.3 mmol/mol) that the magnesium contribution of a diagenetic coating would have minimal effect. Assuming an Mg/Mn ratio of 0.1 mol/mol within a diagenetic coating (de Lange et al., 1992; Pedersen and Price, 1982), the maximum contribution of diagenetic coatings to the Mg/Ca ratio measured would be 0.03 mmol/mol.

Comparison of available *Uvigerina spp.* Mg/Ca-temperature calibrations in the literature shows there is a considerable range in the regression lines (Figure 4.4). The best-fit calibration curve

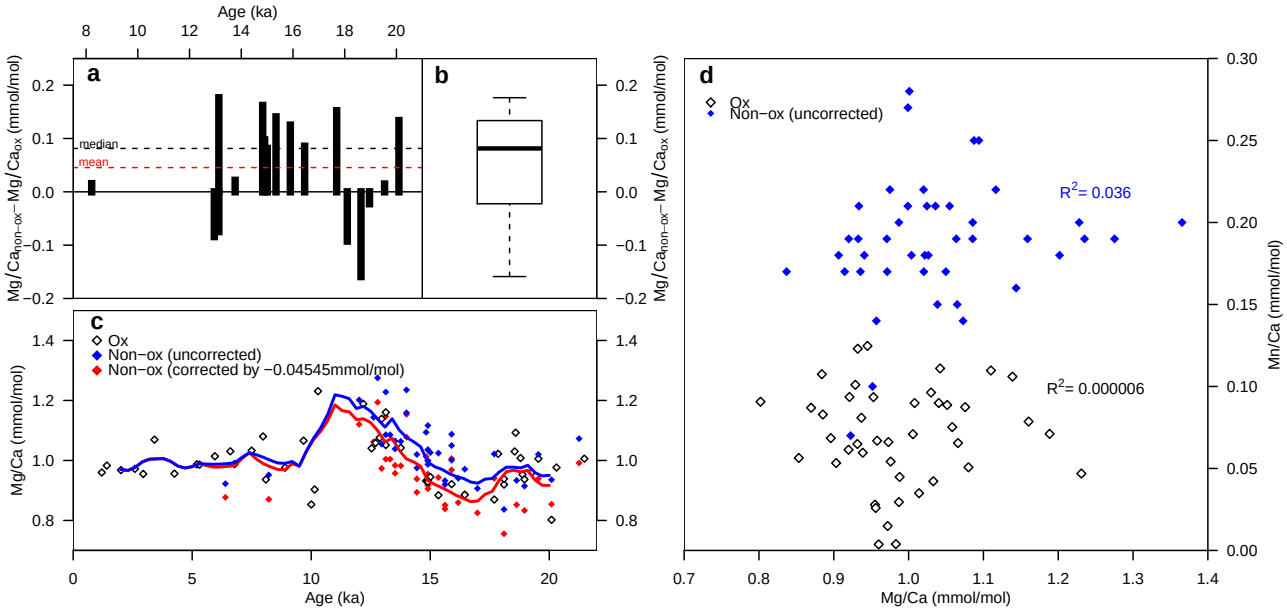

Figure 4.3: Comparison of oxidatively cleaned samples versus non-oxidatively cleaned samples. (A) Difference in Mg/Ca ratio between samples from the same depth interval cleaned non-oxidatively and samples cleaned oxidatively; (B) Barplot summarising the distribution in (A); (C) Time-series showing the difference in the Mg/Ca values of oxidatively cleaned samples (white) compared to non-oxidative samples (blue) and non-oxidative samples corrected by -0.045mmol/mol (red). (D) Crossplot of Mn/Ca versus Mg/Ca for MD07-3076Q.

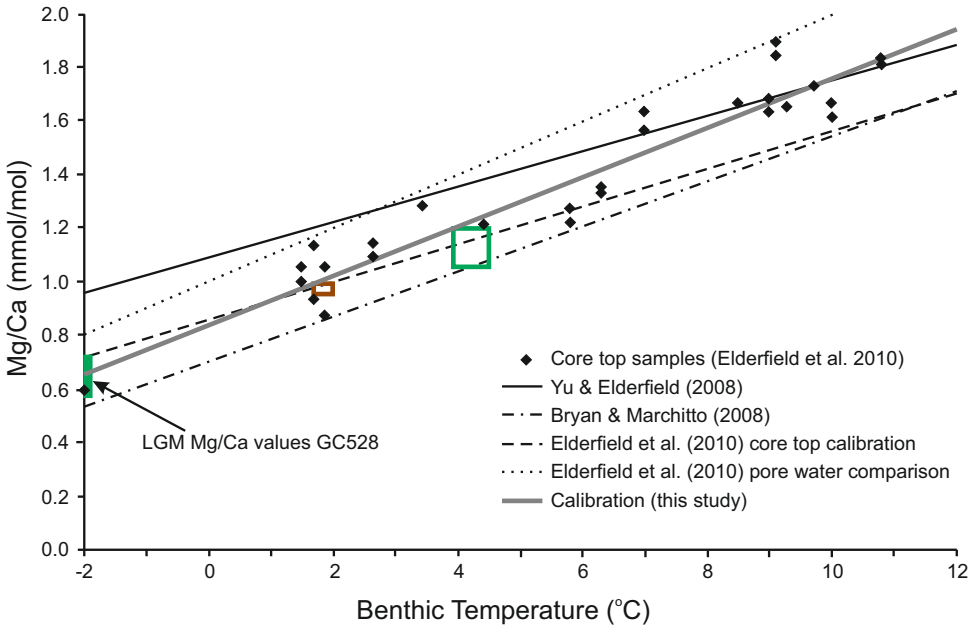

Figure 4.4: Comparison of published *Uvigerina spp.* Mg/Ca-temperature calibration curves (Bryan and Marchitto, 2008; Elderfield et al., 2010; Yu and Elderfield, 2008) with global core top data (Elderfield et al., 2010). Core top data from GC528 (green box) and MD07-3076Q (brown box) and additional minimum temperature constraint (green bar on the y-axis). The new calibration is shown as a bold grey line.

to the core top data from GC528 and MD07-3076Q is provided by the core-top calibration study of Elderfield et al. (2010). However, this calibration generates temperature estimates below the freezing point of seawater for GC528 at the LGM, the minimum temperature being -3.8°C. This may be in part caused by the lack of Mg/Ca core-top constraints for bottom water below 0°C. I attempt to improve the calibration by adding the constraint that the LGM minimum Mg/Ca value measured in GC528 cannot record temperatures below the freezing point of seawater (Figure 4.4).

The new calibration curve is defined as:

$$Mg/Ca = (0.0915 \pm 0.005)\,T + (0.843 \pm 0.035) \tag{4.1}$$

R^2= 0.92; 1σ = ±0.7°C.

4.3.4 Oxygen and stable carbon isotopes

At both sites, $\delta^{18}O$ was measured on the shallow infaunal foraminifera *Uvigerina spp.*, in order that the Mg/Ca-derived benthic temperatures could be coupled to $\delta^{18}O$ measurements to infer seawater $\delta^{18}O$. In contrast, $\delta^{13}C$ was measured on epifaunal foraminifera thought to more faithfully represent the $\delta^{13}C$ of the bottom water rather than a localised signal of porewater $\delta^{13}C$. In core GC528, there were no epibenthic species continuously present across the deglacial period, and so $\delta^{13}C$ was measured on the shallow infaunal species *Oridorsalis umbonatus* and corrected to equilibrium calcite by +1.0‰ (Woodruff et al., 1980). The $\delta^{13}C$ of *O. umbonatus* is inferred to be less influenced by pore-water overprinting than the $\delta^{13}C$ of *U. bifurcata*, based on good correlation with foraminifer/deep-sea coral ^{14}C trends from intermediate water (Burke and Robinson, 2012; de Pol-Holz et al., 2010) (Figure 4.5). However, it is important to acknowledge that the *O. umbonatus* $\delta^{13}C$ record is not a true reflection of bottom water $\delta^{13}C_{\mathrm{DIC}}$, as it is infaunal.

In core MD07-3076Q, $\delta^{13}C$ was measured on the epifaunal species *Cibicides kullenbergi*, a species believed to accurately reflect the $\delta^{13}C$ of the bottom water (Waelbroeck et al., 2011).

Stable isotopes from GC528 were analysed using a Multicarb preparation system coupled to a VG SIRA Mass Spectrometer in the Godwin Laboratory for Palaeoclimate Research, University of Cambridge. Measurements of $\delta^{18}O$ and $\delta^{13}C$ were determined relative to the VPDB standard with an analytical precision of ±0.08‰ for $\delta^{18}O$ and ±0.06‰ for $\delta^{13}C$. Stable isotopes from MD07-3076Q were analysed at the Laboratoire des Sciences du Climat et de l'Environnement. The mean external reproducibility of the carbonate standard is ±0.05‰ for $\delta^{18}O$ and ±0.03‰ for $\delta^{13}C$.

4.3.5 Palaeo-salinity reconstruction

Seawater $\delta^{18}O$ (δ_w) is calculated from the Mg/Ca-derived benthic temperature and the $\delta^{18}O$ of foraminiferal calcite using the linear form of the palaeo-temperature equation of Shackleton (1974):

$$T = 16.9 - 4.0\,(\delta_c - \delta_w + 0.27) \tag{4.2}$$

This calibration produces good agreement between modern measurements of δ_w and the calculated core top δ_w (Figure 4.6).

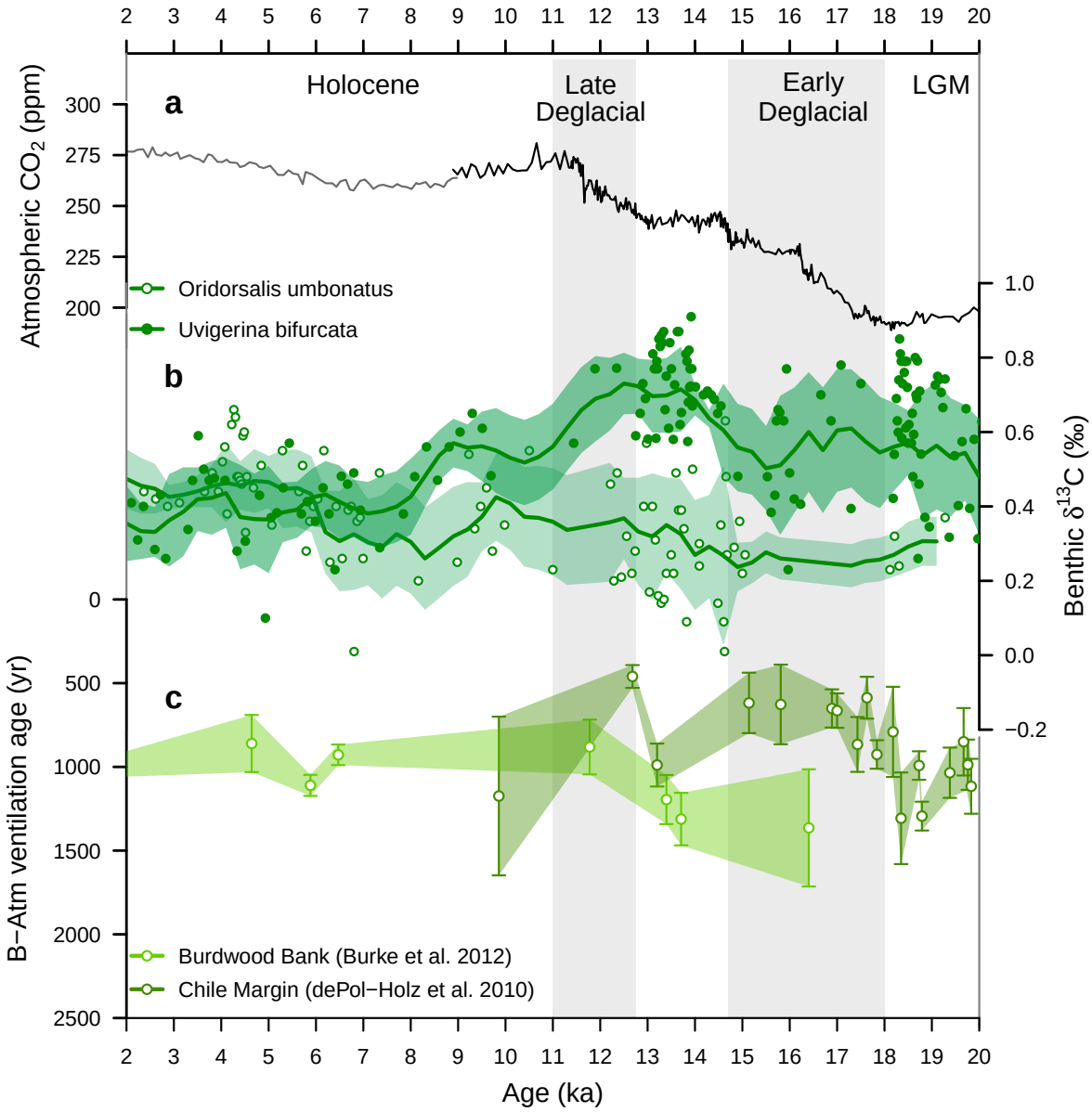

Figure 4.5: Comparion of *O. umbonatus* $\delta^{13}C$ and *U. bifurcata* $\delta^{13}C$ from GC528 with foraminifer/deep-sea coral ^{14}C trends from intermediate water (Burke and Robinson, 2012; de Pol-Holz et al., 2010) across the deglacial period. (A) Atmospheric CO_2 (WAIS Divide, Marcott et al. 2014 – black; EDC, Monnin et al. 2004 - grey); (B) *O. umbonatus* $\delta^{13}C$ (pale green, open symbols) and *U. bifurcata* $\delta^{13}C$ (dark green, closed symbols) measured on core GC528; (C) Radiocarbon ventilation ages from Burdwood Bank (Burke and Robinson, 2012) and the Chilean Margin (de Pol-Holz et al., 2010).

Salinity (S) is determined by applying a region-specific linear S-$\delta^{18}O$ regression based on a compilation of modern data from the South Atlantic (LeGrande and Schmidt, 2006):

$$S = \frac{4\delta_c + T + 53.78}{2.04} \tag{4.3}$$

Over a deglaciation, part of the change in salinity is attributed to the release of freshwater from continental icesheets. The residual salinity, i.e. the difference between the calculated salinity based on $\delta^{18}O$ and the negative salinity (freshwater) input due to the melting of continental icesheets, is the change in salinity that can not be attributed to the melting of continental icesheets, and therefore is a local salinity signal that may reflect changes in the structure and/or circulation of the ocean. In the following chapter I focus primarily on this residual salinity in order to better understand the relationship between changes in the structure of the water column (as expressed by residual salinity) and ocean chemistry.

In order to calculate the salinity change attributed to the melting of continental ice sheets (S_{ice}), I assume a linear relationship between relative sea level (RSL) (Lambeck et al., 2014) and $\delta^{18}O$ of seawater of -0.009‰/m (Schrag et al., 1996). A constant (α) is then added to scale the curve such that the $\delta^{18}O$ of seawater at 0 ka matches the core top value calculated from equation 4.2; the constant for site GC528 is -0.03 ‰, and for MD07-3076Q is -0.30‰. The salinity is then calculated by applying the same linear relationship as used in equation 4.3 (LeGrande and Schmidt, 2006):

$$S_{ice} = \frac{-0.009RSL + 17.4}{0.51} \tag{4.4}$$

The residual salinity (S_R) is then calculated by subtracting the salinity due to ice melt (S_{ice}) from the calculated salinity (S):

$$S_R = S - S_{ice} \tag{4.5}$$

It is important to bear in mind that the effect of melting ice on salinity will have spatial and temporal variations which are masked by the subtraction of a 'global mean' S_{ice}. However, as transient $\delta^{18}O$ and salinity tracer models are not currently available to provide information on local $\delta^{18}O$ and salinity variability over the last deglaciation, the global sea level curve (Lambeck et al., 2014) was taken as the best approximation for ice sheet melt derived changes in whole ocean salinity.

Figure 4.6: Deglacial records from intermediate (GC528) and deep (MD07-3076Q) water. (A) Atmospheric CO_2 (WAIS Divide, Marcott et al. 2014 – black; EDC, Monnin et al. 2004 - grey); (B) Mg/Ca-derived benthic temperatures for the intermediate site and the deep site. Thick bars at the start of each timeseries show modern temperature range; (C) Benthic foraminiferal $\delta^{18}O$ for the same sites as in (B); (D) Benthic salinity for the same sites as in (B). Large circles at the start of each timeseries show modern salinity at each core site. Black dashed/dotted line shows the predicted salinity change at each site attributed to the melting of continental ice sheets; (E) The residual salinity for each site, i.e. the difference between the salinity calculated in (D) and the predicted salinity change based on the melting of continental ice sheets (black dashed/dotted lines in D); (F) In-situ density of the intermediate site and the deep site. Black dashed/dotted line shows the predicted density change at each site attributed to the melting of continental ice sheets; (G) Residual density, i.e. the difference between the density calculated in (F) and the predicted density change based on the melting of continental ice sheets (black dashed/dotted lines in F). In all plots a 1.5 kyr spline and 1σ confidence interval is shown as solid line and shaded area respectively.

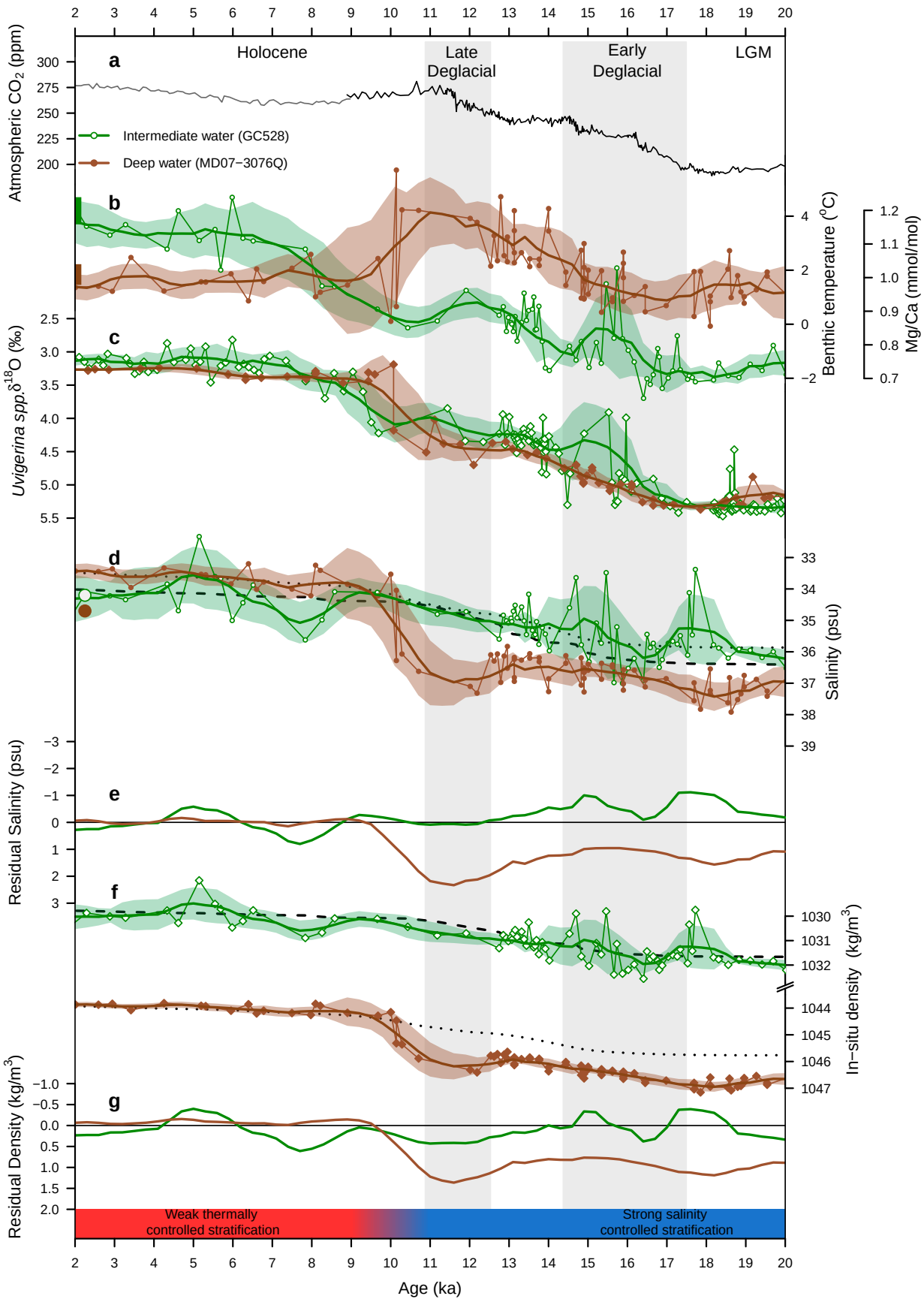
Holocene
Late Deglacial
Early Deglacial
LGM
a
b
c
d
e
f
g
Atmospheric CO2 (ppm)
Intermediate water (GC528)
Deep water (MD07−3076Q)
Benthic temperature (°C)
Mg/Ca (mmol/mol)
Uvigerina spp. δ18O (‰)
Salinity (psu)
Residual Salinity (psu)
In−situ density (kg/m3)
Residual Density (kg/m3)
Weak thermally controlled stratification
Strong salinity controlled stratification
Age (ka)

The modern linear regression between salinity and $\delta^{18}O$ of seawater for the Southern Ocean (LeGrande and Schmidt, 2006) is assumed be constant across the deglacial period. I will come back to this assumption in Section 4.4.4. Furthermore, it is important to note that brine rejection during the formation of sea ice increases salinity without significant isotope fractionation, thus the palaeo-salinity estimates in the deep water site derived from seawater $\delta^{18}O$ should be considered minima. In contrast, palaeo-salinity estimates at the intermediate water site will be maxima salinities.

4.3.6 Palaeo-density reconstructions

In-situ density was calculated from salinity and benthic temperature, using the equation of state (Jackett et al., 2010):

$$\rho\,(S,\theta,p) = \frac{P_n(S,\theta,p)}{P_d(S,\theta,p)} \tag{4.6}$$

where the polynomials $P_n(S,\theta,p)$ and $P_d(S,\theta,p)$ are defined in Table A.9. Similarly to the calculation of salinity, it is possible to calculate a residual density, i.e. the local density change that cannot be attributed to the melting of continental ice sheets.

4.4 Results and Discussion

4.4.1 Deglacial changes in the physical properties of the South Atlantic

Although the magnitude of the deglacial decrease in *Uvigerina spp.* $\delta^{18}O$ is similar in both sites (Figure 4.6c), the Mg/Ca-derived temperature reconstructions (Figure 4.6b) suggest that intermediate waters (GC528) were in fact cooler than the deep water (MD07-3076Q) for the majority of the glacial termination. This temperature inversion between the intermediate and deep sub-Antarctic reverses during the Early Holocene, from 9 ka onwards. It is physically impossible for cold intermediate water to overlie warmer deep water (even accounting for the effect of adiabatic decompression) and remain dynamically stable unless these differences are compensated by salinity. This suggests that during much of the glacial and deglacial period, the density structure of the South Atlantic was primarily governed by salinity differences. This is in stark contrast to the modern South Atlantic in which the density structure is maintained by temperature differences, with cold Antarctic Bottom Water (AABW) underlying warmer Antarctic Intermediate Water (AAIW).

The temperature of the deep water site during the glacial period is perhaps surprising, particularly given that (to my knowledge) no other deep water temperature reconstruction produces such warm LGM values. In the southwest Pacific, at site 1123, deep water temperatures (at 3200m water depth) during the LGM were close to freezing (Elderfield et al., 2010). Similarly cold deep water temperatures were also suggested from pore-water reconstructions (Adkins et al., 2002); although the accuracy of these data has recently been questioned (Miller et al., 2015). In the North Atlantic, it has been shown that deep water (2000-2600 m depth) temperatures reached 4°C during the Bølling-Allerød; but during the LGM, deep water temperatures were between -1 to -2°C (Thiagarajan et al., 2014). The comparison of the temperature record at MD07-3076Q in the deep South

Atlantic to other deep water temperature records serves to highlight the dearth of benthic temperature reconstructions in existence. It is imperative to produce more temperature recontructions from more proximal sites in order to validate or disprove the benthic temperature record presented here.

By deconvolving foraminiferal calcite $\delta^{18}O$ into its principal components, i.e. temperature and δ_w (Section 4.3), it is possible to reconstruct past seawater salinity at the two core sites (Figure 4.6d). Similarly, by taking the global sea level curve over the last deglaciation (Lambeck et al., 2014) and applying a scaling of -0.009‰/m, it is possible to reconstruct a hypothetical curve for the global mean change in ocean salinity (Figure 4.6d - black dashed/dotted line). The difference between this hypothetical salinity curve and the calculated salinity curved of GC528 and MD07-3076Q show the local deviation in salinity from the global mean, which I term the 'residual salinity'. Over the last deglaciation, the residual salinity at the intermediate water site is close to zero (Figure 4.6e) suggesting that most of the deglacial variation in salinity can be accounted for by the melting of continental ice sheets. By contrast, there is a large positive residual salinity during the LGM at the deep site (MD07-3076Q) of 1-2 psu which decreases to zero during the late deglacial (12-9 ka). The observation of high salinity water masses at depth during the LGM is consistent with previous salinity reconstructions based on porewater chloride concentration (Adkins et al., 2002). Although I emphasise that both reconstructions carry substantial uncertainty (Miller et al. 2015 and Section 4.4.4), the convergence of these two independent methods strengthens confidence in the main observation of a high salinity deep ocean during the last glacial period.

Using the palaeo-temperature and palaeo-salinity estimates, it is possible to calculate the in-situ density of the intermediate and deep water sites according to the equation of state (Jackett et al., 2010) (Figure 4.6f). The deglacial density reconstructions indicate the presence of a strong density gradient between intermediate and deep water for the glacial and much of the deglacial period. This density gradient decreases dramatically from 12 ka, and by 10 ka the deep ocean is 2 kg/m^3 less dense than at the LGM. This strong decrease in the density of the deep ocean is perhaps more apparent when considering residual density (Figure 4.6g). Prior to 12 ka the high salinity of the deep water site implies a strong vertical density gradient, despite the temperature inversion of cool intermediate waters overlying warmer deep water. After 10 ka the salinity stratification has broken down, and a weaker density gradient is maintained by the temperature difference between intermediate and deep water. Provided the assumption of zonal seawater density continuity across the sub-Antarctic Atlantic holds true, these density reconstructions indicate a significant mode switch in the primary physical parameters that govern ocean density stratification in the southern high-latitudes through the last deglaciation.

4.4.2 Processes controlling the physical properties of water masses

The calculation of seawater density at the two sites includes many assumptions and uncertainties which, when propogated through the calculation (Section 4.4.4) result in significant uncertainty in the absolute salinities and densities calculated. It therefore becomes problematic to use these absolute values (in temperature-salinity space) to make inferences about the processes controlling the physical properties of the water masses at these two sites over the last deglaciation. Whilst my calculation of salinity carries considerable uncertainty, one alternative approach to understand the important processes controlling the physical properties of these Southern Ocean water masses

is to compare the calculated $\delta^{18}O$ of seawater (δ_w) at a specific timeslice of the last deglaciation with the δ_w of modern Southern Ocean water masses. It is important to consider, however, that part of the deglacial variation in δ_w is the result of the melting of continental ice sheets. In order to compare our calculated δ_w at a particular point in the past with modern Southern Ocean δ_w the isotopic contribution of water locked up in continental ice sheets must be accounted for. I term this ice-volume corrected $\delta^{18}O$ of seawater, δ_{w-ice}. This correction enables the temperature and seawater $\delta^{18}O$ properties of deep and intermediate water masses in the past to be directly compared to the temperature and seawater $\delta^{18}O$ properties of modern water masses in the Southern Ocean (Figure 4.7).

Comparison of intermediate LGM temperature-δ_{w-ice} with modern measurements of seawater temperature and δ_w suggests that LGM intermediate water was analogous to modern Antarctic Surface Water (AASW), which is characterised by near-freezing temperatures (Figure 4.7). Such low temperatures suggest that the source location of intermediate water was strongly influenced by sea ice (which forms from seawater with a temperature of -2°C). Glacial sea ice reconstructions using diatom transfer functions (Allen et al., 2011; Gersonde et al., 2005) predict that winter sea ice could have extended as far north as 57°S at this longitude. We therefore suggest that glacial intermediate water masses at GC528 reflect the cold and fresh signature of surface waters close to the winter sea ice edge that is influenced by seasonal sea ice meltwater. This is in stark contrast to modern intermediate water at GC528, which is strongly influenced by a modified component of upwelled Circumpolar Deep Water (Tomczak and Godfrey, 2001) (Figure 4.7). Whilst we cannot negate the possibility that some component of Circumpolar Deep Water was present during the LGM, we suggest that its contribution was relatively minor in comparison to the contribution from AASW.

The processes controlling the benthic temperature of the deep site are more complex. Deep water formed close to the sea ice margin can only gain heat in two ways; (i) through mixing with other, warmer water masses, and (ii) through the accumulation of geothermal heat in the deep sea. If the source of the warmth in the deep South Atlantic derives from mixing with other water masses, the most probable source of warm water masses during the LGM are Drake Passage through-flow waters from the Pacific. However, there is no evidence supporting the idea that the Pacific was warm during the LGM. Deep water temperature records from the Pacific suggest that Pacific deep water was not significantly warmer than freezing (Elderfield et al., 2010; Woodard et al., 2014); however, these deep water masses were unlikely to flow over the shallow sills of the East Scotia Sea into the South Atlantic. More likely, warm Pacific intermediate waters acted as a source of heat to the deep South Atlantic during glacial times. However, I emphasise that this purely speculative as no published temperature estimates exist for Pacific intermediate water in the southeast Pacific, thus it remains to be determined whether Pacific intermediate waters were significantly warmer and had an influence on southern-sourced deep water in the Atlantic. Alternatively, the source of warmth in the deep South Atlantic may be derived from the accumulation of geothermal heat, assuming that the deep ocean is stagnant and cannot lose heat to the surface (Adkins et al., 2005). It has been shown by a conceptual model that it would take 10 kyrs to heat 2 km of seawater by 2°C, based on a heat flux of 500 mW/m^2 (Adkins et al., 2005). A completely stagnant deep water mass spanning the Atlantic seems physically unlikely, and it not consistent with radiocarbon evidence (Skinner et al., 2010), however, the shallow sills surrounding much of the South Atlantic may result in a localised

pool of poorly-mixed deep water in this region. Thus the glacial warmth observed at MD07-3076Q might reflect localised geothermal heating of this pool of poorly-mixed deep water in the South Atlantic rather than a widespread temperature inversion across the global ocean. The reconcilation of either of these two hypotheses requires similar Mg/Ca-$\delta^{18}O$ studies from other sectors of the global ocean.

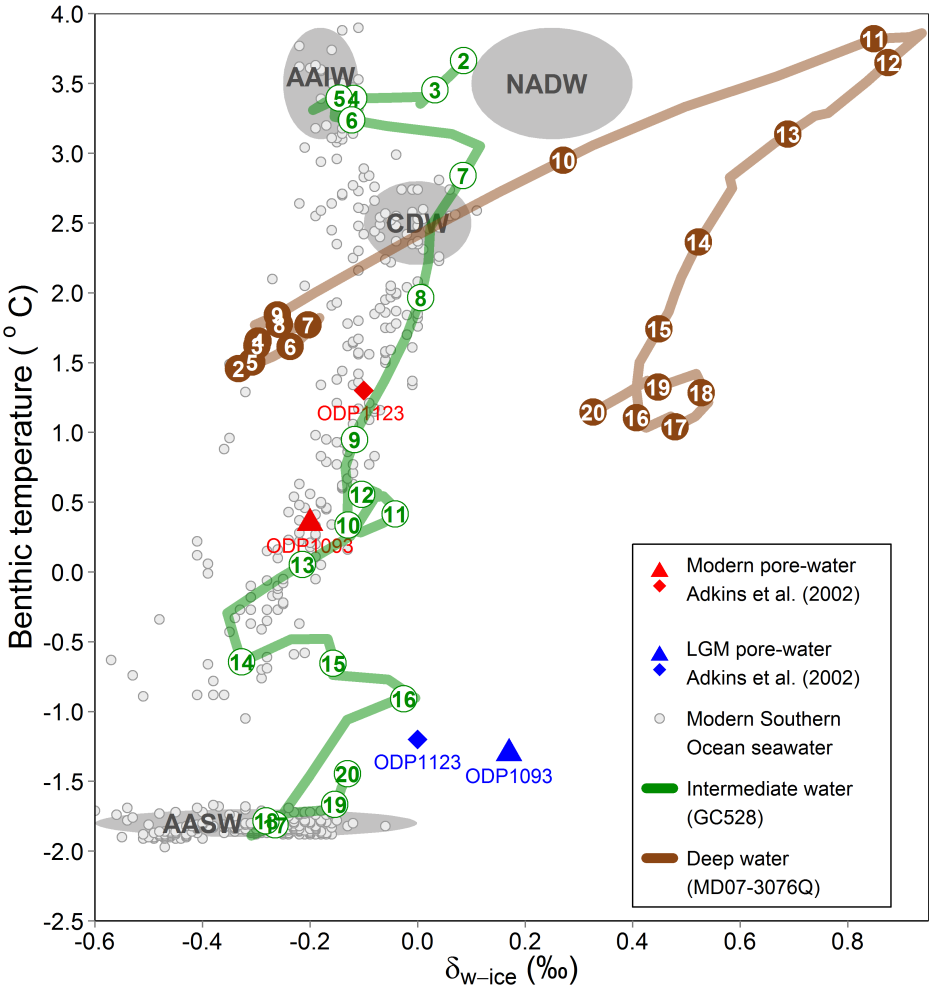

Figure 4.7: Temperature and 'salinity' (δ_{w-ice}) evolution of Southern Ocean Water masses over the last deglaciation. Grey dots represent modern seawater T-δ_{w-ice} (Meredith et al., 1999). Ages in ka shown in circles. Porewater estimates of seawater $\delta^{18}O$ and temperature shown for comparion (Adkins et al., 2002), note that the seawater $\delta^{18}O$ values have been corrected for an 'ice-volume' isotopic contribution.

The deglacial evolution of deep water temperature and δ_{w-ice} (Figure 4.7) can be understood by invoking a combination of (i) changes in the northern versus southern mixing ratio and (ii) changes in the end-member $\delta^{18}O$ of Antarctic Bottom Water (AABW). In the modern Atlantic Ocean, saline North Atlantic Deep Water (NADW) overlies fresh AABW (Figure 4.1). The high $\delta^{18}O$ signature of NADW reflects high rates of evaporation in the North Atlantic prior to subduction, whereas the $\delta^{18}O$ of AABW is comparatively more negative (Meredith et al., 1999). The warming and increase

in δ_{w-ice} over much of the deglaciation (16-12 ka) may indicate a greater proportion of northern-sourced water at MD07-3076Q. This is supported by benthic foraminifer ε_{Nd} data that suggests an increasing contribution of northern-sourced water in the South Atlantic throughout the deglaciation (Skinner et al., 2013). The late deglacial change in deep water δ_{w-ice} to isotopically lighter values after 12 ka is likely driven by a change in the mode of AABW formation. The two different modes of southern-sourced deep water formation, i.e. brine rejection during sea ice formation and supercooling of Ice Shelf Water (ISW) beneath the Antarctic ice shelves (Krueger et al., 2012), impart very different signals on δ_{w-ice}. Brines have a $\delta^{18}O$ signature close to surface water values (~0‰ in the Southern Ocean), whereas ISW has a negative $\delta^{18}O$ signature reflecting incorporation of overlying ice shelf meltwater. The marked decrease in the δ_{w-ice} of deep water at 12 ka is likely related to an increasing contribution of ISW constituting AABW. This change may be associated with a retreat in the grounding line of Weddell Sea ice shelves and an intrusion of relatively warm modified northern-sourced water under the ice shelves, further melting the marine-terminating ice sheets around Antarctica (Adkins, 2013). In summary, the modes of intermediate and deep water formation have a profound impact on the density structure of the sub-Antarctic ocean.

4.4.3 Physical and chemical properties of the ocean and pCO_2

In order to assess the hypothesis of a causal link between the physical and chemical deglacial destratification of the ocean, the timing of changes in the breakdown of the density gradient is compared with changes in benthic foraminifer $\delta^{13}C$ and foraminifer/coral benthic-atmospheric ^{14}C ages at both core locations (Figure 4.8). Benthic foraminifer $\delta^{13}C$ at the intermediate water site (GC528) was 1.5‰ more positive than the $\delta^{13}C$ of the deep site (MD07-3076Q; Waelbroeck et al., 2011) at the LGM (Figure 4.8b). This large $\delta^{13}C$ gradient breaks down over the deglaciation (15-10 ka) resulting in relatively homogeneous $\delta^{13}C$ values at both sites during the Holocene. Foraminifer/coral benthic-atmospheric ^{14}C age offsets between intermediate (Burdwood Bank, Burke and Robinson, 2012; Chile Margin, de Pol-Holz et al., 2010) and deep water (MD07-3076Q, Skinner et al., 2010) are broadly consistent with trends in deep and intermediate water $\delta^{13}C$ (Figure 4.8c). These two records ($\delta^{13}C$ and ^{14}C) provide strong support for glacial chemical stratification, which subsequently breaks down relatively early in the deglaciation.

Comparison of the deglacial density records (Figure 4.8d) and the chemical $\delta^{13}C$ and ^{14}C records (Figure 4.8b-c), shows a marked difference in the timing of the breakdown of density and chemical gradients. At the deep site, both the $\delta^{13}C$ and ^{14}C records suggest increased ventilation early in the deglaciation (17-15 ka), and in the case of the foraminiferal ^{14}C record, these early decreases in the benthic-atmospheric ^{14}C age have been linked to a synchronous rise in atmospheric CO_2 (Skinner et al., 2010). However, there is no concomitant change in the intermediate-deep density gradient at this time (Figure 4.8d). The onset of the physical destratification occurs during the Early Holocene (~10 ka), and appears to lag the late deglacial rise in atmospheric pCO_2. Our proxy records suggest that (i) changes in ocean chemistry in the South Atlantic occur without large-scale reorganisation of the ocean's density structure, challenging the propositions of a close coupling between physical and chemical ocean stratification as suggested by intermediate complexity models (Bouttes et al., 2010), and (ii) the density destratification of the South Atlantic could only have impacted atmospheric pCO_2 during the late deglaciation.

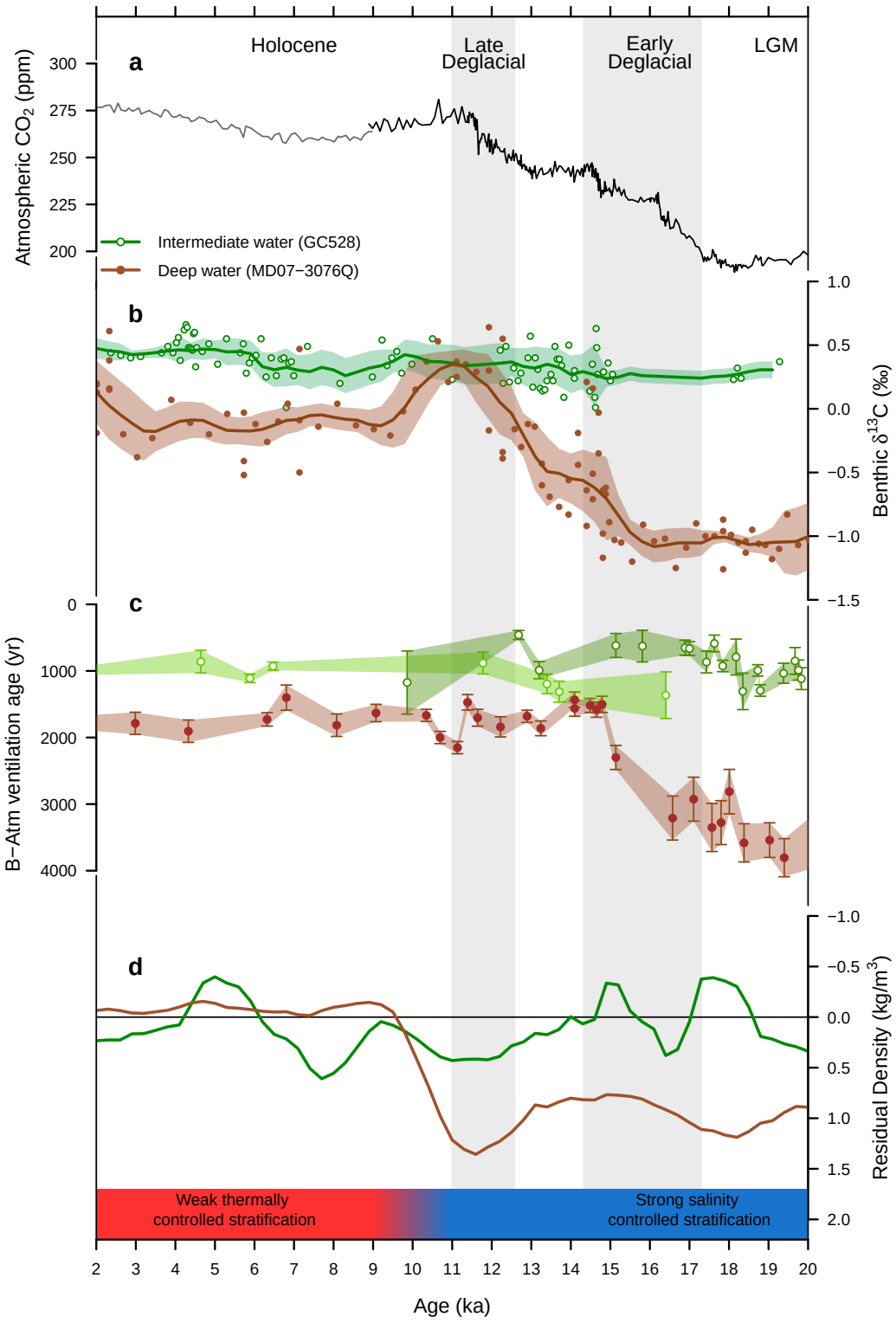

Figure 4.8: Comparison between the intermediate-deep density gradient and the chemical gradient. (A) Atmospheric CO_2 (WAIS Divide, Marcott et al. 2014 – black; EDC, Monnin et al. 2004 - grey); (B) Chemical properties, $\delta^{13}C$ of foraminiferal calcite, for intermediate and deep water; (C) Apparent water mass ventilation age (B-Atm), intermediate water (Burdwood Bank – pale green, open symbols, Burke and Robinson, 2012; Chile Margin – dark green, open symbols, de Pol-Holz et al., 2010) and deep water (MD07-3076Q – brown, closed symbols, Skinner et al., 2010); (D) Residual density of the intermediate site and the deep site.

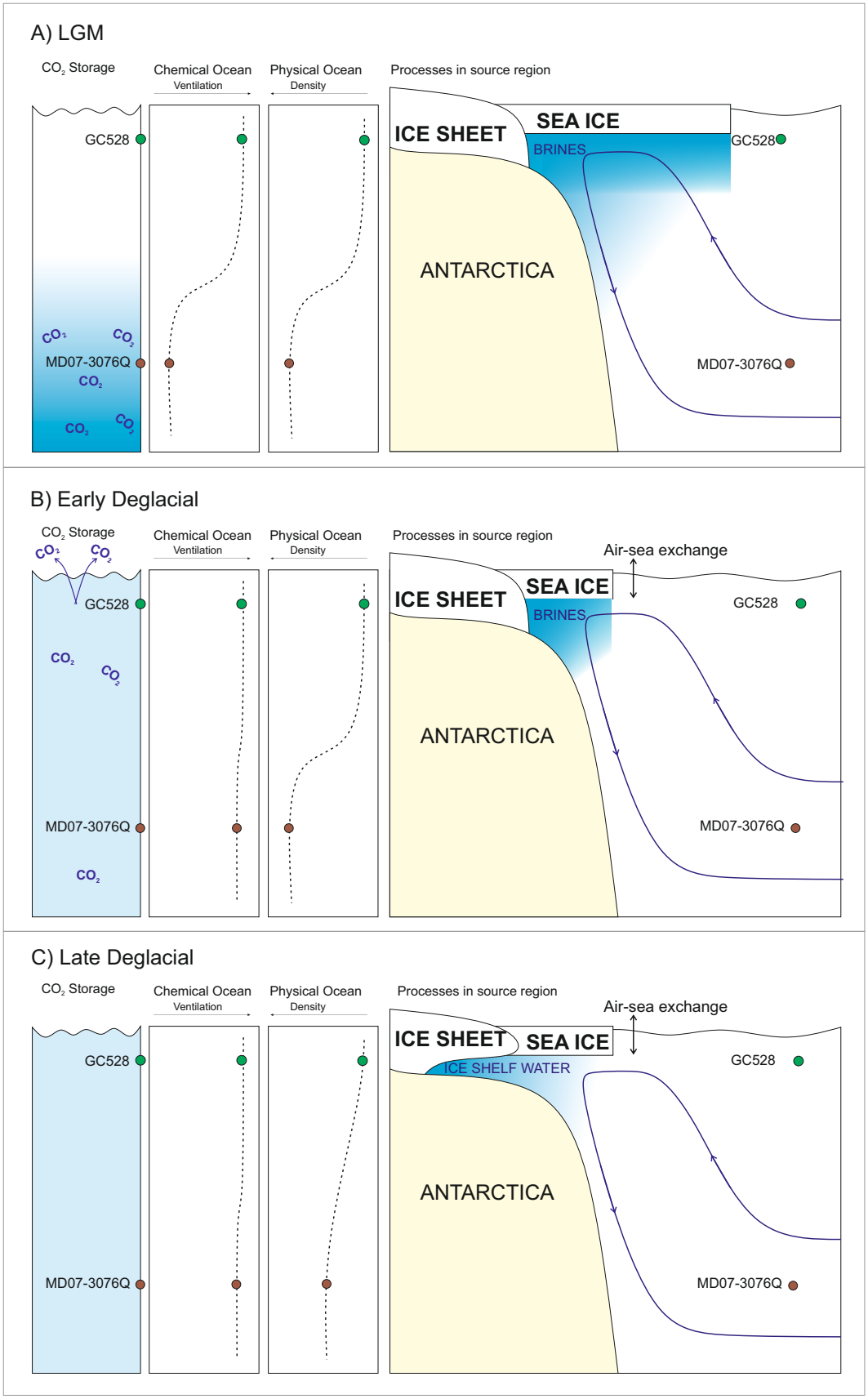

Figure 4.9: Schematic illustrating the sequence of events over the last glacial termination. (A) LGM Scenario; (B) Early Deglacial (17-15 ka) scenario; (C) Late Deglacial (12-10ka) scenario.

CO_2 stored in the deep ocean can be impeded from being released back to the atmosphere by two physical processes; (i) via an increased residence time of deep water masses in the ocean interior, through an increase in deep ocean stratification acting as a lid to deep carbon (Toggweiler, 1999); or (ii) reduced efficiency of air-sea gas exchange in the regions of deep mixing and upwelling (Stephens and Keeling, 2000). During the LGM, it is likely that both of these processes will have contributed to lower atmospheric pCO_2, owing to increased density stratification in the Southern Ocean and because permanent sea ice (Stephens and Keeling, 2000) and/or shallow stratification (François et al., 1997; Gottschalk et al., 2015) acted as a barrier preventing CO_2 from escaping the surface of the Southern Ocean (Figure 4.9a). Indeed, it is plausible that the retreat of summer sea ice during the early deglaciation (Allen et al., 2011; Collins et al., 2012) effectively removed a barrier to air-sea exchange, and thus contributed to the increase in atmospheric pCO_2 through enhanced ventilation of the deep overturning cell (Skinner et al., 2010, 2013) (Figure 4.9b). The hypothesis of an early retreat in the extent of Antarctic sea ice is also supported by the intermediate water warming trend observed in GC528 at 17-15 ka (Figure 4.6b). However the retreat of sea ice cover in the South Atlantic might not have had a significant effect on the density difference between the intermediate and deep overturning cells because the mode of deep water formation, which is controlled by the position of the grounded ice sheet relative to the continental shelf break, did not change. Although the geological evidence for the position of the grounding line in the Weddell Sea is inconsistent (Hillenbrand et al., 2012), there is indication that, at least around the Antarctic Peninsula, the grounding line retreat occurred late in the deglaciation (Johnson et al., 2011; Pudsey et al., 2006). Thus the glacial brine-dominated mode of southern-sourced deep water formation may have persisted until as late as 10 ka (Figure 4.9c). In summary, retreat of permanent sea ice may have occurred earlier than changes in the maximum position of the grounded icesheets, thus it is possible to ventilate the deep ocean without invoking a change in the mode of deep water formation, and thus decreasing its density.

Over the deglacial period (17-11 ka), increasing deep ocean temperatures (Figure 4.6b) coupled with a 0.6‰ increase in benthic foraminifer $\delta^{13}C$ (Waelbroeck et al., 2011) (Figure 4.8b) is indicative of a greater proportion of northern-sourced water in the deep South Atlantic. The impinging of warm modified northern-sourced water on the Antarctic continental shelf has been suggested as a possible mechanism (Adkins, 2013) which could melt back the grounded ice sheets in the Weddell Sea, freeing shelf space for the formation of ISW, resulting in the observed decrease in deep ocean density stratification at 10 ka. Whilst a decrease in the density of deep water has been invoked to explain the deglacial rise in atmospheric pCO_2, via associated changes in the rate of diapycnal mixing and the vertical position of the isopycnal separating the two overturning branches of circulation (Bouttes et al., 2010; Ferrari et al., 2014; Tagliabue et al., 2009), its impact appears to be relatively minor compared to the impact of changes in the rate of air-sea gas exchange in the Southern Ocean.

Although density destratification of the South Atlantic does not appear to play a leading role in regulating atmospheric pCO_2 across the last glacial termination, density destratification may have been important in 'locking in' the incipient transition to an interglacial climate state. Prior to destratification, the ocean was able to return to its 'glacial regime' following a transient perturbation; but not afterwards. Density destratification of the South Atlantic, initiated by a change in mode of formation of deep water, could act as a 'flip switch', eliminating the ocean's ability to re-stock its CO_2 inventory at the expense of the atmosphere, and thus forcing climate to switch to an inter-

glacial state. However, longer records of the density gradient variability within the Southern Ocean are required to test this hypothesis.

4.4.4 Error in palaeo-salinity reconstruction

There are several key assumptions in this reconstruction of palaeo-salinity which have the potential to introduce significant error into the salinity estimates. The first is the assumption that the 'ice-volume' effect is uniform globally. The second is that the modern Southern Ocean salinity-$\delta^{18}O$ regression is assumed to be constant over the last deglaciation. In this section, I first discuss the validity of these assumptions and then calculate the propagated error in my estimates of palaeo-salinity to show that the deglacial decrease in deep ocean salinity is outside the margin of error.

Global 'ice-volume' effect

The global 'ice-volume' effect refers to the isotopic signal of water locked in continental ice sheets, and is calculated by applying a linear scaling factor to the global sea level curve (Lambeck et al., 2014), typically a scaling factor of 0.09‰ per 10 m of sea level fall (Adkins et al., 2002; Lambeck et al., 2014) is used. In Section 4.4.2, the global 'ice-volume' effect was subtracted from the $\delta^{18}O$ of seawater in the calculation of palaeo-salinity to leave a corrected seawater $\delta^{18}O$ (δ_{w-ice}), which is the isotopic offset from the contemporaneous global mean. I make the assumption that by doing this correction, the corrected δ_{w-ice} can be directly compared to modern seawater $\delta^{18}O$. However, it is clear that this approach does not account for localised fluxes of isotopically light meltwater into the ocean, which will have a rapid and large isotopic effect on near-field sites but a more muted effect on more distal sites. Similarly, this becomes important when calculating the residual salinity and residual density.

As discussed earlier, transient $\delta^{18}O$ and salinity tracer models that could provide information on local $\delta^{18}O$ and salinity variability are not currently available, thus the global mean sea level record was taken as the best approximation for ice sheet melt derived changes in ocean δ_w, and thus salinity. Whilst this may be an overly simplistic assumption, deep South Atlantic $\delta^{18}O$ stacked records (Stern and Lisiecki, 2014) do not suggest any significant deviation in the timing of the onset of the termination to other regions in the ocean. Indeed, to force a synchronous breakdown of the physical and chemical gradients in the South Atlantic requires changes in δ_w in MD07-3076Q 5 kyr earlier than the global mean, which is significantly larger than the largest inter-regional differences (4000 years) observed (Stern and Lisiecki, 2014). Therefore, whilst some site-specific deviations from the global mean are masked in this calculation of palaeo-salinity, these deviations are unlikely to be so large as to eradicate the main observation, that timing of the breakdown in the physical stratificiation of the ocean significantly lags the chemical destratification of the ocean.

Invariant salinity-δ^{18}O regression

I make the assumption that the relationship between salinity and seawater $\delta^{18}O$ does not significantly differ between the Holocene and the LGM. There are a couple of lines of evidence which can be used to justify this assumption.

First, I perform a simple thought experiment whereby I test what the salinity-$\delta^{18}O$ relationship would have to have been at the LGM in order to eradicate the late deglacial decrease in salinity at the deep site. The LGM-Holocene difference in seawater $\delta^{18}O$ at MD07-3076Q is 1.8 ‰, of which 0.9 ‰ is attributed to the melting of continental ice sheets. Thus, the other 0.9 ‰ is a local change in the $\delta^{18}O$ of seawater. If no change in the salinity-$\delta^{18}O$ regression occurred over the deglaciation, this would be equivalent to the salinity at the LGM being 1.6 psu higher than in the modern (Figure 4.10; ΔS=1.6). Note that this value is in addition to the salinity change expected from the melting of continental ice sheets.

Instead, if we consider that there was no deglacial salinity change at the core site (other than the salinity change due to melting of ice sheets), then the hypothetical salinity-$\delta^{18}O$ regression (Figure 4.10; dashed line) that this point would lie on would either have a shallow gradient or a relatively low y-intercept value. This hypothetical salinity-$\delta^{18}O$ regression is very different to the main water masses present today in the Southern Ocean (LeGrande and Schmidt, 2006).

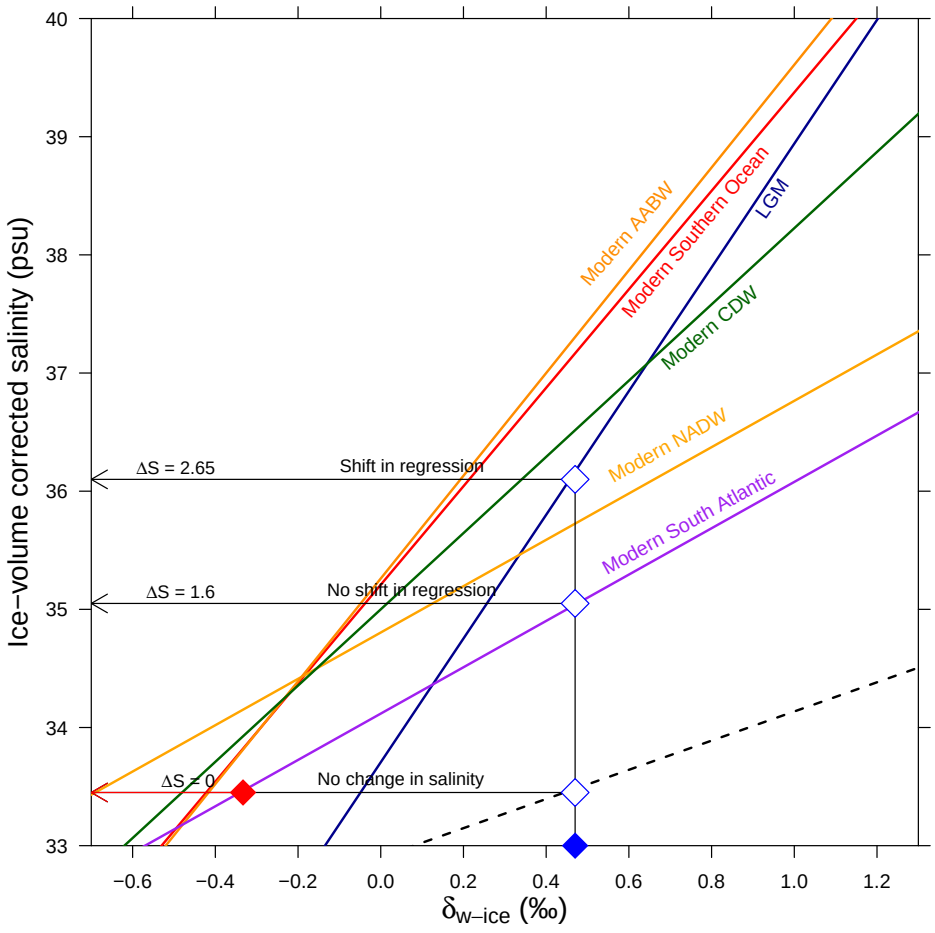

Figure 4.10: Investigating the range of deglacial salinity change possible due to a change in the salinity-$\delta^{18}O$ relationship. The modern and LGM data is shown for MD07-3076Q (red and blue diamonds) overlain onto the salinity-$\delta^{18}O$ relationships for modern water masses (LeGrande and Schmidt, 2006), and the LGM salinity-$\delta^{18}O$ relationship (Adkins et al., 2002). See text for details.

Furthermore, it is possible to reconstruct the salinity-$\delta^{18}O$ regression for Southern Ocean water masses (at 3000-4000m water depth) based on pore-water analysis of cores 1123 and 1093 (Adkins et al., 2002). In order to make a comparison of this regression to modern salinity-$\delta^{18}O$ regressions the 'ice-volume effect' on salinity and $\delta^{18}O$ is removed. As for the palaeo-salinity calculations, I assume the 'ice-volume effect' on salinity is 1.6 psu and the 'ice-volume effect' on seawater $\delta^{18}O$ is 0.9‰. The ice-volume corrected salinity-$\delta^{18}O$ regression is shown in Figure 4.10 (blue line). The corollary of this new regression is that if the LGM salinity-$\delta^{18}O$ regression did change between the LGM and Holocene, during the LGM the salinity-$\delta^{18}O$ regression would have presumably been equivalent to the salinity-$\delta^{18}O$ regression based on pore-water studies. This being the case, it would imply a larger deglacial salinity change than had we invoked no change in the salinity-$\delta^{18}O$ regression.

In summary, in order to eradicate the deglacial change in salinity (that is not due to ice sheet melt), the hypothetical salinity-$\delta^{18}O$ that would be required would be significantly different to any water masses currently present in the Southern Ocean, and significantly different to the LGM salinity-$\delta^{18}O$ regression as inferred by pore-water studies. Therefore, I suggest that a significant deglacial decrease in salinity occurred at site MD07-3076Q in addition to that related to the melting of continental icesheets.

A second line of evidence supporting the idea that a change in the salinity-$\delta^{18}O$ relationship did not occur over the last deglaciation comes from newly published isotope-enabled general circulation model (GCM) studies (Holloway et al., 2015). This study found that the South Atlantic exhibits a relatively constant salinity-$\delta^{18}O$ relationship across spatial and temporal scales supporting the validity of applying a temporally constant salinity-$\delta^{18}O$ relationship to my dataset. However, it is important to emphasise that Holloway et al. primarily focused on the salinity-$\delta^{18}O$ regressions of the surface ocean, and not those at depth.

Propagated error in the salinity and density calculation

Propagating the replicate error ($\sigma_{Mg/Ca}$ = 0.7°C) and the error in the new calibration curve (σ_{calib}= 1.1°C) gives a 1σ uncertainty in the temperature estimate of each sample of ±1.3°C. Previously published calibrations typically give 1σ uncertainties of 0.5-1.0°C (Anand et al., 2003; Elderfield and Ganssen, 2000; McConnell and Thunell, 2005). This difference may be due to a less critical assessment of the errors involved in the calibration curve. However, the errors associated with the calibration curve (σ_{calib}) are largely due to it being based on a compilation of data from different laboratories, with different cleaning procedures. It is likely that improvements in analytical technique have decreased the error associated with the calibration curve. The data used in this study was generated in the same laboratory, using the same method and has been checked for repeatability. Therefore, although the absolute temperatures may be uncertain, the raw Mg/Ca values generated in each core should be directly comparable. Therefore, I assume an error in benthic temperatures of 0.7°C, equivalent to the replicate error in the Mg/Ca measurement.

In order to calculate salinity, seawater $\delta^{18}O$ was calculated via the palaeo-temperature equation (Shackleton, 1974). The error in the $\delta^{18}O$ of seawater (σ_{δ_w}) is a combination of the error in the measurement of $\delta^{18}O$ of *Uvigerina spp.* (σ_{δ_c}= 0.08‰) and the error in the Mg/Ca derived benthic temperature (σ_T= 0.18‰): $\sigma_{\delta_w} = \sqrt{{\sigma_T}^2 + {\sigma_{\delta_c}}^2}$, consequently σ_{δ_w} = 0.19‰. I assume a linear

relationship between $\delta^{18}O$ and salinity, based on the Southern Ocean gridded $\delta^{18}O$ seawater data set (LeGrande and Schmidt, 2006). The variance in salinity σ_S is calculated using the σ_{slope} and σ_{icept} given in LeGrande and Schmidt (2006):

$$\sigma_S = \sqrt{{\sigma_{\delta w}}^2 \left(\frac{\partial S}{\partial \delta w}\right)^2 + {\sigma_{icept}}^2 \left(\frac{\partial S}{\partial icept}\right)^2 + {\sigma_{slope}}^2 \left(\frac{\partial S}{\partial slope}\right)^2} = 1.3‰ \tag{4.7}$$

The amplitude of the deglacial salinity change in MD07-3076Q at 11-9 ka is 3.3 psu, significantly larger than the variance in the salinity.

In-situ density was calculated using the equation of state expressed in Jackett et al. (2010). Variance was calculated similarly to equation 4.7, returning a variance in in-situ density of σ_ρ= 1.48 kg/m^3. This value is smaller than the total deglacial change in density (3 kg/m^3) observed at MD07-3076Q, suggesting that the decrease in density observed at 10 ka in MD07-3076Q is outside of the propagated error in the calculation.

4.5 Conclusion

This chapter discussed the first deglacial record of density changes in the deep and intermediate South Atlantic spanning the last deglaciation. I use paired Mg/Ca-$\delta^{18}O$ on the benthic foraminifera *Uvigerina spp.*, to show that the intermediate ocean was significantly colder than deep waters at the LGM, and explain that this temperature inversion requires that ocean stability is maintained by salinity gradients. This inference of a 'salt-stratified' glacial ocean lends support to previously published salinity reconstructions based on porewater analysis (Adkins et al., 2002), which have recently been called into question (Miller et al., 2015). The agreement in salinity estimates of the two independent methods, my foraminifera-derived approach and the porewater approach (Adkins et al., 2002), should provide support for a salt-stratified ocean during the glacial period.

I suggest that the presence of a salt-stratified ocean during the LGM, is largely driven by an increase in the extent of Antarctic sea ice. This controls the physical properties of the glacial South Atlantic generating cold, fresh intermediate waters in the sub-Antarctic, but also more saline deep water through the generation of brines. Over the deglaciation, intermediate water warmed in response to a retreat in the Antarctic sea ice margin, and the deep South Atlantic started to reflect both a greater proportion of northern-sourced water but also isotopically lighter AABW from the incorporation of Antarctic ice sheet meltwater. A rapid change in the dominant mode of deep water formation at the onset of the Holocene, from brines to super-cooled ISW, likely resulted in the density destratification of the intermediate-deep ocean during the late deglacial period.

These density records help address the question of whether deglacial changes in ocean chemistry are driven by a breakdown in the deep ocean density stratification, as has previously been suggested (Toggweiler, 1999). Comparison of the density records with chemical tracers at the two sites shows that the greatest intermediate-deep change in benthic foraminifer $\delta^{13}C$ and foraminifer/coral ^{14}C occurs prior to the density destratification. This suggests that density destratification was unlikely the driver of the deglacial changes in ocean chemistry, rather, chemical destratification was driven by an increase in air-sea gas exchange as sea ice retreated, which ventilates the deep overturning cell without affecting its density. The late deglacial breakdown in the density gradient of the

South Atlantic occurs at the onset of the Holocene, suggesting deep ocean density destratification did not play a leading role in driving the deglacial rise in atmospheric pCO_2. The difference in the timing of the breakdown of the intermediate-deep chemical gradient compared to the breakdown of the intermediate-deep physical density gradient suggests that chemical and physical stratification is not be as tightly coupled as previously inferred. However, the timing of the density destratification event (at the onset of the Holocene) is certainly curious, and raises the interesting possibility that the density destratification of the South Atlantic, induced by a change in the mode of deep water formation, could act as the 'flip switch' resulting in the transition to a full interglacial state. However, longer records spanning several glacial-interglacial cycles are required to validate this hypothesis.

Chapter 5

Cold Water Route

5.1 Introduction

The Drake Passage is an important region for setting the stability of Atlantic Overturning Circulation (AMOC). Here, low salinity water is advected into the Atlantic as Antarctic Intermediate Water (AAIW). In the modern ocean, the low density of AAIW relative to North Atlantic Deep Water (NADW) acts to stabilise AMOC; any slowing of NADW leads to the build-up of salinity in the North Atlantic and thus increases the density difference between AAIW and NADW that feeds back on and reinvigorates AMOC (Keeling and Stephens, 2001).

The flow of water through the Drake Passage is strongly focused along circumpolar jets (Koenig et al., 2014; Renault et al., 2011). Within the Drake Passage there are three principle circumpolar jets; the Sub-Antarctic Front (SAF), the Polar Front (PF) and the Southern Antarctic Circumpolar Front (SACCF). The flow of low salinity AAIW through the Drake Passage is primarily focused along the SAF (Talley, 1999).

Within the modern Antarctic Circumpolar Current (ACC), the positions of the circumpolar jets are relatively stable on decadal timescales (Graham et al., 2012), although there are significant seasonal variations in the frontal positions (Boehme et al., 2008). The long-term stability in the position of the fronts is due to barotropic component of ACC flow (Graham et al., 2012); the relative homogeneity of the ACC enables the fronts to extend down to the ocean floor (Renault et al., 2011), and thus bottom topography exerts a strong control on the position of the fronts – even in regions with flat topography (Graham et al., 2012). In contrast, the region north of the ACC, the water column is more stratified and the barotropic component of ACC flow reduced. As a result, jets associated with the fronts in these regions are surface intensified and confined to the upper ocean. This decoupling of the flow from the bottom topography enables the fronts in this region to move in response to the overlying wind forcing (Graham et al., 2012). This difference in baroclinicity of ACC flow is therefore an important factor in determining the ability of fronts to move relative to changes in the overlying wind stress.

During the Last Glacial Maximum (LGM), reconstructions of bottom water density in the Southern Ocean (Adkins et al., 2002; Malone et al., 2004; Roberts et al., 2016) suggest that the deep Southern Ocean was significantly more dense than in the modern. Furthermore, there was a strong density difference between the deep ocean (>3500 m) and the overlying intermediate ocean

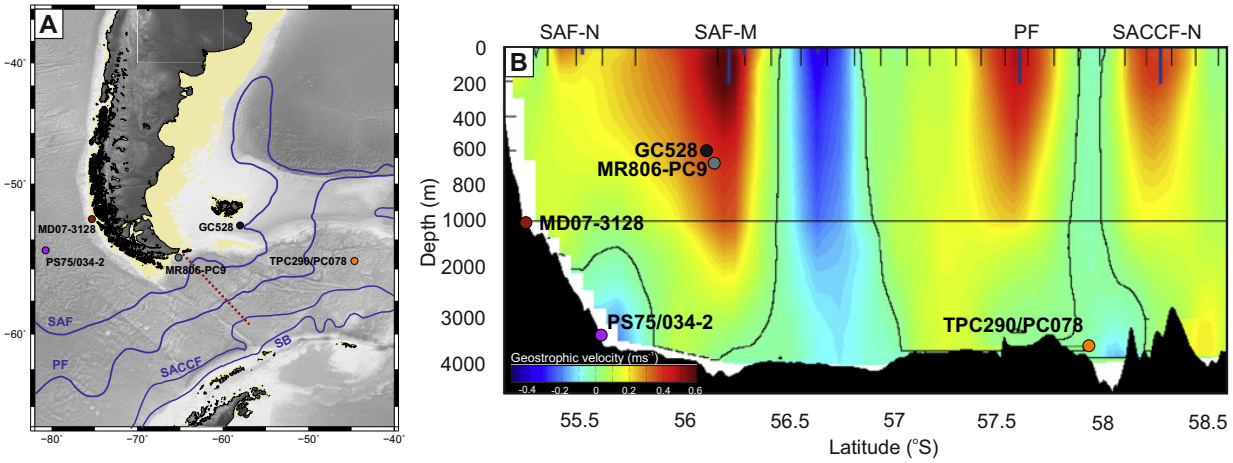

Figure 5.1: Map and transect of the Drake Passage. (A) Map of the Drake Passage showing the annual mean position of the circumpolar jets in blue (Orsi et al., 1995) relative to the cores discussed in this chapter; (B) Geostrophic flow velocities across a transect of the Drake Passage (Red line in (A); Renault et al. 2011). The cores discussed in this chapter have been projected onto the transect.

(~1000 m) (Roberts et al., 2016). This strong density stratification suggests that LGM ACC flow was potentially more baroclinic (i.e. the barotropic component was reduced) than in the modern ocean, and thus may have been more responsive to changes in the overlying wind forcing. These changes in the position of the fronts may have significant implications for the flow of AAIW into the Atlantic and thus on the stability of AMOC.

In this chapter I investigate changes in the position and intensity of the ACC jets over the last two glacial terminations using millennially-resolved sortable silt records from the northern and central ACC immediately downstream of the Drake Passage. I find evidence of a decrease in bottom current speeds in the deep central ACC coincident with the breakdown in the deep ocean density gradient, which I suggest is evidence of an increase in the barotropic component of ACC flow. I argue that this change had significant implications for the position of ACC fronts during the glacial, and thus may have affected flow of AAIW through the Drake Passage with potential consequences for the stability of AMOC.

5.2 Core Locations

In this chapter I reconstruct bottom current flow speeds from two sites immediately downstream of the Drake Passage. At the northern edge of the ACC, cores GC528 and GC642 are at a water depth of 600 m and are located immediately below the modern SAF (Table 5.1; Figure 5.1). In the central ACC, cores TPC290 and PC078 are at a water depth of 3840 m and are currently located in a weak easterly flow between the PF and the SACCF (Figure 5.1; Renault et al. 2011).

I will draw comparison with two other sites that have been published previously; site MD07-3128 is located on the Chilean Margin immediately upstream of the Drake Passage (Table 5.1; Figure 5.1; Lamy et al. 2015) and MR806-PC9 from the Argentine continental slope east of Cape

Horn at the northern margin of the Drake Passage (Lamy et al., 2015).

Table 5.1: Locations of cores discussed in Chapter 5.

Core	Latitude (°N)	Longitude (°E)	Depth (mbsl)	Reference
TPC290/078	-55° 33.00'	-45° 00.90'	3840	this study
GC528	-53° 00.78'	-58° 02.43'	598	this study
GC642	-53° 00.02'	-58° 04.64'	598	this study
MD07-3128	-52° 39.57'	-75° 33.97'	1032	Caniupán et al. 2011; Lamy et al. 2015
MR806-PC9	-55° 42.58'	-66° 08.06'	684	Lamy et al. 2015
PS75/034-2	-54° 22.12'	-80° 05.40'	4436	Ho et al. 2012

5.3 Methods

The primary goal of this chapter to reconstruct changes in the flow of the ACC over the last two glacial terminations. The main proxy that I will use to determine past ACC flow is the sortable silt mean grain size. Complimentary alkenone-derived reconstructions of sea surface temperature (SST), *Neogloboquadrina pachyderma sinistral* Mg/Ca-derived reconstructions of sub-surface temperature and ice-rafted debris records are also discussed.

5.3.1 Age models

GC528: The age model for core GC528 is based on reservoir-age corrected AMS ^{14}C dates on monospecific benthic foraminifera and is described in full in Section 3.1.

GC642: The age model for core GC642 is based on the alignment of alkenone-derived SSTs to Antarctic temperatures (Section 3.2; Figure 5.2a). As will become apparent, this is a rather unsatisfactory age model, because the alkenone-SST record in the younger sister core GC528 (which has alkenone-independent age model) does not resemble Antarctic temperatures (Figure 5.2a). In this chapter I discuss the alkenone-SST record in relation to the sortable silt record from the same core. Irrespective of the age model, the relative phasing of the changes within the core will remain the same.

TPC290/078: In the central ACC site, the age model for cores TC290, PC290 and PC078, which were recovered from the same site, were based on the alignment of their high resolution magnetic susceptibility records with the EPICA Dronning Maud Land (EDML) non-sea salt (nss) Ca^{2+} record (Fischer et al., 2007) and was previously published by Pugh et al. 2009 (Figure 5.2c). The EDML nss-Ca^{2+} record has been interpreted to reflect the signal of Patagonian dust (Pugh et al., 2009) that stimulated productivity leading to changes in bacterial magnetite (Yamazaki and Ikehara, 2012). In contrast to the trigger core TC290, piston core PC290 over-penetrated and so did not recover the

seabed surface. In order to fill this gap, TC290 and PC290 were spliced with PC078 from the same location using the magnetic susceptibility records (Figure 5.2c).

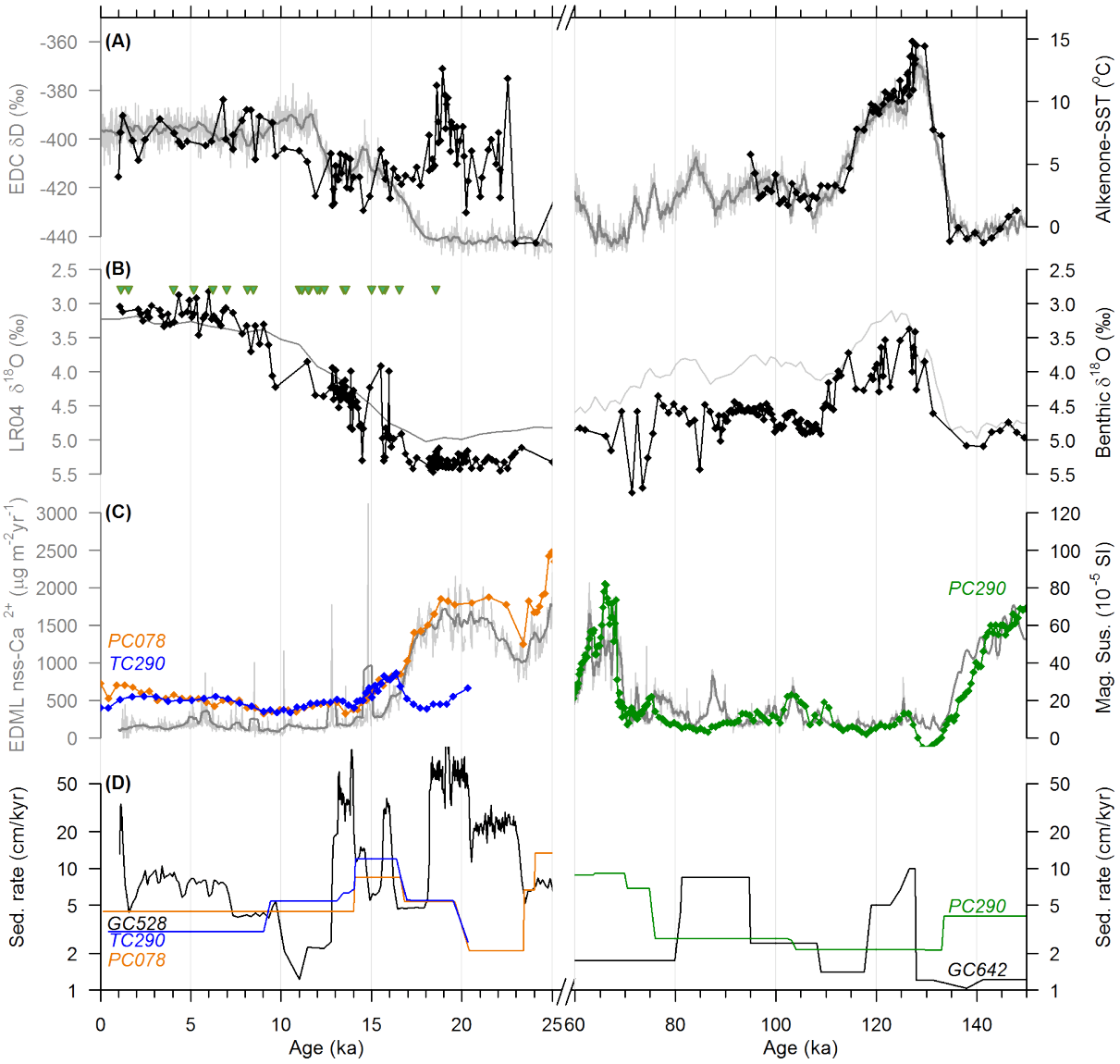

Figure 5.2: Age models for the last deglaciation (left) and the last interglacial (right) for the northern (GC528 and GC642) and central ACC cores (TC290, PC290 and PC078). (A) Stratigraphic alignment of GC642 alkenone-derived sea surface temperature (SST; black) with EPICA Dome C (EDC) δD record (grey) on the AICC2012 age scale (Bazin et al., 2013); (B) *Uvigerina bifurcata* $\delta^{18}O$ (black) record for cores GC528 and GC642 in comparison with the global benthic LR04 stack (Lisiecki and Raymo, 2005) (grey). Green arrows show the radiocarbon age constraints for core GC528; (C) Stratigraphic alignment of the magnetic susceptibility records of the central ACC cores (PC078, orange; TC078, blue; PC290, green) with EPICA Dronning Maud Land (EDML) non-sea salt (nss) Ca^{2+} (Fischer et al., 2007); (D) Sedimentation rates of the cores used in this study.

5.3.2 Sortable silt grain size analysis

The sediment grain sizes in the silt fraction (4-64 μm) are strongly controlled by the geostrophic speed occurring above the bottom mixed layer (McCave et al., 1995); the larger the mean particle size, the faster the overlying erosional flow. In this chapter, the sortable silt proxy is used as a semi-quantitative estimate of the bottom water flow over each core site, and thus used to infer changes in the strength of the Antarctic Circumpolar Current over the last two glacial terminations. A full description of the method of preparing and measuring sediment for sortable silt mean can be found in Section 2.2.13.

5.3.3 Ice-rafted debris

In order to determine the potential bias of ice-rafted debris (IRD) on the sortable silt mean grain size, terrigenous grains over a threshold size (>250 or 300 μm) were manually counted. Ice-rafted debris comprises all grain sizes but we use counts above a threshold grain size as a proxy for IRD because grains in this fraction are unlikely to be transported by other processes.

In GC528 and GC642, terrigenous grains >300 μm from the carbonate-free fraction were counted. Taking into account that cores GC528 and GC642 are located on the upper continental slope, any density flows must have travelled down the Falkland Trough, avoiding the core sites, because no obvious gravitational down-slope deposits are observed in the core. Shards of Southern Andean volcanic ash, or tephra, >300 μm have the potential to be transported significant distances by the SWWs (Narcisi et al., 2012), so grains of tephra were not counted as IRD. We assume that by still including grains of other volcanic-origin in the IRD counts, we capture grains that were ice-rafted through the Drake Passage from western Patagonia and the Western Antarctic Peninsula where the lithology is primarily igneous.

In the central ACC sites (TPC290/078), IRD was estimated from terrigenous grains >250 μm. The slight difference in the size threshold is because of the availability of these data and the size fraction chosen by Pugh (2009). The 50 μm difference in 'IRD' grain size counted does not significantly alter the main interpretations of this study.

5.3.4 Alkenone-derived sea surface temperature

Long-chained ketones (alkenones) formed by surface-dwelling coccolithophores have enabled study of the surface ocean temperatures in the past (Prahl and Wakeham, 1987). There are a growing number of alkenone-derived sea surface temperature records off the western coast of Patagonia, which have been used to develop an understanding of regional ocean dynamics (Caniupán et al., 2011; Ho et al., 2012; Kaiser and Lamy, 2010; Lamy et al., 2004) and glacial-interglacial changes in the Drake Passage through-flow (Lamy et al., 2015). These studies find a strong glacial cooling (2-7^{o}C) relative to interglacial periods, which is attributed to northward expansion of Antarctic cold water and reduced Drake Passage transport (Lamy et al., 2015). To date, similar studies do not exist off the eastern coast of Patagonia. The only sea surface temperature estimate off the eastern coast of Patagonia is based on radiolarian transfer functions from the core PS2250-5 (Gersonde et al., 2003), and suggests strong cooling (> 9^{o}C) at the LGM relative to the Holocene. However, this site is located within the Brazil-Malvinas confluence, and variations in SST may reflect changes in the

position of the confluence rather than direct evidence in changes in the Drake Passage through-flow. In this chapter, the high-resolution well-dated core GC528/642 from the sub-Antarctic southwest Atlantic is used to study the evolution of sea surface temperatures (SSTs) immediately downstream of the Drake Passage over the last two glacial terminations.

The procedure for extracting and measuring relative abundances of di-, tri-, and tetra-unsaturated C_{37} alkenones is described fully in Section 2.2.4. Sea surface temperatures were inferred from the U^K_{37} index (Prahl and Wakeham, 1987). The U^K_{37}-SST calibration of Prahl et al. (1988) was used to generate a SST record for site GC528/642. I use U^K_{37} to derive SSTs rather than the more commonly used $U^{K'}_{37}$ because previous studies from the sub-Antarctic found better agreement in the temporal trend of the U^K_{37}-SST records with other surface temperature records (Ho et al., 2012).

5.3.5 Sub-surface temperature

In order to determine vertical changes in the thermal sturcture of the water column over time, the Mg/Ca ratio of planktonic foraminifera was used as proxy for near-surface temperatures. In core GC528, *Neogloboquadrina pachyderma (sinistral)* was the most continuous species present throughout the glacial period. Because of the small size fraction of the *N. pachyderma (sin)* (63-125 μm), a laser ablation technique was chosen to generate the Mg/Ca record as opposed to the more typical solution method. A full description of the techniques used to measure Mg/Ca using laser ablation, and to evaluate outlying data can be found in Section 2.2.11. Near-surface temperatures were determined using the *N.pachyderma*-specific temperature calibration of Elderfield and Ganssen (2000): $Mg/Ca = 0.5e^{0.1T}$. This calibration produces the closest agreement with modern ocean temperatures at 250 m.

5.3.6 Fidelity of the alkenone-SST record

I assess the possibility that the alkenone-U^K_{37} record may be responding to factors other than SST using the ΣC_{37}:ΣC_{38} ratio, which thought to reflect the dominant alkenone-producing population (McClymont et al., 2005). This data is obtained as a by-product of measuring the alkenone fraction via GC-CIMS (as described in Section 2.2.4).

5.3.7 Modelling the effect of changes in sea level on bottom current flow speed

The effect of glacial-interglacial changes in sea level was examined through numerical modelling – this work was carried out by Ricardo Matano (Oregon State University). The numerical model used in this study is a regional nested implementation of the Regional Ocean Modeling System. At the base there is a parent model, which extends from 20°N to 70°S and from -180° to 180°W with a horizontal resolution of ¼°. The parent model is nudged to the monthly mean climatological values of SODA at its northern (open) boundary. The initial conditions of the parent model are also derived from SODA. Nested into this parent model there is a child model, which covers all the southwestern Atlantic and southeastern Pacific sectors with a horizontal resolution of 1/12°. The nested model configuration is forced with climatological mean wind stress forcing derived from

the ERA-Interim data set. Surface heat and freshwater fluxes are derived from the COADS data set. The numerical experiments also include freshwater discharges from the Rio de la Plata, the Patos Lagoon and tidal forcing with 5 tidal components (M2, S2, N2, K1 and O1 harmonics). The buoyant discharge from Magellan Straits is accounted by a passage connecting the Atlantic and the Pacific basins.

An 'LGM' sea level simulation was run such that the only difference from the control was a 120 m reduction in sea level. The LGM and control simulations were spun-up to dynamical equilibrium and run in diagnostic mode for 5 years. Average values of the last year of the diagnostic run are used in the present analysis. A more detailed technical description of the control model configuration - including the spin-up procedure and implementation of tidal, wind, heat and freshwater forcing, river discharge, boundary conditions and mixing parameterisations as well as comparison with in-situ and remote observations - can be found in Combes and Matano (2014) and Matano et al. (2014).

5.4 Results

5.4.1 Deglacial changes in the bottom current speed

Mean silt grain size at the shallow northern ACC site (GC528) shows considerable variation over T-I, ranging from a low of 18.8 μm at 19 ka, to a high of 34.8 μm at the core top (Figure 5.3b). Similarly the $\overline{SS}$ over T-II shows evidence of a strong deglacial increase in bottom current flow speeds, ranging from a low of 19.2 μm at 138 ka to a high of 30.8 μm at 121 ka. The $\overline{SS}$ records across both terminations show an initial decrease in $\overline{SS}$ at the end of the glacial period (21 ka and 141 ka). These low glacial values are maintained across much of the deglacial period until the late deglacial (14 ka and 133 ka) when an abrupt increase in $\overline{SS}$ occurs. This is followed by a more gradual increase across the end of the deglacial period and throughout the following interglacial period.

In contrast, the deep central ACC site sortable silt record is significantly less variable. Across Termination I, $\overline{SS}$ are a constant value of 21.8 μm until 11 ka then decrease to a minimum of 17.6 μm at 8 ka. Between 8-0 ka, $\overline{SS}$ increases to a maximum of 25.6 μm. A similar pattern is observed across Termination II, with a relatively constant $\overline{SS}$ of 20.1 μm between 150-133 ka, followed by a significant decrease to a minimum of 18.1 μm at 128 ka, and then an increase to the end of the record at 119 ka. Unfortunately, $\overline{SS}$ was not measured across the rest of MIS5e preventing us from determining whether this increasing trend continues after 119 ka, similarly to MIS1.

5.4.2 Influence of sea level on bottom current speeds

In the modern ocean, there is a clear depth dependency of ACC flow (Renault et al., 2011), and thus glacial-interglacial variations in sea level may result in significant non-linear variations in flow speed irrespective of any significant change in overall ACC flow speeds. We test the effect of a sea-level decrease on bottom current velocities using the ROMS model (Shchepetkin and McWilliams, 2005). The LGM simulation in which sea level was lowered by 120 m was compared to the control simulation (in which no sea level change occurred). The model simulation suggests a slight increase

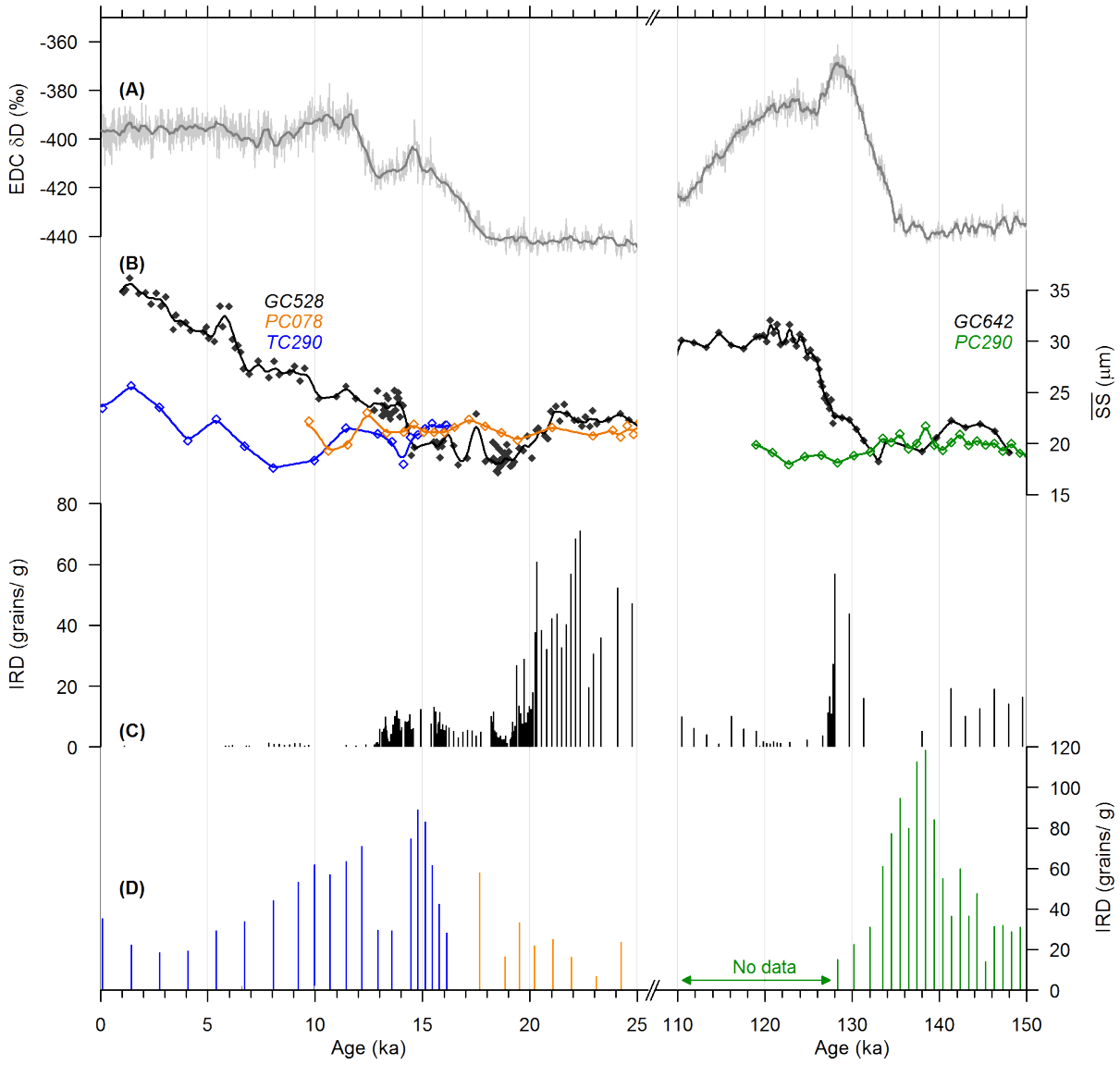

Figure 5.3: Grain size data across Termination I (left) and Termination II (right). (A) EPICA Dome C (EDC) δD record (grey) on the AICC2012 age scale (Bazin et al., 2013); (B) Mean grain size of the sortable silt (10-63 μm) fraction, in the northern ACC cores (GC528 and GC642, black) and central ACC cores (PC078, orange; TC290, blue; PC290, green); (C) Ice-rafted debris (IRD) concentration for GC528 (left) and GC642 (right); (D) Ice-rafted debris (IRD) concentration for central ACC cores (PC078, orange; TC290, blue; PC290, green).

(<0.05 ms^{-1}) in northward advection of bottom water at site GC528/642 during sea level lowstands (Figure 5.4). This increase in bottom current flow appears to be the result of a decrease in flow across the Patagonian shelf which channels greater flow along the shelf break. The model results are inconsistent with my sortable silt reconstructions of bottom water flow at GC528, which suggests weaker bottom water flow during the last glacial period. This discrepancy implies that changes in sea level are not the driver of the deglacial increase in bottom current speed at the shallow northern site, but rather other factors must play a more dominant role in overprinting the expected strengthening of bottom currents at this site.

On the basis of the model simulations I suggest the shallow northern ACC $\overline{SS}$ records (GC528 and GC642) are not adversely affected by near-surface effects and interpret the deglacial increase in $\overline{SS}$ across both terminations as a real increase in ACC flow speeds associated with the SAF and not by changes in sea level.

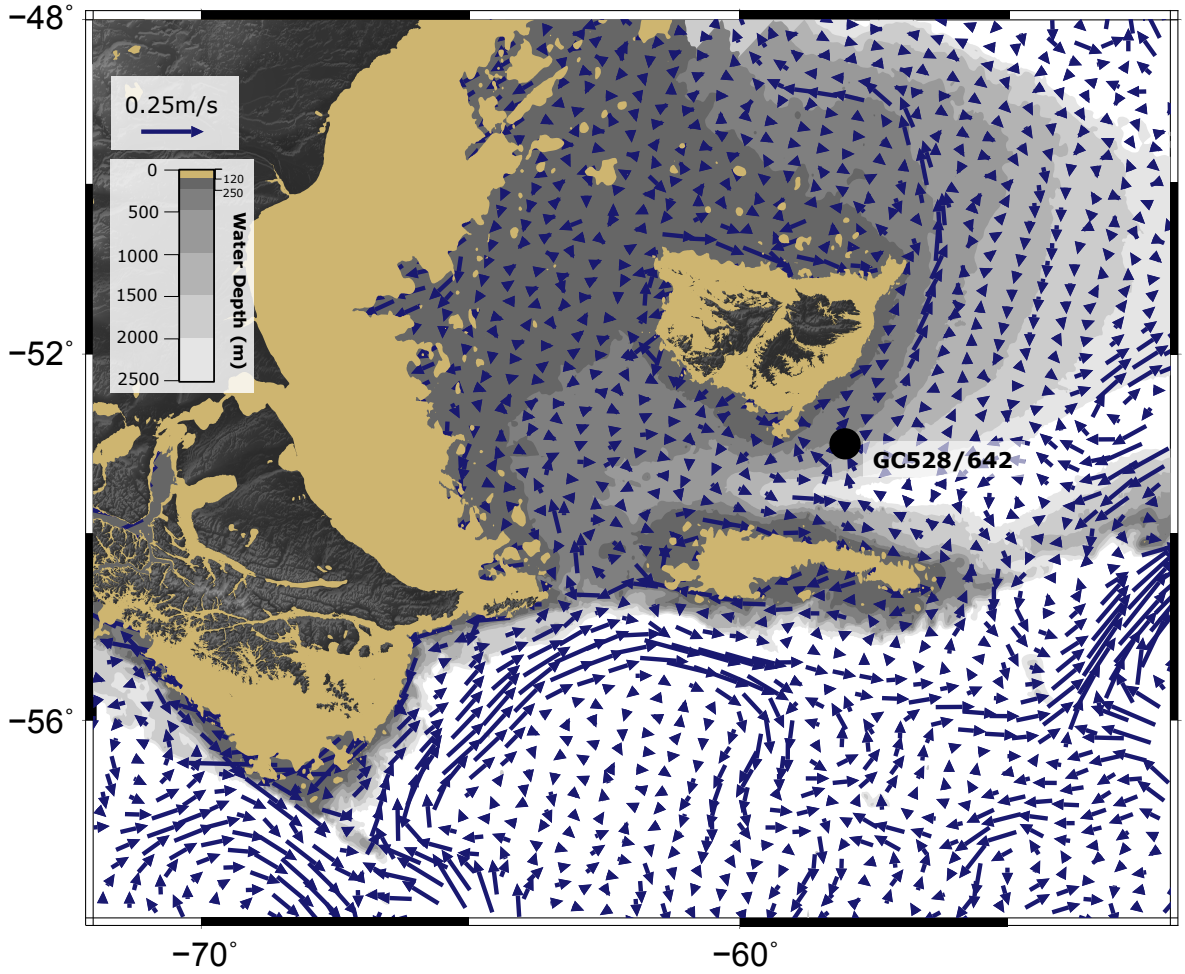

Figure 5.4: Model simulations of the impact of sea level on bottom water flow speeds. LGM-Control anomaly in bottom water flow velocity.

5.4.3 Ice-Rafted Debris

Across the two glacial terminations, the northern shallow site and central deep ACC site have very different patterns of IRD deposition. In the northern sites, the IRD (>300 μm) suggests elevated

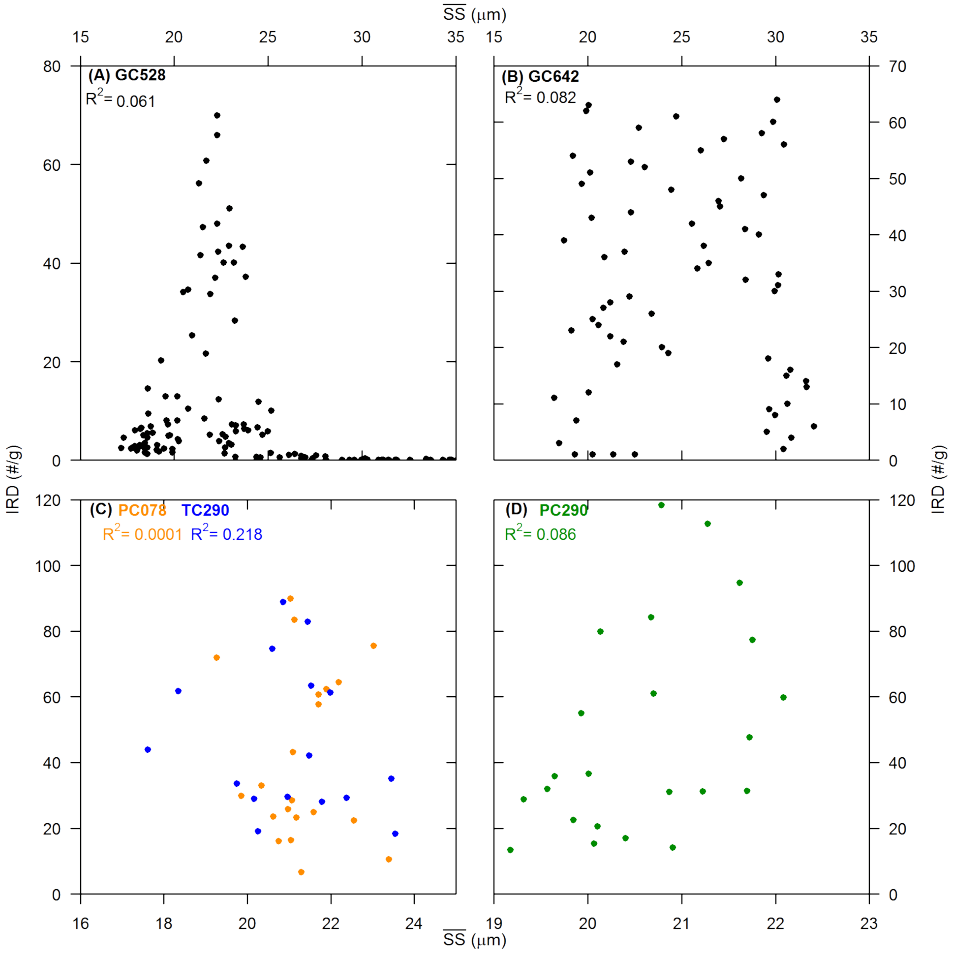

Figure 5.5: Crossplots of IRD and $\overline{SS}$ from the northern and central ACC sites across T-I and T-II. (A-B) Northern ACC sites; (C-D) Central ACC sites.

IRD concentrations during the glacial periods relative to the interglacial periods (Figure 5.3c). During the Eemian, there is an interval between 131-128 ka in which concentrations of IRD at site GC528/GC642 are significantly greater than during the previous glacial maximum. The timing of this apparent spike in IRD is broadly synchronous with the Last Interglacial climatic optimum (as suggested by Antarctic δD; Figure 5.3a). A major ice-rafting event seems surprising for this time period; however, there is no sedimentological evidence of a debris flow or other downslope transport, and thus I suggest that this IRD pulse is real.

IRD records from the central ACC (Figure 5.3d) appear to be anti-phased with IRD concentrations in the northern ACC. Across T-I, IRD concentrations are highest in TPC290/078 during the late glacial and Early Holocene, when a significant reduction in IRD at site GC528 is observed. Similarly, IRD concentrations in TPC290/078 are highest across T-II during the deglacial interval (140-135 ka), when there is a notable reduction in IRD at site GC528/642. A similar pattern of anti-phased IRD records was suggested in a model by Keany et al. (1976). This model proposed IRD accumulation in high latitude regions is characteristic of interglacial periods when a poleward 0^{o}C isotherm in the surface ocean results in significant melting close to the IRD source. By contrast, IRD accumulation in the sub-Antarctic is associated with glacial periods and the expansion

of cold Antarctic surface waters.

The influence of IRD on the $\overline{SS}$ record is assessed by crossplotting the two records; correlation between IRD and $\overline{SS}$ may indicate that unsorted IRD has overprinted the current sorted fraction of the sedimentary record. However, the cross-plots of IRD and $\overline{SS}$ from all sites presented here (Figure 5.5) reveal that there is no correlation between these two records, indicating that there is no significant overprinting of IRD on the sortable silt signal, i.e. all IRD deposited at this site has been current-sorted. Therefore, I regard the $\overline{SS}$ records produced at the two sites as a proxy solely reflecting bottom current speed.

5.4.4 Alkenone-derived sea surface temperatures

An alkenone-SST record was generated from site GC528/642 across T-I between 25-0 ka (Figure 5.6a) and T-II between 150-105 ka. The alkenone-SST record across T-II suggests strong range in SSTs from a low of -1°C at 140 ka to a high of 15°C at 130 ka. In contrast, the alkenone-SST record across T-I suggest that the glacial-interglacial range in SST was significantly more supressed than T-II. Glacial temperatures (25-12 ka) are generally colder than the Holocene (10-0 ka). However, there are two intervals spanning the end of the last glacial period (20-18.5 ka and 23-22 ka) in which SSTs in the southwest Atlantic are elevated by 4-6°C above the glacial mean. Replicates were analysed over this interval to validate the reproducibility of this result, but these warm LGM temperatures were found to be robust. In the following discussion, I evaluate factors which may result in the elevated LGM alkenone-derived SSTs.

A range of factors may bias alkenone-derived SSTs towards warmer temperatures, such as (i) a change in the dominant alkenone-producing population, (ii) post depositional alteration of the organic biomarkers, (iii) the input of reworked alkenones carrying a warmer temperature signal, (iv) advection of alkenones from warmer regions, or (v) changes in seasonality of alkenone production. Here, I discuss these potential mechanisms in relation to site GC528/642, and conclude that there is no reason to question the fidelity of the alkenone-derived SST record at this site.

Variations in the dominant alkenone-producing haptophyte would result in a different regression between U^K_{37} and sea surface temperature. McClymont et al. (2005) suggest that the abundance of ΣC_{37}:ΣC_{38} alkenones within a sediment sample can be used to identify shifts in the dominant alkenone-producing haptophyte population. We identify no significant shift in the ΣC_{37}:ΣC_{38} ratio over the interval studied (Figure 5.6b) with values averaging 1.16, in the range of *Emilinania huxleyi* (0.91-2.26) rather than the other dominant alkenone-producing haptophyte *Gephyrocapsa oceanica* (0.59-0.81)(Volkman et al., 1995). This suggests that no change in the dominant alkenone producing haptophyte population occurred in the interval studied, and thus the U^K_{37}-SST relationship should have remained constant.

Preferential degradation of components with a greater degree of unsaturation may bias the alkenone-SST record towards warmer values (Flügge, 1997; Freeman and Wakeham, 1992; Hoefs et al., 1998). I consider the percentage of the cold tetra-unsaturated $C_{37:4}$ alkenone that would need to be removed in order to produce LGM SSTs as low as during the late deglacial (2.2°C at 11.9 ka). I find that to account for this diagenetic bias of 6°C, at least 70% of the 'original' $C_{37:4}$ would have to be removed from the samples. Such a significant amount of alteration has not been observed experimentally or within sediments studied from this time period (Flügge, 1997).

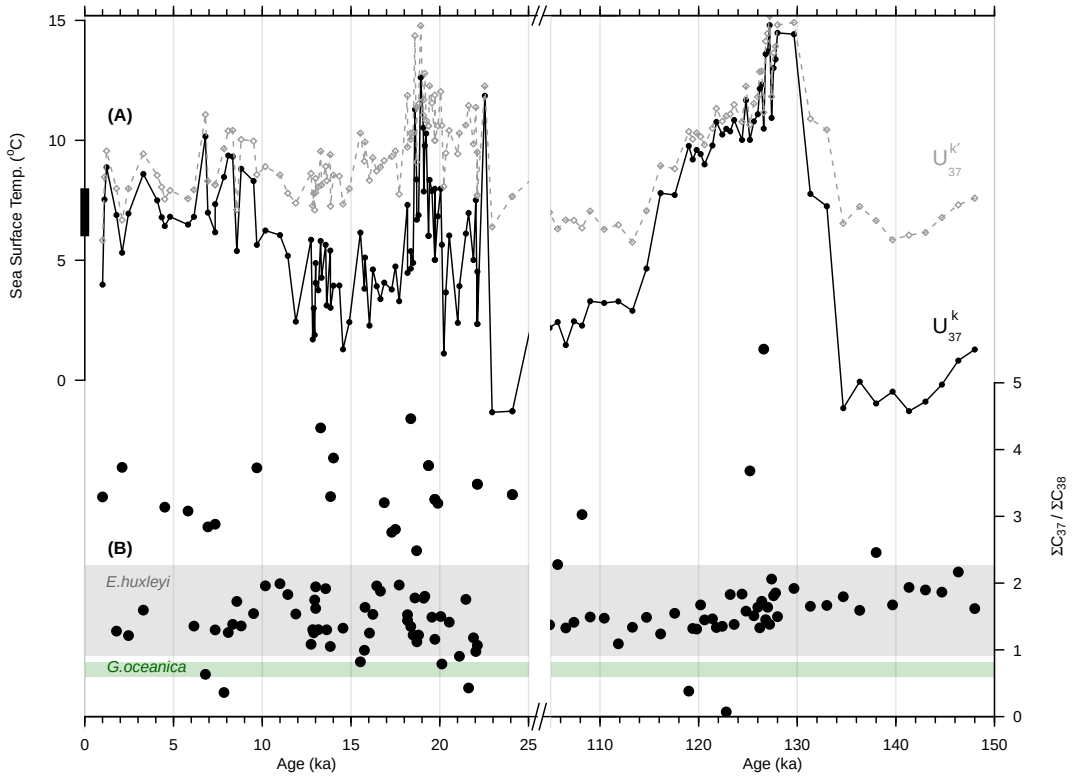

Figure 5.6: Assessing the fidelity of the alkenone-derived SST record. (A) GC528 alkenone derived SSTs based on $U^{K'}_{37}$ (grey open symbols), U^{K}_{37} (black solid symbols), black bar at 0 ka denotes the modern spring-summer SST range at site GC528; (B) Alkenone ΣC_{37}:ΣC_{38}.

Reworked 'fossil' alkenones have been suggested to bias the alkenone-derived SST record in regions such as the NE Atlantic where allochthonous glacio-marine sediments rich in organic matter are present (Rosell-Mele and Koc, 1997). A global compilation of LGM alkenone SSTs suggests that warm alkenone-derived SSTs are a pervasive feature of high latitude regions (Figure 5.7; Lee 2004). It is improbable that sources of fossil alkenones affect solely these high latitude regions.

Advection of warm water alkenones has been used to explain a warm LGM alkenone-SST signal in some regions of the ocean (Müller and Fischer, 2004). Modern alkenone studies from sites influenced by the Falklands Current (Benthien and Müller, 2000) demonstrate that alkenone-derived SSTs from this region are biased towards colder temperatures as a result of strong northwards transport by the Falklands Current. However core-top alkenone-SST data from site GC528 shows good correlation with modern SSTs - suggesting that advection does not strongly bias the alkenone-SST signal at this site.

Changes in the seasonality of alkenone production can affect the temperatures recorded by the alkenones. In high latitude regions, the limitation of light and the extreme surface conditions restrict alkenone production to a short summer growth season (Ternois et al., 2000). A compilation of LGM alkenone records from other sectors of the global ocean shows that high latitude alkenone records are biased towards warmer temperatures in comparison to other surface water temperature sensors, e.g. planktonic foraminifera Mg/Ca (de Vernal et al., 2006). Indeed, in some instances,

the reconstructed LGM alkenone-SSTs are warmer than Holocene SSTs (Figure 5.7; Lee 2004). There is a correlation between the spatial distribution of the sites suggesting warm LGM alkenone-SSTs and reconstructions of LGM winter sea ice extent (Ikehara, 2003; Katsuki and Takahashi, 2005; Sarnthein et al., 2003), potentially suggesting that the seasonal presence of sea ice biases the alkenone production towards warmer summer temperatures. However, changes in the surface ocean conditions associated with the presence of seasonal sea ice, such as shallow stratification, may also account for the warm LGM alkenone-SSTs without necessitating a change in the seasonality of alkenone production. Therefore, the spatial pattern of warm LGM alkenone-SST is insufficient in itself to prove that changes in the seasonality of alkenone production occurred. The seasonality of alkenone production is a difficult parameter to uniquely assess based on bulk alkenone measurements. In order to assess potential changes in seasonality, repeat alkenone measurements on individual coccolithophores are required - a technique which is currently undeveloped. For the purposes of this study, I assume no change in the seasonality of alkenone production. However, it is quite possible that such changes occurred over the last two glacial terminations.

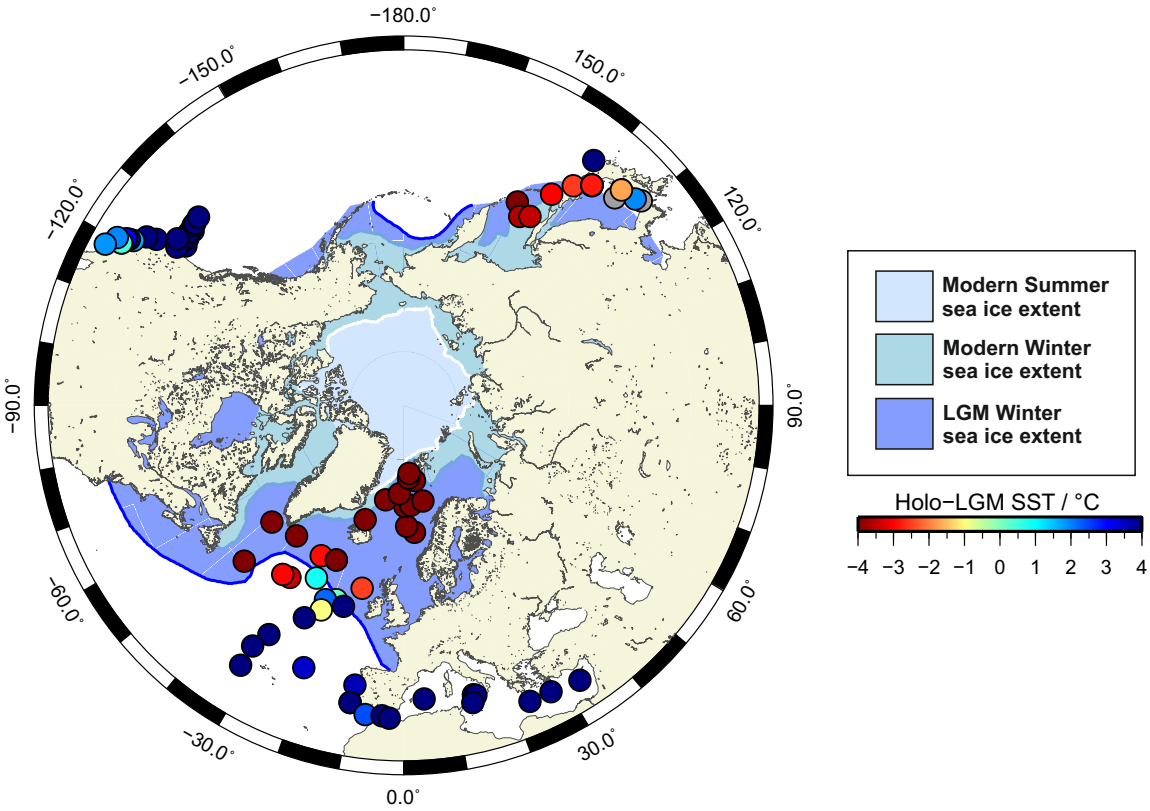

Figure 5.7: North Atlantic and North Pacific alkenone-SST Holocene-LGM anomaly (Lee, 2004). Holocene-LGM difference shown as coloured symbols. Modern winter and summer sea ice limits are based on Fetterer et al. (2002). Winter sea ice limit for LGM as based on diatom transfer functions (Ikehara, 2003; Katsuki and Takahashi, 2005; Sarnthein et al., 2003).

In summary, the alkenone-SST record from the southwest Atlantic suggests that SSTs were generally colder during the glacial than during the interglacial period. However, there are two brief intervals coinciding with the end of the last glacial period (20-18.5 ka and 23-22 ka) in which the alkenone-derived SST records suggest a significant increase in SSTs of 4-6^{o}C. I assessed the evidence of a change in the dominant alkenone-producing population, preferential degradation, advection of warm water alkenones and reworked alkenones, but there is no evidence of any change in these variables. I note that the pattern of warm LGM alkenone-derived SSTs appears to be a pertinent feature of high latitude regions and may be suggestive of a change in seasonality of alkenone production. However, a change in the seasonality of alkenone production does not uniquely explain this spatial correlation; shallow stratification associated with sea ice can also cause an increase in the temperature of the mixed layer without invoking a change in seasonality of alkenone production.

5.4.5 *Neogloboquadrina pachyderma* Mg/Ca-derived temperatures

The alkenone-derived SSTs are compared to near-surface temperatures derived from thermocline dwelling foraminifer, *Neogloboquadrina pachyderma sinistral*, Mg/Ca ratios in order to better understand variations in the thermal structure of the water column over T-I. To determine the depth habitat of *N. pachyderma* in the region, I compare core-top *N. pachyderma* $\delta^{18}O$ with reconstructed $\delta^{18}O$ of calcite precipitated in equilibrium with seawater.

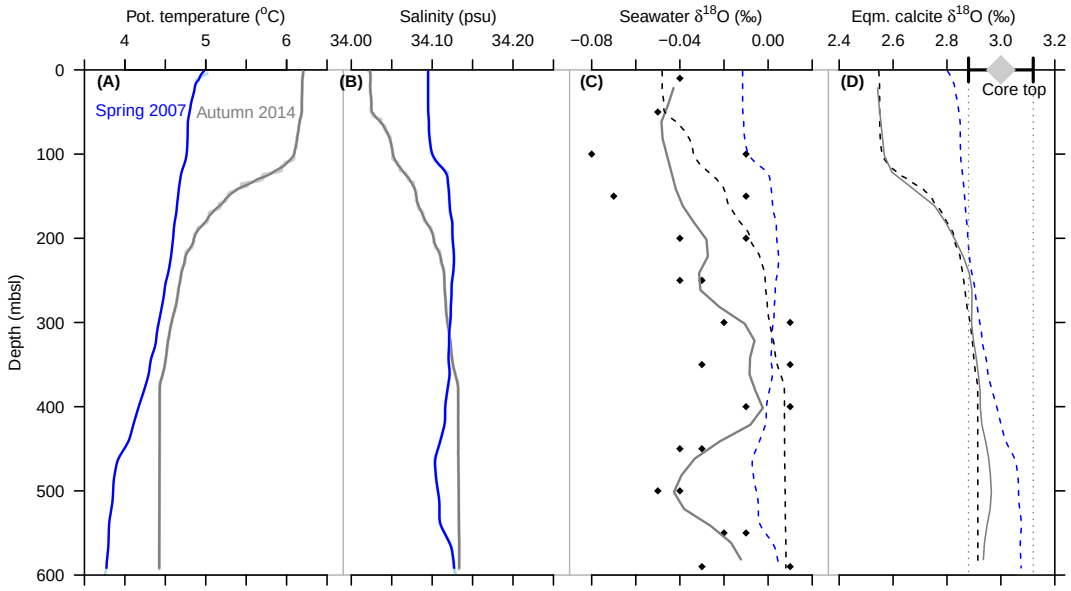

Figure 5.8: Determining the depth habitat of *N. pachyderma (sin).* (A) Potential temperature (Spring 2007 - blue; Autumn 2014 - grey) and (B) Salinity at site GC528; (C) Seawater $\delta^{18}O$ based on in-situ measurements (black points, grey line) and theoretical value based on LeGrande and Schmidt 2006 (Spring 2007 - blue; Autumn 2014 - black dashed line); (D) Calculated $\delta^{18}O$ of calcite in equilibrium with seawater based on the measured seawater $\delta^{18}O$ (grey line) and theoretical seawater $\delta^{18}O$ (Spring 2007 - blue; Autumn 2014 - black dashed line). Core top *N. pachyderma (sin)* $\delta^{18}O$ average (grey diamond) corrected by +1.0‰ for biological fractionation.

Neogloboquadrina pachyderma sinistral calcifies during spring, and therefore it is important to develop a profile of equilibrium calcite $\delta^{18}O$ based on springtime temperatures and seawater $\delta^{18}O$. Unfortunately, there are no direct measurements of springtime seawater $\delta^{18}O$ at this location. A potential work-around is using a linear regression between salinity and seawater $\delta^{18}O$ to calculate seawater $\delta^{18}O$. First, I demonstrate that the linear regression used is appropriate for this site by comparing the calculated seawater $\delta^{18}O$ (based on the linear regression) with direct measurements of seawater $\delta^{18}O$ at this site.

Potential temperature, salinity and seawater $\delta^{18}O$ at site GC528 were measured on cruise JR299 (May 2014) (Figure 5.8a-c). Using the South Atlantic linear regression between salinity and seawater $\delta^{18}O$ (LeGrande and Schmidt, 2006), I calculate a hypothetical seawater $\delta^{18}O$ curve (dashed black line; Figure 5.8c). In general, there is good agreement between the measured seawater $\delta^{18}O$ and the calculated seawater $\delta^{18}O$ curve, which indicates that the South Atlantic linear regression is appropriate for this site.

Using pre-existing CTD data from spring (blue curves Figure 5.8a-b), the calculated seawater $\delta^{18}O$ is combined with potential temperature (Kim and O'Neil, 1997) to derive the $\delta^{18}O$ profile of calcite precipitating in equilibrium with seawater (Figure 5.8d). By accounting for biological fractionation effect of 1.0‰ (Mortyn and Charles, 2003), I demonstrate that the $\delta^{18}O$ of core top *N. pachyderma* from site GC528 agrees with an equilibrium calcite $\delta^{18}O$ value below the thermocline, i.e. depths greater than 120 m. In the following discussion I use the Mg/Ca ratio of *N. pachyderma* to provide information about ocean temperatures below the thermocline and alkenones to track sea surface temperatures. The difference between the two records can be used to understand the evolution of the thermal structure of the water column.

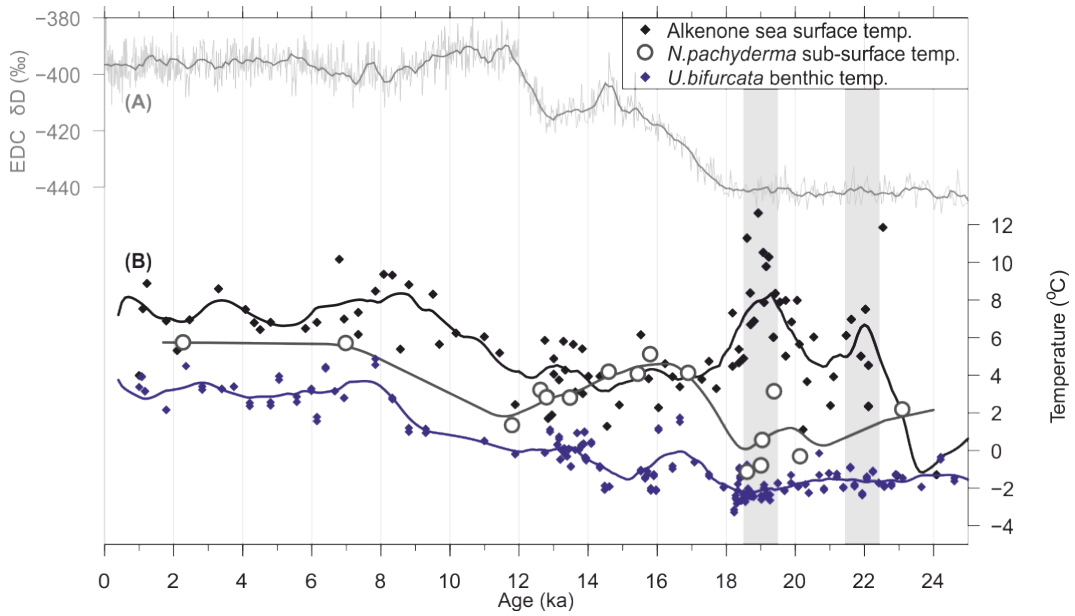

Figure 5.9: Evolution of the thermal structure of the water column over T-I. (A) EPICA Dome C (EDC) δD record (grey) on the AICC2012 age scale (Bazin et al., 2013); (B) Alkenone-derived SSTs (black symbols), *N. pachyderma (sin)* Mg/Ca-derived sub-surface temperature (grey open symbols), *U. bifurcata* Mg/Ca-derived benthic temperature (blue symbols) at site GC528.

The sample-averaged Mg/Ca ratios of *N. pachyderma* indicate (as expected) that temperatures below the thermocline are cooler than the alkenone-derived SSTs (Figure 5.9). However, across Termination I, the temperature structure of the water column varies significantly. Between 17-12 ka, there is no difference between alkenone-SST and *N. pachyderma* Mg/Ca-subsurface temperatures, suggesting either a more homogenous water column or similar depth habitats of *E. huxleyi* and *N. pachyderma*. Prior to 18 ka, the difference in temperatures between alkenone-SST and *N. pachyderma* Mg/Ca-subsurface temperatures is more than 6^{o}C, suggesting a highly stratified water column.

5.5 Discussion: Termination I

5.5.1 The barotropic component of ACC flow

As discussed earlier, the modern ACC has a significant barotropic component and thus the position of the ACC jets are fixed by bottom topography (Graham et al., 2012). However, reconstructions of the density of deep water in the Southern Ocean (Adkins et al., 2002; Malone et al., 2004; Roberts et al., 2016) suggest that ACC flow during the LGM was likely more baroclinic in nature. Indeed the timing of the decrease in bottom water flow in the deep central ACC site is synchronous with the major decrease in deep ocean density at 11 ka (Figure 5.10; Chapter 4). Prior to 11 ka, bottom current flow speeds in the deep central ACC are remarkably invariant suggesting very little influence from circumpolar jets. A decrease in stratification of the deep ocean at 11 ka, would enable ACC jets to extend to the sea floor. In regions beneath the ACC jets, this would result in an increase in bottom current flow speed, however in regions between the ACC jets (e.g. TC290/078; Figure 5.1), the downward extension of weaker easterly jets would result in a reduction in bottom current flows speeds (Figure 5.11a-b).

The implication of this inferred change in the vertical structure of the ACC over glacial-interglacial cycles is that circumpolar jets in the glacial baroclinic ACC would be more decoupled from bottom topography and thus ACC jets should be more responsive to changes in the overlying wind stress field. In contrast, the interval following 11 ka was dominated by barotropic ACC flow and thus ACC jets were fixed in position by bottom topographic constraints.

5.5.2 Holocene increase in bottom current flow speeds

During the Holocene, the ACC flow is barotropic yet all sortable silt records show a steady increase in bottom current flow speeds across the Holocene (Figure 5.10). I suggest that the increase in bottom current speeds at all sites suggests a strengthening of ACC flow with no movement of the fronts (Figure 5.11).

It is difficult to infer the driving mechanism of the increase in ACC flow. The strength of the ACC is controlled by several factors including, (i) the integrated wind stress across the ACC (Allison et al., 2010; Meredith et al., 2011) and (ii) buoyancy forcing at the surface (Hogg, 2010; Watson et al., 2006). However, the relationship with the SWWs and ACC flow is not straightforward. Eddy compensation (Hallberg and Gnanadesikan, 2006) means that higher wind stresses can increase the amount of eddy mixing and thus decrease net ACC transport. Whereas eddy saturation (Munday

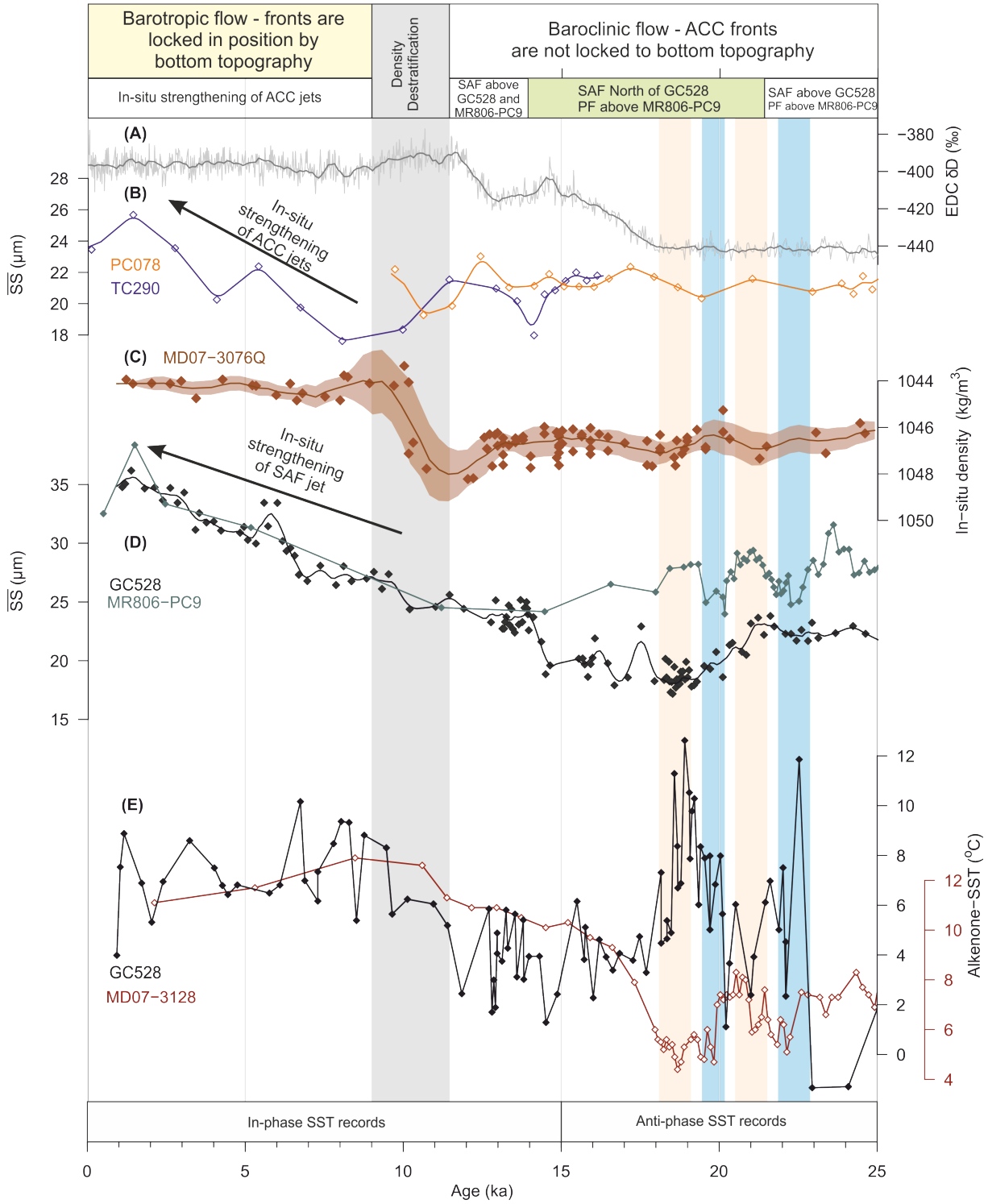

Figure 5.10: Baroclinic versus barotropic ACC flow. (A) EPICA Dome C (EDC) δD record (grey) on the AICC2012 age scale (Bazin et al., 2013); (B) Sortable silt record from the deep central ACC, TPC290/078; (C) Deep ocean density, MD07-3076Q (Chapter 4); (D) Sortable silt record from the northern ACC (GC528 - black, this study; MR806-PC9 - green, Lamy et al. 2015); (E) Alkenone-derived SST records from upstream (MD07-3128 - red, Caniupán et al. 2011) and downstream of the Drake Passage (GC528 - black, this study).

et al., 2013) suggests that eddy mixing has a maximum threshold and thus will not increase linearly with wind stress. An increase in the in-situ flow of ACC jets suggests a reduction in eddy mixing during the Late Holocene but because of eddy saturation and compensation it is not clear whether this is driven by a net increase or a decrease in the intensity of the SWWs. Proxy reconstructions of changes in the intensity of the SWWs provide contradictory information on the changes in the SWWs over the Holocene (Kilian and Lamy, 2012), and hence cannot be use to constrain this problem further. In summary, whilst the data suggest a widespread increase in ACC bottom current flow speeds across the Holocene, the driving mechanism remains unclear.

5.5.3 Glacial shifts in the position of the ACC fronts

Prior to 11 ka, the ACC was likely baroclinic and thus the position of the ACC jets could move in response to changes in the overlying wind field (Allison et al., 2010) and changes in surface buoyancy (Hogg, 2010). The $\overline{SS}$ records from the shallow northern ACC sites can be used to reconstruct changes in the position of the ACC fronts, in particular the SAF and PF.

The sortable silt record at GC528 suggests that bottom current flow speeds were significantly reduced between 21-14 ka (Figure 5.10d). I would argue that this reduction in flow speeds implies that the SAF jet has migrated away from the core site (Figure 5.11). Comparison of the sortable silt record at GC528 with a sortable silt record from the Argentine shelf break within the Drake Passage (MR806-PC4; Lamy et al. 2015) shows a remarkable similarity between the two records between 14-0 ka (Figure 5.10d). In the modern, both these sites are located under the SAF (Figure 5.1); the similarity of these two records between 14-0 ka suggests that both sites are responding to changes in the intensity of the SAF. However, prior to 14 ka, there is a strong divergence between the two records (Figure 5.10d); MR806-PC9 has a high mean $\overline{SS}$ between 25-30 μm whereas the sortable silt mean at GC528 ranges between 18-22 μm. I suggest that this divergence in $\overline{SS}$ reflects the presence of a sub-polar jet over MR806-PC9 but the lack of a jet over GC528 (at least between 20-15 ka). Given the prevailing consensus that frontal systems migrate equatorward during glacial times (e.g. Gersonde et al. 2005; Kaiser et al. 2005), I suggest that prior to 15 ka, the SAF was north of site GC528 and did not flow though the Drake Passage, but instead was truncated by South America (similar to the modern sub-tropical front; Figure 5.11b). The fast flow speeds at MR806-PC9 reflect the presence of the PF at the very northern edge of the Drake Passage (Figure 5.11b).

In summary, the period prior to 11 ka was characterised by baroclinic ACC flow. This decouples the position of the ACC jets from the bottom topography enabling ACC jet position to be controlled by the overlying wind field and/or surface buoyancy. In the interval prior to 15 ka, I suggest that the position of the SAF was significantly northward of its present position, and likely did not pass through the Drake Passage (Figure 5.11b). The high current speeds at MR806-PC9 within the Drake Passage are the result of a northward migration of the PF over the site.

5.5.4 Evidence of pronounced ACC reduction during the LGM

Prior to 15 ka, abrupt changes in the sortable silt record at MR806-PC9 correspond to significant anti-phased SST changes upstream (MD07-3128; Caniupán et al. 2011) and downstream (GC528)

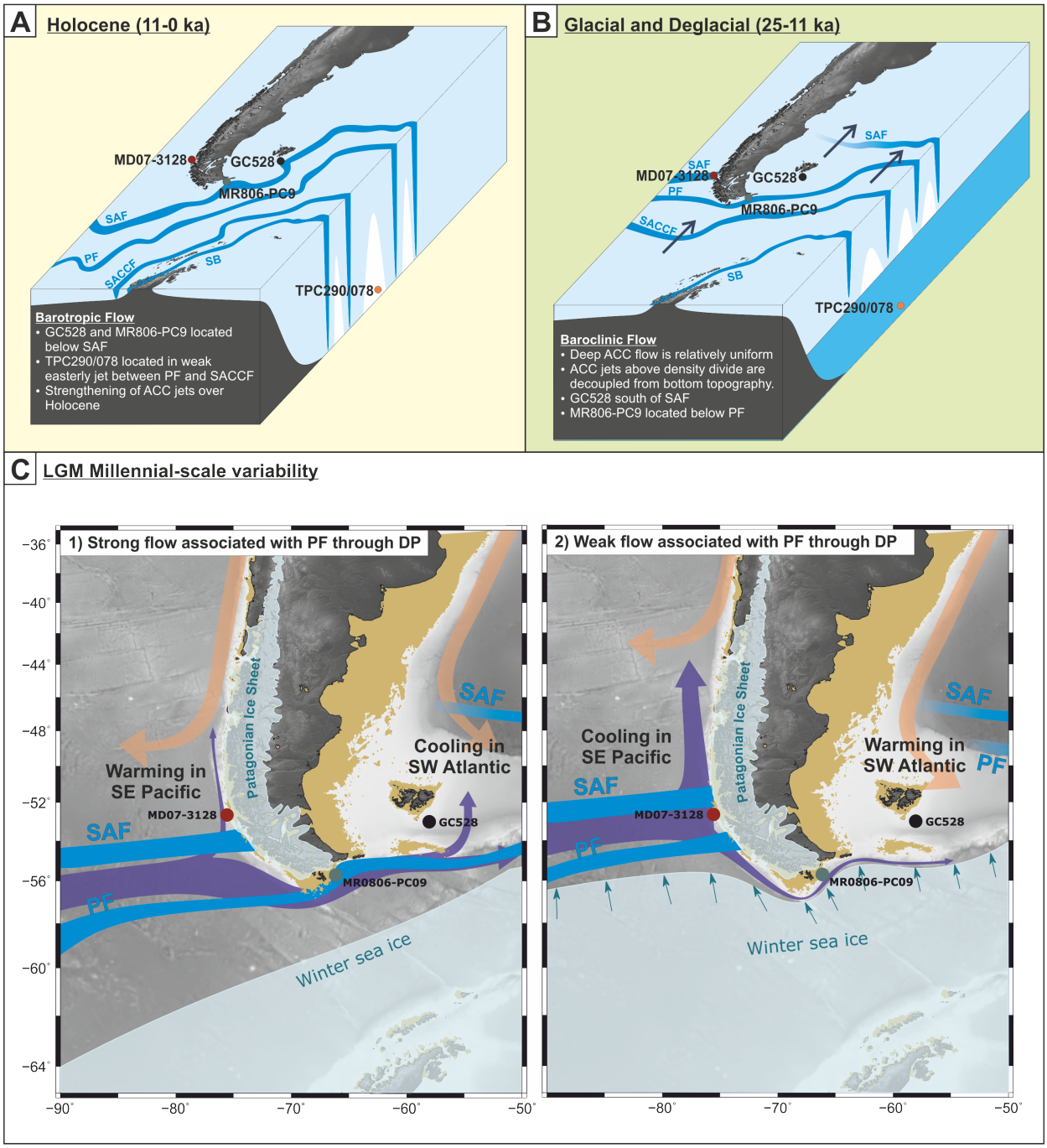

Figure 5.11: Schematic of changes in ACC frontal jets over Termination I. (A) Holocene barotropic ACC flow; (B) Glacial and deglacial baroclinic flow; (C) Millennial-scale variability in the position of the ACC fronts at the end of the last glacial period.

of the Drake Passage (Figure 5.10e). Across the intervals 20-18.5 ka and 23-22 ka, southwest Atlantic SSTs were at a maximum and SSTs in the southeast Pacific were at a minimum. Cross-correlation of these records confirms a significant anti-correlation between 25-18 ka (Figure 5.12b), and a significant positive correlation between 15-3 ka (Figure 5.12a). The transition to in-phase SSTs broadly coincides with the interval of strong positive correlation between the $\overline{SS}$ records from GC528 and MR806-PC9 (Figure 5.10). This interval was interpreted to reflect the flow of the SAF through the Drake Passage. An increase in SAF flow through the Drake Passage would enable temperature anomalies upstream of the Drake Passage to be propagated rapidly to sites downstream of the Drake Passage, accounting for the in-phase SSTs.

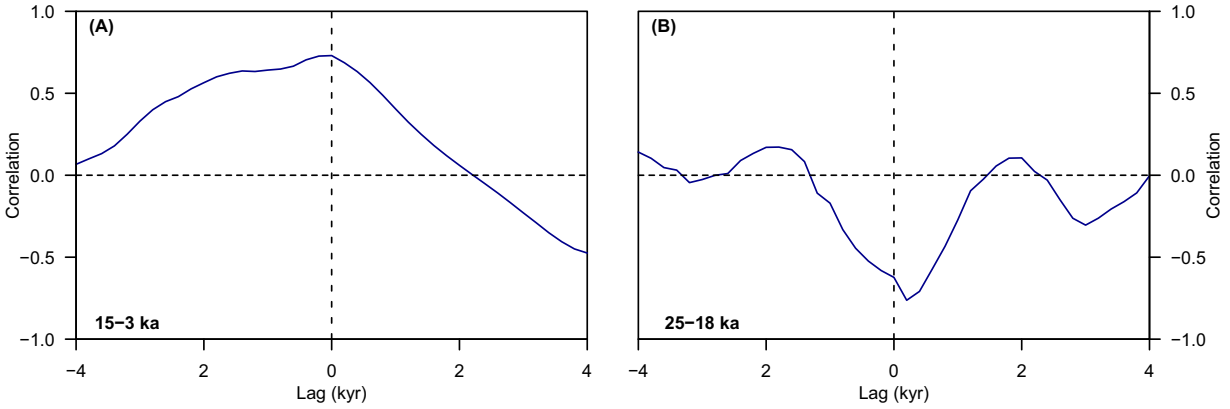

Figure 5.12: Cross-correlation between alkenone-SST records GC528 and MD07-3128 between (A) 15-3 ka; and (B) 25-18 ka.

At the end of the last glacial, strong shifts in SST in the southwest Atlantic and southeast Pacific appear to coincide with $\overline{SS}$ minima/maxima at MR806-PC9 (Figure 5.10d-e). Minimum bottom current speeds within the Drake Passage correspond to abrupt warming in the southwest Atlantic and cooling in the southeast Pacific. Conversely, maximum bottom current speeds within the Drake Passage correspond to abrupt cooling in the southwest Atlantic and warming in the southeast Pacific.

In the southeast Pacific, SSTs are controlled by the balance of cold water upwelled along the Chilean coast and warm surface waters transported southwards by the Chilean Current. Additionally, it has been suggested that significant retreat of the Patagonian Ice sheet may influence the SSTs at MD07-3128 during the last glacial period (Caniupán et al., 2011); however, more recent interpretation of the same data (Lamy et al., 2015) places a stronger emphasis on the balance of cold southern-sourced waters versus warm northern-sourced water. Similarly, the SSTs in the southwest Atlantic can also be considered to be a balance of cold southern-sourced water and warm northern-sourced water. In this region, cold water is transported through the Drake Passage (Talley, 1999), whereas warm water is carried southwards via the Brazil Current. It is therefore plausible that a reduction in Drake Passage through-flow would cause a cooling in the southeast Pacific, as cold southern-sourced waters are piled up (Lamy et al., 2015), and a warming in the southwest Atlantic, on account of a greater contribution of warm northern-sourced water in the region (Figure 5.11). Lamy et al. (2015) suggest that the reduction in Drake Passage through-flow may be the result of an

expansion of Antarctic surface waters or sea ice, resulting in the northward expansion of the ACC jets which deflects much of the ACC back into the South Pacific gyre (Figure 5.11).

Based on the above hypothesis, I would expect that a reduction in the Drake Passage throughflow would have an immediate effect on the SSTs in the southwest Atlantic and southeast Pacific, and thus I would expect the maximum warmth in the southwest Atlantic to coincide with the minimum flow speeds within the Drake Passage. However, the proxy records suggest that the maximum SSTs in the southwest Atlantic occur ~1000 years later than the minimum in bottom current flow speeds within the Drake Passage. Potentially there are inaccuracies in the age model of MR806-PC9 which is based on radiocarbon dating of bulk organic carbon (Shiroya et al., 2013).

In summary, I find evidence for several intervals at the end of the last glacial period during which the PF was displaced northwards, leading to a significant reduction in the flow of cold surface water through the Drake Passage. These millennial-scale events of reduced Drake Passage throughflow have previously been observed to coincide with a strong cooling in SSTs in the SE Pacific (Lamy et al., 2015). However, this is the first time that warming in the southwest Atlantic has been associated with reduced Drake Passage through-flow.

5.5.5 Amplification of SSTs in the southwest Atlantic during the LGM

It is perhaps surprising that the expansion of cold Antarctic surface waters or Antarctic sea ice should result in warmer SSTs in the southwest Atlantic. In the previous discussion, I argue that this is primarily driven by an increased contribution of warm northern-sourced water in the region transported by the Brazil Current; however, there may be additional factors which contribute to the strong warming signal observed during the LGM. In particular, it is important to consider the SST proxy on which our inference of warm SSTs in the southwest Atlantic is based. Alkenones are formed by surface-dwelling coccolithophores that, in high latitudes, typically live for a short summer growth season (Ternois et al., 2000). During this summer season, meltwaters associated with sea ice can create a shallow surface layer which, due to its low density relative to seawater, remains stratified. It is therefore plausible that the presence of meltwater due to expanded Antarctic winter sea ice during 20-18.5 ka and 23-22 ka, resulted in rapid warming of the shallow surface layer, which was recorded by the surface-dwelling coccolithophores. I test this hypothesis by comparing the alkenone-SST record with deeper-dwelling *N. pachyderma* temperature records (Figure 5.9).

There is a considerable discrepancy between 22-18 ka, with alkenone-SSTs suggesting temperatures >6^{o}C higher than *N. pachyderma*-Mg/Ca temperatures. A similar pattern has also been observed in the North Atlantic (de Vernal et al., 2006). Shallow stratification warms the surface ocean at the expense of waters below the mixed layer. *Neogloboquadrina pachyderma* will not record this summer warming as it resides below the mixed layer, whereas the surface dwelling coccolithophores will experience significant increases in summer SSTs, which is subsequently recorded in the alkenone signal.

I generate a simple box model to investigate the change in surface ocean temperature as a result of changes in the depth of the mixed layer (Figure 5.13). In this model, I apply a sinusoidal insolation forcing to 1D layered ocean to simulate the change in insolation forcing over one year. The total insolation at the given latitude can be calculated from Berger (1978). The change in temperature of the mixed layer is a function of the daily insolation at the surface (I), the diffusion of

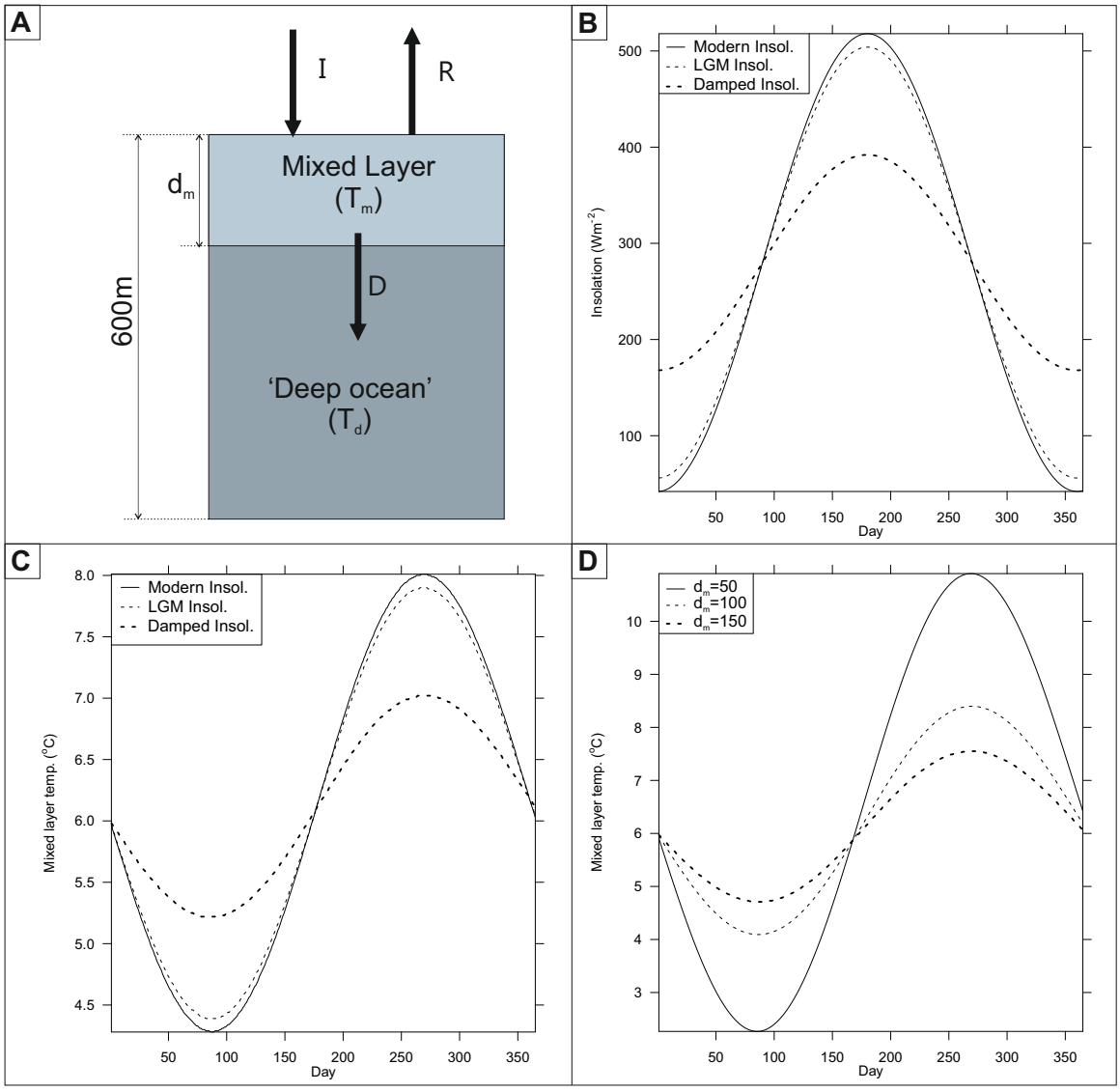

Figure 5.13: Box model illustrating the dependency of sea surface temperature on the depth of the mixed layer. (A) Schematic of main forcings in the box model, see text for details; (B) Daily insolation forcing applied (Modern daily insolation at 53°S, solid line; LGM daily insolation at 53°S, thin dashed line; Halved annual range of insolation forcing, thick dashed line); (C) Temperature of mixed layer in response to the insolation forcings described in (B). Mixed layer maintained at a constant thickness of 150m; (D) Temperature of mixed layer in response to variations in the depth of the mixed layer (Mixed layer thickness = 50m, solid line; Mixed layer thickness = 100m, thin dashed line; Mixed layer thickness = 150m, thick dashed line). In all simulations in (D), the modern insolation forcing was applied.

heat below the thermocline (D), and the radiative heat flux from the surface ocean to the atmosphere (R). In this model I define R as an arbitrary constant so that the temperature of the mixed layer at the beginning and end of the annual cycle is constant (230 Wm^{-2}). The temperature of the mixed layer is therefore defined by the equation:

$$C_m \frac{\partial \Delta T}{\partial t} = I - R - D \tag{5.1}$$

where the mixed layer heat capacity (C_m) is a function of the density of the mixed layer (ρ), the specific heat capacity of seawater (c_p) and the depth of the mixed layer (d_m):

$$C_m = \rho c_p d_m \tag{5.2}$$

The diffusion of heat through the base of the mixed layer (D) is a function of diffusivity (κ), the density of the mixed layer (ρ), the specific heat capacity of seawater (c_p) and the temperature gradient between the mixed layer and the 'deep ocean' box:

$$D = \kappa \rho c_p \frac{dT}{dz} \tag{5.3}$$

Equation 5.1 can be written in a finite difference form in order that the change in the temperature of the mixed layer can be calculated over a given time step. I integrate over time steps of 1 day:

$$\Delta T = \int \frac{I - R - D}{C_m} dt \quad = \frac{t}{C_m} \left(I - R - \kappa \rho c_p \frac{dT}{dz} \right) \tag{5.4}$$

Several scenarios were tested; in the first set of simulations, the daily insolation forcing was varied but the depth of the mixed layer was held constant. The annual range of the insolation forcing was less during the LGM than its is today (Berger 1978; Figure 5.13b). A third scenario was also tested in which the annual range of insolation was halved. The difference in mixed layer temperatures between the 'Modern' and 'LGM' insolation scenarios was less than 0.5°C (Figure 5.13c). Even in the unrealistic case in which the annual insolation range was severely muted, the change in the temperature of the mixed layer is less than 1°C.

In a second set of simulations, the 'Modern' insolation pattern was applied to all simulations and the only variable to change was the depth of the mixed layer (Figure 5.13d). The model illustrates that the seasonal range in temperature is strongly dependent on the depth of the mixed layer; a thinner mixed layer responds more rapidly to the seasonal changes in insolation, with an annual range of ~10°C when the thickness of the mixed layer is reduced to 50 m.

On the basis of this model, I propose that a strong amplification of summer temperatures in a shallow mixed layer may contribute to the strong surface warming observed in the southwest Atlantic during the LGM, that can explain the large alkenone-*N. pachyderma* temperature difference. This shallow stratification is most likely caused by freshwater associated with the seasonal melting of proximal Antarctic sea ice. This interpretation is consistent with diatom-based reconstructions of sea ice presence from the South Atlantic (Shemesh et al., 2002), that evidence two distinct maxima at 23.5 ka and 19 ka.

5.5.6 Impact of reduced Drake Passage through-flow on AMOC

In the modern ocean, the low density nature of AAIW is critical for the stability of AMOC; a slowing of AMOC increases the salinity differences between AAIW and NADW, which feeds back to reinvigorate AMOC circulation (Stommel, 1961). In the previous discussion I propose a severe reduction in Drake Passage through-flow (and thus the export of AAIW) during the intervals 20-18.5 ka and 23-22 ka. A reduction in the delivery of low salinity AAIW into the Atlantic would increase the salinity of Atlantic southern-sourced intermediate water, which has the potential to destabilise AMOC.

Evidence of the reduction in Drake Passage through-flow and the subsequent cooling in the surface waters in the South Pacific can be observed as far north as the equator (Figure 5.14b-d; Caniupán et al. 2011; Kaiser et al. 2005; Lea et al. 2006). Additionally, during these periods of reduced export of AAIW into the Atlantic, a greater contribution of well-oxygenated AAIW is observed in the SE Pacific (Figure 5.14e; Muratli et al. 2009). However, there is no evidence of synchronous changes in AAIW extent in the Atlantic or any significant effect on AMOC (Figure 5.14g-h; Lippold et al. 2009; Pahnke et al. 2008). This suggests that the effect of a severe reduction of Drake Passage through-flow did not exert a significant impact on AMOC, potentially indicating that the flow of water through the cold water route is less important in setting the stability of AMOC than, for example, changes in the density of NADW.

5.6 Discussion: Termination II

The comparison of the alkenone and $\overline{SS}$ records across T-I and T-II suggest some notable similarities and differences. Similarly to T-I, the deep central ACC site suggests evidence of a change from baroclinic to barotropic flow over the deglaciation; between 133-129 ka there is a significant decrease in mean $\overline{SS}$ followed by a slight increase in bottom current flow between 123-119 ka (Figure 5.15c). Across T-I, a decrease in $\overline{SS}$ was observed to coincide with a decrease in deep water density. Unfortunately, deep water density records are not available over this interval to determine whether deep ocean density destratification drives a reduction in bottom current flow speed at this site, however the similarity in the $\overline{SS}$ records across T-I and T-II at this site suggests that a similar mechanism underpins both records.

Baroclinic ACC flow during MIS6 appears to be consistent with the shallow northern ACC site, which similarly to T-I, shows low bottom current flow speeds across the deglacial period (141-130 ka; Figure 5.15d). If the same processes are operating across T-II as during T-I, I infer that this reduction in $\overline{SS}$ may be the result of a northward migration of the SAF away from GC642.

Based on the sortable silt records it would appear that the same deglacial changes in the position of the fronts are occurring across T-I and T-II. However, the alkenone-derived SST record across this interval suggests a very different story. Across T-II, SSTs in the southwest Atlantic increase from a low of -1^{o}C to a maximum of 16^{o}C (Figure 5.15b). Both the magnitude of change and the pattern of warming are very different to T-I.

Unlike the LGM, SSTs in the southwest Atlantic during MIS6 were close to freezing (Figure 5.15b). Based on my previous interpretation of the anti-phased SST records across Termination I, cold SSTs in the southwest Atlantic suggest either a strong through-flow of water through the Drake

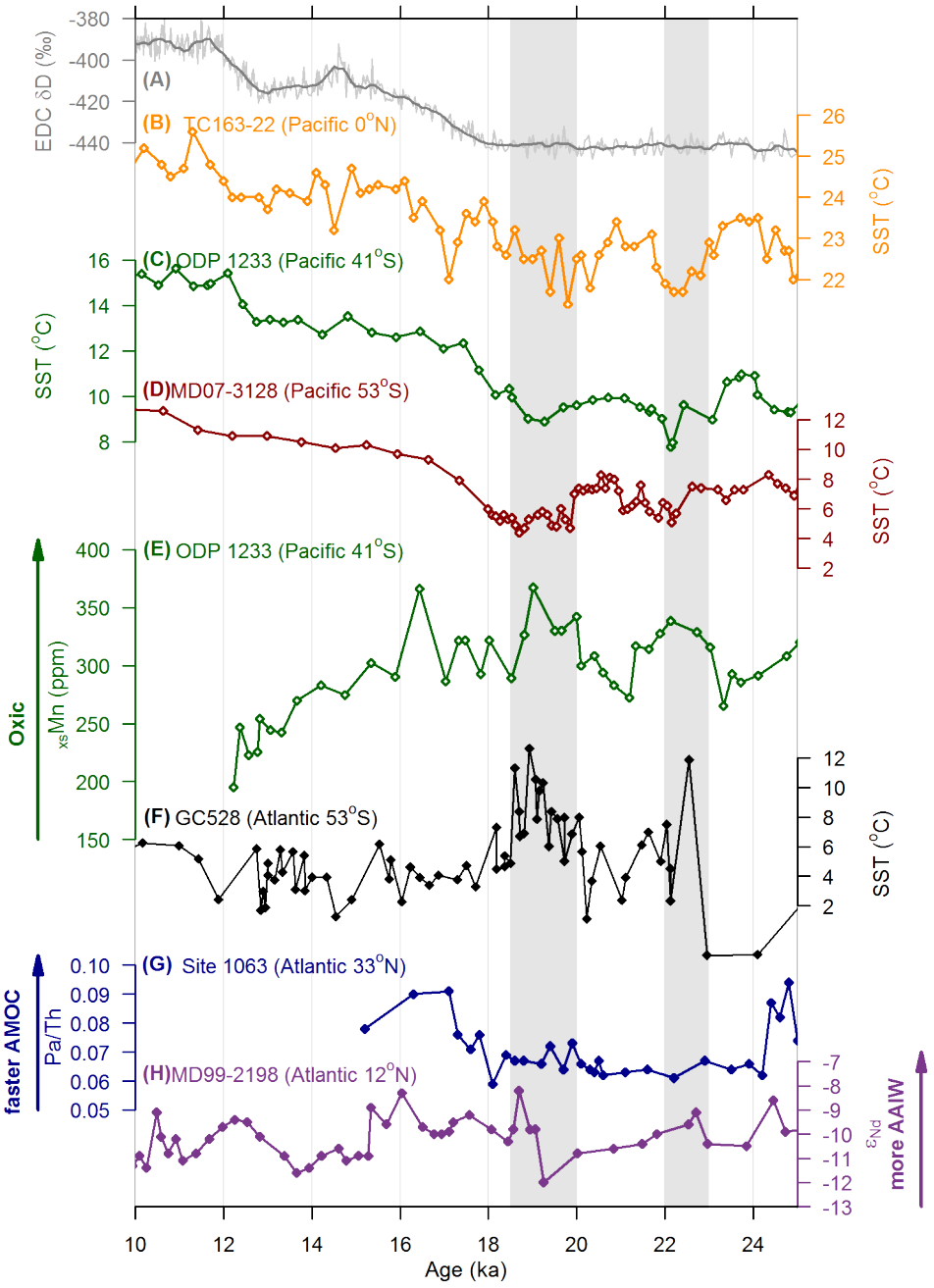

Figure 5.14: Impact of Drake Passage through-flow reduction on AMOC at the end of the last glacial period. (A) EPICA Dome C (EDC) δD record (grey) on the AICC2012 age scale (Bazin et al., 2013); (B-D) SST reconstructions from the Pacific (TC163-22, Lea et al. 2006; ODP1233, Kaiser et al. 2005; MD07-3128, Caniupán et al. 2011) suggest marked cooling during Drake Passage reduced flow intervals (highlighted in grey); (E) Oxidation proxies from the SE Pacific suggest better ventilation of AAIW during these intervals (Muratli et al., 2009); (F) SW Atlantic (GC528) alkenone-derived SST warm during intervals of reduced Drake Passage through-flow; (G) No evidence of changes in AMOC strength in North Atlantic (Site 1063, Lippold et al. 2009); or (H) AAIW extent in the Atlantic (MD99-2198, Pahnke et al. 2008).

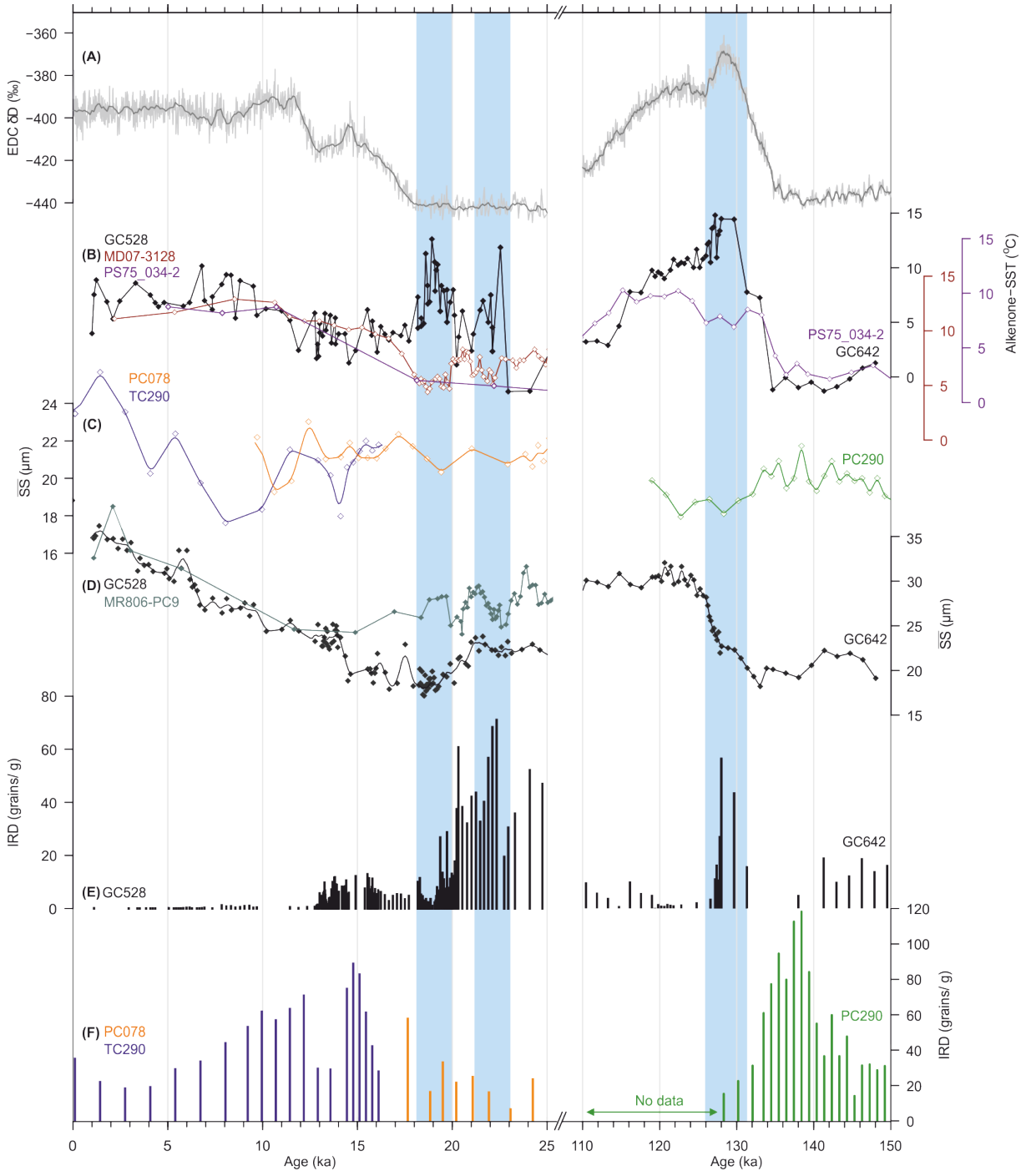

Figure 5.15: ACC circulation changes across Termination I and II. (A) EPICA Dome C (EDC) δD record (grey) on the AICC2012 age scale (Bazin et al., 2013); (B) Alkenone-derived SST records from upstream (MD07-3128 - red, Caniupán et al. 2011; PS75/034-2 - purple, Ho et al. 2012) and downstream of the Drake Passage (GC528/642 - black, this study); (C) Sortable silt record from the deep central ACC, TPC290/078; (D) Sortable silt record from the northern ACC (GC528 - black, this study; MR806-PC9 - green, Lamy et al. 2015); (E) IRD record from the northern ACC (GC528/642); (F) IRD record from central ACC (TPC290/078).

Passage or a weakly stratified surface ocean. In the first instance, this implies that the position of the fronts was less equatorward than during MIS2, and in the second scenario it implies that Antarctic sea ice was less extensive than during MIS2. Both of these inferences suggest, rather surprisingly, that the colder SSTs in the southwest Atlantic may be the result of a generally warmer Southern Ocean during MIS 6 than MIS2.

The hypothesis of a warmer Southern Ocean during MIS6 appears to be supported by IRD records from the Scotia Sea (Figure 5.15e-f). As I described in Section 5.4.3, an anti-phased pattern of IRD between the Antarctic Zone and the sub-Antarctic Zone is expected across glacial-interglacial cycles (Keany et al., 1976). This is because the zone of maximum IRD deposition occurs equatorward of the 0^{o}C isotherm. During glacial periods an expansion of Antarctic surface waters will result in more IRD deposition in the sub-Antarctic zone. Over MIS6, there is substantially less IRD deposited at GC528/642 than during MIS2, and more IRD deposited in the central ACC (TPC290/078). Based on the Keany et al. (1976) model of the spatial pattern of IRD distribution, this suggests that MIS 6 is warmer than MIS2.

Interestingly, a maximum in SSTs and IRD concentrations in GC642 is synchronous with the Last Interglacial climatic optimum. This period of warmth in Antarctica has previously been observed to occur in-phase with a widespread cold reversal in the Southern Ocean (Becquey and Gersonde, 2002; Bianchi and Gersonde, 2002; CLIMAP Project Members, 1984), and potentially could be linked to the collapse of the West Antarctic Ice Sheet (Bradley et al., 2012; Steig et al., 2015)[1]. As I suggested earlier, elevated alkenone-derived SSTs can be caused by shallow stratification of the surface ocean (Section 5.5.5). The collapse of the West Antarctic Ice Sheet may have triggered the release of significant volume of freshwater into the surface ocean resulting in shallow stratification in the Southern Ocean and elevated alkenone-derived SSTs at site GC642.

If a collapse of the West Antarctic Ice Sheet did occur during the Last Interglacial, the release of freshwater into the ocean would result in shallow stratification across much of the Southern Ocean. This being the case, other alkenone-SST records from the Southern Ocean might also be expected to show elevated SSTs over this interval. However, alkenone-SST record from upstream of the Drake Passage (PS75/34-2; Ho et al. 2012) suggests that, in fact, alkenone-SSTs during the climatic optimum were cooler than the interglacial average. A warming in the southwest Atlantic coupled with a relative cooling in the southeast Pacific strongly resembles the anti-phased alkenone-SST trends at the end of MIS2. Over MIS2, I inferred that anti-phased SSTs upstream and downstream of the Drake Passage arose from the advance of Antarctic sea ice that resulted in reduced Drake Passage through-flow. Potentially, the collapse of the West Antarctic Ice Sheet and the subsequent cooling of the surface ocean would have resulted in a rapid resurgence of Antarctic sea ice during the Last Interglacial climatic optimum; however, the SSTs upstream of the Drake Passage seem too high (5-7^{o}C) to accommodate a sustained advance of sea ice.

In summary, the sortable silt records across T-I and T-II document very similar changes in the bottom current flow speeds across the ACC. However, the SSTs across this time period provide a very different story. During MIS6, colder SSTs that parallel SSTs upstream of the Drake Passage suggest that the flow of cold water through the Drake Passage was not reduced (unlike MIS2), indicating that MIS6 was likely less cold than MIS2. Across the deglaciation, there is an interval

[1]It should be noted that evidence of a collapse of the West Antarctic Ice Sheet during the Last Interglacial is very limited, and constraints on the timing of an inferred collapse are very poor (Scherer et al., 1998)

between 131-128 ka during which SSTs in the southwest Atlantic deviated significantly from SSTs upstream of the Drake Passage. This pattern is reminiscent of the anti-phase relationship observed at the end of MIS2, and potentially suggests a reduction in Drake Passage through-flow. This anti-phasing occurs during a widespread Southern Ocean cooling event that is potentially linked to the collapse of the West Antarctic Ice Sheet.

5.7 Conclusion

In this chapter I have reconstructed changes in the speed of water exiting from the Drake Passage over T-I and T-II. Grain size records from the northern and central ACC show that the flow of water through the Drake Passage was not constant over the last two glacial terminations and was strongly controlled by the density structure of the Southern Ocean. I show that a significant decrease in deep ACC flow speed occurs synchronous with the major density destratification event, potentially suggesting an increase in the barotropic component of ACC flow. A major consequence of a more baroclinic ACC during the last glacial period is that the ACC jets are not as tightly coupled to bottom topography, and thus can migrate with changes in the position of the SWWs and changes in surface buoyancy forcing. I show evidence for a significant northward shift in the SAF during MIS2 and argue that during this time the SAF likely did not flow through the Drake Passage, but instead was truncated by South America, similar to the modern STF.

The period at the end of MIS2 shows evidence of anti-phased fluctuations in SST at the entrance and exit of the Drake Passage. Abrupt millennial-scale warming events in the southwest Atlantic coincide with a cooling in the southeast Pacific and a decrease in bottom current flow speeds within the Drake Passage. I propose that during these intervals significant advances of Antarctic sea ice occurred, pushing the ACC frontal systems northward and thus reducing the flow of water through the Drake Passage. The seasonal melting of this Antarctic sea ice may also have played a role in amplifying sea surface temperatures during this time. Whilst there is strong evidence supporting the idea of increased AAIW export northwards along the Chilean Margin, there is no evidence of an impact of reduced Drake Passage through-flow on AMOC. This suggests that the export of AAIW during glacial times does not play a major role in stabilising AMOC, and instead I propose that the density of NADW may be pivotal.

Comparison of the grain size and alkenone-SST records from T-I and T-II show that whilst very similar patterns occur across the two terminations in the grain size records, the SST records are very different. In particular, SSTs in the southwest Atlantic during MIS6 are significantly colder than during MIS2. I argue that the elevated SSTs during MIS2 were the result of an expansion of Antarctic surface water resulting in reduced Drake Passage through-flow and/or shallow stratification in surface ocean, and thus I infer that the cooler temperatures during MIS6 imply a reduced extent of Antarctic surface waters (relative to MIS2) and likely a generally warmer Southern Ocean. Concurrent with the Last Interglacial climatic optimum, there is a major pulse of IRD deposition in the southwest Atlantic, and SSTs in this region increase abruptly whilst SSTs in the southeast Pacific decrease. I propose that this may be evidence of reduction in Drake Passage through-flow linked to the collapse of the West Antarctic Ice Sheet. However I emphasise the need for better age constraints in marine sediment cores across this interval.

Chapter 6

The sub-Antarctic shelf biological pump

6.1 Introduction

It has been hypothesised that changes in the ocean's 'biological pump' can play an important role in regulating the exchange of CO_2 between the atmosphere and deep ocean on glacial-interglacial timescales. Mechanisms that have been proposed to influence surface productivity include, (i) iron fertilisation (Martin, 1990), (ii) the nutrient content of surface waters (Broecker, 1982), (iii) the dominant type of primary production (Archer and Maier-Reimer, 1994) and (iv) nutrient utilisation in the surface ocean (François et al., 1997).

Changes in the strength of the biological pump within the Southern Ocean have been identified to be particularly important in driving changes in atmospheric CO_2 on glacial-interglacial timescales (Knox and McElroy, 1984; Sarmiento and Toggweiler, 1984; Siegenthaler and Wenk, 1984). Here, wind-driven upwelling brings CO_2- and nutrient-rich deep water into direct contact with the atmosphere. The limitation of light and micronutrients, such as iron (Martin, 1990), means that despite the high nutrient content, surface productivity is limited, allowing CO_2 to 'leak' out of the surface ocean. This limitation of micronutrients in the Southern Ocean suggests a large under-utilised potential of the Southern Ocean for drawing down CO_2 by increasing surface productivity through iron fertilisation.

Indeed, proxy data from the last glacial suggests a radically different pattern of productivity in the Southern Ocean. Export production south of the Polar Front (PF) was reduced during the LGM compared to today, whilst in the sub-Antarctic zone productivity was significantly greater during the LGM (Anderson et al., 1998; François et al., 1997; Frank et al., 2000; Kumar et al., 1995; Martínez-Garcia et al., 2011; Nürnberg et al., 1997; Rosenthal et al., 1995). The increase in export production within the sub-Antarctic during glacial periods has been used as evidence supporting the idea that a more efficient biological pump could play a role in lowering atmospheric CO_2 during glacial times (Knox and McElroy, 1984; Sarmiento and Toggweiler, 1984; Siegenthaler and Wenk, 1984).

However, the nature of core sampling locations in the Southern Ocean means that this glacial-interglacial sub-Antarctic productivity trend has been interpreted from a few heavily sampled regions, such as the Cape Basin and the southeast Indian Ocean (Kohfeld et al., 2005, and references therein). These heavily sampled regions are generally located in the abyssal ocean, far from the

influence of continents. Whilst the deep ocean facies accounts for a significant proportion of the ocean floor, annual primary productivity in these regions is several orders of magnitude less than coastal regions (Antoine et al., 1996). The Patagonian Shelf, in particular, is one of the greatest CO_2 sinks per unit area in the world ocean (Bianchi et al., 2009). Estimates of the flux of CO_2 into the South Atlantic between 14 and 50°S suggest that the surface ocean in this region acts as a net CO_2 sink, sequestering 0.3-0.6 $PgCa^{-1}$ (Takahashi et al., 2002), 15-30% of the net oceanic CO_2 uptake in the modern ocean (Sarmiento and Gruber, 2002). A lack of information about the glacial-interglacial variability from these highly productive coastal zones means that key regions of carbon sequestration in the modern sub-Antarctic are relatively unconstrained, potentially biasing our interpretation of the major carbon sinks in the palaeo record.

In this chapter I investigate the variation in ocean productivity in a coastal sub-Antarctic site spanning the last two glacial terminations. Using a multi-proxy approach, I discuss the deglacial changes in the export of carbonate and organic carbon from the surface ocean, and the potential effect that this had on the ocean's ability to sequester CO_2. I use benthic foraminifera assemblages to reconstruct changes in the seasonality, type and quantity of organic carbon fluxed to the sea floor during the last two glacial terminations. I argue that if this site can be considered to be representative of shelf regions in the sub-Antarctic, the changes in the $CaCO_3$:C_{org} rain ratio observed at site GC528/642 likely had significant implications for the ability of the surface ocean to uptake CO_2.

6.2 Methods

In this chapter, a number of different 'productivity' proxy records are generated on the two cores, GC528 and GC642, from the southwest Atlantic across Terminations I and II. A discussion of the different methods for reconstructing surface ocean productivity can be found in this section.

6.2.1 Mass accumulation rate

All of the productivity proxies that will be discussed in this chapter are converted from a concentration of the particular proxy measured in the sediment to an accumulation rate by multiplying the concentration (amount/g) by the mass accumulation rate (g/cm^2/kyr).

Wet bulk sediment weight (x) and dry bulk sediment weight (y) were recorded from ~5 cm^3 samples taken at 2 cm intervals in both cores. These values were used to calculate the dry mud weight (with the salt fraction removed):

$$Y = \frac{y - Sx}{1 - S} \tag{6.1}$$

where S is the salinity of the porewater. I assume a constant salinity of 0.035 g/g (=35 psu). Porosity (P) measured using the MSCL-S was used along with the measured wet and dry bulk sediment weights to calculate the wet sample volume (V_t):

$$V_t = \frac{V_w}{P} = \frac{x - Y}{\rho_w P} \tag{6.2}$$

where V_w is the fluid volume, and ρ_w is the density of seawater (assumed to be 1.025 g/cm^3).

The mass accumulation rate (MAR; g/cm^2/kyr) was calculated from the sedimentation rate (SR), the calculated wet sample volume (V_t) and dry mud less salt (Y), via the equation:

$$MAR = SR\frac{Y}{V_t} \tag{6.3}$$

6.2.2 Productivity proxies

Total alkenone accumulation: Sedimentary C_{37} alkenones have been used in numerous studies (Farrington et al., 1988; Rosell-Mele and Koc, 1997; Sikes and Keigwin, 1994) as indicators of productivity. C_{37} alkenones are produced by the Hapthophyceae class of algae; the concentration of C_{37} alkenones correlates positively with coccolithophore abundances in the surface ocean (Weaver et al., 1999).

Quantification of the total alkenone concentration was achieved by the integrated peak areas of di-, tri-, and tetra-unsaturated C_{37} alkenones to those of the internal standard 5a-cholestane. Details of the method of extracting and measuring alkenones can be found in Section 2.2.4. In this chapter, the alkenone concentration is expressed as an accumulation rate to account for dilution of the alkenone signal because of changes in the sedimentation rate.

Organic carbon analysis: Organic carbon, representing the single largest constituent of organic matter, provides the most direct proxy for surface ocean productivity (Schoepfer et al., 2014). I use the total organic carbon (TOC) concentration in the sediment to understand variations in surface productivity. However, it should be noted that only a fraction of the organic carbon produced by photosynthetic organisms in the surface ocean is exported to depth; a substantial proportion of the carbon is recycled within the mixed layer (Schoepfer et al., 2014).

The carbon isotopic signature of organic carbon can be used to infer changes in the dominant type of primary producer or the degree of nutrient utilisation in the surface ocean. However, there are multiple controls on the $\delta^{13}C$ of organic matter in addition to the dominant type of primary producer variations and in amount of surface productivity in the surface ocean, such as (i) atmospheric $\delta^{13}C$; (ii) variations in the 'preformed' $\delta^{13}C$ from upwelled deep waters; and (iii) preferential degradation of labile forms of organic matter. The procedure for the measurements of organic carbon concentration and $\delta^{13}C$ in the non-carbonate fraction can be found in Section 2.2.5.

Carbonate analyses: The amount of biogenic carbonate in the sediment can be used to infer changes in surface ocean productivity (Wefer et al., 1996). It should be emphasised that in these cores, the bulk of the carbonate in the sediment derives from benthic foraminifera, rather than planktonic foraminifera or coccolithophores. Whilst benthic foraminifera tend to respond to changes in food supply (Herguera and Berger, 1991), and are therefore related to changes in surface ocean productivity, the carbonate concentration in the sediment is a very indirect method to determine changes in surface ocean productivity at this site. Percent carbonate was determined by coulometric titration, and is fully described in Section 2.2.3. The weight percent carbonate was converted into a mass accumulation rate.

XRF Analysis: I use the amount of calcium (normalised against aluminium) to provide an indication of the relative flux of biogenic carbonate versus terrigenous material to the sea floor.

Additionally an attempt was made to reconstruct changes in productivity using barium detected via XRF. Profiles of dissolved barium concentrations in seawater show surface water depletion and deep water enrichment in barium, reflecting the influences of biological cycling (Francois et al., 1995; Wolgemuth and Broecker, 1970). However, in these cores, the XRF barium counts were close to the limit of detection, and in some sections undetectable from the background. Therefore, I do not include downcore variations in barium in the discussion of changes in productivity.

Benthic Foraminifera Accumulation Rate: Benthic Foraminiferal Accumulation Rate (BFAR) estimates have been used as a semi-quantitative proxy for productivity where preservation of carbonate is favourable (Herguera and Berger, 1991). This is based on the linkage between surface productivity and the concentration of benthic life the export flux can support. BFAR was calculated by summing the benthic foraminifera counted in the >63 μm census data, scaling up for any sample splitting. The total benthic concentration was converted to a mass accumulation rate.

Diatom Abundance: Diatoms are the major primary producer in the Southern Ocean. In the southwest Atlantic, the highest diatom concentrations are associated with the main area of influence of Antarctic-originated water masses, and diatom frustules have been shown to be transported long distances from their original source (Romero and Hensen, 2002). A complete description of diatom assemblages was beyond the scope of this project however the downcore abundances were assessed qualitatively from smear slides.

6.2.3 Benthic Foraminifera Assemblages

Benthic foraminifera were counted in the >63 μm size fraction. Data were screened following the methods outlined in Section 2.2.12. Specimens of the most abundant benthic foraminifera counted are shown in Figures 6.1 and 6.2. Detrended correspondence analysis (DCA) was used to define the major benthic foraminifera assemblage groups. Benthic foraminifera are impacted by numerous ecological factors that determine their assemblage composition and abundance, including organic carbon flux to the sea floor (type, quantity, seasonal duration), temperature, salinity, oxygen availability, substrate and energy levels (e.g. Murray 2001; Jorissen et al. 2007; Gooday & Jorissen 2012). The link between particular environmental parameters discussed in this chapter and the presence/absence of specific benthic foraminifera are explained below.

Bottom water oxygen concentration : In the past some authors proposed that benthic foraminifera display an overriding habitat preference based on oxygen levels (e.g. Kaiho 1994); however, recent work has shown that many of the species once considered 'oxic' are found at very low oxygen levels (Jorissen et al., 2007), and many species are able to survive in anoxic water by active denitrification (Høgslund et al., 2008; Piña-Ochoa et al., 2010), such that it is now considered only at very low oxygen levels <0.5 ml/l that the fauna is controlled by oxygen (Jorissen et al., 2007; Murray, 2001). In addition, many species are infaunal and therefore respond to local pore-water oxygen levels that are much lower than bottom water. It is therefore problematic to use benthic

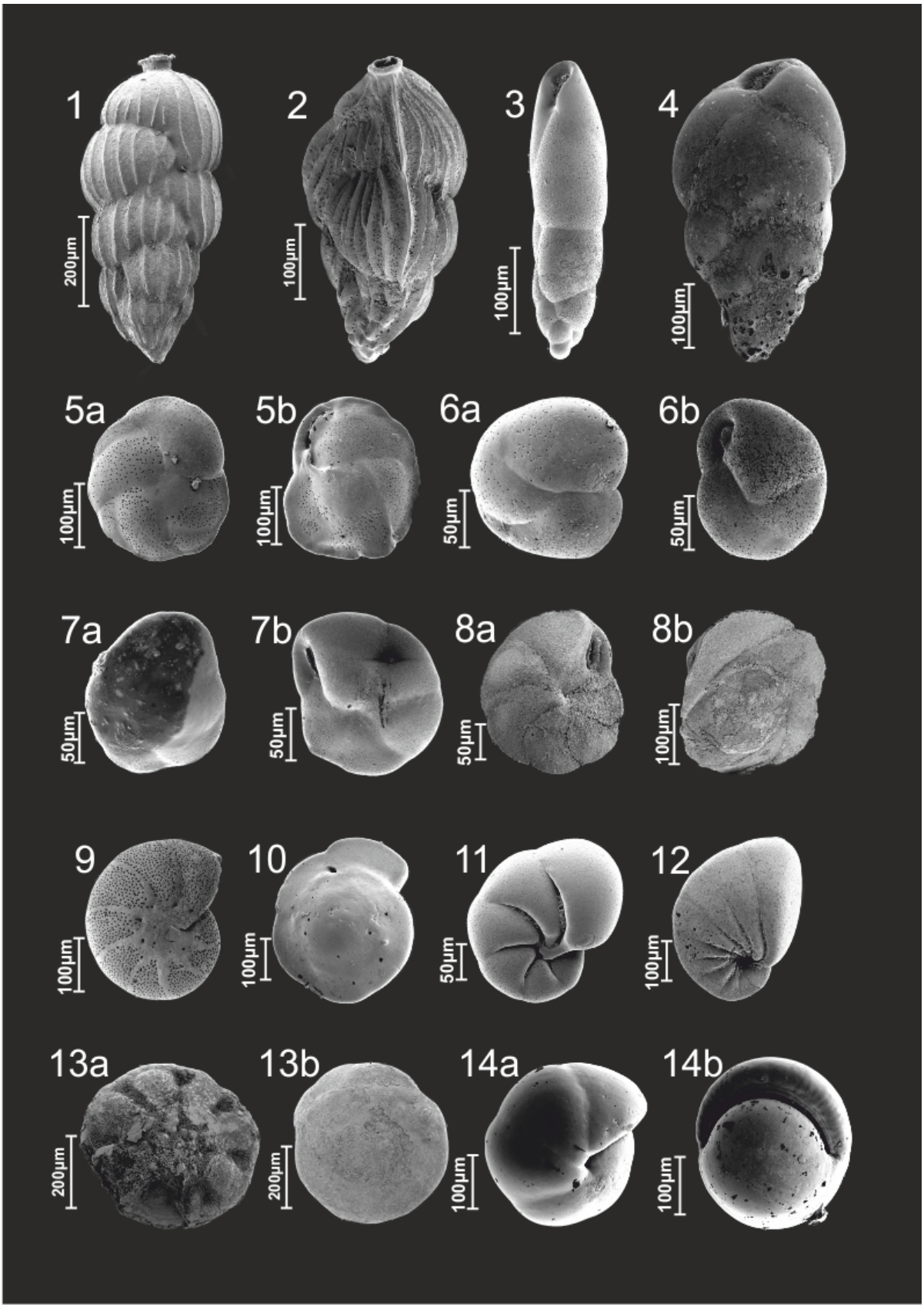

Figure 6.1: Benthic foraminifera assemblage Plate 1: (1) *Uvigerina bifurcata*; (2) *Angulogerina angulosa*; (3) *Fursenkoina fusiformis*; (4) *Bulimina aculeata*; (5) *Cassidulina carinata*; (6) *Cassidulina crassa*; (7) *Epistominella exigua*; (8) *Epistominella pulchella*; (9) *Melonis barleeanum*; (10) *Oridorsalis umbonatus*; (11) *Nonionella auris*; (12) *Nonionella pulchella*; (13) *Nuttallides umbonifera*; (14) *Pullenia bulloides*.

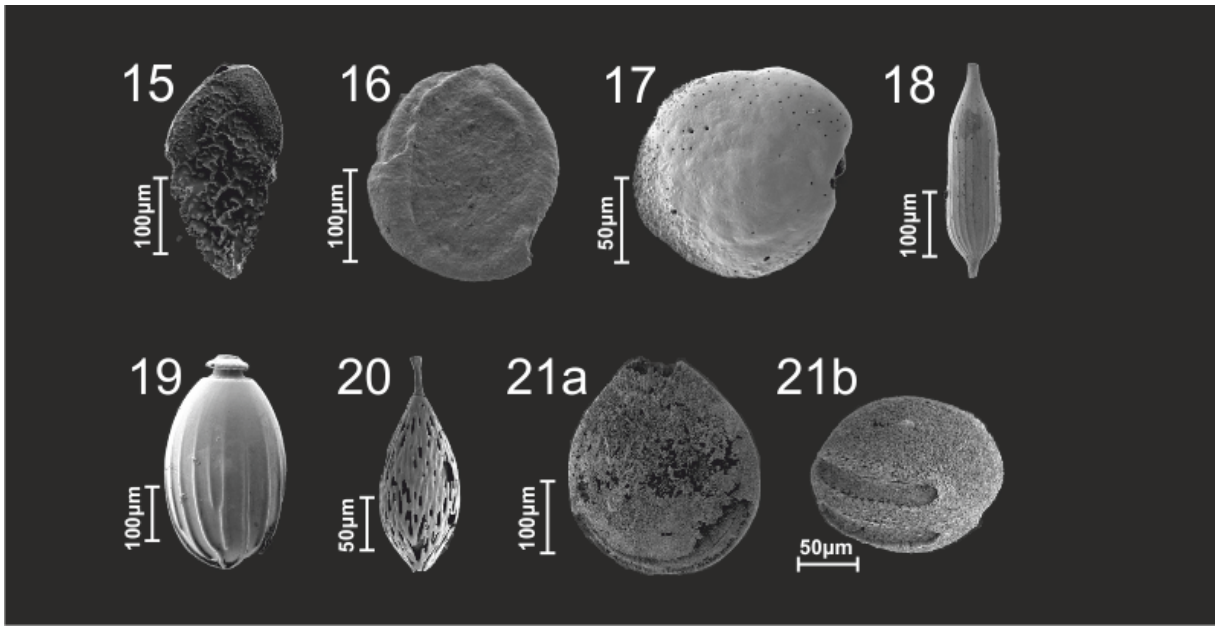

Figure 6.2: Benthic foraminifera assemblage Plate 2: (15) *Bolivina sp.*; (16) *Cyclogyra cf. involvens*; (17) *Alabaminella weddellensis*; (18) *Lagena distoma*; (19) *Oolina margaritae*; (20) *Lagena striata*; (21) *Fissurina bisulcata.*

foraminifera assemblages to quantify bottom water oxygen concentrations, but the proportion of epibenthic to infaunal species can be used to qualitatively infer relative changes in bottom water oxygen; epibenthic species are typically intolerant of dysoxic/anoxic conditions (Gooday and Jorissen, 2012; Jorissen et al., 2007; Murray, 2001).

High Productivity: An abundance of shallow infaunal species typify regions of high surface productivity and high export flux. Different species appear to show affinities for particular patterns of productivity, e.g. continuous organic carbon flux versus highly seasonal pulses, or labile versus refractory organic carbon. In defining a 'high productivity' group, I do not make the distinction between the type or seasonality of organic carbon flux to the sediment, but simply group species that are associated with eutrophic conditions. *Uvigerina sp.*, *Bulimina aculeata* and *Cassidulina crassa* are associated with high, continuous surface productivity and high organic matter rain rates, combined with low to moderate oxygen depletion in the bottom and porewaters (Zarriess and Mackensen 2010, and references therein). In contrast, *Fursenkoina fusiformis*, *Bolivina sp.*, *Epistominella exigua* in combination with *Alabaminella weddellensis*, show a strong affinity for labile phytodetritus (Gooday and Alve, 2001; Shepherd et al., 2007; Sun et al., 2006).

Seasonality: The benthic species associated with highly seasonal pulses of phytodetritus are separated out of the 'high productivity' group. The relative abundance of one species alone (*E. exigua* or *A. weddellensis*) is not a strong indicator of seasonality (Sun et al., 2006); however, in cores GC528 and GC642, *E. exigua* and *A. weddellensis* nearly always co-occur suggesting their presence is a response to highly seasonal pulses of productivity.

Low porewater oxygen/nitrate respiration: Recent studies (Høgslund et al., 2008; Piña-Ochoa et al., 2010) have observed nitrate-reduction being used by a number of different benthic foraminifera as an adaptive strategy to cope with low oxygen conditions within the sediment. Within the sediment, oxygen is consumed by oxic respiration of organic carbon, and typically decreases exponentially with depth below the sediment-water interface (e.g. Sørensen et al., 1979). Low porewater oxygen concentrations may be indicative of a large supply of organic carbon to the sediment, promoting oxic respiration. The proportion of nitrate-reducing benthic foraminifera was compared to the number of benthic species known to be incapable of nitrate-reduction in order to qualitatively assess the oxygen concentration of the porewaters.

Bottom current speed: In the sub-Antarctic Pacific, intermediate water assemblages dominated by *Cassidulina carinata* and *Angulogerina angulosa* have been associated with coarse substrates under well-oxygenated, high energy regimes and sustained food supply (Hayward et al., 2002).

Table 6.1 summarises the various environmental parameters assessed in this chapter, and the different species in the core that have been linked to each specific environmental parameter.

Table 6.1: Environmental parameters reconstructed using benthic foraminifera in core GC528/642.

Environmental parameter	**Indicator species**		**Reference**
Low oxygen/nitrate respiration	Denitrifiers	*Uvigerina bifurcata*, *Uvigerina sp.*, *Fursenkoina fusiformis*, *Bulimina aculeata*, *Melonis barleeanus*, *Bolivina sp.*, *Globobulimina sp.*	Høgslund et al. 2008; Piña-Ochoa et al. 2010
	Incapable of denitrification	*Epistominella exigua, Triloculina sp.*	
High productivity	*Uvigerina bifurcata*, *Uvigerina sp.*, *Fursenkoina fusiformis*, *Bolivina sp. Cassidulina crassa*, *Bulimina aculeata*, *Epistominella exigua*, *Alabaminella weddellensis*		Gooday and Jorissen 2012; Jorissen et al. 2007; Murray 2001
High seasonality	*Epistominella exigua*, *Alabaminella weddellensis, Fursenkoina fusiformis, Bolivina sp,*		Gooday and Alve 2001; Sun et al. 2006
High bottom water [O_2]	*Cibicidoides sp.*, *Pyrgo sp.*		Gooday and Jorissen 2012; Jorissen et al. 2007; Murray 2001
Fast bottom currents	*Cassidulina carinata, Angulogerina angulosa*		Hayward et al. 2002

6.3 Results

6.3.1 Mass accumulation rate

The mass accumulation rate of cores GC528 and GC642 varies immensely across the two glacial terminations (Figure 6.3b). Across T-I, there is a peak in mass accumulation rate during the LGM (20.3-18.5 ka) and during the ACR (14.0-12.7 ka) with accumulation rates reaching up to

50 g/cm^2/kyr. The accumulation rates during the rest of MIS2 and the Holocene are relatively consistent (5-10 g/cm^2/kyr). Across T-II there is a large increase in accumulation rate from 1 g/cm^2/kyr during MIS6 to a maximum of 8 g/cm^2/kyr during the climatic optimum of MIS5e. The accumulation rate for the remaining part of MIS5e are elevated (5 g/cm^2/kyr) compared to MIS6, but relatively consistent.

Core GC528, which has the best age constraints (^{14}C dating), displays the greatest variability in sedimentation rate. In Chapter 3, I demonstrated that significant changes in the sedimentation rate within these cores are expected; however, it is apparent that slight inaccuracies in the age model will be reflected in the proxy accumulation rates.

6.3.2 Glacial-interglacial variability in productivity

The glacial-interglacial pattern of productivity suggested by carbonate-based proxies and organic-based proxies has the opposite sense across the glacial terminations. Carbonate proxies such as the carbonate accumulation rate (Figure 6.3c), the benthic foraminiferal accumulation rate (Figure 6.3d) and Ca/Al (Figure 6.3e) suggest that productivity during the interglacial period was higher than during glacial periods. However, as I described in Section 6.2.2, the majority of biogenic carbonate in cores GC528 and GC642 is derived from benthic foraminifera, which respond indirectly to changes in surface productivity (Herguera and Berger, 1991). Therefore, a deglacial increase in carbonate within the sediments may be the result of a number of factors other than changes in surface productivity, such as bottom water oxygen concentrations, benthic temperatures or bottom water carbonate ion concentration (i.e. corrosivity).

Alkenone accumulation rate and total organic carbon are more directly linked to surface ocean productivity (Schoepfer et al., 2014). Alkenone accumulation rates (Figure 6.3f) increase over both T-I and T-II, suggesting greater coccolithophore productivity during interglacial periods. In contrast, the total organic carbon mass accumulation rate (Figure 6.3g) is lower in the Holocene than during MIS2, but higher in MIS5 relative to MIS6.

Small inaccuracies in the age model can result in significant changes in the sediment mass accumulation rate, and thus proxy accumulation rates. Step-wise changes in the sediment mass accumulation rate that occur due to the tiepoint-method used to generate the age model in core GC642 are likely unrealistic. In order to bypass this potential problem, I study the alkenone:TOC ratio (Figure 6.3h). The alkenone:TOC ratio records the proportion of the total export flux that is derived from coccolithophore production. Across the two terminations, the alkenone:TOC ratio increases during interglacial periods relative to glacial periods, suggesting a greater proportion of coccolithophore production during interglacials.

Curiously, a change in diatom abundance is also observed across the glacial terminations, with a greater abundance of diatoms during interglacial periods. This is in stark contrast to other sites from the sub-Antarctic zone, which note a significant deglacial decrease in diatom and opal accumulation (Anderson et al., 2002; François et al., 1997; Kumar et al., 1995)[1]. Without conducting a thorough study of diatom assemblages and diatom preservation it is impossible to infer whether the deglacial increase in diatom abundance observed in site GC528/642 reflects the original surface production

[1]Low diatom abundance during the glacial sections of this core may highlight that the productivity regime at this site is not representaive of the wider sub-Antarctic zone.

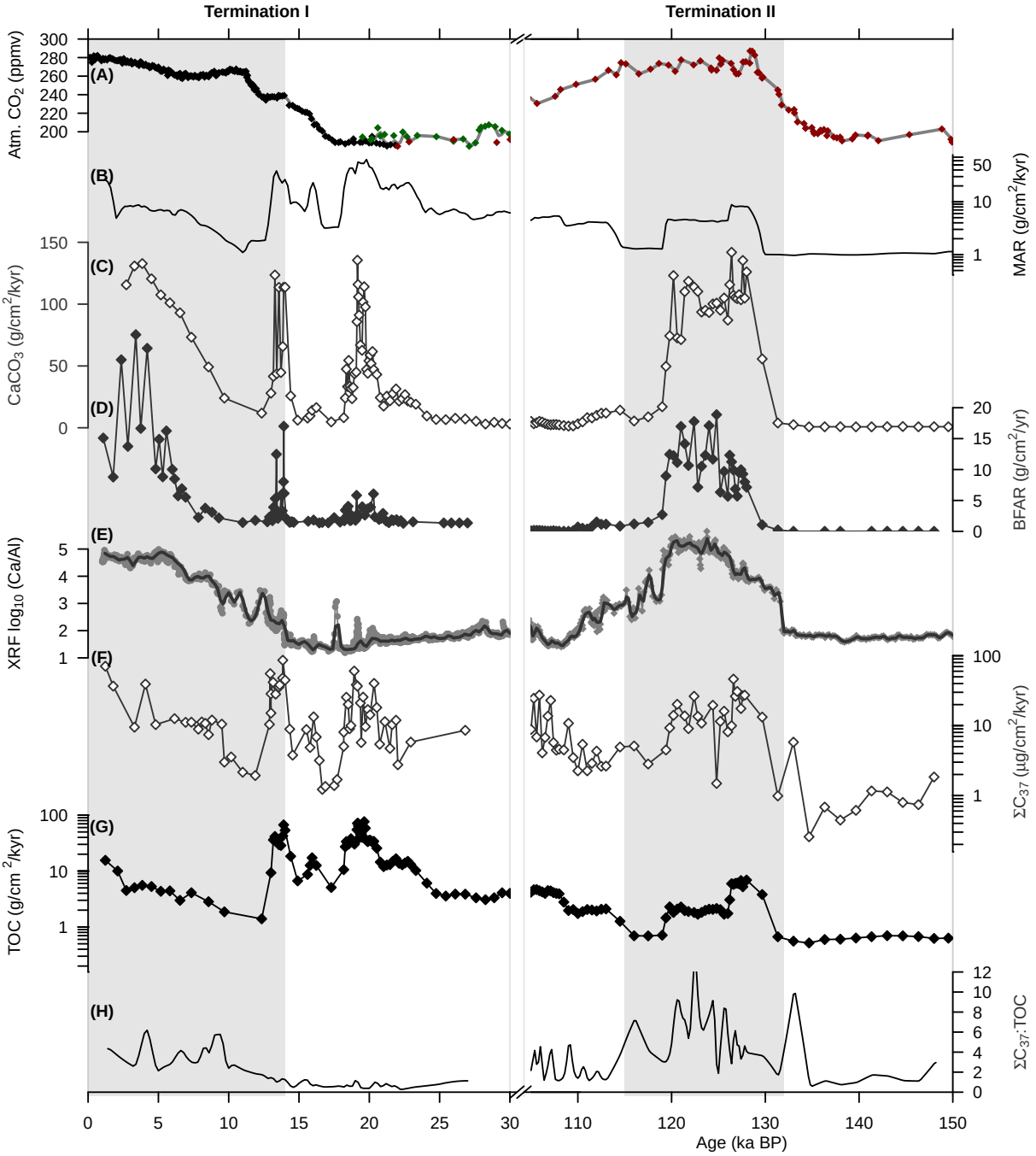

Figure 6.3: Productivity changes over Termination I and Termination II. (A) Antarctic CO_2 compilation (Vostok, Petit et al. 1999, red; EDC, Monnin et al. 2004, black; Byrd, Ahn and Brook 2008, green); (B) Mass accumulation rate (MAR, g/cm^2/kyr). Note the logarithmic y-axis; (C) Calcium carbonate ($CaCO_3$) accumulation rate (g/cm^2/yr). ; (D) Benthic Foraminifera Accumulation Rate (BFAR, g/cm^2/yr); (E) Downcore Ca/Al ratio as measured by XRF; (F) Total alkenone accumulation rate (µg/cm^2/kyr). Note the logarithmic y-axis; (G) Total organic carbon (TOC) mass accumulation rate (g/cm^2/kyr). Note the logarithmic y-axis; (H) Total alkenone:total organic carbon ratio.

or is a secondary feature driven by poor diatom preservation during the glacial period.

In summary, the records of productivity from the southwest Atlantic show evidence for a change in the type of surface ocean productivity during interglacials; coccolithophores play a more dominant role in interglacial net primary production, and diatoms may be more abundant. Across both terminations there is a strong increase in carbonate accumulation rate; however these records are largely a reflection of changes in benthic foraminiferal mass accumulation rate, and therefore are only indirectly related to surface ocean productivity. With all of these productivity records there is the possibility that slight inaccuracies in the age model result in significant artefacts in the mass accumulation rate. These uncertainties make it difficult to determine absolute glacial-interglacial changes in net primary productivity in the region. In the following discussion I use benthic foraminiferal assemblages to qualitatively determine glacial-interglacial changes in the export of organic matter to the sediment, which can be related to changes in surface productivity. However, carbonate records can be significantly altered by syn- or post-depositional dissolution. I therefore first assess downcore carbonate preservation.

6.3.3 Carbonate preservation

High resolution SEM images were taken of foraminiferal tests from specific samples to determine the potential effect of dissolution on foraminifera in core GC528. There is no single thin-walled species (e.g. *Nonionella sp.* or *Fursenkoina fusiformis*) that is present continuously downcore, therefore, I use a range of different species to assess dissolution. Between 21-16 ka, there is a strong bias in the benthic foraminifera assemblage towards the thin-walled species *Fursenkoina fusiformis*. This species showed no evidence of any partial dissolution - reflected by the smooth test wall (Figure 6.4a). Between 16-1 ka, *Epistominella exigua* and *Cassidulina carinata* are present in the benthic assemblage. These species appeared pristine and glassy under the optical microscope, and high resolution SEM imaging revealed no evidence of dissolution of the test-wall (Figure 6.4b). In this image the holes in the test wall are pores thought to be linked to availability of oxygen in the environment in which the foraminifera resides, and are not a feature of dissolution. In contrast, prior to 25 ka, only thick-shelled foraminifera such as *Uvigerina bifurcata*, *Bulimina aculeata* and *Nuttallides umbonifera* are present. The high-resolution images of these samples revealed evidence of extensive dissolution of foraminiferal tests; the outer layer of the test has been partially removed and looks broken and 'pockmarked' under the electron microscope (Figure 6.4c-d).

In summary, there is strong evidence for extensive dissolution of foraminifera prior to 25 ka, but samples younger than 21 ka appear pristine and show no evidence of dissolution. Additionally, an interval of dissolution was visually observed prior to the Last Interglacial (150-131 ka). An abrupt increase in the Ca/Al ratio at 131 ka (Figure 6.3e) marks the onset of well-preserved benthic assemblages.

6.3.4 Benthic foraminiferal assemblages

I examine the changes in the benthic foraminifera assemblages to develop a greater understanding of glacial-interglacial variations in productivity type, seasonality and quantity of export flux. There are significant changes to the benthic foraminiferal assemblages and in the diversity of these as-

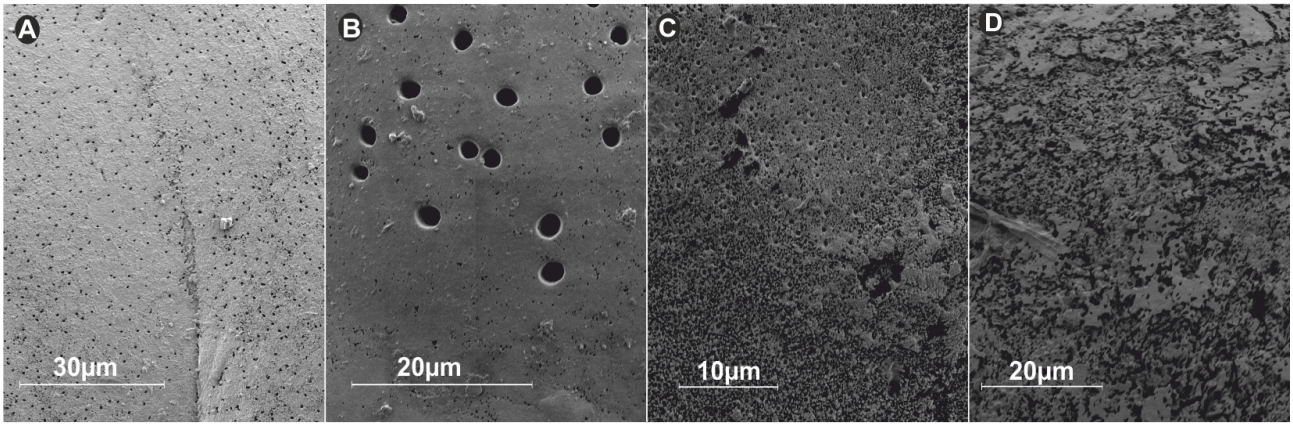

Figure 6.4: Assessing the evidence for dissolution in GC528. High resolution SEM images of the tests of forminifera to determine dissolution. (A) *Fursenkoina fusiformis*; (B) *Cassidulina carinata*; (C) *Bulimina aculeata*; (D) *Nuttallides umbonifera*.

semblages over each glacial termination (Figure 6.5). Both interglacial periods (MIS5e and MIS1) are characterised by high diversity assemblages relative to the glacial periods.

I use detrended correspondence analysis (DCA; a multivariate statistical technique) to explore the major changes. The two major axes of the DCA show that the samples cluster into thee assemblages (Figure 6.5d). High values on Axis 1 are characterised by *U. bifurcata*, *B. aculeata*, *F. fusiformis* and *N. umbonifera*, the low values on this axis correspond to the species *E. exigua*, *C. carinata* and *M. barleeanum*. High values on Axis 2 correspond to the species *U. bifurcata* and *B. aculeata*, whereas the low values of this axis are characterised by *F. fusiformis*. Assemblage 1 is characterised by low scores on both Axis 1 and moderate-low scores on Axis 2. Assemblage 2 is characterised by high scores on Axis 1 but low scores and Axis 2. Assemblage 2 has high scores on both Axis 1 and 2. I assess the environmental parameters that may be driving the transition between each assemblage using the indicator species described in Table 6.1.

Both Assemblage 3 and 2 are dominated by nitrate-reducing benthic foraminifera and high productivity/low oxygen species (Figure 6.6b-c), but Assemblage 2 contains a greater abundance of phytodetritus-associated species (Figure 6.6d). The transition from Assemblage 2 to Assemblage 1 is characterised by a marked decline in the proportion of denitrifying benthic foraminifera (Figure 6.6b), and an increase in epibenthic foraminifera (Figure 6.6e) indicating oxic bottom water and porewater conditions. Additionally, there is also a marked increase in species indicative of fast bottom currents (Figure 6.6f). Assemblage 1 may indicate that increases in bottom water flow speed at the onset of the interglacial increased the ventilation of bottom waters at site GC528, driving an increase in bottom water oxygen concentration and changing conditions at the sediment water interface resulting in an increase in porewater oxygen concentration.

In summary, analysis of benthic foraminifera assemblages from cores GC528 and GC642 in the southwest Atlantic reveals significant changes in assemblage across the last two glacial terminations. Interglacial periods are characterised by high diversity benthic foraminifera assemblages whereas the glacial assemblages are considerably less diverse. The DCA of the high-resolution record from GC528 spanning the last 30 ka identifies three assemblages are present during this time. Assemblage 3 between 30-25 ka appears to be highly dissolved; the remaining assemblage

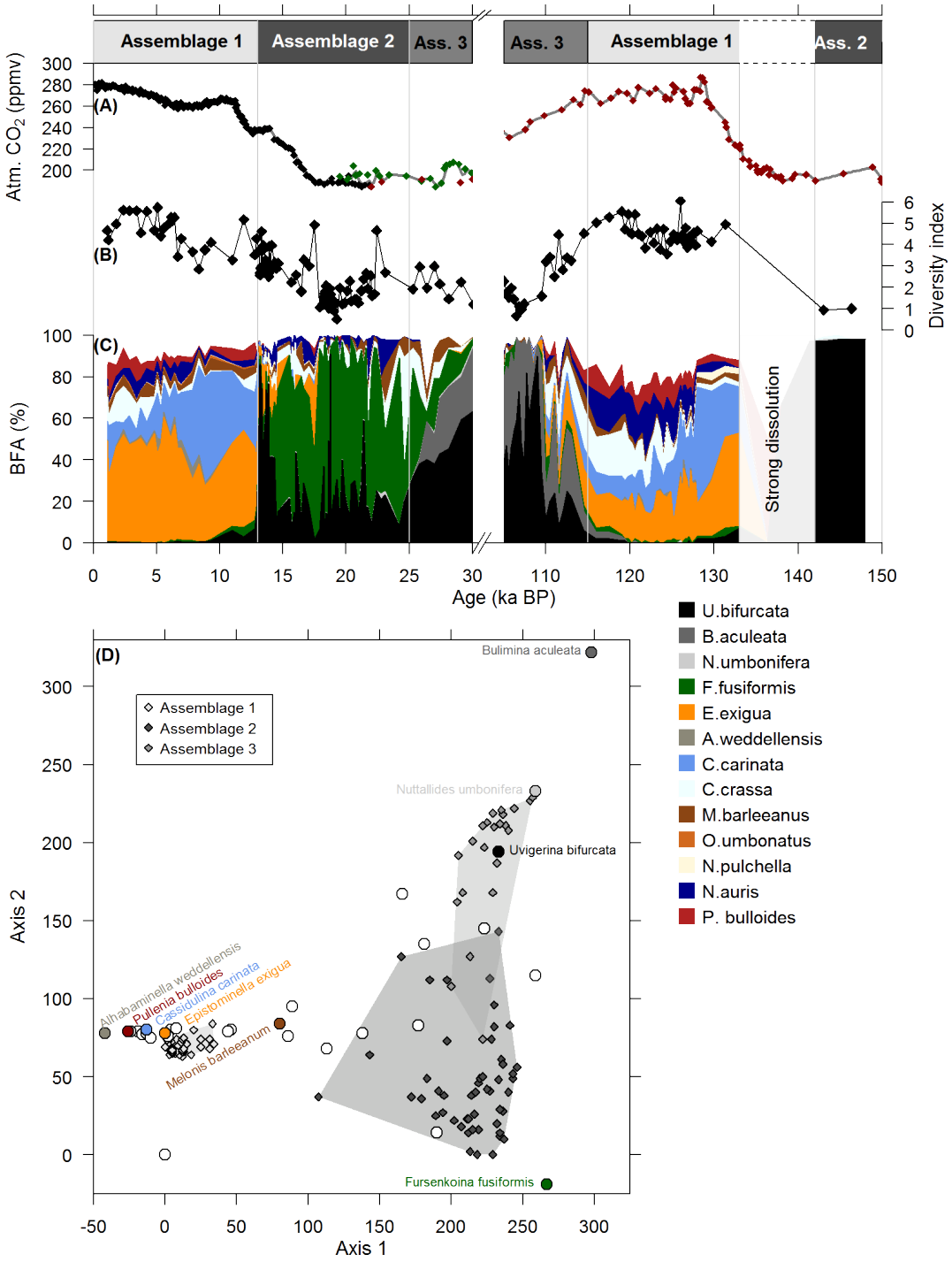

Figure 6.5: Benthic foraminifera assemblage analysis over Termination I and II. (A) Antarctic CO_2 compilation (Vostok, Petit et al. 1999, red; EDC Monnin et al. 2004, black; Byrd Ahn and Brook 2008, green); (B) Fisher's diversity index (Fisher et al., 1943); (C) Benthic foraminifera assemblages (%), species indicated by the legend; (D) Crossplot of the Axis 1 and Axis 2 based on DCA analysis. The dependence of individual species to each axis is shown by the white circles - some of the important species discussed in the text are identified with the same colour scheme as in (C). The polygons indicate the groupings of samples into three assemblages, which are as also displayed above the time series.

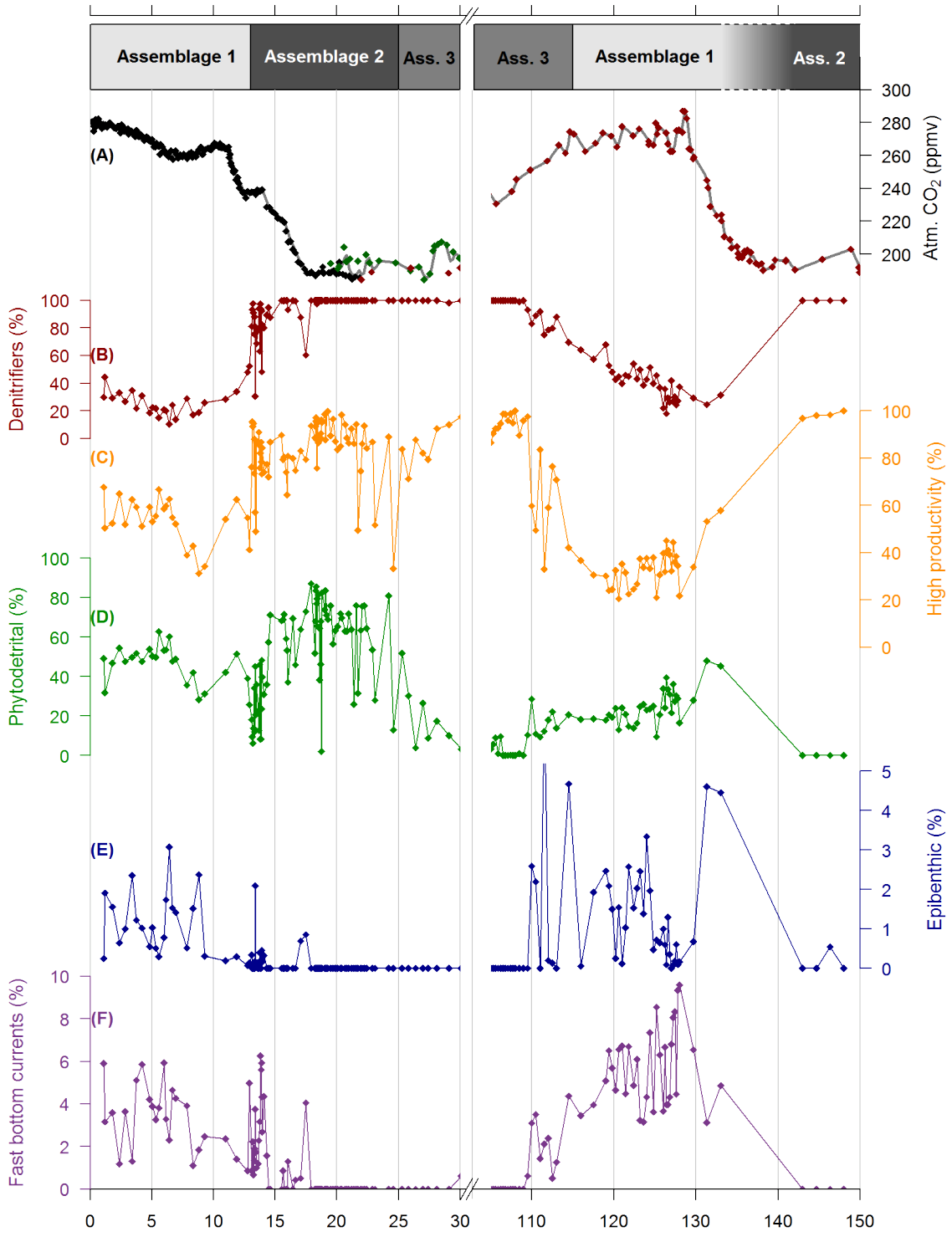

Figure 6.6: Environmental changes suggested by indicator species. (A) Antarctic CO_2 compilation (Vostok, Petit et al. 1999, red; EDC, Monnin et al. 2004, black; Byrd, Ahn and Brook 2008, green); Percentage of benthic foraminifera indicative of (B) nitrate reduction; (C) 'high productivity'; (D) seasonal high fluxes of phytodetritus; (E) epibenthic/oxic bottom waters; (F) fast bottom current flow. See Table 6.1 for a list of foraminifera used in each classification.

is dominated by the high productivity/low oxygen benthic species *B. aculeata* and *U. bifurcata*. Assemblage 2 between 25-12 ka is dominated by *F. fusiformis* and is indicative of elevated fluxes of organic carbon to the sediment, likely in highly seasonal pulses. The transition to the diverse interglacial Assemblage 1 at 12 ka occurs synchronous with a decrease in nitrate-reducing benthic foraminifera, an increase in epibenthic foraminifera and an increase in bottom current speeds.

6.4 Discussion

In this discussion I look in detail at environmental factors driving the major shifts in benthic foraminifera assemblage. I focus primarily on Termination I as this interval has the best carbonate preservation.

6.4.1 Termination I: onset of the LGM

The DCA suggests a significant benthic foraminifera assemblage change between 25-22 ka. Over this interval the thick-walled *B.aculeata* is replaced by an abundance of pristine, thin-walled *F. fusiformis* (Figure 6.7a-b). Both *F. fusiformis* and *B. aculeata* are indicative of relatively high export fluxes. Prior to 25 ka, there is strong evidence of dissolution within the core; therefore, it is likely that less robust foraminifera have been preferentially removed from this record. However, the lack of the thick-walled species *B. aculeata* in the benthic assemblage following 25 ka is a real feature of the record and not an artefact of variable preservation.

Several studies of benthic foraminifera assemblages around the Antarctic Peninsula (Kilfeather et al., 2011; Peck et al., 2015) have noted that *F. fusiformis* appears to replace *B. aculeata* during intervals of high phytodetrital flux to the sediment. In the modern ocean, surface water chlorophyll levels are well known to be elevated in regions associated with glacial melt and icebergs (Schwarz and Schodlok, 2009; Smith et al., 2007) owing to the meltwaters containing significant concentrations of iron and other nutrients (Wadham et al., 2013). The demise of *B.aculeata* and the advent of the *F. fusiformis* in GC528 between 25-21 ka coincides with a major increase in IRD accumulation (Figure 6.7c) indicative of iceberg melt above the site. This iceberg melt acts to stimulate productivity in the surface ocean resulting in an increase in phytodetritus flux to the seafloor and the competitive replacement of *B. aculeata* by *F. fusiformis*.

The stimulation of surface productivity by the presence of icebergs at the onset of the LGM is perhaps surprising in this region of the ocean given that the site is located immediately downstream of dust blown off the Patagonian Shelf. During glacial times it has been hypothesised that a greater export of Patagonian dust to the sub-Antarctic stimulated productivity (Martin, 1990; Martínez-Garcia et al., 2009). However, evidence of the changes in dust over MIS3-2 from Antarctic ice cores (Figure 6.7d; Fischer et al. 2007) suggests that dust concentrations were already elevated before 25 ka, and thus an increase in dust is not consistent with the timing of the benthic foraminifera assemblage change at GC528. Our observation that peak productivity in the southwest Atlantic appears be linked to iceberg melt rather than dust places a greater emphasis on the role of iceberg melt in fertilising the sub-Antarctic.

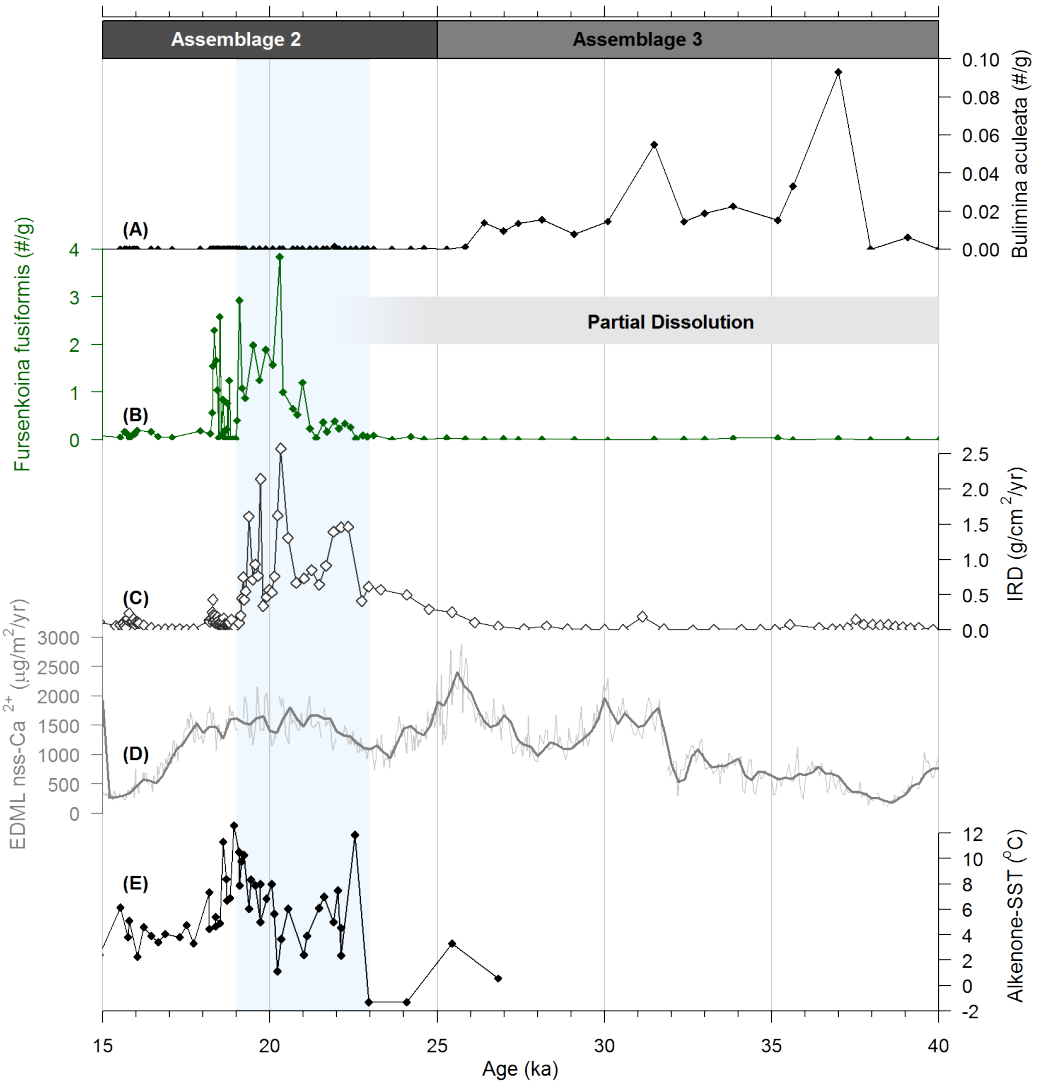

Figure 6.7: Reconstructing oceanographic changes at the onset of the LGM. (A) *Bulimina aculeata* concentration (#/g); (B) *Fursenkoina fusiformis* concentration (#/gm); (C) IRD flux at site GC528 (g/cm^2/yr); (D) EDML non-sea salt Ca^{2+} record, a proxy for Patagonian dust (Fischer et al., 2007); (E) Alkenone-SST at site GC528 (Chapter 5).

Additional support for the presence of meltwater at the onset of the LGM comes from the alkenone-SST record at site GC528 (described in Chapter 5). In Section 5.5.5, I explained how meltwater-induced stratification could result in elevated summer temperatures in the shallow mixed layer. The peak in *F. fusiformis* is broadly consistent with elevated alkenone-SSTs (Figure 6.7e), and likely suggests that intense productivity in the summer months results in a large seasonal phytodetritus flux that increases the abundance of *F. fusiformis* in the benthic foraminifera assemblage.

In summary, both benthic assemblages before and after 25 ka are indicative of high fluxes of organic carbon to the sediment, and the replacement of *B. aculeata* by *F. fusiformis* suggests a higher, more seasonal flux of organic carbon to the sediment following 25 ka. The change to this assemblage appears to have been driven by an increase in icebergs to the region, potentially

promoting surface productivity, resulting in *B. aculeata* being out-competed by more opportunistic foraminifera.

6.4.2 Glacial dissolution of shelf carbonates

In the previous discussion, I mention that that the assemblage change between 25-22 ka is difficult to pinpoint because of strong dissolution prior to 25 ka. In fact both records spanning Termination I and II are marked by a significant carbonate dissolution in the glacial intervals immediately prior to the glacial termination (150-133 ka; 30-25 ka). The evidence of dissolution during the glacials suggests either the presence of corrosive intermediate waters, or subsurface processes (e.g. oxic remineralisation) act to decrease the calcium carbonate saturation state of the porewaters.

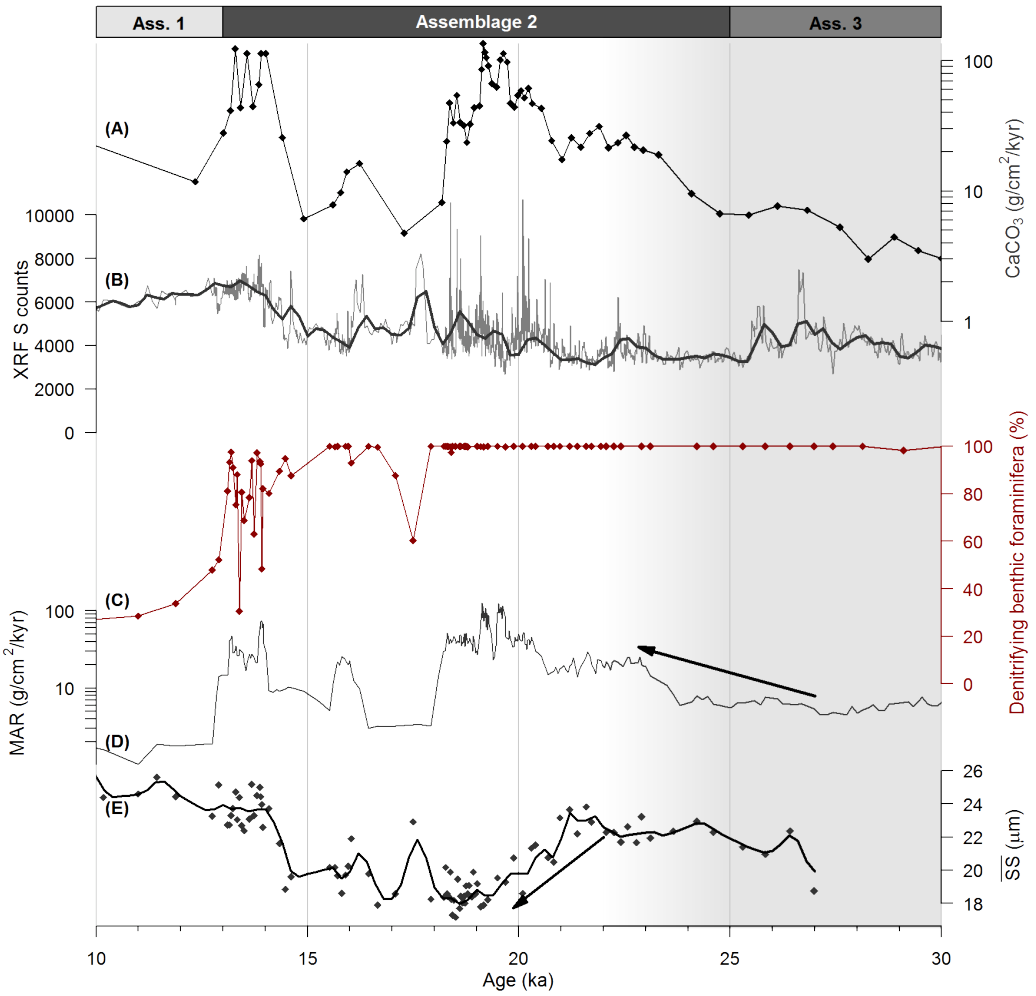

Figure 6.8: Glacial dissolution caused by enhanced oxic repiration. (A) Carbonate MAR (g/cm^2/yr); (B) XRF Sulphur counts; (C) Percentage of foraminifera with denitrification capability; (D) Bulk sediment MAR (g/cm^2/yr); (E) Sortable silt mean grain size (μm).

Given that the benthic foraminifera assemblages during these intervals (150-133 ka; 30-25 ka) reflect a relatively high flux of organic carbon to the sediment (Gooday and Jorissen, 2012; Jorissen

et al., 2007), it is likely that the carbonate dissolution is the result of oxic remineralisation of organic carbon. The respiration of organic matter through oxidisation can result in in-situ carbonate dissolution, by increasing porewater DIC relative to alkalinity. This decreases the carbonate ion concentration and thus decreases the calcium carbonate saturation state in the porewaters. Therefore, the strong dissolution in the intervals 150-133 ka and 30-25 ka could reflect significant oxic remineralisation of organic matter.

Alternatively, dissolution could be caused by a reduction in the carbonate ion concentration of waters at the seafloor. In the southeast Atlantic, *B. aculeata* has been linked to the presence of relatively corrosive Upper Circumpolar Deep Water (UCDW), whilst the abundance of *N. umbonifera* is negatively correlated with carbonate saturation (Mackensen et al., 1993). It is possible that the glacial benthic foraminifera assemblages are driven by the presence of corrosive UCDW overlying site GC528/642. The shoaling of UCDW during glacial stages is consistent with other studies (Ronge et al., 2015). These authors suggest that sea ice meltwater freshens AAIW, decreasing its density and causing the AAIW-UCDW boundary to shoal. However, at the shallow depths of core GC528/642 (600m) the influence of pressure on the solubility of carbonate is negligible, thus the carbonate ion concentration of the bottom water needs to be extremely low in order to result in carbonate dissolution. Such low carbonate ion concentrations have not been observed in reconstructions of carbonate ion concentration at other intermediate depth sites (Allen et al., 2015). Thus, the bathing of the site in UCDW is unlikely to be the sole driver of the strong dissolution during the glacial periods; however, it may be a contributing factor.

It is perhaps surprising that the 'high productivity' *F. fusiformis* assemblage between 25-14.7 ka does not show the same evidence of dissolution as the interval prior to 25 ka. This may imply a change in the dominant remineralisation reaction, from oxic to anoxic remineralisation such as denitrification or sulphate reduction. Unlike oxic remineralisation, denitrification and sulphate reduction of organic matter increases both DIC and alkalinity in a near 1:1 ratio (Berner, 1971; Hu and Cai, 2011), and therefore does not result in significant carbonate dissolution. However, evidence supporting the idea of an increase in sulphate or nitrate reduction in GC528 at 25 ka is scarce. There is no significant change observed in the XRF sulphur counts (Figure 6.8b) or the percentage of denitrifying foraminifera (Figure 6.8c). A lack of change in the percentage of denitrifying foraminifera does not necessarily imply constant porewater oxygen concentrations; many denitrifying benthic foraminifera have the ability to respire organic matter both aerobically and anaerobically, and thus the presence of denitrifying benthic foraminifera does not necessarily imply continual low-oxygen conditions. Changes in the sediment mass accumulation rate at 24 ka (Figure 6.8d) may provide tenuous support for a change in the dominant organic matter remineralisation reaction. An abrupt increase in the mass accumulation rate at 24 ka would reduce the ability to replenish porewater oxygen, and thus could limit the oxic respiration within the sediment column. Alternatively, a reduction in bottom water flow speed can result in a decrease in porewater oxygen concentrations (Figure 6.8e). In Chapter 5, I discuss the potential for reductions in the speed of Drake Passage through-flow during glacial periods. A reduction in bottom current speeds at 22 ka would reduce the turbulent processes in surface sediment layer (Vanderborght et al., 1977) and potentially reduce the concentration of oxygen in the porewaters.

To summarise, there is strong evidence of carbonate dissolution from the glacial intervals of core GC528/642. Whilst this could indicate a shoaling of the AAIW-UCDW boundary, resulting

in the site being bathed by more corrosive UCDW, the decrease in carbonate ion concentration required to cause widespread dissolution at this depth is fairly improbable. Instead, I suggest that the dissolution is caused by oxic respiration of organic matter within the sediment. High bottom water oxygen concentrations coupled with moderate-low sedimentation rates and a continual supply of organic matter to the sediment provide optimal conditions for the oxic respiration of organic matter, increasing porewater DIC and thus dissolving carbonate within the sediment. I speculate that the increase in carbonate preservation at 25 ka could be the result of an increase in the sediment accumulation rate of the core site or slow bottom current flow speeds, preventing the replenishment of porewater oxygen within the sediment. However, beside from changes in sediment mass accumulation rate and reconstructions of bottom current flow speeds, there is little evidence supporting the idea of a decrease in oxic respiration. Reconstructions of porewater oxygen concentrations based on redox sensitive metals might provide useful insights here.

6.4.3 Termination I: Deglacial variations between the LGM and Holocene

Between 22-12.7 ka, the benthic foraminifera assemblage is dominated exclusively by high productivity associated species. *Fursenkoina fusiformis* is the most abundant species until 14.5 ka, although the abundance of *U. bifurcata* varies significantly, with maxima at 20.7-19.8, 16.7-16.0 and 14.5-12.7 ka (Figure 6.9c-d). These intervals of abundant *U. bifurcata* coincide with intervals of bottom water warming (Figure 6.9d). This link between *U. bifurcata* abundance and warmer bottom water temperatures (BWTs) suggests that *U. bifurcata* may be less tolerant of low BWTs than *F. fusiformis*. *Uvigerina bifurcata* abundance significantly decreases when BWTs fall below -1^{o}C.

Interestingly, the local BWT maximum of 0-2^{o}C at 17-16 ka is accompanied by an abundance of the high-productivity associated species which are characteristic of interglacial assemblages, such as *M .barleeanus*, *E. exigua* and *C. carinata*. This suggests that similarly to *U. bifurcata* these species are also intolerant of cold temperatures but the minimum temperatures that these species can tolerate is warmer than that of *U. bifurcata*.

As explained in Chapter 4, fluctuations in the temperature of intermediate waters are likely linked to the proximity of Antarctic sea ice and the tunnelling of cold Antarctic Surface Water to intermediate water depths forming AAIW. In the interval that *F. fusiformis* dominates the benthic assemblage, sea ice is likely more proximal to the core site, and as a result, BWTs are near-freezing. The increase in BWTs at 18 ka is indicative of the initial deglacial retreat of Antarctic sea ice; when BWTs increase above -1^{o}C *U. bifurcata* takes over as the dominant species. In intervals when the BWTs rose above 0^{o}C (17-16 ka), high productivity associated species such as *M. barleeanus*, *E. exigua* and *C. carinata*, which are more characteristic of the later interglacial assemblage, are present suggesting that the general absence of these species could be temperature-dependent rather than supply-driven. The termination of the *F. fusiformis* assemblage and the advent of a more diverse assemblage at 12.7 ka suggests not only a warming in the bottom waters at site GC528 (related to the final retreat of Antarctic sea ice) but a change in surface productivity.

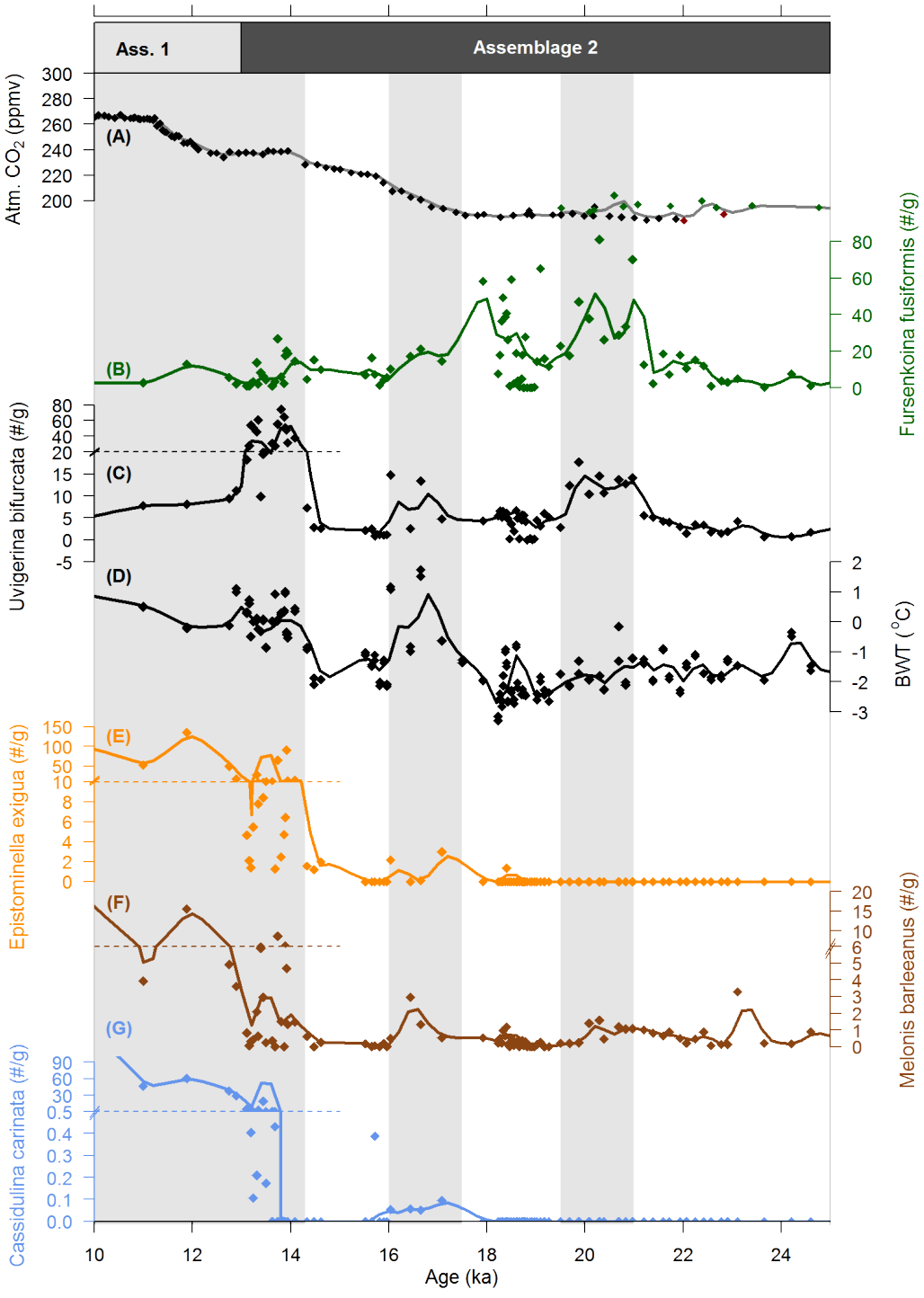

Figure 6.9: Temperature dependence of phytodetrital benthic foraminifera at site GC528. (A) Antarctic CO_2 compilation (Vostok, Petit et al. 1999, red; EDC, Monnin et al. 2004, black; Byrd, Ahn and Brook 2008, green); (B) *Fursenkoina fusiformis* concentration (#/gm); (C) *Uvigerina bifurcata* concentration (#/gm); (D) Bottom water temperature (BWT) reconstruction at GC528 (Chapter 4); (E) *Epistominella exigua* concentration (#/gm); (F) *Melonis barleeanus* concentration (#/gm); (G) *Cassidulina carinata* concentration (#/gm).

6.4.4 Termination I: the Holocene

The diverse Holocene benthic foraminifera assemblage is somewhat bipolar in terms of characteristics; on the one hand, species such as *E. exigua*, *A. weddellensis*, *C. carinata* and *M. barleeanus* indicate significant fluxes of phytodetrital material (Sun et al., 2006; Zarriess and Mackensen, 2010), yet *O. umbonatus* and *P. bulloides* suggest an oligotrophic environment (Burke et al., 1993; Katz and Thunell, 1984). I suggest these two seemingly incompatible observations indicate a low productivity background punctuated by short seasonal pulses of high productivity.

I propose that the transition to a more diverse benthic assemblage at 12 ka may be linked to increases in eustatic sea level. Sea level reconstructions suggest a rapid rise in sea level of ~40 m across the Antarctic Cold Reversal (14-12 ka) (Figure 6.10c; Lambeck et al. 2014). This increase in sea level may have resulted in important regional changes in the flow of nutrient-rich sub-surface water during this time. In particular, the flooding of the Patagonian Shelf as a result of increases in sea level could lead to a greater scavenging of nutrients from the water column. The modern Falkland Current flows over the North Scotia Ridge in two locations, the main branch flows to the east of Burdwood Bank whilst the other, less-dense class of AAIW (Piola and Gordon, 1989), flows out in between Burdwood Bank and Isla Estados. The flow of this less-dense branch of the Falkland Current is important in supplying nutrients to the surface waters above site GC528/642. During sea level lowstands, the flow of this less dense class of AAIW between Burdwood Bank and Isla Estados is restricted (Section 5.4.2), and flow is directed around the east of Burdwood Bank. As sea level increases, a greater proportion of the less-dense class of AAIW (important for supplying nutrients to the surface waters) flows along the western branch, passing over the Patagonian continental shelf where high surface productivity strips out key nutrients (Paparazzo et al., 2010), limiting the available nutrients downstream at GC528/642 (Figure 6.11).

The idea of an increase in nutrient utilisation within surface waters in this region is consistent with the record of organic carbon $\delta^{13}C$ from GC528. Between 15-14 ka, there is a 1.5‰ positive excursion in the $\delta^{13}C_{\mathrm{TOC}}$ across the ACR (Figure 6.10b). Highly productive surface waters upstream of GC528 would result in a net increase in the $\delta^{13}C$ of DIC in the surface water. Thus, the signature of organic carbon formed further downstream in equilibrium with the surface waters will record this enriched $\delta^{13}C$ signal. However, it is also possible that the shift in $\delta^{13}C_{\mathrm{TOC}}$ could relate to a change in the dominant type of phytoplankton. As I discussed in Section 6.3.2, there is evidence of an increase in the dominance of coccolithophores (and potentially an increase in diatom abundance) at 12 ka.

In summary, I propose that the Holocene benthic foraminiferal assemblage provides evidence of highly seasonal surface productivity in the southwest Atlantic shelf environment. I argue that an increase in sea level resulted in the re-routing of the nutrient-bearing, low-density class of AAIW over the Patagonian Shelf which likely played a major role in setting this strong seasonality. As a greater proportion of the nutrient-rich surface waters, which were ultimately destined for GC528/642, passed over the Patagonian shelf, highly productive surface waters stripped out much of the nutrients before they reach site GC528/642. Thus, high productivity can only be sustained in relatively short highly-seasonal blooms.

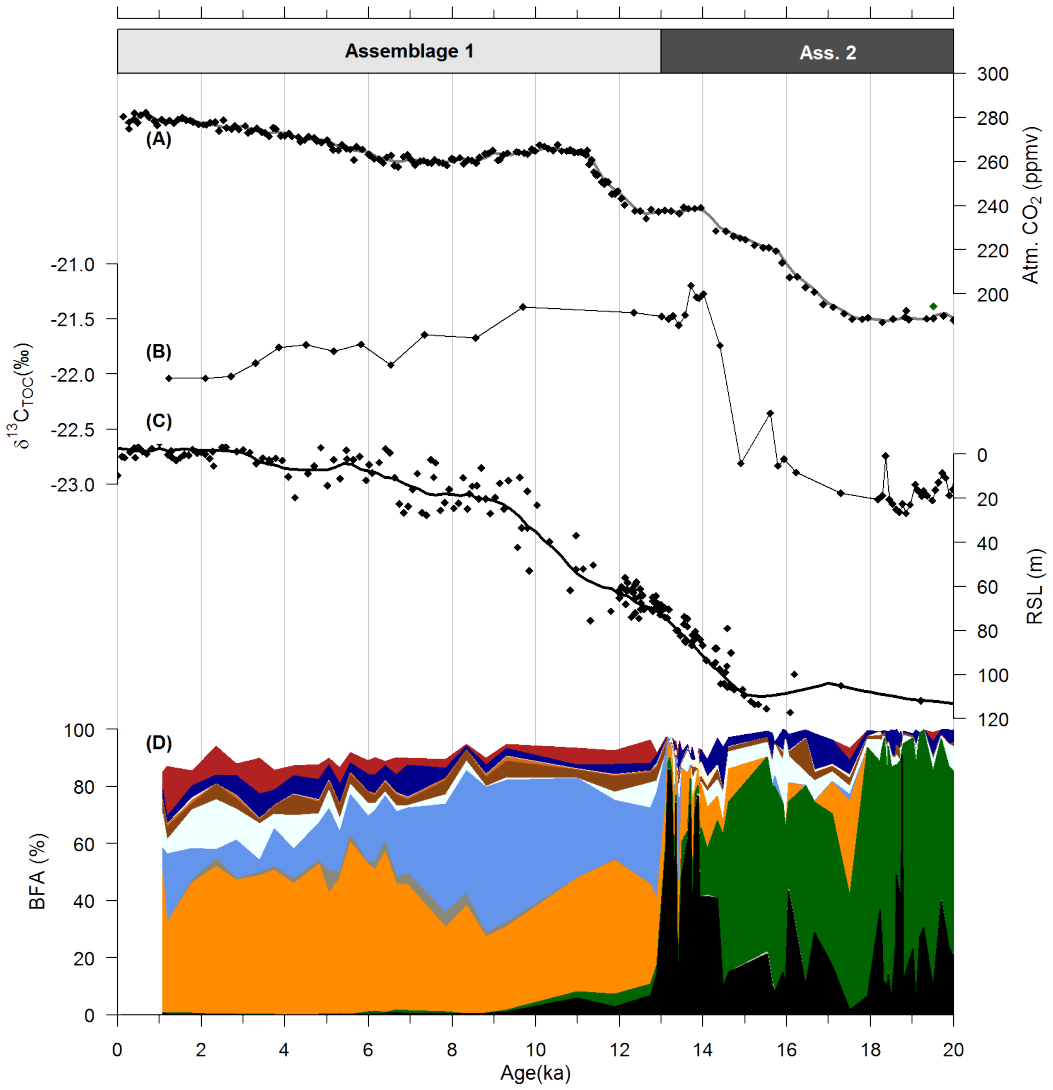

Figure 6.10: Change in seasonality of productivity during the Holocene. (A) Antarctic CO_2 compilation (Vostok, Petit et al. 1999, red; EDC, Monnin et al. 2004, black; Byrd, Ahn and Brook 2008, green); (B) Total organic carbon (TOC) $\delta^{13}C$; (C) Relative sea level change from global compilation (Lambeck et al., 2014); (D) Benthic foraminifera assemblage changes at the onset of the Holocene. Different species indicated by colours, which are the same as Figure 6.5.

6.4.5 Termination I: Summary

In summary, the benthic foraminifera assemblage DCA identifies three main assemblages across Termination I. In the previous discussion I have compared the changes in the benthic foraminifera assemblage with other proxy records from site GC528 in order to understand the main environmental factors driving these benthic foraminifera assemblage changes, which are summarised in Figure 6.11.

I suggest that the main difference between the glacial and interglacial assemblages relates to changes in sea level. A deglacial increase in sea level results in the flooding of the shallow Patago-

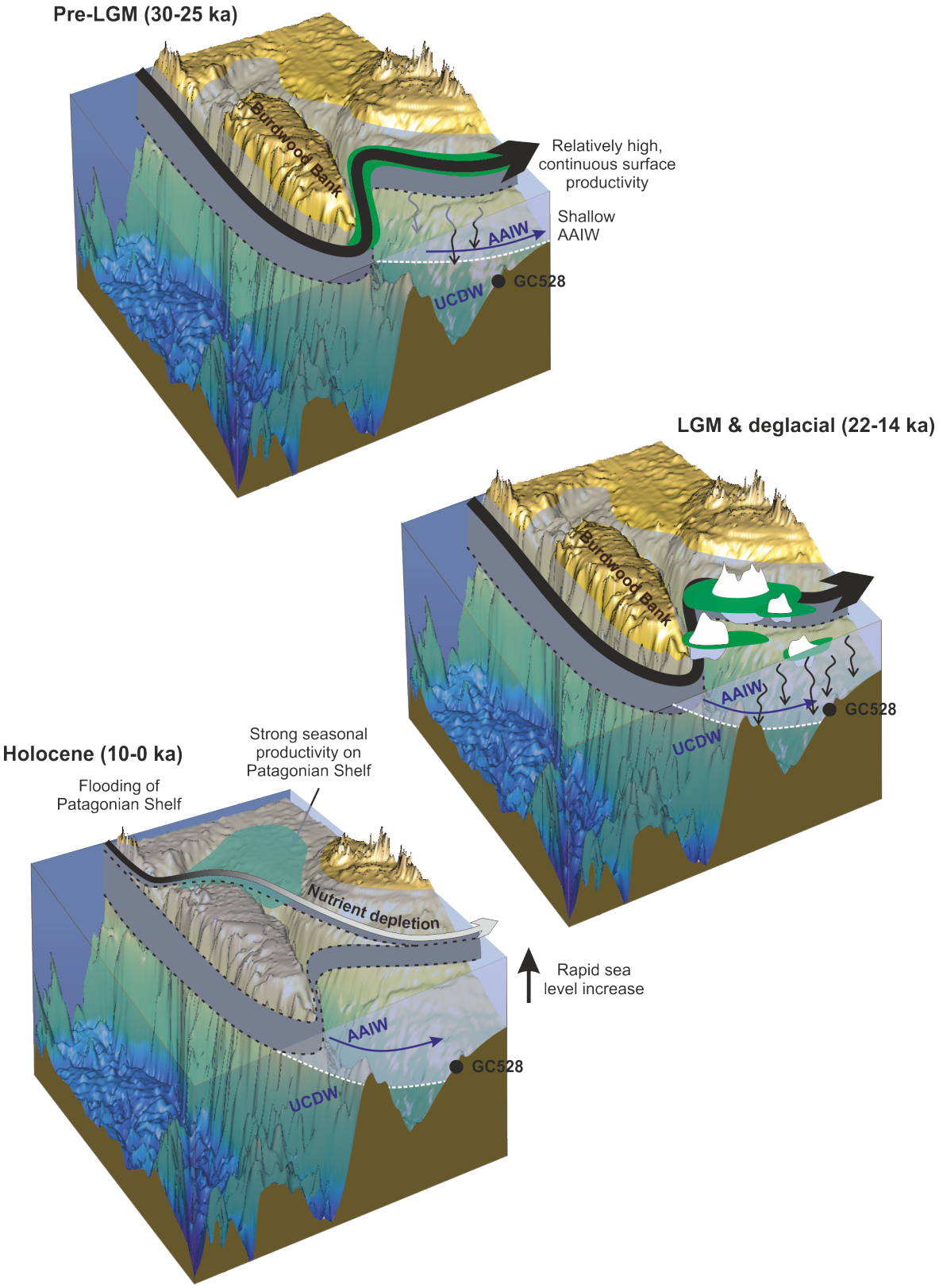

Figure 6.11: Schematic representation of the changes in the southwest Atlantic over Termination I. N.B. The location of GC528 has been projected onto the N-S vertical plane.

nian Shelf, stimulating productivity in this region. The increase in productivity strips out nutrients from the surface ocean resulting in highly seasonal patterns of productivity in the region. In contrast, productivity at GC528 during the glacial period was generally higher and associated with the upwelling of nutrient-rich waters along the sub-Antarctic Front.

Prior to the LGM, there is evidence of a significantly different benthic assemblage to that of the LGM and last deglaciation. Additionally, the pre-LGM assemblage shows evidence of partial dissolution. I suggest that the assemblage change at 25 ka may be related to an increase in surface productivity stimulated by an influx of IRD to the region. An increase in phytodetrital flux to the sediment results in *F. fusiformis* out-competing *B. aculeata.* The dissolution associated with the *B. aculeata* assemblage may reflect significant oxic remineralisation during this time, or a shoaling of AAIW. In contrast, there is no evidence of partial dissolution in the *F. fusiformis* assemblage, which I suggest may be the result of a change from oxic respiration to nitrate or sulphate respiration driven by a lack of oxygen available in the porewaters. The decrease in oxygen is linked to an increase in sediment accumulation rate and/or a decrease in bottom current flow speeds during this time.

6.5 Conclusion

The 'productivity' records discussed in this chapter generally indicate a significant glacial-interglacial change in the seasonality of surface ocean productivity in the southwest Atlantic. However, inferring the magnitude of the glacial-interglacial change in productivity, or even the sense of change has proved problematic.

In general, the benthic foraminifera assemblage changes indicate that there was a greater, or more continual, export flux of organic carbon during glacial periods relative to interglacial periods. However, deconvolving seasonality from quantity is difficult based on benthic foraminifera assemblages alone.

Other 'productivity' proxies that have been assessed in this chapter include carbonate proxies such as benthic foraminifera mass accumulation rate and total carbonate mass accumulation rate. However, these carbonate-based proxies in these shallow shelf sediments are largely driven by changes in the number of benthic foraminifera and therefore are only indirectly related to surface ocean productivity. Organic-based proxies such as alkenone and TOC mass accumulation rates can provide a means of assessing changes in productivity. However, there is the concern when expressing data as mass accumulation rates that inaccuracies in the age model can bias the records of 'productivity'. On that basis, I recommend using the ratio of alkenone to total organic carbon accumulation to avoid this difficulty. The alkenone:TOC ratio at site GC528/642 shows a consistent glacial-interglacial pattern of higher alkenone:TOC ratio during interglacials, and elevated $\delta^{13}C_{\mathrm{TOC}}$. This likely reflects a change in the dominance of coccolithophores in driving net primary productivity during interglacial periods. This change in the type of net primary productivity could have significant implications for this region's ability to uptake atmospheric CO_2. A deglacial increase in coccolithophore production relative to other non-carbonate based primary productivity would lead to an increase in carbonate export relative to organic carbon. An increase in the $CaCO_3/C_{org}$ rain ratio will decrease alkalinity relative to DIC, and thus reduce the surface ocean's ability to uptake CO_2 (Archer and Maier-Reimer, 1994). Given that the Patagonian Shelf

is today one of the most important regions in terms of the uptake of CO_2, this implies that during glacial times the uptake of CO_2 was potentially even greater. Based on this logic, I suggest that these sub-Antarctic shelf regions played a significant role in drawing down CO_2 from the atmosphere during glacial times through alterations of the $CaCO_3/C_{org}$ rain ratio. However, it is important to note that the $CaCO_3/C_{org}$ recorded in the sediment may not reflect surface productivity $CaCO_3/C_{org}$ (Ridgwell, 2003). Furthermore, I emphasise the need to validate that the trends observed in this site are representative of the sub-Antarctic shelf region as a whole.

Chapter 7

Conclusion

The work presented in this thesis has attempted to develop a greater understanding of the relative importance of different processes within the South Atlantic in terms of regulating the amount of CO_2 stored within the deep ocean on glacial-interglacial timescales. In particular, I have focussed on the last two glacial terminations. This final chapter discusses the new developments that this work has provided to the state of knowledge regarding glacial terminations and the remaining questions that require further attention.

7.1 Density stratification of the South Atlantic

One of the key questions that I endeavoured to answer during this study is *'What role does deep ocean density play in storing CO_2 in the deep ocean during glacial periods?'*. There are two aspects of this question that I have addressed in this thesis; in Chapter 4 I evaluate how strong stratification in the South Atlantic may prevent CO_2 from being released to the atmosphere, and in Chapter 5 I assessed the implications of a change in the vertical structure of the ACC on global overturning circulation.

In Chapter 4, I make the first reconstruction of the density evolution of the deep and intermediate South Atlantic using paired Mg/Ca-$\delta^{18}O$ measurements on benthic foraminifera. I find the surprising result that the temperature of the deep ocean was warmer than the intermediate ocean during the LGM. I argue that this temperature difference must be balanced by a strong salinity gradient. My reconstructions of seawater salinity (based on $\delta^{18}O_w$) suggest that the temperature 'inversion' was more than compensated by salinity differences, and in fact the deep ocean was 2-3 psu more saline than it is today. This finding is consistent with reconstructions of LGM salinity based on porewater profile modelling (Adkins et al., 2002).

The new insight that this work provides over the porewater studies is that we can now reconstruct the *evolution* of seawater density over the last deglaciation, rather than just the LGM timeslice. This allows us to be able to assess the relative timing of the changes in the ocean density gradient relative to the chemical gradient ($\delta^{13}C$ and ^{14}C). I find that the breakdown in the deep ocean density gradient significantly lags the breakdown in the chemical divide and the rise in atmospheric CO_2 suggesting that deep ocean density destratification does not play a major role in driving the deglacial rise in atmospheric CO_2. This is a significant finding as previously it was assumed

that changes in deep ocean density were paralleled by the deep ocean chemical gradient, and thus a decrease in deep ocean density was linked to the deglacial rise in atmospheric CO_2 (Toggweiler, 1999). My data clearly shows that the physical properties of the deep ocean and its chemical properties are decoupled across the last deglaciation, challenging this previous assumption. I propose that the chemical properties of the deep ocean are set by the efficiency of air-sea gas exchange in the Southern Ocean, whilst the physical properties of the ocean are controlled by the modes of deep water formation (brine rejection versus iceshelf water formation). However, I emphasise that these mechanisms are highly speculative, and require both model and proxy data to substantiate these claims.

Whilst the decrease in deep ocean density does not appear to driving the deglacial increase in atmospheric CO_2, I suggest that it may still be important in 'locking in' the interglacial climate state, by preventing the ocean from restocking its CO_2 inventory. It would be interesting to explore this idea further by generating longer records of deep ocean density across multiple glacial terminations, to observe the timing of deep ocean density destratification across the various Pleistocene glacial terminations, which all have slight differences in the magnitude and duration of the warming trend. Additionally, the last glacial period (MIS4-2), a time of generally cool global mean temperatures featuring several abrupt millennial-scale variations, would be a fascinating time period to study if, and how, deep ocean density variations are linked to these rapid changes in global temperature and atmospheric CO_2.

In Chapter 5, I discuss the role that the density structure of the ocean may have had on global overturning circulation. In particular, I suggest that the density structure of the ACC may be important for enabling the Antarctic Circumpolar Fronts to migrate. A long-standing controversy in oceanography is the fact that palaeo-oceanographers infer large changes in the position of the ACC fronts during the last glacial period (e.g. Gersonde et al., 2005; Kaiser et al., 2005); however, the significant barotropic component of the modern ACC means that the position of the fronts are locked in position by bottom topography (Graham et al., 2012). My reconstructions of South Atlantic density appear to reconcile these two distinct schools of thought. If the deep South Atlantic was significantly more dense than the overlying intermediate water during the glacial periods, it might imply that ACC flow was more baroclinic. In a more baroclinic flow, jets are surface-localised and thus are more able to move in response to changes in the overlying wind (Allison et al., 2010) or buoyancy forcing (Hogg, 2010). In summary, a major reorganisation of the vertical density structure of the ACC likely has implications for the ability of the ACC fronts to migrate due to changes in the wind and buoyancy forcing.

However, I emphasise that I have reconstructed seawater density at just two sites which are separated both zonally and in depth. Further work is required to determine whether the patterns observed in the South Atlantic are replicated in the South Pacific and Indian Oceans, and it is also important to better constrain changes in the depth of the main pycnocline over the last glacial termination. Ideally, I would look to carry out a similar study on a depth transect in order to understand not only the large-scale breakdown in the density gradient, but also variations in the depth of the main pycnocline. Changes in the pycnocline depth relative to rough topography have been suggested to be important in terms of generating turbulent mixing in the water column (Ferrari et al., 2014), and thus could be important for regulating the ocean's ability to store CO_2, an aspect that cannot be assessed by my reconstruction of deep and intermediate water density.

7.2 Cold water route

Oceanic gateways act as major 'choke-points' in the circulation of water around the global ocean. Understanding changes in the transport of water through these important regions is fundamental for determining the stability of the ocean conveyor. The Drake Passage is an important pathway for the return of cold, low-salinity Antarctic Intermediate Water (AAIW) into the Atlantic. The export of AAIW into the Atlantic is considered to be a critical stabilising component of global overturning circulation, providing a negative salinity feedback to counter a slowing of Atlantic Meridional Overturning Circulation (AMOC) (Keeling and Stephens, 2001; Rickaby and Elderfield, 2005). In Chapter 5, I reconstructed changes bottom current speeds within Drake Passage over the last two glacial terminations, with particular focus on the high resolution record across the T-I. As I discussed in Section 7.1, one of the interesting findings to come out of this chapter is the observation that ACC flow appears to be strongly linked to changes in its density structure. Strong reductions in bottom current flow speeds at the northern margin of Drake Passage during the last glacial are likely the result of a northward migration of the SAF such that it did not flow through Drake Passage but instead was truncated by South America, similar to the modern STF. Across T-I, the timing of the switch in the SAF to flow through the Drake Passage during the Bølling-Allerød appears to coincide with a reinvigoration of AMOC (Barker et al., 2010; Knorr and Lohmann, 2003; Skinner et al., 2013). This suggests that a greater through-flow of AAIW into the Atlantic sets up a strong intermediate meridional density gradient which promotes a greater southward deep circulation in the Atlantic.

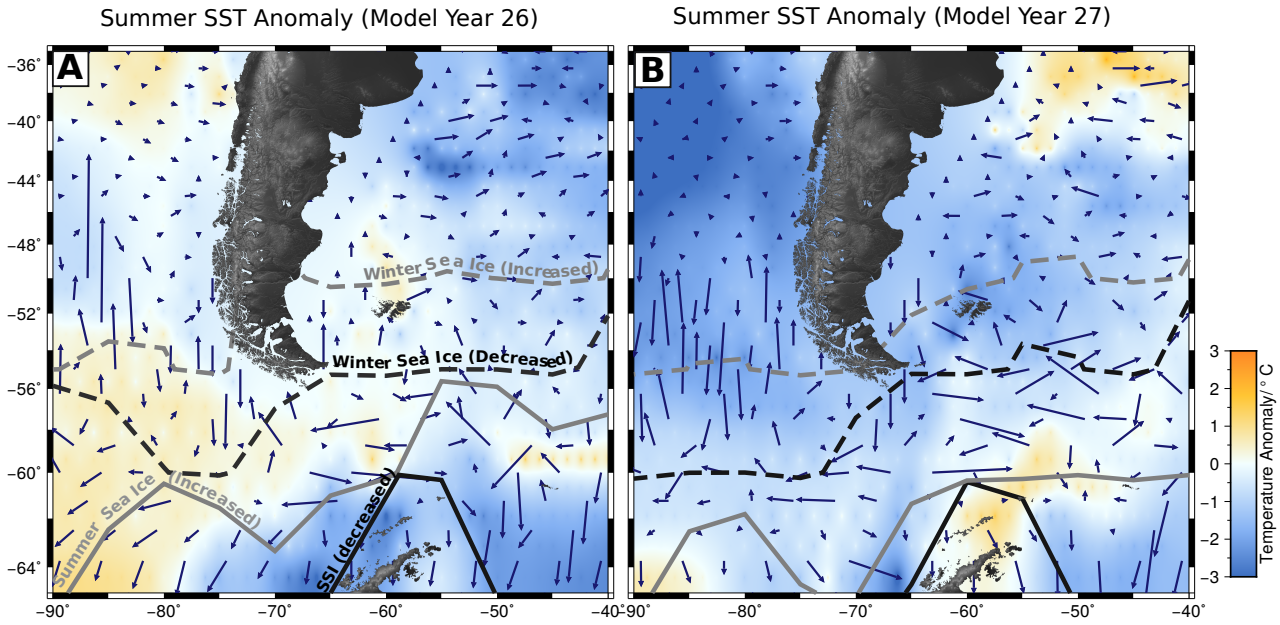

Figure 7.1: Model simulations of summer SST anomaly (Increased-Decreased) as a result of changes in Antarctic sea ice extent. Surface velocity anomaly vectors are shown as blue arrows. The position of the summer (solid) and winter (dashed) sea ice margins are shown for both simulations (Increased simulation = grey; Decrease simulation = black); (A) Model Year 26; (B) Model Year 27.

Superimposed onto the larger glacial-interglacial ACC flow speed variability occurring across T-I, are several abrupt millennial-scale events at the end of the last glacial period. Remarkable anti-phased SSTs in the southwest Atlantic and the southeast Pacific are observed at the end of the last glacial period, and are likely linked to variations in the through-flow of water through Drake Passage (Lamy et al., 2015). I argue that these millennial-scale reductions in Drake Passage through-flow are likely related to the expansion of Antarctic sea ice leading to northward migration of the PF and pronounced reductions in cold water flowing through the Drake Passage. Shallow stratification of the surface ocean related to melting of winter sea ice may further amplify summer SSTs recorded by alkenones during this time.

This interpretation is somewhat undermined by the alkenone-SSTs records across T-II which suggest that similar anti-phased SSTs also occurring during the Last Interglacial climatic optimum. During this time, SSTs upstream of Drake Passage were ~8^{o}C, clearly too warm for sea ice to be present. Interestingly, this interval of warming SSTs in the southwest Atlantic and cooling in the southeast Pacific is synchronous with a major pulse of IRD at site GC528, potentially related to the collapse of the West Antarctic Ice Sheet. The presence of IRD during the Last Interglacial climatic optimum highlights the possibility that there may be multiple mechanisms which result in the anti-phased SSTs at either end of Drake Passage. Certainly warm alkenone-SSTs appear to be related to surface stratification, but whether this stratification is related to the melting of sea ice (as I suspect is the case during MIS2), or to the melting of continentally-derived ice, remains unknown. An interesting follow up to this study would be to determine the source of the inferred meltwater lid either through a provenance study of the IRD deposited during the Last Interglacial or by measuring alkenone δD, which can determine the source of the freshwater signal.

The anti-phased SST relationship between the southwest Atlantic and the southeast Pacific is a striking feature of the end of the last glacial period. Recently, I have been working with Max Holloway (British Antarctic Survey) to test the hypothesis that anti-phased SSTs are the result of an expansion in Antarctic sea ice using a fully-coupled general circulation model. We use HadCM3 under LGM boundary conditions and apply a small negative/positive heat flux to the surface ocean to promote ('Increased' simulation) or reduce ('Decreased' simulation) the growth of Antarctic sea ice relative to an 'unforced' LGM simulation. This work is in very early stages, however the preliminary results suggest that it is possible to produce a weak anti-phasing in the summer SST anomaly between the southeast Pacific and the southwest Atlantic by increasing Antarctic sea ice extent in the Drake Passage region [Figure 7.1a]. However, the model also produces significant inter-annual variability in the summer SST anomaly [Figure 7.1a-b]. These strong variations in the summer SST anomaly appear to linked to a change in the meridional surface transport upstream of the Drake Passage - supporting the idea that a reduction in Drake Passage through-flow can result in strong cooling in the southeast Pacific (Lamy et al., 2015) and warming in the southwest Atlantic (Chapter 5). We are currently investigating to see how robust these model results are by running longer simulations; however, these initial results appear to be broadly consistent with the ideas presented in Chapter 5.

7.3 The sub-Antarctic shelf biological pump

In Chapter 6, I used a multi-proxy approach to reconstruct glacial-interglacial changes in productivity in the sub-Antarctic shelf regions over the last two glacial terminations. In the modern ocean, the Patagonian Shelf has one of the highest rates of primary production in the global ocean and therefore acts as an important pathway for CO_2 to get into the interior ocean. Understanding how this might have changed over glacial terminations adds an important piece in the puzzle of reconstructing changes in the global carbon budget on glacial-interglacial timescales.

The results from this chapter have shown that there are significant changes in productivity over the glacial terminations, although quantifying the change in organic carbon and carbonate export in this region is problematic. In general, there is an increase in carbonate burial and a decrease in organic carbon burial over the glacial terminations. I argue that these observations can be reconciled by invoking a change in the dominant type of primary producer. Further work to characterise the exact changes in the type of primary producer, in particular, a thorough analysis of diatom assemblages is required. However, if the $CaCO_3$:C_{org} ratio within the sediment is reflective of changes in surface productivity, it suggests a much greater potential for the ocean to draw down CO_2 from the atmosphere during glacial times. Given that the Patagonian Shelf is a major sink of atmospheric CO_2 today, my results would suggest that this CO_2 sink was potentially even greater during glacial times.

I use benthic foraminifera assemblages to better understand the drivers of changes in surface ocean productivity over the last two glacial terminations, focusing in particular on the well-preserved high-resolution sequence spanning the last deglaciation. The major shifts in benthic foraminifera assemblage appear to be driven by changes in the type and seasonality of organic matter exported to the sediment. I suggest that the major shift glacial to interglacial assemblage transition is driven by a change in seasonality of productivity, triggered by a sea level rise which results in the least dense classes of AAIW (the main inflow of nutrient-rich water) being channelled over the Patagonian Shelf, where highly productive surface water strips out key nutrients. This interpretation places a strong emphasis on the importance of eustatic flooding of the shallow shelf regions in driving the main glacial-interglacial change in productivity.

I also note that the end of the last glacial period is characterised by highly opportunistic benthic foraminifera that are suggestive of high rates of organic carbon export to the sediment and low oxygen concentrations. Interestingly, the inferred increase in organic carbon burial coincides with an increase in IRD in the region, and thus I conclude that productivity stimulated by the melting of icebergs may be responsible for the increase in organic carbon burial. This is contrary to many studies from the sub-Antarctic that place a strong emphasis on iron fertilisation by Patagonian dust. Site GC528 lies immediately downwind of Patagonia, and yet the pattern of productivity does not appear to coincide with changes in dust expressed in Antarctic ice core records. This discrepancy either indicates that the Antarctic dust records are recording dust signals from other regions in addition to Patagonia or that Patagonian dust is not a major driver stimulating surface productivity during glacial periods. I emphasise that these conclusions are based on observation from one core location that may not be representative of the sub-Antarctic shelf regions as a whole. Therefore, further work is needed to test whether the changes observed in GC528/642 are replicated in other, more globally distributed, sub-Antarctic sites.

7.4 General Summary

Based on the observations of the oceanographic changes in the South Atlantic across Termination I and II, I draw the following conclusions:

1. Changes in the density of the deep South Atlantic are not the direct cause of the deglacial increase in atmospheric CO_2. I suggest air-sea gas exchange in the Southern Ocean may play an more important role in driving the increase in atmospheric CO_2.

2. If the density structures that I observe in the South Atlantic can be applied to the Antarctic Circumpolar Current, it suggests a major re-organisation of the vertical structure during glacial periods relative to the modern. This has implications for the ability of the ACC fronts to migrate latitudinally.

3. Abrupt anti-phased SST variations either side of Drake Passage appear to be related to the presence of meltwater in the surface ocean, although it is not apparent whether it is sea ice- or glacially-derived. These events appear to have little impact on AMOC.

4. The benthic foraminifera community in the southwest Atlantic appear to be strongly controlled by changes in the source and seasonality of organic carbon exported to the sediment, which in turn is controlled by Drake Passage through-flow and the eustatic flooding of the Patagonian Shelf.

5. Patagonian dust does not appear to be the main driver of the increase in surface productivity in the southwest Atlantic during the last glacial period. I suggest that the melting of icebergs is potentially more important in fertilising surface waters in the sub-Antarctic zone.

6. Significant changes in the dominant primary producer over the Patagonian Shelf occur over the last two glacial terminations that reduce the surface ocean's ability to uptake CO_2 during interglacial periods. Primary productivity over shallow shelf regions in the sub-Antarctic is likely an important player in driving the glacial-interglacial changes in pCO_2.

References

Adkins, J. F. (2013). The role of deep ocean circulation in setting glacial climates. *Paleoceanography*, 28(3):539–561.

Adkins, J. F., Ingersoll, A. P., and Pasquero, C. (2005). Rapid climate change and conditional instability of the glacial deep ocean from the thermobaric effect and geothermal heating. *Quaternary Science Reviews*, 24(5-6):581–594.

Adkins, J. F., McIntyre, K., and Schrag, D. P. (2002). The salinity, temperature, and δ^{18}O of the glacial deep ocean. *Science*, 298(5599):1769–73.

Ahn, J. and Brook, E. J. (2008). Atmospheric CO_2 and climate on millennial time scales during the last glacial period. *Science*, 322(5898):83–5.

Ahn, J. and Brook, E. J. (2014). Siple Dome ice reveals two modes of millennial CO_2 change during the last ice age. *Nature communications*, 5:3723.

Allen, C. S., Pike, J., and Pudsey, C. J. (2011). Last glacial-interglacial sea-ice cover in the SW Atlantic and its potential role in global deglaciation. *Quaternary Science Reviews*, 30(19-20):2446–2458.

Allen, K. A., Sikes, E. L., Hönisch, B., Elmore, A. C., Guilderson, T. P., Rosenthal, Y., and Anderson, R. F. (2015). Southwest pacific deep water carbonate chemistry linked to high southern latitude climate and atmospheric co_2 during the last glacial termination. *Quaternary Science Reviews*, 122:180–191.

Allison, L. C., Johnson, H. L., Marshall, D. P., and Munday, D. R. (2010). Where do winds drive the Antarctic Circumpolar Current? *Geophysical Research Letters*, 37(12).

Anand, P., Elderfield, H., and Conte, M. H. (2003). Calibration of Mg/Ca thermometry in planktonic foraminifera from a sediment trap time series. *Paleoceanography*, 18(2):1050.

Anderson, R., Kumar, N., Mortlock, R., Froelich, P., Kubik, P., Dittrich-Hannen, B., and Suter, M. (1998). Late-Quaternary changes in productivity of the Southern Ocean. *Journal of Marine Systems*, 17(1-4):497–514.

Anderson, R. F., Chase, Z., Fleisher, M. Q., and Sachs, J. (2002). The southern ocean's biological pump during the last glacial maximum. *Deep Sea Research Part II: Topical Studies in Oceanography*, 49(9):1909–1938.

Antoine, D., André, J.-M., and Morel, A. (1996). Oceanic primary production: 2. Estimation at global scale from satellite (Coastal Zone Color Scanner) chlorophyll. *Global Biogeochemical Cycles*, 10(1):57–69.

Archer, D. and Maier-Reimer, E. (1994). Effect of deep-sea sedimentary calcite preservation on atmospheric CO_2 concentration. *Nature*, 367(6460):260–263.

Barker, S., Greaves, M., and Elderfield, H. (2003). A study of cleaning procedures used for foraminiferal Mg/Ca paleothermometry. *Geochemistry, Geophysics, Geosystems*, 4(9).

Barker, S., Knorr, G., Vautravers, M. J., Diz, P., and Skinner, L. C. (2010). Extreme deepening of the atlantic overturning circulation during deglaciation. *Nature Geoscience*, 3(8):567–571.

Baumann, K.-H. and Freitag, T. (2004). Pleistocene fluctuations in the northern Benguela Current system as revealed by coccolith assemblages. *Marine Micropaleontology*, 52(1-4):195–215.

Bazin, L., Landais, A., Lemieux-Dudon, B., Toyé Mahamadou Kele, H., Veres, D., Parrenin, F., Martinerie, P., Ritz, C., Capron, E., Lipenkov, V. Y., Loutre, M.-F., Raynaud, D., Vinther, B. M., Svensson, A., Rasmussen, S. O., Severi, M., Blunier, T., Leuenberger, M., Fischer, H., Masson-Delmotte, V., Chappellaz, J. A., and Wolff, E. W. (2013). The Antarctic ice core chronology (AICC2012). *Climate of the Past*, 9:1715–1731.

Becquey, S. and Gersonde, R. (2002). Past hydrographic and climatic changes in the Subantarctic Zone of the South Atlantic - The Pleistocene record from ODP Site 1090. *Palaeogeography, Palaeoclimatology, Palaeoecology*, 182(3-4):221–239.

Benthien, A. and Müller, P. J. (2000). Anomalously low alkenone temperatures caused by lateral particle and sediment transport in the Malvinas Current region, western Argentine Basin. *Deep Sea Research Part I: Oceanographic Research Papers*, 47(12):2369–2393.

Bereiter, B., Luthi, D., Siegrist, M., Schupbach, S., Stocker, T. F., and Fischer, H. (2012). Mode change of millennial CO_2 variability during the last glacial cycle associated with a bipolar marine carbon seesaw. *Proceedings of the National Academy of Sciences*, 109(25):9755–9760.

Berger, A. L. (1978). Long-Term Variations of Daily Insolation and Quaternary Climatic Changes. *Journal of Atmospheric Sciences*, 35:2362–2367.

Berner, R. (1971). *Principles of Chemical Sedimentology*. New York.

Bianchi, A. A., Pino, D. R., Perlender, H. G. I., Osiroff, A. P., Segura, V., Lutz, V., Clara, M. L., Balestrini, C. F., and Piola, A. R. (2009). Annual balance and seasonal variability of sea-air CO_2 fluxes in the Patagonia Sea: Their relationship with fronts and chlorophyll distribution. *Journal of Geophysical Research*, 114(C3):C03018.

Bianchi, C. and Gersonde, R. (2002). The Southern Ocean surface between Marine Isotope Stages 6 and 5d: Shape and timing of climate changes. *Palaeogeography, Palaeoclimatology, Palaeoecology*, 187(1-2):151–177.

Bianchi, G., Hall, I., McCave, I., and Joseph, L. (1999). Measurement of the sortable silt current speed proxy using the Sedigraph 5100 and Coulter Multisizer IIe: precision and accuracy. *Sedimentology*, 46(6):1001–1014.

Blaauw, M. and Christen, J. A. (2011). Flexible paleoclimate age-depth models using an autoregressive gamma process. *Bayesian Analysis*, 6(3):457–474.

Boehme, L., Meredith, M. P., Thorpe, S. E., Biuw, M., and Fedak, M. (2008). Antarctic Circumpolar Current frontal system in the South Atlantic: Monitoring using merged Argo and animal-borne sensor data. *Journal of Geophysical Research*, 113(C9):C09012.

Bollmann, J., Baumann, K.-H., and Thierstein, H. R. (1998). Global dominance of *Gephyrocapsa* coccoliths in the Late Pleistocene: Selective dissolution, evolution, or global environmental change? *Paleoceanography*, 13(5):517–529.

Bouttes, N., Paillard, D., and Roche, D. M. (2010). Impact of brine-induced stratification on the glacial carbon cycle. *Climate of the Past*, 6(5):575–589.

Boyle, E. A. (1988). The role of vertical chemical fractionation in controlling late Quaternary atmospheric carbon dioxide. *Journal of Geophysical Research*, 93(C12):15701–15714.

Bradley, S., Siddall, M., Milne, G., Masson-Delmotte, V., and Wolff, E. (2012). Where might we find evidence of a Last Interglacial West Antarctic Ice Sheet collapse in Antarctic ice core records? *Global and Planetary Change*, 88-89:64–75.

Brodniewicz, I. (1965). Recent and some Holocene Foraminifera of the southern Baltic Sea. *Acta Palaeontologica Polonica*, 10(2):131–226.

Broecker, W. S. (1982). Ocean chemistry during glacial time. *Geochimica et Cosmochimica Acta*, 46(10):1689–1705.

Broecker, W. S. and Peng, T.-H. (1974). Gas exchange rates between air and sea. *Tellus*, 26(1-2):21–35.

Broecker, W. S. and Peng, T.-H. (1987). The oceanic salt pump: Does it contribute to the glacial-interglacial difference in atmospheric CO_2 content? *Global Biogeochemical Cycles*, 1(3):251–259.

Broecker, W. S. and van Donk, J. (1970). Insolation changes, ice volumes, and the δ^{18}O record in deep-sea cores. *Reviews of Geophysics*, 8(1):169–198.

Bryan, S. P. and Marchitto, T. M. (2008). Mg/Ca-temperature proxy in benthic foraminifera: New calibrations from the Florida Straits and a hypothesis regarding Mg/Li. *Paleoceanography*, 23(2):PA2220.

Burke, A. and Robinson, L. F. (2012). The Southern Ocean's role in carbon exchange during the last deglaciation. *Science*, 335(6068):557–61.

Burke, S. K., Berger, W. H., Coulbourn, W. T., and Vincent, E. (1993). Benthic foraminifera in box core ERDC 112, Ontong Java Plateau. *The Journal of Foraminiferal Research*, 23(1):19–39.

Caniupán, M., Lamy, F., Lange, C. B., Kaiser, J., Arz, H., Kilian, R., Baeza Urrea, O., Aracena, C., Hebbeln, D., Kissel, C., Laj, C., Mollenhauer, G., and Tiedemann, R. (2011). Millennial-scale sea surface temperature and Patagonian Ice Sheet changes off southernmost Chile (53^oS) over the past 60 kyr. *Paleoceanography*, 26(3):PA3221.

Capron, E., Govin, A., Stone, E. J., Masson-Delmotte, V., Mulitza, S., Otto-Bliesner, B., Rasmussen, T. L., Sime, L. C., Waelbroeck, C., and Wolff, E. W. (2014). Temporal and spatial structure of multi-millennial temperature changes at high latitudes during the Last Interglacial. *Quaternary Science Reviews*, 103:116–133.

Catherine, J. P., Jean Francois, S., Marie Jose, U., and Giraudeau (2001). Stable isotope record of the last 500 k.y. at Site 1087 (Southern Cape Basin). *Proceedings of the Ocean Drilling Program, Scientific Results, College Station, TX (Ocean Drilling Program)*, 175:1–22.

Cheng, H., Adkins, J., Edwards, R., and Boyle, E. A. (2000). U-Th dating of deep-sea corals. *Geochimica et Cosmochimica Acta*, 64(14):2401–2416.

CLIMAP Project Members (1984). The Last Interglacial Ocean. *Quaternary Research*, 21:123–224.

Collins, L. G., Pike, J., Allen, C. S., and Hodgson, D. A. (2012). High-resolution reconstruction of southwest Atlantic sea-ice and its role in the carbon cycle during marine isotope stages 3 and 2. *Paleoceanography*, 27(3):PA3217.

Combes, V. and Matano, R. P. (2014). A two-way nested simulation of the oceanic circulation in the Southwestern Atlantic. *Journal of Geophysical Research: Oceans*, 119(2):731–756.

Dammshäuser, A., Wagener, T., and Croot, P. L. (2011). Surface water dissolved aluminum and titanium: Tracers for specific time scales of dust deposition to the Atlantic? *Geophysical Research Letters*, 38(24).

DaSilva, J. L., Anderson, J. B., and Stravers, J. (1997). Seismic facies changes along a nearly continuous 24^o latitudinal transect: the fjords of Chile and the northern Antarctic Peninsula. *Marine Geology*, 143(1-4):103–123.

de Baar, H. J. W., de Jong, J. T. M., Bakker, D. C. E., Löscher, B. M., Veth, C., Bathmann, U., and Smetacek, V. (1995). Importance of iron for plankton blooms and carbon dioxide drawdown in the Southern Ocean. *Nature*, 373(6513):412–415.

de Lange, G., van Os, B., and Poorter, R. (1992). Geochemical composition and inferred accretion rates of sediments and managanese nodules from a submarine hill in the Madeira Abyssal Plain, eastern North Atlantic. *Marine Geology*, 109(1-2):171–194.

de Noblet, N. I., Prentice, I. C., Joussaume, S., Texier, D., Botta, A., and Haxeltine, A. (1996). Possible role of atmosphere-biosphere interactions in triggering the Last Glaciation. *Geophysical Research Letters*, 23(22):3191–3194.

de Pol-Holz, R., Keigwin, L., Southon, J., Hebbeln, D., and Mohtadi, M. (2010). No signature of abyssal carbon in intermediate waters off Chile during deglaciation. *Nature Geoscience*, 3(3):192–195.

de Vernal, A., Rosell-Melé, A., Kucera, M., Hillaire-Marcel, C., Eynaud, F., Weinelt, M., Dokken, T., and Kageyama, M. (2006). Comparing proxies for the reconstruction of LGM sea-surface conditions in the northern North Atlantic. *Quaternary Science Reviews*, 25(21-22):2820–2834.

de Villiers, S., Greaves, M., and Elderfield, H. (2002). An intensity ratio calibration method for the accurate determination of Mg/Ca and Sr/Ca of marine carbonates by ICP-AES. *Geochemistry Geophysics Geosystems*, 3(1).

Degens, E. (1969). Biogeochemistry of stable carbon isotopes. In Eglington, G. and Murphy, M., editors, *Organic Geochemistry: Methods and results*, pages 304–329. Springer.

Delmas, R. J., Ascencio, J.-M., and Legrand, M. (1980). Polar ice evidence that atmospheric CO_2 20,000 yr BP was 50% of present. *Nature*, 284(5752):155–157.

Eggins, S., Grün, R., Pike, A. W., Shelley, M., and Taylor, L. (2003). ^{238}U, ^{232}Th profiling and U-series isotope analysis of fossil teeth by laser ablation-ICPMS. *Quaternary Science Reviews*, 22(10-13):1373–1382.

Eggins, S. M., Grün, R., McCulloch, M. T., Pike, A. W., Chappell, J., Kinsley, L., Mortimer, G., Shelley, M., Murray-Wallace, C. V., Spötl, C., and Taylor, L. (2005). In situ U-series dating by laser-ablation multi-collector ICPMS: new prospects for Quaternary geochronology. *Quaternary Science Reviews*, 24(23-24):2523–2538.

Elderfield, H. and Ganssen, G. (2000). Past temperature and δ^{18}O of surface ocean waters inferred from foraminiferal Mg/Ca ratios. *Nature*, 405(6785):442–5.

Elderfield, H., Greaves, M., Barker, S., Hall, I., Tripati, A., Ferretti, P., Crowhurst, S., Booth, L., and Daunt, C. (2010). A record of bottom water temperature and seawater δ^{18}O for the Southern Ocean over the past 440 kyr based on Mg/Ca of benthic foraminiferal *Uvigerina spp*. *Quaternary Science Reviews*, 29(1-2):160–169.

Elmore, A. C., McClymont, E. L., Elderfield, H., Kender, S., Cook, M. R., Leng, M. J., Greaves, M., and Misra, S. (2015). Antarctic Intermediate Water properties since 400 ka recorded in infaunal (*Uvigerina peregrina*) and epifaunal (*Planulina wuellerstorfi*) benthic foraminifera. *Earth and Planetary Science Letters*, 428:193–203.

Farrington, J. W., Davis, A. C., Sulanowski, J., McCaffrey, M. A., McCarthy, M., Clifford, C., Dickinson, P., and Volkman, J. K. (1988). Biogeochemistry of lipids in surface sediments of the Peru Upwelling Area at 15°S. *Organic Geochemistry*, 13(4-6):607–617.

Ferrari, R., Jansen, M. F., Adkins, J. F., Burke, A., Stewart, A. L., and Thompson, A. F. (2014). Antarctic sea ice control on ocean circulation in present and glacial climates. *Proceedings of the National Academy of Sciences of the United States of America*, 111(24):8753–8758.

Fetterer, F., Knowles, K., Meier, W., and Savoie, M. (2002). Sea Ice Index, Version 1. National Snow and Ice Data Center.

Fischer, H., Fundel, F., Ruth, U., Twarloh, B., Wegner, A., Udisti, R., Becagli, S., Castellano, E., Morganti, A., Severi, M., Wolff, E., Littot, G., Röthlisberger, R., Mulvaney, R., Hutterli, M. A., Kaufmann, P., Federer, U., Lambert, F., Bigler, M., Hansson, M., Jonsell, U., de Angelis, M., Boutron, C., Siggaard-Andersen, M.-L., Steffensen, J. P., Barbante, C., Gaspari, V., Gabrielli, P., and Wagenbach, D. (2007). Reconstruction of millennial changes in dust emission, transport and regional sea ice coverage using the deep EPICA ice cores from the Atlantic and Indian Ocean sector of Antarctica. *Earth and Planetary Science Letters*, 260(1-2):635–636.

Fisher, R. A., Corbet, S. A., and Williams, C. B. (1943). The Relation Between the Number of Species and the Number of Individuals in a Random Sample of an Animal Population. *Journal of Animal Ecology*, 12(1):42–58.

Flores, J., Gersonde, R., and Sierro, F. (1999). Pleistocene fluctuations in the Agulhas Current Retroflection based on the calcareous plankton record. *Marine Micropaleontology*, 37(1):1–22.

Flores, J., Sierro, F., Francés, G., Vázquez, A., and Zamarreno, I. (1997). The last 100,000 years in the western Mediterranean: sea surface water and frontal dynamics as revealed by coccolithophores. *Marine Micropaleontology*, 29(3-4):351–366.

Flügge, A. (1997). Variabilität von ungesättigten C 37 Methylketonen (Alkenone) in Sinkstoffallenmaterial der Norwegischen See und deren Abbildung in Oberflächensedimenten. *PhD thesis*.

François, R., Altabet, M. A., Yu, E.-F. F., Sigman, D. M., Bacon, M. P., Frank, M., Bohrmann, G., Bareille, G., and Labeyrie, L. D. (1997). Contribution of Southern Ocean surface-water stratification to low atmospheric CO_2 concentrations during the last glacial period. *Nature*, 389(6654):929–936.

Francois, R., Honjo, S., Manganini, S. J., and Ravizza, G. E. (1995). Biogenic barium fluxes to the deep sea: Implications for paleoproductivity reconstruction. *Global Biogeochemical Cycles*, 9(2):289–303.

Frank, M., Gersonde, R., van der Loeff, M. R., Bohrmann, G., Nürnberg, C. C., Kubik, P. W., Suter, M., and Mangini, A. (2000). Similar glacial and interglacial export bioproductivity in the Atlantic Sector of the Southern Ocean: Multiproxy evidence and implications for glacial atmospheric CO 2. *Paleoceanography*, 15(6):642–658.

Freeman, E., Skinner, L. C., Reimer, R., Scrivner, A., and Fallon, S. (2016). Graphitization of small carbonate samples for paleoceanographic research at the Godwin Radiocarbon Laboratory, University of Cambridge. *Radiocarbon*, 58(1):89–97.

Freeman, K. H. and Wakeham, S. G. (1992). Variations in the distributions and isotopic composition of alkenones in Black Sea particles and sediments. *Organic Geochemistry*, 19(1-3):277–285.

Gersonde, R., Abelmann, A., Brathauer, U., Becquey, S., Bianchi, C., Cortese, G., Grobe, H., Kuhn, G., Niebler, H.-S., Segl, M., Siger, R., Zielinski, U., and Futterer, D. (2003). Last glacial sea surface temperatures and sea-ice extent in the Southern Ocean (Atlantic-Indian sector): A multiproxy approach. *Paleoceanography*, 18(3).

Gersonde, R., Crosta, X., Abelmann, A., and Armand, L. (2005). Sea-surface temperature and sea ice distribution of the Southern Ocean at the EPILOG Last Glacial Maximum - a circum-Antarctic view based on siliceous microfossil records. *Quaternary Science Reviews*, 24(7-9):869–896.

Goldstein, S. J., Lea, D. W., Chakraborty, S., Kashgarian, M., and Murrell, M. T. (2001). Uranium-series and radiocarbon geochronology of deep-sea corals: implications for Southern Ocean ventilation rates and the oceanic carbon cycle. *Earth and Planetary Science Letters*, 193(1-2):167–182.

Gooday, A. J. and Alve, E. (2001). Morphological and ecological parallels between sublittoral and abyssal foraminiferal species in the ne atlantic: a comparison of stainforthia fusiformis and stainforthia sp. *Progress in Oceanography*, 50(1):261–283.

Gooday, A. J. and Jorissen, F. J. (2012). Benthic foraminiferal biogeography: controls on global distribution patterns in deep-water settings. *Annual review of marine science*, 4:237–62.

Gottschalk, J., Skinner, L. C., and Waelbroeck, C. (2015). Contribution of seasonal sub-Antarctic surface water variability to millennial-scale changes in atmospheric CO_2 over the last deglaciation and Marine Isotope Stage 3. *Earth and Planetary Science Letters*, 411:87–99.

Graham, R. M., de Boer, A. M., Heywood, K. J., Chapman, M. R., and Stevens, D. P. (2012). Southern Ocean fronts: Controlled by wind or topography? *Journal of Geophysical Research*, 117(C8):C08018.

Hallberg, R. and Gnanadesikan, A. (2006). The Role of Eddies in Determining the Structure and Response of the Wind-Driven Southern Hemisphere Overturning: Results from the Modeling Eddies in the Southern Ocean (MESO) Project. *Journal of Physical Oceanography*, 36(12):2232–2252.

Harland, W. B. (1964). Critical evidence for a great infra-Cambrian glaciation. *Geologische Rundschau*, 54(1):45–61.

Hayward, B. W., Neil, H., Carter, R., Grenfell, H. R., and Hayward, J. J. (2002). Factors influencing the distribution patterns of Recent deep-sea benthic foraminifera, east of New Zealand, Southwest Pacific Ocean. *Marine Micropaleontology*, 46(1-2):139–176.

Herguera, J. C. and Berger, W. H. (1991). Paleoproductivity from benthic foraminifera abundance: Glacial to postglacial change in the west-equatorial Pacific. *Geology*, 19(12):1173–1176.

Hillenbrand, C.-D., Kuhn, G., Smith, J. A., Gohl, K., Graham, A. G. C., Larter, R. D., Klages, J. P., Downey, R., Moreton, S. G., Forwick, M., and Vaughan, D. G. (2012). Grounding-line retreat of the West Antarctic Ice Sheet from inner Pine Island Bay. *Geology*, 41(1):35–38.

Ho, S. L., Mollenhauer, G., Lamy, F., Martínez-Garcia, A., Mohtadi, M., Gersonde, R., Hebbeln, D., Nunez-Ricardo, S., Rosell-Melé, A., and Tiedemann, R. (2012). Sea surface temperature variability in the Pacific sector of the Southern Ocean over the past 700 kyr. *Paleoceanography*, 27(4).

Hodell, D., Charles, C., Curtis, J., Mortyn, P., Ninnemann, U., and Venz, K. (2003a). Data report: Oxygen isotope stratigraphy of ODP Leg 177 Sites 1088, 1089, 1090, 1093, and 1094. Technical report.

Hodell, D., Venz, K., Charles, C., and Ninnemann, U. (2003b). Pleistocene vertical carbon isotope and carbonate gradients in the South Atlantic sector of the Southern Ocean. *Geochemistry, Geophysics, Geosystems*, 4(1):1–19.

Hoefs, M. J. L., Versteegh, G. J. M., Rijpstra, W. I. C., de Leeuw, J. W., and Damsté, J. S. S. (1998). Postdepositional oxic degradation of alkenones: Implications for the measurement of palaeo sea surface temperatures. *Paleoceanography*, 13(1):42–49.

Hoffman, P. F. (1998). A Neoproterozoic Snowball Earth. *Science*, 281(5381):1342–1346.

Hogg, A. M. (2010). An Antarctic Circumpolar Current driven by surface buoyancy forcing. *Geophysical Research Letters*, 37(23).

Høgslund, S., Revsbech, N. P., Cedhagen, T., Nielsen, L. P., and Gallardo, V. A. (2008). Denitrification, nitrate turnover, and aerobic respiration by benthic foraminiferans in the oxygen minimum zone off chile. *Journal of Experimental Marine Biology and Ecology*, 359(2):85–91.

Holloway, M. D., Sime, L. C., Singarayer, J. S., Tindall, J. C., and Valdes, P. J. (2015). Reconstructing paleosalinity from δ^{18}O: Coupled model simulations of the Last Glacial Maximum, Last Interglacial and Late Holocene. *Quaternary Science Reviews*, 131:350–364.

Hopcroft, P. O. and Valdes, P. J. (2014). Last glacial maximum constraints on the Earth System model HadGEM2-ES. *Climate Dynamics*, 45(5-6):1657–1672.

Hu, X. and Cai, W.-J. (2011). The impact of denitrification on the atmospheric CO_2 uptake potential of seawater. *Marine Chemistry*, 127(1-4):192–198.

Ikehara, K. (2003). Late Quaternary Seasonal Sea-Ice History of the Northeastern Japan Sea. *Journal of Oceanography*, 59(5):585–593.

Imbrie, J., Berger, A., Boyle, E. A., Clemens, S. C., Duffy, A., Howard, W. R., Kukla, G., Kutzbach, J., Martinson, D. G., McIntyre, A., Mix, A. C., Molfino, B., Morley, J. J., Peterson, L. C., Pisias, N. G., Prell, W. L., Raymo, M. E., Shackleton, N. J., and Toggweiler, J. R. (1993). On the structure and origin of major glaciation cycles 2. The 100,000-year cycle. *Paleoceanography*, 8(6):699–735.

Imbrie, J., McIntyre, A., and Mix, A. (1989). Oceanic Response to Orbital Forcing in the Late Quaternary: Observational and Experimental Strategies. In Berger, A., Schneider, S. H., and Duplessy, J. C., editors, *Climate and Geosciences, A Challenge for Science and Society in the 21th Century.*, pages 121–164. Boston (Kuwer Academic).

Indermühle, A., Monnin, E., Stauffer, B., Stocker, T. F., and Wahlen, M. (2000). Atmospheric CO_2 concentration from 60 to 20 kyr BP from the Taylor Dome Ice Core, Antarctica. *Geophysical Research Letters*, 27(5):735–738.

IPCC (2014). Climate Change 2014: Impacts, Adaptation, and Vulnerability. Part A: Global and Sectoral Aspects. *Contribution of Working Group II to the Fifth Assessment Report of the Intergovernmental Panel on Climate Change*, page 1132.

Ivanovich, M. (1994). Uranium Series Disequilibrium: Concepts and Applications. *Radiochimica Acta*, 64(2):81–94.

Jackett, D. R., McDougall, T. J., Feistel, R., Wright, D. G., and Griffies, S. M. (2010). Algorithms for Density, Potential Temperature, Conservative Temperature, and the Freezing Temperature of Seawater. *Journal of Atmospheric and Oceanic Technology*, 23:1709–1728.

Johnson, J. S., Bentley, M. J., Roberts, S. J., Binnie, S. A., and Freeman, S. P. (2011). Holocene deglacial history of the northeast Antarctic Peninsula - A review and new chronological constraints. *Quaternary Science Reviews*, 30(27-28):3791–3802.

Jorissen, F. J., Fontanier, C., and Thomas, E. (2007). Paleoceanographical proxies based on deep-sea benthic foraminiferal assemblage characteristics. In Hillaire-Marcel, C. and de Vernal, A., editors, *Proxies in Late Cenozoic Paleoceanography*, pages 263–326. Elsevier.

Jouzel, J., Masson-Delmotte, V., Cattani, O., Dreyfus, G., Falourd, S., Hoffmann, G., Minster, B., Nouet, J., Barnola, J. M., Chappellaz, J., Fischer, H., Gallet, J. C., Johnsen, S., Leuenberger, M., Loulergue, L., Luethi, D., Oerter, H., Parrenin, F., Raisbeck, G., Raynaud, D., Schilt, A., Schwander, J., Selmo, E., Souchez, R., Spahni, R., Stauffer, B., Steffensen, J. P., Stenni, B., Stocker, T. F., Tison, J. L., Werner, M., and Wolff, E. W. (2007). Orbital and millennial Antarctic climate variability over the past 800,000 years. *Science*, 317(5839):793–6.

Kaiho, K. (1994). Benthic foraminiferal dissolved-oxygen index and dissolved-oxygen levels in the modern ocean. *Geology*, 22(8):719–722.

Kaiser, J. and Lamy, F. (2010). Links between Patagonian Ice Sheet fluctuations and Antarctic dust variability during the last glacial period (MIS 4-2). *Quaternary Science Reviews*, 29(11-12):1464–1471.

Kaiser, J., Lamy, F., and Hebbeln, D. (2005). A 70-kyr sea surface temperature record off southern Chile (Ocean Drilling Program Site 1233). *Paleoceanography*, 20(4).

Katsuki, K. and Takahashi, K. (2005). Diatoms as paleoenvironmental proxies for seasonal productivity, sea-ice and surface circulation in the Bering Sea during the late Quaternary. *Deep Sea Research Part II: Topical Studies in Oceanography*, 52(16-18):2110–2130.

Katz, M. E. and Thunell, R. C. (1984). Benthic foraminiferal biofacies associated with middle Miocene to early Pliocene oxygen-deficient conditions in the eastern Mediterranean. *The Journal of Foraminiferal Research*, 14(3):187–202.

Keany, J., Ledbetter, M., Watkins, N., and Huang, T.-C. (1976). Diachronous deposition of ice-rafted debris in sub-Antarctic deep-sea sediments. *Geological Society of America Bulletin*, 87(6):873–882.

Keeling, R. F. and Stephens, B. B. (2001). Antarctic sea ice and the control of Pleistocene climate instability. *Paleoceanography*, 16(1):112–131.

Khodri, M., Leclainche, Y., Ramstein, G., Braconnot, P., Marti, O., and Cortijo, E. (2001). Simulating the amplification of orbital forcing by ocean feedbacks in the last glaciation. *Nature*, 410(6828):570–4.

Kienast, M., Calvert, S., Pelejero, C., and Grimalt, J. (2001). A critical review of marine sedimentary δ^{13}C-pCO_2 estimates: New palaeorecords from the South China Sea and a revisit of other low-latitude d13Corg-pCO2 records. *Global Biogeochemical Cycles*, 15(1):113–127.

Kilfeather, A. A., Cofaigh, C. O., Lloyd, J. M., Dowdeswell, J. A., Xu, S., and Moreton, S. G. (2011). Ice-stream retreat and ice-shelf history in Marguerite Trough, Antarctic Peninsula: Sedimentological and foraminiferal signatures. *Geological Society of America Bulletin*, 123(5-6):997–1015.

Kilian, R. and Lamy, F. (2012). A review of Glacial and Holocene paleoclimate records from southernmost Patagonia (49-55oS). *Quaternary Science Reviews*, 53:1–23.

Kim, S.-T. and O'Neil, J. R. (1997). Equilibrium and nonequilibrium oxygen isotope effects in synthetic carbonates. *Geochimica et Cosmochimica Acta*, 61(16):3461–3475.

Knorr, G. and Lohmann, G. (2003). Southern ocean origin for the resumption of atlantic thermohaline circulation during deglaciation. *Nature*, 424(6948):532–536.

Knox, F. and McElroy, M. B. (1984). Changes in Atmospheric CO_2: Influence of the Marine Biota at High Latitude. *Journal of Geophysical Research*, 89(D3):4629–4637.

Koenig, Z., Provost, C., Ferrari, R., Sennéchael, N., and Rio, M.-H. (2014). Volume transport of the Antarctic Circumpolar Current: Production and validation of a 20 year long time series obtained from in situ and satellite observations. *Journal of Geophysical Research: Oceans*, 119(8):5407–5433.

Koenitz, D., White, N., McCave, I. N., and Hobbs, R. (2008). Internal structure of a contourite drift generated by the Antarctic Circumpolar Current. *Geochemistry, Geophysics, Geosystems*, 9(6).

Kohfeld, K., Graham, R., de Boer, A., Sime, L., Wolff, E., Le Quéré, C., and Bopp, L. (2013). Southern Hemisphere westerly wind changes during the Last Glacial Maximum: paleo-data synthesis. *Quaternary Science Reviews*, 68:76–95.

Kohfeld, K. E., Le Quéré, C., Harrison, S. P., and Anderson, R. F. (2005). Role of marine biology in glacial-interglacial CO_2 cycles. *Science*, 308(5718):74–8.

Kornilova, O. and Rosell-Melé, A. (2003). Application of microwave-assisted extraction to the analysis of biomarker climate proxies in marine sediments. *Organic Geochemistry*, 34(11):1517–1523.

Krueger, S., Leuschner, D., Ehrmann, W., Schmiedl, G., and Mackensen, A. (2012). North Atlantic Deep Water and Antarctic Bottom Water variability during the last 200ka recorded in an abyssal sediment core off South Africa. *Global and Planetary Change*, 80-81:180–189.

Kumar, N., Anderson, R. F., Mortlock, R. A., Froelich, P. N., Kubik, P., Dittrich-Hannen, B., and Suter, M. (1995). Increased biological productivity and export production in the glacial Southern Ocean. *Nature*, 378(6558):675–680.

Lambeck, K., Rouby, H., Purcell, A., Sun, Y., and Sambridge, M. (2014). Sea level and global ice volumes from the Last Glacial Maximum to the Holocene. *Proceedings of the National Academy of Sciences of the United States of America*, 111(43):15296–15303.

Lamy, F., Arz, H. W., Kilian, R., Lange, C. B., Lembke-Jene, L., Wengler, M., Kaiser, J., Baeza-Urrea, O., Hall, I. R., Harada, N., and Tiedemann, R. (2015). Glacial reduction and millennial-scale variations in Drake Passage throughflow. *Proceedings of the National Academy of Sciences of the United States of America*, 112(44):13496–501.

Lamy, F., Kaiser, J., Ninnemann, U., Hebbeln, D., Arz, H. W., and Stoner, J. (2004). Antarctic timing of surface water changes off Chile and Patagonian ice sheet response. *Science*, 304(5679):1959–62.

Lea, D. W., Pak, D. K., Belanger, C. L., Spero, H. J., Hall, M. A., and Shackleton, N. J. (2006). Paleoclimate history of Galápagos surface waters over the last 135,000 yr. *Quaternary Science Reviews*, 25(11-12):1152–1167.

Lee, K. E. (2004). Compilation of alkenone LGM SST data. Technical report.

LeGrande, A. N. and Schmidt, G. A. (2006). Global gridded data set of the oxygen isotopic composition in seawater. *Geophysical Research Letters*, 33(12):L12604.

Lippold, J., Grützner, J., Winter, D., Lahaye, Y., Mangini, A., and Christl, M. (2009). Does sedimentary ^{231}Pa/ ^{230}Th from the Bermuda Rise monitor past Atlantic Meridional Overturning Circulation? *Geophysical Research Letters*, 36(12):L12601.

Lisiecki, L. E. and Raymo, M. E. (2005). A Pliocene-Pleistocene stack of 57 globally distributed benthic δ^{18}O records. *Paleoceanography*, 20(1).

Lupi, C. (2009). Biostratigraphic correlation and paleoceanographic interpretation of Pleistocene calcareous nannofossils from the Subtropical Front to the Antarctic Divergence. *Micropaleontology*, 55(4):383–395.

Lüthi, D., Bereiter, B., Stauffer, B., Winkler, R., Schwander, J., Kindler, P., Leuenberger, M., Kipfstuhl, S., Capron, E., Landais, A., Fischer, H., and Stocker, T. F. (2010). CO_2 and O_2/N_2 variations in and just below the bubble-clathrate transformation zone of Antarctic ice cores. *Earth and Planetary Science Letters*, 297(1-2):226–233.

Mackensen, A., Fütterer, D., Grobe, H., and Schmiedl, G. (1993). Benthic foraminiferal assemblages from the eastern South Atlantic Polar Front region between 35° and 57°S: Distribution, ecology and fossilization potential. *Marine Micropaleontology*, 22(1-2):33–69.

Malone, M. J., Martin, J. B., Schönfeld, J., Ninnemann, U. S., Nürnburg, D., and White, T. S. (2004). The oxygen isotopic composition and temperature of Southern Ocean bottom waters during the last glacial maximum. *Earth and Planetary Science Letters*, 222(1):275–283.

Marcott, S. A., Bauska, T. K., Buizert, C., Steig, E. J., Rosen, J. L., Cuffey, K. M., Fudge, T. J., Severinghaus, J. P., Ahn, J., Kalk, M. L., McConnell, J. R., Sowers, T., Taylor, K. C., White, J. W. C., and Brook, E. J. (2014). Centennial-scale changes in the global carbon cycle during the last deglaciation. *Nature*, 514(7524):616–619.

Marshall, J. and Speer, K. (2012). Closure of the meridional overturning circulation through Southern Ocean upwelling. *Nature Geoscience*, 5(3):171–180.

Martin, J. H. (1990). Glacial-interglacial CO_2 change: The Iron Hypothesis. *Paleoceanography*, 5(1):1–13.

Martínez-Garcia, A., Rosell-Melé, A., Geibert, W., Gersonde, R., Masqué, P., Gaspari, V., and Barbante, C. (2009). Links between iron supply, marine productivity, sea surface temperature, and CO_2 over the last 1.1 Ma. *Paleoceanography*, 24(PA1207).

Martínez-Garcia, A., Rosell-Melé, A., Jaccard, S. L., Geibert, W., Sigman, D. M., and Haug, G. H. (2011). Southern Ocean dust-climate coupling over the past four million years. *Nature*, 476(7360):312–5.

Matano, R. P., Combes, V., Piola, A. R., Guerrero, R., Palma, E. D., Ted Strub, P., James, C., Fenco, H., Chao, Y., and Saraceno, M. (2014). The salinity signature of the cross-shelf exchanges in the Southwestern Atlantic Ocean: Numerical simulations. *Journal of geophysical research. Oceans*, 119(11):7949–7968.

McCave, I. N., Crowhurst, S. J., Kuhn, G., Hillenbrand, C.-D., and Meredith, M. P. (2014). Minimal change in Antarctic Circumpolar Current flow speed between the last glacial and Holocene. *Nature Geoscience*, 7(2):113–116.

McCave, I. N., Manighetti, B., and Robinson, S. G. (1995). Sortable silt and fine sediment size/composition slicing: Parameters for palaeocurrent speed and palaeoceanography. *Paleoceanography*, 10(3):593–610.

McClymont, E. L., Rosell-Melé, A., Giraudeau, J., Pierre, C., and Lloyd, J. M. (2005). Alkenone and coccolith records of the mid-Pleistocene in the south-east Atlantic: Implications for the $U^{K'}_{37}$ index and South African climate. *Quaternary Science Reviews*, 24(14-15):1559–1572.

McConnell, M. C. and Thunell, R. C. (2005). Calibration of the planktonic foraminiferal Mg/Ca paleothermometer: Sediment trap results from the Guaymas Basin, Gulf of California. *Paleoceanography*, 20(2):PA2016.

McCulloch, R. D., Bentley, M. J., Purves, R. S., Hulton, N. R. J., Sugden, D. E., and Clapperton, C. M. (2000). Climatic inferences from glacial and palaeoecological evidence at the last glacial termination, southern South America. *Journal of Quaternary Science*, 15(4):409–417.

Meredith, M. P., Grose, K. E., McDonagh, E. L., Heywood, K. J., Frew, R. D., and Dennis, P. F. (1999). Distribution of oxygen isotopes in the water masses of Drake Passage and the South Atlantic. *Journal of Geophysical Research*, 104(C9):20949–20962.

Meredith, M. P., Woodworth, P. L., Chereskin, T. K., Marshall, D. P., Allison, L. C., Bigg, G. R., Donohue, K., Heywood, K. J., Hughes, C. W., Hibbert, A., Hogg, A. M., Johnson, H. L., Jullion, L., King, B. A., Leach, H., Lenn, Y.-D., Morales Maqueda, M. A., Munday, D. R., Naveira Garabato, A. C., Provost, C., Sallée, J.-B., and Sprintall, J. (2011). Sustained monitoring of the southern ocean at Drake Passage: past achievements and future priorities. *Reviews of Geophysics*, 49(4):RG4005.

Milankovitch, M. (1930). Mathematische Klimalehre und Astronomische Theorie der Klimaschwankungen. *Handbuch der Klimatologie*, Band 1(Teil A).

Miller, M. D., Simons, M., Adkins, J. F., and Minson, S. E. (2015). The Information Content of Pore Fluid δ^{18}O and [Cl^-]. *Journal of Physical Oceanography*, 45(8):2070–2094.

Moffa-Sanchez, P., Hall, I. R., Thornalley, D. J., Barker, S., and Stewart, C. (2015). Changes in the strength of the Nordic Seas Overflows over the past 3000 years. *Quaternary Science Reviews*, 123:134–143.

Monnin, E., Steig, E. J., Siegenthaler, U., Kawamura, K., Schwander, J., Stauffer, B., Stocker, T. F., Morse, D. L., Barnola, J.-M., Bellier, B., Raynaud, D., and Fischer, H. (2004). Evidence for substantial accumulation rate variability in Antarctica during the Holocene, through synchronization of CO_2 in the Taylor Dome, Dome C and DML ice cores. *Earth and Planetary Science Letters*, 224(1-2):45–54.

Mortyn, P. G. and Charles, C. D. (2003). Planktonic foraminiferal depth habitat and δ^{18}O calibrations: Plankton tow results from the Atlantic sector of the Southern Ocean. *Paleoceanography*, 18(2).

Müller, P. J. and Fischer, G. (2004). C_{37}-Alkenones as Paleotemperature Tool: Fundamentals Based on Sediment Traps and Surface Sediments from the South Atlantic Ocean. In Wefer, G., Mulitza, S., and Ratmeyer, V., editors, *The South Atlantic in the Late Quaternary*, pages 167–193. Springer Berlin Heidelberg, Berlin, Heidelberg.

Munday, D. R., Johnson, H. L., and Marshall, D. P. (2013). Eddy Saturation of Equilibrated Circumpolar Currents. *Journal of Physical Oceanography*, 43(3):507–532.

Muratli, J. M., Chase, Z., Mix, A. C., and McManus, J. (2009). Increased glacial-age ventilation of the Chilean margin by Antarctic Intermediate Water. *Nature Geoscience*, 3(1):23–26.

Murray, J. (2001). The niche of benthic foraminifera, critical thresholds and proxies. *Marine Micropaleontology*, 41(1-2):1–7.

Narcisi, B., Petit, J. R., Delmonte, B., Scarchilli, C., and Stenni, B. (2012). A 16,000-yr tephra framework for the Antarctic ice sheet: a contribution from the new Talos Dome core. *Quaternary Science Reviews*, 49:52–63.

Neftel, A., Oeschger, H., Schwander, J., Stauffer, B., and Zumbrunn, R. (1982). Ice core sample measurements give atmospheric CO_2 content during the past 40,000 yr. *Nature*, 295(5846):220–223.

Nürnberg, C. C., Bohrmann, G., Schlüter, M., and Frank, M. (1997). Barium accumulation in the Atlantic sector of the Southern Ocean: Results From 190,000-year records. *Paleoceanography*, 12(4):594–603.

Orsi, A. H., Whitworth, T., and Nowlin, W. D. (1995). On the meridional extent and fronts of the Antarctic Circumpolar Current. *Deep Sea Research Part I: Oceanographic Research Papers*, 42(5):641–673.

Pagani, M., Zachos, J. C., Freeman, K. H., Tipple, B., and Bohaty, S. (2005). Marked decline in atmospheric carbon dioxide concentrations during the Paleogene. *Science*, 309(5734):600–3.

Pahnke, K., Goldstein, S. L., and Hemming, S. R. (2008). Abrupt changes in Antarctic Intermediate Water circulation over the past 25,000 years. *Nature Geoscience*, 1(12):870–874.

Paparazzo, F. E., Bianucci, L., Schloss, I. R., Almandoz, G. O., Solís, M., and Esteves, J. L. (2010). Cross-frontal distribution of inorganic nutrients and chlorophyll-a on the Patagonian Continental Shelf of Argentina during summer and fall. *Revista de biología marina y oceanografía*, 45(1):107–119.

Parnell, A., Haslett, J., Allen, J., Buck, C., and Huntley, B. (2008). A flexible approach to assessing synchroneity of past events using Bayesian reconstructions of sedimentation history. *Quaternary Science Reviews*, 27(19-20):1872–1885.

Past Interglacials Working Group of PAGES (2016). Interglacials of the last 800,000 years. *Reviews of Geophysics*.

Peck, V. L., Allen, C. S., Kender, S., McClymont, E. L., and Hodgson, D. A. (2015). Oceanographic variability on the West Antarctic Peninsula during the Holocene and the influence of upper circumpolar deep water. *Quaternary Science Reviews*, 119:54–65.

Pedersen, T. and Price, N. (1982). The geochemistry of manganese carbonate in Panama Basin sediments. *Geochimica et Cosmochimica Acta*, 46(1):59–68.

Petit, J. R., Jouzel, J., Raynaud, D., Barkov, N. I., Barnola, J.-M., Basile, I., Bender, M., Chappellaz, J., Davis, M., Delaygue, G., Delmotte, M., Kotlyakov, V. M., Legrand, M., Lipenkov, V. Y., Lorius, C., Pepin, L., Ritz, C., Saltzman, E., and Stievenard, M. (1999). Climate and atmospheric history of the past 420,000 years from the Vostok ice core, Antarctica. *Nature*, 399(6735):429–436.

Piña-Ochoa, E., Høgslund, S., Geslin, E., Cedhagen, T., Revsbech, N. P., Nielsen, L. P., Schweizer, M., Jorissen, F., Rysgaard, S., and Risgaard-Petersen, N. (2010). Widespread occurrence of nitrate storage and denitrification among Foraminifera and Gromiida. *Proceedings of the National Academy of Sciences of the United States of America*, 107(3):1148–53.

Piola, A. R. and Gordon, A. L. (1989). Intermediate waters in the southwest South Atlantic. *Deep Sea Research Part A. Oceanographic Research Papers*, 36(1):1–16.

Prahl, F. G., Muehlhausen, L. A., and Zahnle, D. L. (1988). Further evaluation of long-chain alkenones as indicators of paleoceanographic conditions. *Geochimica et Cosmochimica Acta*, 52(9):2303–2310.

Prahl, F. G. and Wakeham, S. G. (1987). Calibration of unsaturation patterns in long-chain ketone compositions for palaeotemperature assessment. *Nature*, 330(6146):367–369.

Pudsey, C. J., Murray, J. W., Appleby, P., and Evans, J. (2006). Ice shelf history from petrographic and foraminiferal evidence, Northeast Antarctic Peninsula. *Quaternary Science Reviews*, 25(17-18):2357–2379.

Pugh, R. (2009). Late Quaternary Changes in the Antarctic Circumpolar Current. *PhD thesis*, page 192.

Pugh, R., McCave, I., Hillenbrand, C.-D., and Kuhn, G. (2009). Circum-Antarctic age modelling of Quaternary marine cores under the Antarctic Circumpolar Current: Ice-core dust-magnetic correlation. *Earth and Planetary Science Letters*, 284(1-2):113–123.

Pujos, A. and Giraudeau, J. (1993). Répartition des Noelaerhabdaceae (nannofossiles calcaires) dans le Quaternaire moyen et supérieur des océans Atlantique et Pacifique. *Oceanologica Acta*, 16(4):349–362.

Rau, G. H., Takahashi, T., Des Marais, D. J., Repeta, D. J., and Martin, J. H. (1992). The relationship between δ^{13}C of organic matter and [CO_2(aq)] in ocean surface water: data from a JGOFS site in the northeast Atlantic Ocean and a model. *Geochimica et cosmochimica acta*, 56:1413–9.

Reimer, P., Bard, E., Bayliss, A., Beck, J., Blackwell, P., Ramsey, C., Buck, C., Cheng, H., Edwards, R., Friedrich, M., Grootes, P., Guilderson, T., Haflidason, H., Hajdas, I., Hatte, C., Heaton, T., Hoffman, D., Hogg, A., Hughen, K., Kaiser, K., Kromer, B., Manning, S., Niu, M., Reimer, R., Richards, D., Scott, E., Southon, J., Staff, R., Turney, C., and van der Plicht, J. (2013). IntCal13 and Marine13 Radiocarbon Age Calibration Curves 0-50,000 Years cal BP. *Radiocarbon*, 55(4):1869–1887.

Renault, A., Provost, C., Sennéchael, N., Barré, N., and Kartavtseff, A. (2011). Two full-depth velocity sections in the Drake Passage in 2006-Transport estimates. *Deep Sea Research Part II: Topical Studies in Oceanography*, 58(25-26):2572–2591.

Richter, T. O., van der Gaast, S., Koster, B., Vaars, A., Gieles, R., de Stigter, H. C., de Haas, H., and van Weering, T. C. E. (2006). The Avaatech XRF Core Scanner: technical description and applications to NE Atlantic sediments. *Geological Society, London, Special Publications*, 267(1):39–50.

Rickaby, R. E. M. and Elderfield, H. (2005). Evidence from the high-latitude North Atlantic for variations in Antarctic Intermediate water flow during the last deglaciation. *Geochemistry, Geophysics, Geosystems*, 6(5).

Ridgwell, A. J. (2003). An end to the 'rain ratio' reign? *Geochemistry, Geophysics, Geosystems*, 4(6).

Rintoul, S. R. and England, M. H. (2002). Ekman Transport Dominates Local Air-Sea Fluxes in Driving Variability of Subantarctic Mode Water. *Journal of Physical Oceanography*, 32(5):1308–1321.

Roberts, J., Gottschalk, J., Skinner, L. C., Peck, V. L., Kender, S., Elderfield, H., Waelbroeck, C., Vázquez Riveiros, N., and Hodell, D. A. (2016). Evolution of South Atlantic density and chemical stratification across the last deglaciation. *Proceedings of the National Academy of Sciences of the United States of America*, 113(3):514–519.

Robinson, L. F., Adkins, J. F., Frank, N., Gagnon, A. C., Prouty, N. G., Brendan Roark, E., and van de Flierdt, T. (2014). The geochemistry of deep-sea coral skeletons: A review of vital effects and applications for palaeoceanography. *Deep Sea Research Part II: Topical Studies in Oceanography*, 99:184–198.

Robinson, L. F., Adkins, J. F., Keigwin, L. D., Southon, J., Fernandez, D. P., Wang, S.-L., and Scheirer, D. S. (2005). Radiocarbon variability in the western North Atlantic during the last deglaciation. *Science*, 310(5753):1469–73.

Romero, O. and Hensen, C. (2002). Oceanographic control of biogenic opal and diatoms in surface sediments of the southwestern atlantic. *Marine Geology*, 186(3):263–280.

Ronge, T. A., Steph, S., Tiedemann, R., Prange, M., Merkel, U., Nürnberg, D., and Kuhn, G. (2015). Pushing the boundaries: Glacial/interglacial variability of intermediate and deep waters in the southwest Pacific over the last 350,000 years. *Paleoceanography*, 30(2):23–38.

Rosell-Mele, A., Carter, J. F., Parry, A. T., and Eglinton, G. (1995). Determination of the U^K_{37} index in geological samples. *Analytical Chemistry*, 67(7):1283–1289.

Rosell-Mele, A. and Koc, N. (1997). Paleoclimatic significance of the stratigraphic occurrence of photosynthetic biomarker pigments in the Nordic seas. *Geology*, 25(1):49–52.

Rosenthal, Y., Boyle, E. A., Labeyrie, L., and Oppo, D. (1995). Glacial enrichments of authigenic Cd and U in subantarctic sediments: A climatic control on the elements' oceanic budget? *Paleoceanography*, 10(3):395–413.

Russell, J. L., Dixon, K. W., Gnanadesikan, A., Stouffer, R. J., and Toggweiler, J. R. (2006). The Southern Hemisphere Westerlies in a Warming World: Propping Open the Door to the Deep Ocean. *Journal of Climate*, 19(24):6382–6390.

Sadekov, A., Eggins, S. M., de Deckker, P., and Kroon, D. (2008). Uncertainties in seawater thermometry deriving from intratest and intertest Mg/Ca variability in *Globigerinoides ruber*. *Paleoceanography*, 23(1).

Sarmiento, J. L. and Gruber, N. (2002). Sinks for anthropogenic carbon. *Physics Today*, 55(8):30–36.

Sarmiento, J. L. and Toggweiler, J. R. (1984). A new model for the role of the oceans in determining atmospheric pCO_2. *Nature*, 308(5960):621–624.

Sarnthein, M., Pflaumann, U., and Weinelt, M. (2003). Past extent of sea ice in the northern North Atlantic inferred from foraminiferal paleotemperature estimates. *Paleoceanography*, 18(2):n/a–n/a.

Scherer, R. P., Aldahan, A., Tulaczyk, S., Possnert, G., Engelhardt, H., and Kamb, B. (1998). Pleistocene collapse of the west antarctic ice sheet. *Science*, 281(5373):82–85.

Schilt, A., Baumgartner, M., Schwander, J., Buiron, D., Capron, E., Chappellaz, J., Loulergue, L., Schüpbach, S., Spahni, R., Fischer, H., and Stocker, T. F. (2010). Atmospheric nitrous oxide during the last 140,000 years. *Earth and Planetary Science Letters*, 300(1-2):33–43.

Schoepfer, S. D., Shen, J., Wei, H., Tyson, R. V., Ingall, E., and Algeo, T. J. (2014). Total organic carbon, organic phosphorus, and biogenic barium fluxes as proxies for paleomarine productivity. *Earth-Science Reviews*, 149:23–52.

Schrag, D. P., Hampt, G., and Murray, D. W. (1996). Pore fluid constraints on the temperature and oxygen isotopic composition of the glacial ocean. *Science*, 272(5270):1930–1932.

Schröder, C. J. (1988). Subsurface preservation of agglutinated foraminifera in the Northwest Atlantic Ocean. *Abhandlungen der Geologischen Bundesantstalt*, 41:325–226.

Schwarz, J. and Schodlok, M. (2009). Impact of drifting icebergs on surface phytoplankton biomass in the Southern Ocean: Ocean colour remote sensing and in situ iceberg tracking. *Deep Sea Research Part I: Oceanographic Research Papers*, 56(10):1727–1741.

Seidov, D. (2001). Meltwater and the global ocean conveyor: northern versus southern connections. *Global and Planetary Change*, 30(3-4):257–270.

Shackleton, N. J. (1974). Attainment of Isotopic Equilibrium Between Ocean Water and the Benthonic Foraminifera Genus Uvigerina: Isotopic Changes in the Ocean During the Last Glacial. *Colloques Internationaux. Centre National de la Reserche Scientifique*, 219:203–209.

Shakun, J. D., Clark, P. U., He, F., Marcott, S. A., Mix, A. C., Liu, Z., Otto-Bliesner, B., Schmittner, A., and Bard, E. (2012). Global warming preceded by increasing carbon dioxide concentrations during the last deglaciation. *Nature*, 484(7392):49–54.

Shchepetkin, A. F. and McWilliams, J. C. (2005). The Regional Ocean Modeling System: A split-explicit, free-surface, topography following coordinates ocean model. *Ocean Modelling*, 9:347–404.

Shemesh, A., Hodell, D., Crosta, X., Kanfoush, S., Charles, C., and Guilderson, T. (2002). Sequence of events during the last deglaciation in Southern Ocean sediments and Antarctic ice cores. *Paleoceanography*, 17(4):8–1–8–7.

Shepherd, A. S., Rathburn, A. E., and Pérez, M. E. (2007). Living foraminiferal assemblages from the southern california margin: a comparison of the> 150, 63–150, and> 63 μm fractions. *Marine Micropaleontology*, 65(1):54–77.

Shiroya, K., Yokoyama, Y., Obrochta, S., Harada, N., Miyairi, Y., and Matsuzaki, H. (2013). Melting history of the Patagonian Ice Sheet during Termination I inferred from marine sediments. *Geochemical Journal*, 47(2):107–117.

Siegenthaler, U. and Wenk, T. (1984). Rapid Atmospheric CO_2 Variations and Ocean Circulation. *Nature*, 308(5960):624–626.

Sigman, D. M. and Boyle, E. A. (2000). Glacial/interglacial variations in atmospheric carbon dioxide. *Nature*, 407(6806):859–69.

Sigman, D. M., Hain, M. P., and Haug, G. H. (2010). The polar ocean and glacial cycles in atmospheric CO_2 concentration. *Nature*, 466(7302):47–55.

Sikes, E., Samson, C., Guilderson, T., and Howard, W. (2000). Old radiocarbon ages in the southwest Pacific Ocean during the last glacial period and deglaciation. *Nature*, 405(6786):555–9.

Sikes, E. L. and Keigwin, L. D. (1994). Equatorial Atlantic sea surface temperature for the last 30 kyr: A comparison of U^K_{37} , $\delta^{18}O$ and foraminiferal assemblage temperature estimates. *Paleoceanography*, 9(1):31–45.

Sime, L. C., Kohfeld, K. E., Le Quéré, C., Wolff, E. W., de Boer, A. M., Graham, R. M., and Bopp, L. (2013). Southern Hemisphere westerly wind changes during the Last Glacial Maximum: model-data comparison. *Quaternary Science Reviews*, 64:104–120.

Skinner, L. C., Fallon, S., Waelbroeck, C., Michel, E., and Barker, S. (2010). Ventilation of the deep Southern Ocean and deglacial CO_2 rise. *Science*, 328(5982):1147–1151.

Skinner, L. C., Scrivner, A. E., Vance, D., Barker, S., Fallon, S., and Waelbroeck, C. (2013). North Atlantic versus Southern Ocean contributions to a deglacial surge in deep ocean ventilation. *Geology*, 41(6):667–670.

Sloyan, B. M. and Rintoul, S. R. (2001). The Southern Ocean Limb of the Global Deep Overturning Circulation. *Journal of Physical Oceanography*, 31(1):143–173.

Smith, K. L., Robison, B. H., Helly, J. J., Kaufmann, R. S., Ruhl, H. A., Shaw, T. J., Twining, B. S., and Vernet, M. (2007). Free-drifting icebergs: hot spots of chemical and biological enrichment in the Weddell Sea. *Science*, 317(5837):478–82.

Sørensen, J., Jørgensen, B. B., and Revsbech, N. P. (1979). A comparison of oxygen, nitrate, and sulfate respiration in coastal marine sediments. *Microbial Ecology*, 5(2):105–115.

Speich, S., Blanke, B., and Madec, G. (2001). Warm and cold water routes of an O.G.C.M. thermohaline conveyor belt. *Geophysical Research Letters*, 28(2):311–314.

Spooner, P. T., Chen, T., Robinson, L. F., and Coath, C. D. (2016). Rapid uranium-series age screening of carbonates by laser ablation mass spectrometry. *Quaternary Geochronology*, 31:28–39.

Steig, E. J., Huybers, K., Singh, H. A., Steiger, N. J., Ding, Q., Frierson, D. M., Popp, T., and White, J. W. (2015). Influence of west antarctic ice sheet collapse on antarctic surface climate. *Geophysical Research Letters*, 42(12):4862–4868.

Stephens, B. and Keeling, R. (2000). The influence of Antarctic sea ice on glacial-interglacial CO_2 variations. *Nature*, 404(6774):171–174.

Stern, J. V. and Lisiecki, L. E. (2014). Termination 1 timing in radiocarbon-dated regional benthic δ^{18}O stacks. *Paleoceanography*, 29(12):1127–1142.

Stommel, H. (1961). Thermohaline Convection with Two Stable Regimes of Flow. *Tellus*, 13(2):224–230.

Sun, X., Corliss, B. H., Brown, C. W., and Showers, W. J. (2006). The effect of primary productivity and seasonality on the distribution of deep-sea benthic foraminifera in the North Atlantic. *Deep Sea Research Part I: Oceanographic Research Papers*, 53(1):28–47.

Tagliabue, A., Bopp, L., Roche, D. M., Bouttes, N., Dutay, J.-C., Alkama, R., Kageyama, M., Michel, E., and Paillard, D. (2009). Quantifying the roles of ocean circulation and biogeochemistry in governing ocean carbon-13 and atmospheric carbon dioxide at the last glacial maximum. *Climate of the Past*, 5(4):695–706.

Takahashi, T., Sutherland, S. C., Sweeney, C., Poisson, A., Metzl, N., Tilbrook, B., Bates, N., Wanninkhof, R., Feely, R. A., Sabine, C., Olafsson, J., and Nojiri, Y. (2002). Global sea-air CO2 flux based on climatological surface ocean pCO_2, and seasonal biological and temperature effects. *Deep Sea Research Part II: Topical Studies in Oceanography*, 49(9-10):1601–1622.

Talley, L. D. (1999). Some aspects of ocean heat transport by the shallow, intermediate and deep overturning Circulations. In *Mechanisms of Global Climate Change at Millennial Time Scales*, pages 1–22.

Ternois, Y., Kawamura, K., Ohkouchi, N., and Keigwin, L. (2000). Alkenone sea surface temperature in the Okhotsk Sea for the last 15 kyr. *Geochemical Journal*, 34(4):283–293.

Thiagarajan, N., Subhas, A. V., Southon, J. R., Eiler, J. M., and Adkins, J. F. (2014). Abrupt pre-bolling-allerod warming and circulation changes in the deep ocean. *Nature*, 511(7507):75–78.

Thierstein, H. R., Geitzenauer, K. R., Molfino, B., and Shackleton, N. J. (1977). Global synchroneity of late Quaternary coccolith datum levels Validation by oxygen isotopes. *Geology*, 5(7):400–404.

Toggweiler, J., Russell, J., and Carson, S. (2006). Midlatitude westerlies, atmospheric CO_2, and climate change during the ice ages. *Paleoceanography*, 21(2).

Toggweiler, J. R. (1999). Variation of atmospheric CO_2 by ventilation of the ocean's deepest water. *Paleoceanography*, 14(5):571–588.

Tomczak, M. and Godfrey, J. (2001). Antarctic Oceanography. In *Regional Oceanography: an Introduction*, pages 63–83.

Uemura, R., Masson-Delmotte, V., Jouzel, J., Landais, A., Motoyama, H., and Stenni, B. (2012). Ranges of moisture-source temperature estimated from Antarctic ice cores stable isotope records over glacial-interglacial cycles. *Climate of the Past*, 8(3):1109–1125.

Vanderborght, J.-P., Wollast, R., and Billen, G. (1977). Kinetic models of diagenesis in disturbed sediments. Part 1. Mass transfer properties and silica diagenesis. *Limnology and Oceanography*, 22(5):787–793.

Vogel, J., Southon, J., Nelson, D., and Brown, T. (1984). Performance of catalytically condensed carbon for use in accelerator mass spectrometry. *Nuclear Instruments and Methods in Physics Research Section B: Beam Interactions with Materials and Atoms*, 5(2):289–293.

Volkman, J. K., Barrerr, S. M., Blackburn, S. I., and Sikes, E. L. (1995). Alkenones in *Gephyrocapsa oceanica*: Implications for studies of paleoclimate. *Geochimica et Cosmochimica Acta*, 59(3):513–520.

Wadham, J. L., De'ath, R., Monteiro, F. M., Tranter, M., Ridgwell, A., Raiswell, R., and Tulaczyk, S. (2013). The potential role of the Antarctic Ice Sheet in global biogeochemical cycles. *Earth and Environmental Science Transactions of the Royal Society of Edinburgh*, 104(01):55–67.

Waelbroeck, C., Skinner, L. C., Labeyrie, L., Duplessy, J.-C., Michel, E., Vazquez Riveiros, N., Gherardi, J.-M., and Dewilde, F. (2011). The timing of deglacial circulation changes in the Atlantic. *Paleoceanography*, 26(3):PA3213.

Watson, A. J. A., Garabato, A. C. N., and Naveira Garabato, A. (2006). The role of Southern Ocean mixing and upwelling in glacial-interglacial atmospheric CO_2 change. *Tellus*, 58(1):73–87.

Weaver, A. J., Saenko, O. A., Clark, P. U., and Mitrovica, J. X. (2003). Meltwater pulse 1A from Antarctica as a trigger of the Bølling-Allerød warm interval. *Science*, 299(5613):1709–13.

Weaver, P. P. E., Chapman, M. R., Eglinton, G., Zhao, M., Rutledge, D., and Read, G. (1999). Combined coccolith, foraminiferal, and biomarker reconstruction of paleoceanographic conditions over the past 120 kyr in the northern North Atlantic (59°N, 23°W). *Paleoceanography*, 14(3):336–349.

Weber, M., Kuhn, G., Sprenk, D., Rolf, C., Ohlwein, C., and Ricken, W. (2012). Dust transport from Patagonia to Antarctica - A new stratigraphic approach from the Scotia Sea and its implications for the last glacial cycle. *Quaternary Science Reviews*, 36:177–188.

Wefer, G., Berger, W. H., Siedler, G., and Webb, D. J. (1996). *The South Atlantic*. Springer Berlin Heidelberg, Berlin, Heidelberg.

Wells, P. and Okada, H. (1997). Response of nannoplankton to major changes in sea-surface temperature and movements of hydrological fronts over Site DSDP 594 (south Chatham Rise, southeastern New Zealand), during the last 130 kyr. *Marine Micropaleontology*, 32(3-4):341–363.

Weltje, G. J. and Tjallingii, R. (2008). Calibration of XRF core scanners for quantitative geochemical logging of sediment cores: Theory and application. *Earth and Planetary Science Letters*, 274(3-4):423–438.

Wolgemuth, K. and Broecker, W. (1970). Barium in sea water. *Earth and Planetary Science Letters*, 8(5):372–378.

Woodard, S. C., Rosenthal, Y., Miller, K. G., Wright, J. D., Chiu, B. K., and Lawrence, K. T. (2014). Antarctic role in Northern Hemisphere glaciation. *Science*, 346(6211):847–51.

Woodruff, F., Savin, S. M., and Douglas, R. G. (1980). Biological fractionation of oxygen and carbon isotopes by recent benthic foraminifera. *Marine Micropaleontology*, 5:3–11.

Yamazaki, T. and Ikehara, M. (2012). Origin of magnetic mineral concentration variation in the Southern Ocean. *Paleoceanography*, 27(2):PA2206.

Yu, J. and Elderfield, H. (2008). Mg/Ca in the benthic foraminifera *Cibicidoides wuellerstorfi* and *Cibicidoides mundulus*: Temperature versus carbonate ion saturation. *Earth and Planetary Science Letters*, 276(1-2):129–139.

Zarriess, M. and Mackensen, A. (2010). The tropical rainbelt and productivity changes off northwest africa: a 31,000-year high-resolution record. *Marine Micropaleontology*, 76(3):76–91.

Zielinski, U. and Gersonde, R. (2002). Plio–pleistocene diatom biostratigraphy from odp leg 177, atlantic sector of the southern ocean. *Marine Micropaleontology*, 45(3):225–268.

Appendix A

Data Tables

A.1 Age Models

A.1.1 GC528

Table A.1: Radiocarbon dates obtained from GC528 on the benthic foraminifera *U. bifurcata*.

Core depth (cm)	^{14}C AMS age (yr B.P.)	1σ (yr)	Reservoir age (yr)	1σ (yr)	Laboratory
0	2540	30	967	110	Beta Analytic
5.5	2090	30	967	110	Beta Analytic
30	4972	45	967	110	Godwin/UB
41	6178	39	967	110	Godwin/UB
49	7150	30	967	110	Beta Analytic
58	9383	48	967	110	Godwin/UB
61	7876	51	967	110	Godwin/UB
61	9026	48	967	110	Godwin/UB
66	11925	48	987	110	Godwin/UB
72	12562	55	1031	110	Godwin/UB
78	12652	53	1040	110	Godwin/UB
82	12295	53	1077	110	Godwin/UB
88	12611	47	1077	110	Godwin/UB
98	13251	50	1084	110	Godwin/UB
109.5	12234	65	1150	110	Godwin/UB
111.5	13079	63	1175	110	Godwin/UB
119	13670	70	1298	110	Godwin/UB
124	14410	81	1325	110	Godwin/UB
139.5	14651	80	1330	110	Godwin/UB
149	16380	90	1364	110	Beta Analytic
199	17340	101	1364	110	Godwin/UB
229	17220	70	1364	110	Beta Analytic
289	18260	108	1364	110	Godwin/UB
350	20628	140	1364	110	Godwin/UB
416	29475	372	1364	110	Godwin/UB
448	33440	210	1364	110	Beta Analytic

Table A.2: Data from GC528 used to align GC642 onto equivalent depth scale. *Uvigerina bifurcata* = Uvi. *Neogloboquadrina pachyderma sinistral* = Nps. Magnetic Susceptibility = Mag. Sus.

Depth, cm	Age, ka	Uvi. $\delta^{18}O$, ‰PDB	Uvi. $\delta^{13}C$, ‰PDB	Nps. $\delta^{18}O$, ‰PDB	Nps. $\delta^{13}C$, ‰PDB	Mag. Sus., SI	TOC $\delta^{13}C$, ‰PDB
1	1.079	3.04	-0.79	3.04	-0.79		
2	1.110						
3	1.140					58.69	
4	1.172					58.28	
5	1.228	3.12	-0.51	3.12	-0.51	59.48	-22.04
6	1.362					61.12	
7	1.593						
8	1.787					64.89	
9	1.958					68.93	
10	2.103	3.08	-0.59	3.08	-0.59	73.14	-22.04
11	2.237	3.15	-0.69	3.15	-0.69	72.07	
12	2.359	3.25	-0.60	3.25	-0.60	70.91	
13	2.462					71.63	
14	2.598	3.12	-0.72	3.12	-0.72		
15	2.716	3.20	-0.57	3.20	-0.57	61.20	-22.02
16	2.829	3.03	-0.74	3.03	-0.74	48.33	
17	2.937					61.66	
18	3.039					59.55	
19	3.170					65.58	
20	3.300	3.09	-0.66	3.09	-0.66	63.96	-21.90
21	3.395	3.18	-0.53	3.18	-0.53	71.69	
22	3.515	3.33	-0.41	3.33	-0.41	71.75	
23	3.631	3.29	-0.50	3.29	-0.50	76.14	
24	3.745	3.15	-0.53	3.15	-0.53	71.26	
25	3.855	3.30	-0.52	3.30	-0.52	69.53	-21.76
26	3.973					69.01	
27	4.080	3.27	-0.53	3.27	-0.53	72.01	
28	4.204						
29	4.334	2.87	-0.72	2.87	-0.72		
30	4.507	3.15	-0.69	3.15	-0.69	71.01	-21.73
31	4.672					68.73	
32	4.807	3.12	-0.57	3.12	-0.57	70.21	
33	4.932	2.95	-0.90	2.95	-0.90	68.81	
34	5.053	3.20	-0.63	3.20	-0.63	67.07	
35	5.174	3.15	-0.62	3.15	-0.62	88.09	-21.79
36	5.308	2.92	-0.55	2.92	-0.55	62.81	
37	5.437	3.46	-0.43	3.46	-0.43	62.26	
38	5.568	2.27	-0.89	2.27	-0.89	60.44	

Depth, cm	Age, ka	Uvi. $\delta^{18}O$, ‰PDB	Uvi. $\delta^{13}C$, ‰PDB	Nps. $\delta^{18}O$, ‰PDB	Nps. $\delta^{13}C$, ‰PDB	Mag. Sus., SI	TOC $\delta^{13}C$, ‰PDB
39	5.693	3.21	-0.62	3.21	-0.62	59.97	
40	5.818	3.16	-0.59	3.16	-0.59	63.26	-21.73
41	5.987	2.82	-0.64	2.82	-0.64	64.68	
42	6.150	3.23	-0.55	3.23	-0.55	62.80	
43	6.275	3.18	-0.62	3.18	-0.62	62.50	
44	6.401	3.23	-0.77	3.23	-0.77	62.65	
45	6.536	3.27	-0.52	3.27	-0.52	68.58	-21.92
46	6.666	3.32	-0.54	3.32	-0.54	66.29	
47	6.797	3.11	-0.51	3.11	-0.51	63.64	
48	6.936	3.06	-0.61	3.06	-0.61	63.75	
49	7.102					60.32	
50	7.346	3.13	-0.71	3.13	-0.71	51.86	-21.64
51	7.598					54.68	
52	7.843	3.44	-0.62	3.44	-0.62	58.30	
53	8.084	3.32	-0.52	3.32	-0.52	55.25	
54	8.333	3.70	-0.44	3.70	-0.44	51.75	
55	8.566	3.32	-0.53	3.32	-0.53		-21.67
56	8.811	3.59	-0.44	3.59	-0.44		
57	9.042	3.30	-0.40	3.30	-0.40		
58	9.299	3.60	-0.35	3.60	-0.35		
59	9.509	4.06	-0.39	4.06	-0.39	57.86	
60	9.694	4.22	-0.52	4.22	-0.52	57.02	-21.39
61	10.176					52.29	
62	10.996					60.76	
63	11.439	3.85	-0.43	3.85	-0.43	54.44	
64	11.890	4.34	-0.23	4.34	-0.23	42.44	
65	12.346	4.35	-0.23	4.35	-0.23	39.36	-21.44
66	12.749	4.23	-0.41	4.23	-0.41	38.89	
67	12.843	3.94	-0.35	3.94	-0.35	44.63	
68	12.899	4.40	-0.27	4.40	-0.27	38.29	
69	12.953	4.23	-0.31	4.23	-0.31	33.57	
70	13.007	3.98	-0.42	3.98	-0.42	43.75	-21.48
71	13.059					37.13	
72	13.111	4.24	-0.19	4.24	-0.19	27.67	
73	13.142	4.29	-0.23	4.29	-0.23	27.29	
74	13.160	4.25	-0.23	4.25	-0.23	23.47	
75	13.177	4.33	-0.42	4.33	-0.42	22.97	-21.50
76	13.194	4.52	-0.21	4.52	-0.21	19.71	
77	13.210	4.37	-0.23	4.37	-0.23	19.55	
78	13.237	4.31	-0.15	4.31	-0.15	21.36	
79	13.264	4.37	-0.17	4.37	-0.17	19.29	
80	13.288	4.25	-0.14	4.25	-0.14	19.14	-21.47
81	13.310	4.41	-0.16	4.41	-0.16	20.54	
82	13.339	4.26	-0.13	4.26	-0.13	19.88	
83	13.369	4.16	-0.34	4.16	-0.34	18.63	
84	13.394	4.23	-0.25	4.23	-0.25	18.27	
85	13.418	4.23	-0.55	4.23	-0.55	15.97	-21.56
86	13.443	4.29	-0.39	4.29	-0.39	18.32	
87	13.469	4.26	-0.16	4.26	-0.16	16.35	

Depth, cm	Age, ka	Uvi. $\delta^{18}O$, ‰PDB	Uvi. $\delta^{13}C$, ‰PDB	Nps. $\delta^{18}O$, ‰PDB	Nps. $\delta^{13}C$, ‰PDB	Mag. Sus., SI	TOC $\delta^{13}C$, ‰PDB
88	13.501	4.34	-0.23	4.34	-0.23	15.99	
89	13.542	4.12	-0.42	4.12	-0.42	15.76	
90	13.571	4.22	-0.27	4.22	-0.27	13.76	-21.46
91	13.601					15.51	
92	13.628	4.40	-0.13	4.40	-0.13	12.33	
93	13.658	4.38	-0.13	4.38	-0.13	18.16	
94	13.685	4.35	-0.38	4.35	-0.38	18.41	
95	13.713	4.38	-0.35	4.38	-0.35	20.22	-21.20
96	13.741	3.94	-0.76	3.94	-0.76	21.03	
97	13.773	3.18	-0.74	3.18	-0.74	23.05	
98	13.809	4.44	-0.19	4.44	-0.19	27.61	
99	13.833	4.81	-0.21	4.81	-0.21	30.47	
100	13.847	4.33	-0.43	4.33	-0.43	34.22	-21.30
101	13.861	3.99	-0.32	3.99	-0.32	29.30	
102	13.873	4.51	-0.18	4.51	-0.18	32.17	
103	13.887	4.35	-0.28	4.35	-0.28	34.50	
104	13.897	4.38	-0.23	4.38	-0.23	35.69	
105	13.908	4.31	-0.28	4.31	-0.28	34.97	-21.31
106	13.919	4.48	-0.09	4.48	-0.09	37.33	
107	13.932	4.50	-0.23	4.50	-0.23	42.40	
108	13.944	4.84	-0.33	4.84	-0.33	41.26	
109	13.963	4.16	-0.66	4.16	-0.66		
110	14.011	4.27	-0.28	4.27	-0.28		-21.27
111	14.093						
112	14.181	4.44	-0.30	4.44	-0.30		
113	14.263	4.53	-0.29	4.53	-0.29		
114	14.342	4.79	-0.30	4.79	-0.30		
115	14.408	4.77	-0.31	4.77	-0.31		-21.74
116	14.480	5.30	-0.35	5.30	-0.35		
117	14.548	4.83	-0.33	4.83	-0.33	46.50	
118	14.618					65.42	
119	14.721					41.28	
120	14.904	4.23	-0.52	4.23	-0.52	37.15	-22.81
121	15.065					42.52	
122	15.232					41.78	
123	15.389					46.42	
124	15.528	3.91	-0.52	3.91	-0.52	44.87	
125	15.607	4.97	-0.62	4.97	-0.62	46.30	-22.36
126	15.652					47.26	
127	15.686	5.30	-0.57	5.30	-0.57	50.77	
128	15.718	5.24	-0.37	5.24	-0.37	30.96	
129	15.754	5.25	-0.34	5.25	-0.34	50.10	
130	15.789	4.83	-0.35	4.83	-0.35	49.40	-22.83
131	15.817					49.18	
132	15.843					44.25	
133	15.872	4.90	-0.37	4.90	-0.37	43.65	
134	15.903	4.94	-0.04	4.94	-0.04	43.34	
135	15.932	4.93	-0.23	4.93	-0.23	42.36	-22.77
136	15.967	3.99	-0.77	3.99	-0.77	38.30	

Depth, cm	Age, ka	Uvi. $\delta^{18}O$, ‰PDB	Uvi. $\delta^{13}C$, ‰PDB	Nps. $\delta^{18}O$, ‰PDB	Nps. $\delta^{13}C$, ‰PDB	Mag. Sus., SI	TOC $\delta^{13}C$, ‰PDB
137	15.997	4.98	-0.51	4.98	-0.51	42.85	
138	16.039					44.15	
139	16.095	5.10	-0.58	5.10	-0.58	46.03	
140	16.230	4.98	-0.59	4.98	-0.59	45.48	-22.89
141	16.446	4.64	-0.89	4.64	-0.89	42.56	
142	16.657	4.91	-0.30	4.91	-0.30	88.45	
143	16.871	5.20	-0.37	5.20	-0.37	54.41	
144	17.082	5.32	-0.22	5.32	-0.22	53.07	
145	17.293	5.42	-0.61	5.42	-0.61	49.77	-23.08
146	17.502	5.26	-0.27	5.26	-0.27	49.64	
147	17.713	5.90	0.16	5.90	0.16	47.57	
148	17.924					41.82	
149	18.100					42.52	
150	18.183	5.38	-0.58	5.38	-0.58	75.37	-23.14
151	18.206	5.27	-0.46	5.27	-0.46	65.93	
152	18.229					40.89	
153	18.251	5.37	-0.31	5.37	-0.31	45.65	
154	18.271	5.35	-0.37	5.35	-0.37	37.10	
155	18.291	5.35	-0.40	5.35	-0.40	38.29	-23.11
156	18.305	5.33	-0.26	5.33	-0.26	41.60	
157	18.319	5.44	-0.15	5.44	-0.15	42.61	
158	18.336	5.37	-0.19	5.37	-0.19	44.25	
159	18.354	5.30	-0.21	5.30	-0.21	43.83	
160	18.366	5.42	-0.42	5.42	-0.42	44.14	-22.74
161	18.382	5.39	-0.27	5.39	-0.27	45.38	
162	18.400	5.35	-0.21	5.35	-0.21	45.00	
163	18.417	5.47	-0.24	5.47	-0.24	43.70	
164	18.434	5.37	-0.21	5.37	-0.21	45.72	
165	18.452	5.39	-0.39	5.39	-0.39	48.79	-23.14
166	18.467	5.33	-0.21	5.33	-0.21	47.59	
167	18.482	5.23	-0.28	5.23	-0.28	46.33	
168	18.499	5.24	-0.43	5.24	-0.43	46.11	
169	18.517	5.25	-0.38	5.25	-0.38	44.62	
170	18.535	5.28	-0.93	5.28	-0.93	45.72	-23.18
171	18.552					46.60	
172	18.569	5.17	-0.43	5.17	-0.43	46.79	
173	18.586	5.17	-0.35	5.17	-0.35	45.03	
174	18.600	4.76	-0.52	4.76	-0.52	42.43	
175	18.617	5.38	-0.41	5.38	-0.41	43.72	-23.23
176	18.630					44.94	
177	18.649	5.40	-0.20	5.40	-0.20	43.32	
178	18.665	5.38	-0.30	5.38	-0.30	44.13	
179	18.682	5.27	-0.31	5.27	-0.31	44.81	
180	18.695	5.33	-0.21	5.33	-0.21	43.33	-23.25
181	18.708	4.47	-0.74	4.47	-0.74	41.38	
182	18.727	5.12	-0.54	5.12	-0.54	41.77	
183	18.743	5.37	-0.29	5.37	-0.29	41.79	

Depth, cm	Age, ka	Uvi. $\delta^{18}O$, ‰PDB	Uvi. $\delta^{13}C$, ‰PDB	Nps. $\delta^{18}O$, ‰PDB	Nps. $\delta^{13}C$, ‰PDB	Mag. Sus., SI	TOC $\delta^{13}C$, ‰PDB
184	18.756	4.07	-0.95	4.07	-0.95	43.73	
185	18.772	5.35	-0.46	5.35	-0.46	45.66	-23.18
186	18.790					42.33	
187	18.806					44.85	
188	18.823					42.02	
189	18.839					42.14	
190	18.854	5.28	-0.63	5.28	-0.63	42.54	-23.26
191	18.871					48.71	
192	18.890					48.15	
193	18.912					49.68	
194	18.927					48.31	
195	18.947	5.38	-0.65	5.38	-0.65	45.58	-23.19
196	18.971					43.88	
197	18.994					43.08	
198	19.019					45.32	
199	19.051					44.42	
200	19.072	5.36	-0.27	5.36	-0.27	44.92	-23.00
201	19.085						
202	19.096					44.80	
203	19.105						
204	19.113					44.04	
205	19.121	5.40	-0.25	5.40	-0.25		-23.05
206	19.128					39.94	
207	19.134						
208	19.142					45.44	
209	19.148					44.22	
210	19.156	5.38	-0.26	5.38	-0.26	34.09	-23.06
211	19.165					28.77	
212	19.174					39.25	
213	19.182					43.16	
214	19.189					42.99	
215	19.196	5.29	-0.29	5.29	-0.29	44.30	-23.08
216	19.204					44.93	
217	19.210					43.19	
218	19.216						
219	19.227					42.78	
220	19.232	5.31	-0.33	5.31	-0.33		-23.11
221	19.239					42.97	
222	19.246						
223	19.258					41.37	
224	19.267						
225	19.278	5.40	-0.26	5.40	-0.26	40.31	-23.06
226	19.286						
227	19.297					40.15	
228	19.312						
229	19.338					41.18	
230	19.367	5.38	-0.68	5.38	-0.68		-23.11

Depth, cm	Age, ka	Uvi. $\delta^{18}O$, ‰PDB	Uvi. $\delta^{13}C$, ‰PDB	Nps. $\delta^{18}O$, ‰PDB	Nps. $\delta^{13}C$, ‰PDB	Mag. Sus., SI	TOC $\delta^{13}C$, ‰PDB
231	19.397					40.17	
232	19.425						
233	19.445					42.36	
234	19.465					44.79	
235	19.482	5.40	-0.46	5.40	-0.46	42.87	-23.15
236	19.497					44.03	
237	19.513					48.11	
238	19.525					43.09	
239	19.541					41.93	
240	19.559	5.29	-0.60	5.29	-0.60	39.92	-23.05
241	19.572					39.83	
242	19.589					43.28	
243	19.608						
244	19.621					45.22	
245	19.638	5.35	-0.43	5.35	-0.43		-22.98
246	19.654					48.65	
247	19.672						
248	19.687					49.07	
249	19.703						
250	19.722	5.34	-0.34	5.34	-0.34	49.29	-22.90
251	19.739						
252	19.756					45.37	
253	19.769						
254	19.784					45.46	
255	19.797	5.20	-0.61	5.20	-0.61		-22.94
256	19.815					46.98	
257	19.834					47.32	
258	19.855					44.19	
259	19.877					47.72	
260	19.892	5.42	-0.42	5.42	-0.42	46.61	-23.10
261	19.908					54.64	
262	19.926					51.42	
263	19.943					51.03	
264	19.961					53.50	
265	19.974	5.23	-0.69	5.23	-0.69	51.42	-23.05
266	19.988					49.17	
267	20.003					50.15	
268	20.020					51.24	
269	20.039					51.99	
270	20.055	5.32	-0.37	5.32	-0.37	50.44	-23.00
271	20.073					48.71	
272	20.087					51.34	
273	20.106					50.68	
274	20.119					49.84	
275	20.131	5.21	-0.47	5.21	-0.47	49.62	-22.93
276	20.150					49.17	
277	20.169					52.08	

Depth, cm	Age, ka	Uvi. $\delta^{18}O$, ‰PDB	Uvi. $\delta^{13}C$, ‰PDB	Nps. $\delta^{18}O$, ‰PDB	Nps. $\delta^{13}C$, ‰PDB	Mag. Sus., SI	TOC $\delta^{13}C$, ‰PDB
278	20.191					50.62	
279	20.207					50.55	
280	20.228	5.31	-0.31	5.31	-0.31	55.52	-22.97
281	20.245					51.54	
282	20.264					60.20	
283	20.280					38.26	
284	20.298					57.52	
285	20.320	5.15	-0.76	5.15	-0.76	55.07	-22.87
286	20.340					52.91	
287	20.364					51.86	
288	20.391					52.67	
289	20.445					63.10	
290	20.534	5.41	-0.31	5.41	-0.31	62.94	-22.74
291	20.596					56.66	
292	20.642					68.61	
293	20.691					67.09	
294	20.738					63.79	
295	20.780	5.28	-0.40	5.28	-0.40	60.70	-22.88
296	20.830					58.62	
297	20.874					62.22	
298	20.927					57.03	
299	20.974					60.39	
300	21.017	5.41	-0.37	5.41	-0.37	60.69	-22.91
301	21.060					55.27	
302	21.108					52.09	
303	21.160					63.52	
304	21.205					65.57	
305	21.247	5.31	-0.47	5.31	-0.47	67.09	-22.82
306	21.282					60.77	
307	21.327					63.34	
308	21.389					63.07	
309	21.435					64.88	
310	21.471	5.25	-0.47	5.25	-0.47	67.39	-22.81
311	21.513					69.39	
312	21.558					75.26	
313	21.593					73.93	
314	21.623					77.81	
315	21.673	5.29	-0.40	5.29	-0.40	65.97	-22.72
316	21.715					62.07	
317	21.763					64.97	
318	21.820					68.42	
319	21.858					69.52	
320	21.899	5.31	-0.17	5.31	-0.17	67.43	-22.70
321	21.938					75.59	
322	21.983					69.59	
323	22.031					69.93	
324	22.071					72.66	

Depth, cm	Age, ka	Uvi. $\delta^{18}O$, ‰PDB	Uvi. $\delta^{13}C$, ‰PDB	Nps. $\delta^{18}O$, ‰PDB	Nps. $\delta^{13}C$, ‰PDB	Mag. Sus., SI	TOC $\delta^{13}C$, ‰PDB
372	26.412					90.52	
373	26.550	5.11	-0.05	5.11	-0.05	84.79	
374	26.684					83.83	
375	26.824	4.89	-0.51	4.89	-0.51	94.33	-22.71
376	26.985					94.56	
377	27.131	4.86	-0.15	4.86	-0.15	91.44	
378	27.284					93.64	
379	27.429					88.85	
380	27.594	4.80	-0.43	4.80	-0.43	99.49	-22.52
381	27.749					78.94	
382	27.880	4.80	-0.20	4.80	-0.20	89.77	
383	28.007					54.92	
384	28.134					55.46	
385	28.263	4.88	-0.18	4.88	-0.18	92.51	-22.44
386	28.383					89.57	
387	28.514	5.01	-0.22	5.01	-0.22	83.26	
388	28.643					91.41	
389	28.756					87.15	
390	28.883	4.81	-0.67	4.81	-0.67	85.54	-22.62
391	28.998					83.88	
392	29.106	4.92	-0.30	4.92	-0.30	80.00	
393	29.213					73.33	
394	29.330					67.91	
395	29.447	5.01	-0.03	5.01	-0.03	72.77	-22.53
396	29.542	4.93	-0.15	4.93	-0.15	73.46	
397	29.655					75.16	
398	29.780	4.84	-0.24	4.84	-0.24	68.72	
399	29.900	4.90	-0.31	4.90	-0.31	65.82	
400	30.002	5.03	-0.17	5.03	-0.17	64.52	-22.44
401	30.105					65.58	
402	30.225	4.88	-0.22	4.88	-0.22		
403	30.324					72.46	
404	30.441					65.88	
405	30.558	4.97	-0.05	4.97	-0.05	63.12	-22.29
406	30.687						
407	30.798	4.75	-0.28	4.75	-0.28	69.90	
408	30.910					63.34	
409	31.027					64.22	
410	31.128	4.83	-0.06	4.83	-0.06		-22.27
411	31.237						
412	31.352					54.47	
413	31.485	4.76	-0.45	4.76	-0.45	50.97	
414	31.614						
415	31.771	4.80	-0.35	4.80	-0.35		-22.12
416	32.015					40.59	
417	32.235					35.92	
418	32.377	4.80	-0.30	4.80	-0.30	33.29	

Depth, cm	Age, ka	Uvi. $\delta^{18}O$, ‰PDB	Uvi. $\delta^{13}C$, ‰PDB	Nps. $\delta^{18}O$, ‰PDB	Nps. $\delta^{13}C$, ‰PDB	Mag. Sus., SI	TOC $\delta^{13}C$, ‰PDB
419	32.508						
420	32.637	4.89	-0.20	4.89	-0.20	34.23	-22.16
421	32.748					35.91	
422	32.876	4.77	-0.39	4.77	-0.39	35.30	
423	33.007						
424	33.133					21.54	
425	33.268	4.64	-0.42	4.64	-0.42	27.45	-22.11
426	33.386					29.75	
427	33.519	4.77	-0.37	4.77	-0.37		
428	33.666					25.61	
429	33.851	4.67	-0.27	4.67	-0.27	21.51	
430	34.091	4.69	-0.35	4.69	-0.35	21.02	-22.08
431	34.268						
432	34.392					19.28	
433	34.498	4.53	-0.45	4.53	-0.45	25.87	
434	34.572					24.14	
435	34.665	4.67	-0.52	4.67	-0.52		-21.85
436	34.754						
437	34.843	4.70	-0.39	4.70	-0.39	14.77	
438	34.934					9.30	
439	35.012						
440	35.096	4.75	-0.40	4.75	-0.40		-21.86
441	35.188					7.61	
442	35.272	4.70	-0.44	4.70	-0.44	8.24	
443	35.366					7.68	
444	35.451						
445	35.542	4.81	-0.33	4.81	-0.33	7.20	-21.97
446	35.645	4.72	-0.29	4.72	-0.29	5.89	
447	35.753					6.53	
448	35.914						
449	36.153					7.12	
450	36.414	4.64	-0.66	4.64	-0.66	7.17	-22.08
451	36.553					6.57	
452	36.630						
453	36.703					6.54	
454	36.759	4.79	-0.20	4.79	-0.20	6.48	
455	36.811	4.89	-0.43	4.89	-0.43	7.19	-22.16
456	36.857						
457	36.904					7.21	
458	36.945	4.85	-0.25	4.85	-0.25	7.15	
459	36.994					7.13	
460	37.041	4.85	-0.57	4.85	-0.57		-22.16
461	37.098						
462	37.140	4.89	-0.29	4.89	-0.29	7.09	
463	37.187					7.18	
464	37.230						
465	37.269	4.74	-0.25	4.74	-0.25		-22.08

Depth, cm	Age, ka	Uvi. $\delta^{18}O$, ‰PDB	Uvi. $\delta^{13}C$, ‰PDB	Nps. $\delta^{18}O$, ‰PDB	Nps. $\delta^{13}C$, ‰PDB	Mag. Sus., SI	TOC $\delta^{13}C$, ‰PDB
466	37.313					6.60	
467	37.354					7.09	
468	37.407					7.74	
469	37.467						
470	37.514	4.82	-0.29	4.82	-0.29	7.75	-22.14
471	37.559					7.73	
472	37.607					8.32	
473	37.661						
474	37.703					8.22	
475	37.750	4.75	-0.40	4.75	-0.40	8.12	-22.17
476	37.800					8.26	
477	37.853						
478	37.908					7.56	
479	37.963					8.24	
480	38.013	4.94	-0.28	4.94	-0.28	8.17	-22.05
481	38.053						
482	38.083					7.49	
483	38.142					6.27	
484	38.184					2.91	
485	38.240	4.81	-0.07	4.81	-0.07		-22.35
486	38.278						
487	38.338					9.56	
488	38.380					7.72	
489	38.440						
490	38.485	4.77	-0.21	4.77	-0.21		-21.89
491	38.526					7.72	
492	38.563					7.72	
493	38.601					7.75	
494	38.645						
495	38.688	4.85	-0.26	4.85	-0.26	7.76	-21.90
496	38.741					7.75	
497	38.788					7.68	
498	38.830						
499	38.883					7.50	
500	38.916	4.87	-0.12	4.87	-0.12	7.67	-22.00
501	38.956					7.57	
502	39.006						
503	39.067					0.00	
504	39.108					7.51	
505	39.145	4.86	-0.47	4.86	-0.47	6.46	-21.91
506	39.197						
507	39.254					6.97	
508	39.299					6.96	
509	39.337					7.02	
510	39.396	4.78	-0.11	4.78	-0.11		-21.88
511	39.458						
512	39.526					7.60	

Depth, cm	Age, ka	Uvi. $\delta^{18}O$, ‰PDB	Uvi. $\delta^{13}C$, ‰PDB	Nps. $\delta^{18}O$, ‰PDB	Nps. $\delta^{13}C$, ‰PDB	Mag. Sus., SI	TOC $\delta^{13}C$, ‰PDB
513	39.597					7.63	
514	39.703					7.69	
515	39.819	4.89	0.08	4.89	0.08	7.15	-21.79
516	40.008					7.08	
517	40.159					7.57	
518	40.334					7.09	
519	40.535					7.77	
520	40.826	4.79	0.00	4.79	0.00	7.17	-21.80
521	41.019					7.19	
522	41.175					8.39	
523	41.301					7.26	
524	41.444					7.76	
525	41.600	4.78	0.24	4.78	0.24	7.65	-25.36
526	41.730					6.53	
527	41.832	4.68	0.08	4.68	0.08	7.80	
528	41.960					5.82	
529	42.057					6.42	
530	42.191	4.70	-0.69	4.70	-0.69	7.69	-25.03
531	42.329					7.69	
532	42.428					6.99	
533	42.510					7.57	
534	42.639					7.03	
535	42.750	4.74	-0.07	4.74	-0.07	6.43	-24.40
536	42.910					5.85	
537	43.014	5.00	-0.28	5.00	-0.28	6.51	
538	43.137					6.51	
539	43.235					7.10	
540	43.344	4.79	-0.34	4.79	-0.34	6.52	-22.94
541	43.465					6.56	
542	43.595	5.06	-0.32	5.06	-0.32	6.46	
543	43.675					5.85	
544	43.800					5.92	
545	43.935	4.53	-0.01	4.53	-0.01	6.54	-22.16
546	44.047					6.59	
547	44.161					6.54	
548	44.303					6.50	
549	44.397					7.11	
550	44.518					7.12	-22.05
551	44.633					5.93	
552	44.750					6.54	
553	44.856					6.59	
554	44.970					6.59	
555	45.074	4.78	-0.07	4.78	-0.07	5.94	-22.10
556	45.198					6.61	
557	45.306	4.66	-0.18	4.66	-0.18	6.60	
558	45.420					6.09	
559	45.525					7.26	

Depth, cm	Age, ka	Uvi. $\delta^{18}O$, ‰PDB	Uvi. $\delta^{13}C$, ‰PDB	Nps. $\delta^{18}O$, ‰PDB	Nps. $\delta^{13}C$, ‰PDB	Mag. Sus., SI	TOC $\delta^{13}C$, ‰PDB
560	45.636	4.68	-0.30	4.68	-0.30	6.67	-22.05
561	45.776					5.99	
562	45.899					6.77	
563	46.039					10.30	
564	46.142					6.60	
565	46.284	4.80	-0.20	4.80	-0.20	6.69	-22.09
566	46.411					6.12	
567	46.501					6.68	
568	46.633					7.41	
569	46.732					7.33	
570	46.844	4.79	-0.33	4.79	-0.33	7.42	-22.40
571	46.922					7.27	
572	47.015					7.15	
573	47.193					8.31	
574	47.309					7.81	
575	47.431	4.81	-0.23	4.81	-0.23	7.93	-22.16
576	47.574					7.88	
577	47.723					8.66	
578	47.834					8.45	
579	47.940					7.84	
580	48.040	4.83	-0.09	4.83	-0.09	8.96	-22.16
581	48.128					8.32	
582	48.237					7.79	
583	48.341					7.62	
584	48.453					7.75	
585	48.563	4.96	-0.04	4.96	-0.04	0.00	-22.24
586	48.668					7.41	
587	48.822					6.92	
588	48.915					7.62	
589	49.001					7.63	
590	49.095	4.48	-0.51	4.48	-0.51	7.53	-22.22
591	49.195					7.53	
592	49.314					7.06	
593	49.403					6.93	
594	49.524					6.93	
595	49.603	4.69	-0.06	4.69	-0.06	6.34	-22.13
596	49.703					6.97	
597	49.836	4.52	-0.09	4.52	-0.09	6.90	
598	49.959	4.50	-0.03	4.50	-0.03	7.34	
599	50.077					6.79	
600	50.191	4.54	-0.26	4.54	-0.26	6.77	-21.71
601	50.324					6.93	
602	50.452	4.51	-0.14	4.51	-0.14	7.53	
603	50.588					2.92	
604	50.695					6.51	
605	50.781	4.55	-0.19	4.55	-0.19	7.02	-21.75
606	50.887					6.92	

Depth, cm	Age, ka	Uvi. $\delta^{18}O$, ‰PDB	Uvi. $\delta^{13}C$, ‰PDB	Nps. $\delta^{18}O$, ‰PDB	Nps. $\delta^{13}C$, ‰PDB	Mag. Sus., SI	TOC $\delta^{13}C$, ‰PDB
607	51.001					7.02	
608	51.144					6.47	
609	51.275	4.47	-0.29	4.47	-0.29	5.82	
610	51.354	4.46	-0.59	4.46	-0.59	5.24	-21.90
611	51.466					6.31	
612	51.563	4.35	-0.12	4.35	-0.12	6.88	
613	51.705					6.89	
614	51.828					7.45	
615	51.967	4.70	-0.17	4.70	-0.17	7.33	-22.02
616	52.093					7.29	
617	52.235	4.47	-0.15	4.47	-0.15	7.79	
618	52.381	4.50	-0.05	4.50	-0.05	7.07	
619	52.495					7.83	
620	52.563	4.72	-0.28	4.72	-0.28	7.37	-22.03
621	52.679					7.45	
622	52.818	4.46	-0.02	4.46	-0.02	7.93	
623	52.913					7.48	
624	53.013					7.46	
625	53.121	4.58	-0.35	4.58	-0.35	7.02	-22.26
626	53.248					7.57	
627	53.361					7.61	
628	53.487					6.99	
629	53.581					7.73	
630	53.726	4.60	-0.44	4.60	-0.44	7.68	-22.33
631	53.823					6.98	
632	53.957					7.69	
633	54.083					8.26	
634	54.209					3.56	
635	54.359	4.71	-0.23	4.71	-0.23	7.61	-22.50
636	54.506					8.29	
637	54.649					8.28	
638	54.783					7.64	
639	54.932					7.14	
640	55.091	4.66	-0.71	4.66	-0.71	7.02	-22.60
641	55.251					7.19	
642	55.395					8.85	
643	55.538					6.41	
644	55.676					7.01	
645	55.802	4.62	-0.50	4.62	-0.50	7.02	-22.38
646	55.943					7.10	
647	56.081					6.50	
648	56.215					6.48	
649	56.327					7.17	
650	56.442	4.69	-0.65	4.69	-0.65	6.46	-22.28
651	56.560					6.48	
652	56.683					7.06	
653	56.835					6.55	

Depth, cm	Age, ka	Uvi. $\delta^{18}O$, ‰PDB	Uvi. $\delta^{13}C$, ‰PDB	Nps. $\delta^{18}O$, ‰PDB	Nps. $\delta^{13}C$, ‰PDB	Mag. Sus., SI	TOC $\delta^{13}C$, ‰PDB
655	57.060	4.55	-0.26	4.55	-0.26	6.41	-22.18
656	57.156					6.41	
657	57.254					6.99	
658	57.347					6.44	
659	57.462					7.09	
660	57.612	4.45	-0.81	4.45	-0.81	6.99	-22.13
661	57.721					6.45	
662	57.851					7.67	
663	57.957					7.65	
664	58.099					7.64	
665	58.206	4.61	-0.48	4.61	-0.48	7.01	-22.67
666	58.300					6.39	
667	58.406					6.34	
668	58.518					6.95	
669	58.649					7.54	
670	58.761	4.42	-0.88	4.42	-0.88	6.95	-21.98
671	58.898					7.48	
672	59.004					7.48	
673	59.110					7.48	
674	59.212					8.62	
675	59.331	4.84	-0.34	4.84	-0.34	7.47	-22.03
676	59.428					6.93	
677	59.571					7.05	
678	59.677					7.64	
679	59.767					5.83	
680	59.899	4.54	-0.82	4.54	-0.82	5.42	-22.25
681	60.039					5.87	
682	60.159					7.14	
683	60.278					6.86	
684	60.369					7.38	
685	60.465	4.86	-0.70	4.86	-0.70	7.26	-22.24
686	60.585					0.00	
687	60.694					5.82	
688	60.802					5.38	
689	60.923	4.86	-0.50	4.86	-0.50	4.77	
690	61.029	4.68	-0.75	4.68	-0.75	5.39	-22.27
691	61.148					5.45	
692	61.261	4.66	-0.54	4.66	-0.54	5.48	
693	61.369	4.39	-0.73	4.39	-0.73	5.41	
694	61.492	4.70	-0.52	4.70	-0.52	4.22	
695	61.591	4.84	-0.64	4.84	-0.64	5.39	-22.29
696	61.713	4.75	-0.51	4.75	-0.51	0.00	
697	61.811	4.87	-0.48	4.87	-0.48	6.07	
698	61.897	4.82	-0.58	4.82	-0.58	5.52	
699	62.013	4.82	-0.51	4.82	-0.51	6.10	
700	62.116	4.82	-0.55	4.82	-0.55	6.05	-22.33
701	62.236	4.74	-0.61	4.74	-0.61	5.49	

Depth, cm	Age, ka	Uvi. $\delta^{18}O$, ‰PDB	Uvi. $\delta^{13}C$, ‰PDB	Nps. $\delta^{18}O$, ‰PDB	Nps. $\delta^{13}C$, ‰PDB	Mag. Sus., SI	TOC $\delta^{13}C$, ‰PDB
702	62.350	4.82	-0.57	4.82	-0.57	6.69	
703	62.479	4.76	-0.54	4.76	-0.54	6.06	
704	62.606	4.72	-0.62	4.72	-0.62	6.05	
705	62.722	4.80	-0.60	4.80	-0.60	6.86	-22.37
706	62.843	4.50	-0.55	4.50	-0.55	6.13	
707	62.970	4.73	-0.57	4.73	-0.57	5.48	
708	63.105	4.91	-0.44	4.91	-0.44	6.15	
710	63.378	4.63	-0.84	4.63	-0.84	7.22	-22.66
712	63.646	4.83	-0.48	4.83	-0.48	6.63	
713	63.783	4.41	-0.82	4.41	-0.82	6.76	

A.1.2 GC642

Table A.3: Data from GC642 used in alignment to GC528. *Uvigerina bifurcata* = Uvi. *Neogloboquadrina pachyderma sinistral* = Nps. Magnetic Susceptibility = Mag. Sus.

Depth, cm	Age, ka	Uvi. $\delta^{18}O$, ‰PDB	Uvi. $\delta^{13}C$, ‰PDB	Nps. $\delta^{18}O$, ‰PDB	Nps. $\delta^{13}C$, ‰PDB	Mag. Sus., SI	TOC $\delta^{13}C$, ‰PDB
285	17.000	5.53	-0.02	4.94	1.34	0.00	-22.66
287	17.500	5.38	-0.26	4.12	0.51	62.94	-22.52
289	18.000	5.37	-0.03	4.15	0.36	72.68	-22.60
291	18.500	5.30	-0.19	4.77	1.09	73.29	-22.62
293	19.000	5.40	-0.19	3.87	-0.62	85.25	-22.37
295	19.500	5.42	-0.13	4.18	0.82	77.44	-22.58
301	21.000	5.28	-0.33	5.21	1.05	88.73	-22.55
311	23.500	5.27	-0.21	4.23	0.76	72.82	-22.54
313	24.000	5.50	0.13	4.81	1.14	75.03	-22.56
315	24.500	5.37	0.00	5.00	1.19	85.22	-22.65
317	25.000	5.49	0.13	2.66	0.13	95.91	-22.57
321	28.538	5.28	0.00	4.16	0.96	87.88	-22.46
323	30.308	5.05	-0.07	4.22	0.93	87.32	-22.15
325	32.077	5.11	-0.02	4.10	0.89	81.49	-21.93
327	33.846	4.95	-0.03	4.75	1.28	61.04	-21.96
329	35.615	5.41	0.14	4.36	1.15	77.68	-22.14
331	37.385	5.15	-0.08	4.44	0.85	72.24	-22.05
333	39.154	5.27	0.18	4.14	0.99	56.30	-22.03
335	40.923	4.88	-0.28	3.88	0.73	64.46	-22.03
337	42.692	5.01	-0.02	4.49	1.08	68.23	-22.02
339	44.462	4.85	-0.21	4.67	1.69	63.51	-21.94
341	46.231	5.12	0.04	4.74	1.32	58.13	-21.93
343	48.000	4.84	-0.54	4.22	1.07		-22.11

Depth, cm	Age, ka	Uvi. $\delta^{18}O$, ‰PDB	Uvi. $\delta^{13}C$, ‰PDB	Nps. $\delta^{18}O$, ‰PDB	Nps. $\delta^{13}C$, ‰PDB	Mag. Sus., SI	TOC $\delta^{13}C$, ‰PDB
349	54.500	4.91	-0.17				-22.01
351	56.667	4.98	-0.02				-22.09
353	58.833					43.81	-21.95
355	61.000	4.82	-0.12			37.83	-22.07
357	62.038	4.85	-0.15				-22.20
359	63.077					31.82	-21.85
361	64.115	4.93	-0.16	4.06	1.05	26.44	-21.98
363						16.62	
365	66.192	4.94	-0.18			19.14	-21.83
367	67.231	5.15	0.04			20.38	-21.82
369	68.269					10.69	-21.75
371	69.308	4.58	-0.42			10.08	-21.74
373	70.346	2.89	-1.29			9.01	-21.70
375	71.385	5.77	0.23			8.85	-21.68
377	72.423	4.58	0.09			7.65	-21.59
379	73.462	5.70	0.75			8.33	-21.54
381	74.500	5.26	0.45			7.62	-21.48
383	75.538	4.90	0.24			8.17	-21.59
385	76.577	4.35	-0.13			8.95	-21.66
387	77.615	4.50	-0.13			8.37	-21.86
389	78.654	4.60	-0.17			7.30	-21.74
391	79.692	4.47	-0.11			7.94	-21.65
393	80.731	4.61	-0.05				-21.87
395	81.769	4.54	-0.17			7.80	-21.98
397	82.808	4.76	-0.24			7.83	-22.15
399	83.846	4.71	-0.09				-22.05
401	84.885	5.43	0.08				-22.05
403	85.923	4.48	-0.36				-22.02
405	86.962	4.58	-0.24			7.71	-22.01
407	88.000	4.83	-0.08			7.81	-22.05
409	88.343	4.81	-0.03			8.25	-22.13
411	88.687	4.64	-0.12			7.68	-22.13
413	89.030	5.01	0.08			8.39	-22.08
415	89.374	4.84	-0.04			6.49	-22.03
417	89.717	4.64	-0.11			7.03	-21.86
419	90.061	4.72	0.00				-21.75
421	90.404	4.72	-0.12			5.83	-21.91
423	90.747	4.58	-0.26				-21.87
425	91.091	4.56	-0.18			5.36	-21.75
427	91.434	4.60	-0.05				-21.67
429	91.778	4.44	-0.02			5.48	-21.67
431	92.121	4.58	-0.26				-21.75
433	92.465	4.56	-0.12			5.89	-21.71
435	92.808	4.49	-0.26			4.15	-21.69
437	93.152	4.56	-0.13			5.35	-21.78
439	93.495	4.56	-0.10			6.97	-21.71
441	93.838	4.58	-0.11			6.93	-21.74

Depth, cm	Age, ka	Uvi. $\delta^{18}O$, ‰PDB	Uvi. $\delta^{13}C$, ‰PDB	Nps. $\delta^{18}O$, ‰PDB	Nps. $\delta^{13}C$, ‰PDB	Mag. Sus., SI	TOC $\delta^{13}C$, ‰PDB
443	94.182	4.56	-0.17			6.93	-21.76
445	94.525	4.53	-0.21	3.16	1.84	7.53	-21.82
447	94.869	4.57	-0.26	2.94	0.68		-21.88
449	95.212	4.57	-0.24	3.59	0.83		-21.88
451	95.556	4.54	-0.16	3.87	1.04		-21.88
453	95.899	4.54	-0.27	3.64	0.53		-21.91
455	96.242	4.62	-0.25	3.89	1.23	7.02	-21.92
457	96.586	4.63	-0.27	3.59	1.15	6.98	-21.92
459	96.929	4.50	-0.34			8.09	-22.01
461	97.273	4.55	-0.25			6.45	-22.04
463	97.616	4.70	-0.30			6.31	-22.08
466	98.131	4.47	-0.27			6.56	-22.13
468	98.475	4.58	-0.24			7.04	-22.16
470	98.818	4.54	-0.25			7.70	-22.26
472	99.162	4.62	-0.30				-22.23
474	99.505	4.70	-0.22				-22.37
476	99.848	4.88	-0.35				-22.33
478	100.192	4.81	-0.31	3.99	-0.04		-22.35
480	100.535	4.82	-0.21	3.02	1.48	7.74	-22.34
482	100.879	4.78	-0.23			7.83	-22.29
484	101.222	4.83	-0.06			8.16	-22.23
486	101.566	4.79	-0.17	3.93	0.91	8.40	-22.30
488	101.909	4.64	-0.51			8.36	-22.26
490	102.253	4.67	-0.45			8.40	
492	102.596	4.61	-0.38			7.13	-21.99
494	102.939	4.60	-0.46				-21.85
496	103.283	4.59	-0.42	3.88	0.75	7.21	-22.17
498	103.626	4.60	-0.46	3.92	0.74		-21.98
500	103.970	4.73	-0.49	3.55	0.62	7.76	-21.98
502	104.313	4.75	-0.27	3.42	0.21		-21.98
504	104.657	4.83	-0.39	3.41	0.00	7.73	-22.25
506	105.000	4.70	-0.55	1.43	-0.85		-22.24
508	105.300	4.89	-0.50	3.72	0.22	7.33	-22.28
510	105.600	4.86	-0.41	3.23	-0.22	8.01	-22.20
512	105.900	4.91	-0.55			7.30	-22.24
514	106.200	4.75	-0.40	3.56	-0.20	7.33	-22.49
516	106.500	4.76	-0.64			7.92	-22.57
518	106.800	4.88	-0.57	3.45	-0.23	8.56	-22.61
520	107.100	4.81	-0.58			6.76	-22.65
522	107.400	4.87	-0.53			7.19	-22.70
524	107.700	4.82	-0.54			7.81	-22.79
526	108.000	4.77	-0.47			7.25	-22.85
528	108.500	4.85	-0.57			7.68	-22.92
530	109.000	4.91	-0.55			7.57	-22.93
532	109.500	4.53	-0.39	2.72	0.80	7.97	-22.93
534	110.000	4.47	-0.49	2.45	0.71	10.11	-23.01
536	110.500	4.16	-0.39	2.17	0.56	12.06	-22.92

Depth, cm	Age, ka	Uvi. $\delta^{18}O$, ‰PDB	Uvi. $\delta^{13}C$, ‰PDB	Nps. $\delta^{18}O$, ‰PDB	Nps. $\delta^{13}C$, ‰PDB	Mag. Sus., SI	TOC $\delta^{13}C$, ‰PDB
538	111.000	4.52	-0.31	2.95	0.72	9.64	-23.09
540	111.500	4.55	-0.29	2.53	0.62	9.22	-23.02
542	112.000	4.10	-0.44	2.82	0.79	8.08	-22.94
544	112.500	3.99	-0.55	2.69	0.79	8.76	-22.96
546	113.000	4.05	-0.58	2.14	0.49	6.59	-23.03
548	114.500	3.72	-0.57	2.54	0.67	8.29	-22.70
550	116.000	4.25	-0.45	2.00	0.19	8.06	-22.81
552	117.500	4.27	-0.49	2.22	0.44	8.77	-22.76
554	119.000	4.06	-0.36	2.51	0.22	8.37	-22.98
556	119.400	4.11	-0.52	2.71	0.58	5.03	-22.95
558	119.800	3.95	-0.78	2.11	0.26	6.81	-22.95
560	120.200	3.89	-0.58	1.79	0.08	6.21	-22.93
562	120.600	4.29	-0.55	2.13	0.10	5.23	-22.87
564	121.000	3.64	-0.76	2.01	0.16	10.65	-23.34
566	121.400	4.06	-0.20	1.90	0.07	4.49	-22.97
568	121.800	3.53	-0.44	1.79	-0.15	3.39	-23.10
571	122.400			1.97	0.06	0.00	-23.15
573	122.800	4.22	-0.79	1.73	-0.07	4.48	-23.11
575	123.200			2.13	0.20	4.60	-23.09
577	123.600			1.94	-0.02	5.30	-23.15
579	124.000			2.13	0.20	5.30	-23.08
581	124.400			2.03	0.01	5.71	-22.77
583	124.800	3.54	-0.45	1.94	-0.03	5.15	-22.46
585	125.200			1.89	-0.13	2.31	-22.75
587	125.600			1.76	-0.13	5.28	-22.85
589	126.000			1.74	-0.33	5.79	-22.81
591	126.200			1.82	-0.34	5.73	-22.57
593	126.400	5.35	-0.58	1.75	-0.35	5.66	-22.11
595	126.600	3.37	-0.67	1.87	-0.28	6.43	-22.07
597	126.800			1.89	-0.28	5.31	-22.04
599	127.000			1.75	-0.32	5.96	-22.02
601	127.200	4.00	-0.86	1.77	-0.13	5.92	-21.98
603	127.400	3.64	-0.79	1.75	-0.54	5.36	-21.88
605	127.600	3.76	-0.39	1.81	-0.06	6.01	-22.21
607	127.800	3.41	-0.77	1.97	-0.34	5.36	-21.94
609	128.000	4.26	-0.49	1.59	-0.56	5.44	-21.79
611	129.667	3.85	-0.48	1.79	-0.66	5.89	-21.65
613	131.333	4.61	-0.56	1.55	-0.68	8.22	-22.15
615	133.000			2.12	-0.63	9.35	-22.79
617	134.667					9.48	-22.89
619	136.333					17.10	-22.82
621	138.000	5.08	-0.63			19.32	-22.90
623	139.667					14.21	-22.87
625	141.333	5.09	-0.40			11.88	-22.86
627	143.000	4.88	-0.72			14.58	-22.65
629	144.667	4.86	-0.62			18.00	-22.64
631	146.333	4.74	-0.68			22.78	-22.70

Depth, cm	Age, ka	Uvi. $\delta^{18}O$, ‰PDB	Uvi. $\delta^{13}C$, ‰PDB	Nps. $\delta^{18}O$, ‰PDB	Nps. $\delta^{13}C$, ‰PDB	Mag. Sus., SI	TOC $\delta^{13}C$, ‰PDB
633	148.000	4.89	-0.67			24.35	-22.79
635	149.529	4.96	-0.80			27.56	-23.03
637	151.176	4.89	-0.90			29.67	-22.77
639	152.824	4.99	-0.58			34.19	-22.65
641	154.471	5.01	-0.56			31.21	-22.79
643	156.118					29.32	-22.88
645	157.765	5.01	-0.80			45.36	-23.00
647	159.412	5.10	-0.60	4.22	0.55	0.00	-22.91
649	161.059	4.97	-0.62	4.13	0.55	58.28	-22.79
651	162.706	3.80	-1.36	4.98	1.17	58.43	-22.67
653	164.353	5.04	-0.48	4.03	0.21	52.49	-22.59
655	166.000	4.72	-0.77	4.17	0.33	56.61	-22.45
657	167.415	4.66	-1.19			48.07	-22.54
659	168.829	3.45	-1.60			52.44	-22.72
661	170.244	4.65	-1.09				-22.87
663	171.659					25.47	-22.73
665	173.073					37.39	-22.89
668	175.195					31.01	-22.93
670	176.610					41.99	-22.87
672	178.024	4.53	-1.21			44.84	-22.87
674	179.439	4.60	-1.24			52.60	-23.09
676	180.854	4.64	-0.79	3.76	0.20	58.37	-22.88
678	182.268	4.48	-1.55	3.86	0.56	49.18	-22.78
680	183.683	4.42	-1.01	3.89	0.62	45.85	-22.65
682	185.098	4.41	-0.93	4.15	0.78	41.12	-22.72
684	186.512	4.58	-1.30	3.81	0.48	30.64	-22.86
686	187.927	4.37	-0.81	3.69	0.32		-22.59
688	189.341	4.17	-0.82	3.93	0.38	22.89	-22.71
690	190.756	4.25	-0.89	3.66	0.69	14.66	-22.87
692	192.171	4.30	-0.41	3.83	0.46	15.09	-22.34
694	193.585	3.81	-0.76	3.34	-0.10	11.60	-22.37
696	195.000	3.64	-0.76	2.99	0.08	13.97	-22.14
698	199.833	3.60	-0.55	2.17	-0.18		-22.12
700	204.667	3.44	-0.84	3.76	0.34	7.94	-21.95
702	209.500	3.42	-0.87	2.51	-0.55		-22.59
704	214.333	3.59	-0.46	2.31	-0.63	13.50	-22.13
706	219.167	3.67	-0.64	2.23	-0.82	8.20	-22.05
708	224.000	4.32	-1.15	2.52	-0.53	10.29	-22.41
710	224.643	3.61	-0.82	2.67	-0.14	11.58	-22.34
712	225.286	4.35	-0.72	3.28	0.34	12.36	-22.54
714	225.929	4.37	-0.75	3.25	0.57		-22.53
716	226.571	4.40	-0.80	2.37	-0.25	11.74	-22.54
718	227.214	4.71	-0.64	-1.15	-1.70	11.89	-22.57
720	227.857	4.18	-0.80	3.27	-0.11	13.80	-22.66
722	228.500	4.54	-0.75	-3.57	-3.10	12.55	-22.57
724	229.143	4.61	-0.45	2.04	-0.59	14.67	-22.51
726	229.786	4.50	-0.68	2.61	0.02	14.83	-22.72

Table A.4: GC642 Alkenone Data

Depth, cm	Age, ka	U^K_{37}	SST, °C	C_{37} conc., μg/g	ΣC_{37}:ΣC_{38}
506	105.0	0.266	5.78	1.98	1.389
508	105.3	0.220	4.25	5.11	1.110
510	105.6	0.161	2.28	1.37	1.384
512	105.9	0.169	2.54	5.55	1.167
514	106.2	0.184	3.03	0.80	1.356
516	106.5	0.178	2.83	1.32	1.457
518	106.8	0.218	4.17	2.67	2.292
520	107.1	0.148	1.84	4.43	1.352
522	107.4	0.158	2.17	1.07	1.417
524	107.7	0.145	1.73	0.83	1.270
526	108.0	0.196	3.44	0.86	2.429
528	108.5	0.175	2.72	1.02	1.447
530	109.0	0.158	2.18	3.08	1.375
532	109.5	0.166	2.42	0.97	2.278
534	110.0	0.137	1.47	0.60	1.329
536	110.5	0.167	2.46	1.41	1.413
538	111.0	0.161	2.28	0.56	3.027
540	111.5	0.192	3.29	0.70	1.492
542	112.0	0.190	3.22	1.05	1.475
544	112.5	0.192	3.29	0.64	1.091
546	113.0	0.180	2.90	0.65	1.339
548	114.5	0.233	4.66	1.80	1.487
550	116.0	0.327	7.80	3.82	1.239
552	117.5	0.325	7.72	2.18	1.548
554	119.0	0.386	9.77		0.382
556	119.4	0.369	9.20	1.51	1.321
558	119.8	0.381	9.60	2.01	1.312
560	120.2	0.376	9.43	3.10	1.674
562	120.6	0.363	9.00	4.51	1.449
564	121.0	0.185	3.08	1.65	1.524
566	121.4	0.387	9.79	3.01	1.465
568	121.8	0.416	10.77	1.98	1.335
571	122.4	0.400	10.24	5.81	1.353
573	122.8	0.407	10.48	3.06	0.071
575	123.2	0.404	10.38	2.52	1.829
577	123.6	0.418	10.85		0.000
581	124.4	0.394	10.02	4.52	1.836
583	124.8	0.443	11.67	0.35	1.580

Depth, cm	Age, ka	U_{37}^{K}	SST, °C	C_{37} conc., μg/g	ΣC_{37}:ΣC_{38}
585	125.2	0.394	10.02	2.71	3.681
587	125.6	0.417	10.79	3.68	1.511
589	126.0	0.426	11.09	1.85	1.639
591	126.2	0.458	12.15	12.79	1.330
593	126.4	0.463	12.32	1.53	1.728
595	126.6	0.408	10.49	5.54	5.505
597	126.8	0.501	13.60	3.24	1.452
599	127.0	0.504	13.71	3.79	1.639
601	127.2	0.537	14.80	16.04	1.382
603	127.4	0.421	10.93	2.14	2.061
605	127.6	0.483	13.01	3.24	1.811
607	127.8	0.494	13.38	3.37	1.853
609	128.0	0.527	14.48	12.56	1.498
611	129.7	0.526	14.43	2.96	1.920
613	131.3	0.326	7.77	0.98	1.653
615	133.0	0.311	7.25	5.90	1.666
617	134.7	0.058	-1.17	0.26	1.796
619	136.3	0.091	-0.06	0.67	1.592
621	138.0	0.064	-0.97	0.44	2.458
623	139.7	0.079	-0.48	0.62	1.674
625	141.3	0.054	-1.29	1.17	1.936

Table A.5: Tiepoints used in the age model for GC642.

Depth, cm	Age, ka	Alignment method
285	17	Tuning benthic $\delta^{18}O$ to LR04 with constant offset of 0.8‰
317	25	Tuning benthic $\delta^{18}O$ to LR04 with constant offset of 0.8‰
343	48	Tuning benthic $\delta^{18}O$ to LR04 with constant offset of 0.8‰
355	61	Tuning benthic $\delta^{18}O$ to LR04 with constant offset of 0.8‰
407	88	Tuning benthic $\delta^{18}O$ to LR04 with constant offset of 0.8‰
506	105	Tuning alkenone-derived SST to Antarctic temperatures
526	108	Tuning alkenone-derived SST to Antarctic temperatures
546	113	Tuning alkenone-derived SST to Antarctic temperatures
554	119	Tuning alkenone-derived SST to Antarctic temperatures
579	124	Tuning alkenone-derived SST to Antarctic temperatures
609	128	Tuning alkenone-derived SST to Antarctic temperatures
633	148	Tuning alkenone-derived SST to Antarctic temperatures
655	166	Tuning benthic $\delta^{18}O$ to LR04 with constant offset of 0.8‰
696	195	Tuning benthic $\delta^{18}O$ to LR04 with constant offset of 0.8‰
708	224	Tuning benthic $\delta^{18}O$ to LR04 with constant offset of 0.8‰
736	233	Tuning benthic $\delta^{18}O$ to LR04 with constant offset of 0.8‰

A.2 Chapter 4: Stable isotope and ICP-OES Data

A.2.1 GC528

Table A.6: All $\delta^{18}O$ and $\delta^{13}C$ data measured on *Uvigerina bifurcata* and *Oridorsalis umbonatus* in core GC528 between 0-350cm.

Depth, cm	Uvi. $\delta^{18}O$, ‰PDB	Uvi. $\delta^{13}C$, ‰PDB	Or. $\delta^{18}O$, ‰PDB	Or. $\delta^{13}C$, ‰PDB
1	3.04	-0.79		
2			3.03	-0.31
4			3.08	-0.43
5	3.12	-0.51	3.03	-0.29
8			3.07	-0.46
9			3.11	-0.40
10	3.08	-0.59	2.97	-0.31
11	3.15	-0.69	3.06	-0.24
12	3.25	-0.60	3.02	-0.33
14	3.12	-0.72		
15	3.20	-0.57	2.94	-0.45
16	3.03	-0.74	3.03	-0.39
20	3.09	-0.66	2.93	-0.40
21	3.18	-0.53	3.03	-0.32
22	3.33	-0.41	2.99	-0.36
23	3.29	-0.50	2.96	-0.32
24	3.15	-0.53	2.91	-0.39
25	3.30	-0.52	2.87	-0.35
27	3.27	-0.53	2.92	-0.37
29	2.87	-0.72	3.00	-0.40
30	3.15	-0.69	2.93	-0.47
32	3.12	-0.57	3.01	-0.39
33	2.95	-0.90	2.95	-0.37
34	3.20	-0.63	3.07	0.18
35	3.15	-0.62	2.94	-0.36
36	2.92	-0.55	3.01	-0.39
37	3.46	-0.43	3.10	0.10
38	2.27	-0.89	2.43	-0.67
39	3.21	-0.62	2.93	-0.39
40	3.16	-0.59	2.99	-0.35
41	2.82	-0.64	3.04	-0.27
42	3.23	-0.55	3.08	-0.33
43	3.18	-0.62	3.04	-0.20

Depth, cm	Uvi. $\delta^{18}O$, ‰PDB	Uvi. $\delta^{13}C$, ‰PDB	Or. $\delta^{18}O$, ‰PDB	Or. $\delta^{13}C$, ‰PDB
43	3.18	-0.62	3.04	-0.20
44	3.23	-0.77	3.12	-0.42
45	3.27	-0.52	2.97	-0.46
46	3.32	-0.54	2.91	-0.46
47	3.11	-0.51	2.69	-0.66
48	3.06	-0.61	2.84	-0.50
50	3.13	-0.71	3.01	-0.51
52	3.44	-0.62	2.91	-0.39
53	3.32	-0.52	3.07	-0.28
54	3.70	-0.44	2.40	-0.81
55	3.32	-0.53	3.12	-0.41
56	3.59	-0.44	3.20	-0.39
57	3.30	-0.40	3.22	-0.56
58	3.60	-0.35	3.13	-0.39
59	4.06	-0.39	2.76	-0.60
60	4.22	-0.52	3.11	-0.58
63	3.85	-0.43	0.69	-1.42
64	4.34	-0.23	3.16	-0.54
65	4.35	-0.23	3.13	-0.17
66	4.23	-0.41	2.95	-0.37
67	3.94	-0.35	3.50	-0.37
68	4.40	-0.27	3.21	-0.53
69	4.23	-0.31		
70	3.98	-0.42	3.24	-0.34
72	4.24	-0.19	3.11	-0.44
73	4.29	-0.23	2.91	-0.46
74	4.25	-0.23		
75	4.33	-0.42	3.98	-0.61
76	4.52	-0.21	3.94	-0.64
77	4.37	-0.23		
78	4.31	-0.15		
79	4.37	-0.17		
80	4.25	-0.14		
81	4.41	-0.16	3.66	-0.66
82	4.26	-0.13	3.08	-0.53
83	4.16	-0.34	3.09	-0.45
84	4.23	-0.25	3.14	-0.55
85	4.23	-0.55	3.21	-0.25
86	4.29	-0.39	2.97	-0.39
87	4.26	-0.16	3.24	-0.64
88	4.34	-0.23		
89	4.12	-0.42		
90	4.22	-0.27	3.09	-0.44
92	4.40	-0.13		
93	4.38	-0.13		
94	4.35	-0.38		
95	4.38	-0.35		

Depth, cm	Uvi. $\delta^{18}O$, ‰PDB	Uvi. $\delta^{13}C$, ‰PDB	Or. $\delta^{18}O$, ‰PDB	Or. $\delta^{13}C$, ‰PDB
96	3.94	-0.76	3.71	-0.04
97	3.18	-0.74	3.36	-0.08
98	4.44	-0.19	3.02	-0.51
99	4.81	-0.21	3.30	-0.32
100	4.33	-0.43		
101	3.99	-0.32		
102	4.51	-0.18	0.06	-1.69
103	4.35	-0.28	3.57	-0.09
104	4.38	-0.23	4.05	-0.62
105	4.31	-0.28	3.56	-0.98
106	4.48	-0.09		
107	4.50	-0.23		
108	4.84	-0.33	4.07	-0.52
109	4.16	-0.66		
110	4.27	-0.28	3.62	-0.71
112	4.44	-0.30		
113	4.53	-0.29		
114	4.79	-0.30		
115	4.77	-0.31		
116	5.30	-0.35		
117	4.83	-0.33		
120	4.23	-0.52		
124	3.91	-0.52		
125	4.97	-0.62		
127	5.30	-0.57		
128	5.24	-0.37		
129	5.25	-0.34		
130	4.83	-0.35		
133	4.90	-0.37		
134	4.94	-0.04		
135	4.93	-0.23		
136	3.99	-0.77		
137	4.98	-0.51		
139	5.10	-0.58		
140	4.98	-0.59		
141	4.64	-0.89		
142	4.91	-0.30		
143	5.20	-0.37		
144	5.32	-0.22		
145	5.42	-0.61	3.36	-0.76
146	5.26	-0.27		
147	5.90	0.16		
150	5.38	-0.58		
151	5.27	-0.46		
153	5.37	-0.31		
154	5.35	-0.37		
155	5.35	-0.40		

Depth, cm	Uvi. $\delta^{18}O$, ‰PDB	Uvi. $\delta^{13}C$, ‰PDB	Or. $\delta^{18}O$, ‰PDB	Or. $\delta^{13}C$, ‰PDB
156	5.33	-0.26		
157	5.44	-0.15		
158	5.37	-0.19		
159	5.30	-0.21		
160	5.42	-0.42		
161	5.39	-0.27		
162	5.35	-0.21		
163	5.47	-0.24		
164	5.37	-0.21		
165	5.39	-0.39		
166	5.33	-0.21		
167	5.23	-0.28	3.45	-0.12
168	5.24	-0.43		
169	5.25	-0.38		
170	5.28	-0.93		
172	5.17	-0.43	1.43	-1.55
173	5.17	-0.35		
174	4.76	-0.52		
175	5.38	-0.41		
177	5.40	-0.20		
178	5.38	-0.30		
179	5.27	-0.31		
180	5.33	-0.21	2.93	-0.33
181	4.47	-0.74		
182	5.12	-0.54		
183	5.37	-0.29		
184	4.07	-0.95		
185	5.35	-0.46		
190	5.28	-0.63		
195	5.38	-0.65		
200	5.36	-0.27		
205	5.40	-0.25		
210	5.38	-0.26		
215	5.29	-0.29		
220	5.31	-0.33		
225	5.40	-0.26		
230	5.38	-0.68		
235	5.40	-0.46		
240	5.29	-0.60		
245	5.35	-0.43		
250	5.34	-0.34		
255	5.20	-0.61		
260	5.42	-0.42		
265	5.23	-0.69		
270	5.32	-0.37		
275	5.21	-0.47		
280	5.31	-0.31		

Depth, cm	Uvi. $\delta^{18}O$, ‰PDB	Uvi. $\delta^{13}C$, ‰PDB	Or. $\delta^{18}O$, ‰PDB	Or. $\delta^{13}C$, ‰PDB
285	5.15	-0.76		
290	5.41	-0.31		
295	5.28	-0.40		
300	5.41	-0.37		
305	5.31	-0.47		
310	5.25	-0.47		
315	5.29	-0.40		
320	5.31	-0.17		
325	5.45	-0.36		
330	5.33	-0.32		
335	5.42	-0.30		
340	5.25	-0.50		
345	5.19	-0.28		

Table A.7: GC528 Benthic temperature, *Uvigerina bifurcata* $\delta^{18}O$, seawater $\delta^{18}O$. Numbers in bold have been interpolated from Table A.6 rather than directly measured. Ox = oxidative cleaning. Non-ox = clay removal and silicate removal only. See Barker et al. (2003) for details.

Depth, cm	Age, ka	Uvi. Mg/Ca, mmol/mol	Cleaning	Benthic Temp, °C	Uvi. $\delta^{18}O$, ‰PDB	Seawater $\delta^{18}O$, ‰SMOW
1	1.0185	1.20	Ox	3.93	3.04	0.07
4	1.104	1.13	Ox	3.15	**2.64**	-0.52
8	1.3835	1.07	Ox	2.42	**2.79**	-0.56
12	1.8014	1.28	Ox	4.79	3.25	0.49
16	2.2908	1.18	Ox	3.63	3.03	-0.01
21	2.8824	1.15	Ox	3.30	3.18	0.05
24	3.2789	1.18	Ox	3.69	3.15	0.11
28	4.3329	1.10	Ox	2.78	**3.12**	-0.14
32	4.6171	1.23	Ox	4.20	3.20	0.29
34	5.1459	1.13	Ox	3.10	2.27	-0.91
38	5.5475	1.16	Ox	3.51	2.82	-0.26
41	5.6922	1.03	Ox	2.00	3.23	-0.23
42	5.9825	1.27	Ox	4.70	3.23	0.45
44	6.2541	1.13	Ox	3.18	3.32	0.16
46	6.5146	1.13	Ox	3.08	3.06	-0.12
48	7.8357	1.10	Ox	2.78	3.70	0.44
52	8.259	0.97	Ox	1.41	3.59	-0.01
54	8.581	0.97	Ox	1.39	3.60	0.00
56	9.6605	0.89	Ox	0.56	3.98	0.16

Depth, cm	Age, ka	Uvi. Mg/Ca, mmol/mol	Cleaning	Benthic Temp, °C	Uvi. $\delta^{18}O$, ‰PDB	Seawater $\delta^{18}O$, ‰SMOW
58	10.4321	0.83	Ox	-0.13	4.34	0.35
62	11.1809	0.85	Ox	0.12	**4.23**	0.31
64	11.9125	0.96	Ox	1.25	4.40	0.75
66	12.7489	0.87	Ox	0.33	4.24	0.37
68	12.8543	0.90	Ox	0.65	4.25	0.46
72	12.9339	0.82	Ox	-0.27	4.52	0.49
74	12.9829	0.87	Ox	0.25	4.31	0.41
76	13.051	0.85	Ox	0.06	4.41	0.47
78	13.0705	0.84	Ox	0.00	4.26	0.30
81	13.1094	0.82	Ox	-0.27	4.23	0.21
82	13.1533	0.87	Ox	0.28	4.29	0.41
84	13.2041	0.79	Ox	-0.62	4.34	0.23
86	13.3183	0.85	Ox	0.07	4.40	0.46
88	13.3807	0.95	Ox	1.15	4.35	0.68
59	4.06	-0.39	2.76	-0.60		
60	4.22	-0.52	3.11	-0.58		
63	3.85	-0.43	0.69	-1.42		
64	4.34	-0.23	3.16	-0.54		
65	4.35	-0.23	3.13	-0.17		
66	4.23	-0.41	2.95	-0.37		
67	3.94	-0.35	3.50	-0.37		
68	4.40	-0.27	3.21	-0.53		
69	4.23	-0.31				
70	3.98	-0.42	3.24	-0.34		
72	4.24	-0.19	3.11	-0.44		
73	4.29	-0.23	2.91	-0.46		
74	4.25	-0.23				
75	4.33	-0.42	3.98	-0.61		
76	4.52	-0.21	3.94	-0.64		
77	4.37	-0.23				
78	4.31	-0.15				
79	4.37	-0.17				
80	4.25	-0.14				
81	4.41	-0.16	3.66	-0.66		
82	4.26	-0.13	3.08	-0.53		
83	4.16	-0.34	3.09	-0.45		
84	4.23	-0.25	3.14	-0.55		
85	4.23	-0.55	3.21	-0.25		
86	4.29	-0.39	2.97	-0.39		
87	4.26	-0.16	3.24	-0.64		
88	4.34	-0.23				
89	4.12	-0.42				
90	4.22	-0.27	3.09	-0.44		
92	4.40	-0.13				
93	4.38	-0.13				
94	4.35	-0.38				
95	4.38	-0.35				

Depth, cm	Age, ka	Uvi. Mg/Ca, mmol/mol	Cleaning	Benthic Temp, °C	Uvi. $\delta^{18}O$, ‰PDB	Seawater $\delta^{18}O$, ‰SMOW
96	13.5918	0.89	Ox	0.55	4.51	0.70
98	13.6268	0.94	Ox	1.01	4.38	0.68
102	13.6617	0.82	Ox	-0.21	4.48	0.47
104	13.6958	0.83	Ox	-0.19	4.84	0.84
106	13.7564	0.90	Ox	0.66	4.36	0.57
108	13.8413	0.79	Ox	-0.64	4.79	0.67
111	13.9194	0.70	Ox	-1.62	**5.30**	0.94
114	14.0218	0.69	Ox	-1.71	4.63	0.25
116	14.5321	0.77	Ox	-0.81	3.91	-0.24
118	14.6986	0.72	Ox	-1.33	**5.13**	0.85
124	14.8324	0.78	Ox	-0.64	5.24	1.12
126	15.0274	0.70	Ox	-1.60	**4.85**	0.49
128	15.2133	0.78	Ox	-0.68	4.94	0.82
131	15.3368	0.71	Ox	-1.45	**3.99**	-0.32
134	15.4616	0.98	Ox	1.49	5.04	1.46
136	15.6597	0.80	Ox	-0.52	4.64	0.56
138	15.7319	1.03	Ox	2.08	4.91	1.47
141	15.8757	0.79	Ox	-0.54	5.32	1.23
142	16.0205	0.76	Ox	-0.96	5.26	1.07
144	16.1717	0.72	Ox	-1.40	5.73	1.42
146	16.4087	0.59	Ox	-2.74	5.32	0.68
148	16.4961	0.66	Ox	-2.02	**5.35**	0.89
152	16.5785	0.64	Ox	-2.23	**5.33**	0.82
154	16.6556	0.67	Ox	-1.87	5.37	0.95
156	16.7691	0.76	Ox	-0.90	5.39	1.21
158	16.8064	0.73	Ox	-1.21	5.35	1.09
161	16.8822	0.63	Ox	-2.37	5.37	0.82
162	17.0341	0.66	Ox	-1.99	5.24	0.79
164	17.1492	0.69	Ox	-1.73	5.22	0.84
168	17.2634	0.80	Ox	-0.43	4.76	0.70
171	17.3391	0.69	Ox	-1.69	**5.39**	1.01
174	17.5277	0.66	Ox	-2.04	4.47	0.00
176	17.5669	0.67	Ox	-1.90	**5.12**	0.69
181	17.6448	0.66	Ox	-1.97	4.07	-0.38
182	17.7216	0.65	Ox	-2.13	5.33	0.85
184	18.1829	0.65	Ox	-2.06	5.37	0.90
186	18.3125	0.71	Ox	-1.44	**5.38**	1.06
198	18.5549	0.67	Ox	-1.91	**5.35**	0.91
202	18.8271	0.66	Ox	-1.97	**5.38**	0.94
212	19.1117	0.71	Ox	-1.48	**5.38**	1.05
224	19.4133	0.69	Ox	-1.71	**5.34**	0.96
236	19.6965	0.77	Ox	-0.79	**5.38**	1.23
248	20.0261	0.67	Ox	-1.87	**5.28**	0.86
259	20.3356	0.70	Ox	-1.52	**5.19**	0.85
272	20.4386	0.66	Ox	-1.97	**5.31**	0.86
284	20.5805	0.75	Ox	-1.02	**5.33**	1.12
288	20.6819	0.68	Ox	-1.75	**5.30**	0.91

Depth, cm	Age, ka	Uvi. Mg/Ca, mmol/mol	Cleaning	Benthic Temp, °C	Uvi. $\delta^{18}O$, ‰PDB	Seawater $\delta^{18}O$, ‰SMOW
293	20.8091	0.76	Ox	-0.93	**5.38**	1.19
296	21.0209	0.76	Ox	-0.88	**5.33**	1.16
299	21.1898	0.69	Ox	-1.72	**5.28**	0.89
304	21.403	0.76	Ox	-0.88	**5.28**	1.10
308	21.5292	0.71	Ox	-1.51	**5.29**	0.96
313	21.737	0.67	Ox	-1.91	**5.34**	0.91
316	21.861	0.76	Ox	-0.92	**5.42**	1.24
321	22.0256	0.77	Ox	-0.80	**5.38**	1.22
324	22.1914	0.71	Ox	-1.45	**5.36**	1.04
328	22.3602	0.71	Ox	-1.48	**5.39**	1.06
332	22.5754	0.72	Ox	-1.32	**5.24**	0.95
336	22.7023	0.74	Ox	-1.08	**5.20**	0.97
341	22.8685	0.74	Ox	-1.17	**5.14**	0.89
344	22.8685	0.74	Ox	-1.17	**5.14**	0.89

A.2.2 MD07-3076Q

Table A.8: MD07-3076Q Benthic temperature, *Uvigerina bifurcata* $\delta^{18}O$, seawater $\delta^{18}O$. Numbers in bold have been interpolated rather than directly measured. Ox = oxidative cleaning. Non-ox = clay removal and silicate removal only. See Barker et al. (2003) for details.

Depth, cm	Age, ka	Uvi. Mg/Ca, mmol/mol	Cleaning	Benthic Temp, °C	Uvi. $\delta^{18}O$, ‰PDB	Seawater $\delta^{18}O$, ‰SMOW
1.5	1.203	0.960	Ox	0.960	1.27	3.23
3.5	1.414	0.983	Ox	0.983	1.53	3.24
8.5	2.010	0.968	Ox	0.968	1.36	**3.26**
11.5	2.593	0.972	Ox	0.972	1.41	3.26
13.5	2.945	0.955	Ox	0.955	1.22	3.26
16.5	3.417	1.069	Ox	1.069	2.47	**3.25**
19.5	4.255	0.956	Ox	0.956	1.23	3.25
23.5	5.196	0.987	Ox	0.987	1.57	3.27
24.5	5.311	0.986	Ox	0.986	1.56	**3.28**
27.5	5.953	1.014	Ox	1.014	1.86	3.35
30.5	6.395	0.922	Non-ox	0.877	0.37	3.39
32.5	6.602	1.030	Ox	1.030	2.04	**3.39**
33.5	6.780	0.988	Ox	0.988	1.58	3.39
37.5	7.497	1.033	Ox	1.033	2.07	3.38
39.5	7.976	1.080	Ox	1.080	2.59	3.36
40.5	8.216	0.952	Non-ox	0.906	0.69	3.34

Depth, cm	Age, ka	Uvi. Mg/Ca, mmol/mol	Cleaning	Benthic Temp, °C	Uvi. $\delta^{18}O$, ‰PDB	Seawater $\delta^{18}O$, ‰SMOW
40.5	8.096	0.936	Ox	0.936	1.02	3.34
43.5	8.904	0.976	Ox	0.976	1.45	3.46
47.5	9.678	1.066	Ox	1.066	2.43	3.40
49.5	10.003	0.853	Ox	0.853	0.11	3.63
50.5	10.144	1.365	Non-ox	1.320	5.21	3.75
50.5	10.144	0.903	Ox	0.903	0.65	3.75
51.5	10.286	1.231	Ox	1.231	4.24	**3.89**
54.5	10.708	1.229	Non-ox	1.184	3.72	**4.30**
64.5	12.015	1.202	Non-ox	1.156	3.42	**4.62**
65.5	12.189	1.188	Ox	1.188	3.77	4.64
67.5	12.536	1.040	Ox	1.040	2.15	**4.43**
68.5	12.621	1.144	Non-ox	1.098	2.79	4.37
69.5	12.705	1.058	Ox	1.058	2.35	**4.36**
70.5	12.790	1.275	Non-ox	1.230	4.22	**4.36**
71.5	12.874	1.076	Ox	1.076	2.54	**4.35**
72.5	12.959	1.055	Non-ox	1.009	1.81	4.37
72.5	12.959	1.139	Ox	1.139	3.23	4.37
74.5	13.134	1.086	Non-ox	1.040	2.15	4.47
74.5	13.134	1.228	Non-ox	1.183	3.71	4.47
74.5	13.134	1.160	Ox	1.160	3.46	4.47
74.5	13.134	1.052	Ox	1.052	2.27	4.47
76.5	13.314	1.086	Non-ox	1.040	2.15	4.51
78.5	13.524	1.039	Non-ox	0.993	1.64	4.54
78.5	13.524	1.065	Non-ox	1.020	1.93	4.54
80.5	13.764	1.064	Non-ox	1.018	1.91	4.53
80.5	13.764	1.042	Ox	1.042	2.17	4.53
82.5	14.003	1.235	Non-ox	1.190	3.78	4.62
82.5	14.003	1.159	Non-ox	1.114	2.95	4.62
86.5	14.439	1.020	Non-ox	0.975	1.43	4.74
86.5	14.439	0.975	Non-ox	0.930	0.94	4.74
92.5	14.828	1.094	Non-ox	1.048	2.24	**4.90**
92.5	14.828	0.932	Ox	0.887	0.47	**4.90**
94.5	14.902	0.999	Non-ox	0.954	1.21	4.95
94.5	14.902	1.117	Non-ox	1.071	2.49	4.95
94.5	14.902	0.987	Non-ox	0.942	1.07	4.95
94.5	14.902	1.036	Non-ox	0.990	1.61	4.95
94.5	14.902	0.999	Non-ox	0.954	1.20	4.95
94.5	14.902	0.932	Ox	0.932	0.96	4.95
94.5	14.902	0.929	Ox	0.929	0.93	4.95
96.5	15.005	1.026	Non-ox	0.981	1.50	4.84
96.5	15.005	0.945	Ox	0.945	1.11	4.84
100.5	15.344	1.024	Non-ox	0.979	1.48	4.99
100.5	15.344	0.884	Ox	0.884	0.44	4.99
102.5	15.621	0.933	Non-ox	0.887	0.48	5.04
102.5	15.621	0.920	Non-ox	0.875	0.34	5.04
104.5	15.898	1.050	Non-ox	1.004	1.76	4.99
104.5	15.898	1.001	Non-ox	0.956	1.23	4.99

Depth, cm	Age, ka	Uvi. Mg/Ca, mmol/mol	Cleaning	Benthic Temp, °C	Uvi. $\delta^{18}O$, ‰PDB	Seawater $\delta^{18}O$, ‰SMOW
104.5	15.898	1.087	Non-ox	1.042	2.17	4.99
104.5	15.898	0.921	Ox	0.921	0.85	4.99
106.5	16.174	0.941	Non-ox	0.895	0.57	5.07
108.5	16.451	0.971	Non-ox	0.925	0.90	5.26
108.5	16.451	0.885	Ox	0.885	0.46	5.26
112.5	16.982	0.906	Non-ox	0.861	0.19	5.30
118.5	17.690	1.022	Non-ox	0.976	1.45	**5.35**
118.5	17.690	0.870	Ox	0.870	0.29	**5.35**
120.5	17.853	1.022	Ox	1.022	1.95	5.36
122.5	18.100	0.837	Non-ox	0.791	-0.57	**5.33**
122.5	18.100	0.920	Ox	0.920	0.83	**5.33**
122.5	18.100	0.939	Ox	0.939	1.04	**5.33**
127.5	18.547	1.030	Ox	1.030	2.04	5.23
128.5	18.629	0.934	Non-ox	0.888	0.49	**5.21**
128.5	18.588	1.092	Ox	1.092	2.72	**5.21**
130.5	18.794	1.008	Ox	1.008	1.80	5.24
131.5	18.877	0.953	Ox	0.953	1.20	5.30
132.5	18.959	0.915	Non-ox	0.869	0.28	5.23
132.5	18.959	0.937	Ox	0.937	1.02	5.23
136.5	19.268	0.960	Ox	0.960	1.28	**5.04**
138.5	19.542	1.020	Non-ox	0.975	1.44	5.19
138.5	19.542	1.006	Ox	1.006	1.77	5.19
142.5	20.096	0.936	Non-ox	0.890	0.51	5.17
142.5	20.096	0.802	Ox	0.802	-0.45	5.17
144.5	20.304	0.976	Ox	0.976	1.45	**5.19**
150.5	21.252	1.073	Non-ox	1.027	2.01	5.25
152.5	21.474	1.006	Ox	1.006	1.78	**5.23**
162.5	23.036	0.971	Non-ox	0.926	0.90	**5.10**
164.5	23.346	1.110	Ox	1.110	2.91	5.08
171.5	24.433	0.896	Ox	0.896	0.57	**5.12**
172.5	24.588	0.957	Non-ox	0.911	0.74	**5.13**
181.5	25.595	0.973	Ox	0.973	1.42	4.98
182.5	25.702	1.004	Non-ox	0.958	1.26	**5.01**
185.5	26.021	0.958	Ox	0.958	1.25	5.05

A.2.3 Equation of State

In-situ density was calculated from salinity and benthic temperature, using the equation of state (Jackett et al., 2010):

$$\rho\,(S,\theta,p) = \frac{P_n(S,\theta,p)}{P_d(S,\theta,p)}$$

where the polynomials $P_n(S,\theta,p)$ and $P_d(S,\theta,p)$ are defined in Table A.9.

Table A.9: Terms and coefficients of the polynomials $P_n(S,\theta,p)$ and $P_d(S,\theta,p)$ that define the equation of state.

$\mathbf{P_n(S,\theta,p)}$	**Coefficients**	$\mathbf{P_d(S,\theta,p)}$	**Coefficients**
Constant	9.998×10^{2}	Constant	1.0
θ	7.347×10^{0}	θ	7.281×10^{3}
θ^2	5.321×10^{2}	θ^2	4.478×10^{5}
θ^3	3.649×10^{4}	θ^3	3.385×10^{7}
S	2.588×10^{0}	θ^4	1.3651×10^{10}
$S\theta$	6.716×10^{3}	S	1.763×10^{3}
S^2	1.920×10^{3}	$S\theta$	8.806×10^{6}
p	1.179×10^{2}	$S\theta^3$	1.883×10^{10}
$p\theta^2$	9.892×10^{8}	$S^{3/2}$	5.746×10^{6}
pS	4.699×10^{6}	$S^{3/2}\theta^2$	1.471×10^{9}
p^2	2.586×10^{8}	p	6.710×10^{6}
$p^2\theta^2$	3.292×10^{12}	$p^2\theta^3$	2.446×10^{17}
		$p^3\theta$	9.153×10^{18}

A.3 Chapter 5: Grain Size Data

A.3.1 GC528

Table A.10: GC528 sortable silt data.

Depth, cm	Age, ka	$\overline{SS}$, μm	Depth, cm	Age, ka	$\overline{SS}$, μm
1	1.079	34.77	61	10.176	24.38
4	1.172	35.06	62	10.996	24.59
6	1.362	36.18	63	11.439	25.61
8	1.787	34.66	64	11.890	24.42
10	2.103	34.76	66	12.749	23.27
12	2.359	33.65	68	12.899	25.14
14	2.598	34.70	72	13.111	22.73
16	2.829	33.44	74	13.160	22.72
18	3.039	34.31	76	13.194	23.30
21	3.395	31.14	78	13.237	23.72
22	3.515	32.56	81	13.310	24.71
24	3.745	31.76	82	13.339	23.04
26	3.973	31.85	84	13.394	24.38
28	4.204	31.07	86	13.443	22.69
32	4.807	30.89	88	13.501	22.39
33	4.932	31.39	92	13.628	23.08
34	5.053	30.28	94	13.685	25.17
36	5.308	29.97	96	13.741	23.29
38	5.568	33.44	98	13.809	24.50
39	5.693	31.44	102	13.873	24.99
41	5.987	33.43	104	13.897	24.44
42	6.150	30.18	106	13.919	23.95
43	6.275	29.34	108	13.944	22.59
44	6.401	29.59	111	14.093	23.71
45	6.536	28.94	114	14.342	21.61
46	6.666	27.31	116	14.480	18.85
48	6.936	26.78	118	14.618	19.60
50	7.346	28.09	124	15.528	20.17
52	7.843	26.44	126	15.652	20.19
53	8.084	28.04	128	15.718	19.68
54	8.333	26.76	131	15.817	18.62
56	8.811	26.99	134	15.903	19.71
57	9.042	27.56	136	15.967	20.25
58	9.299	26.11	138	16.039	21.90
59	9.509	27.36	141	16.446	19.78

Depth, cm	Age, ka	$\overline{SS}$, μm
144	17.082	18.57
146	17.502	22.92
148	17.924	18.26
152	18.229	18.36
154	18.271	20.16
156	18.305	18.58
158	18.336	18.44
161	18.382	19.90
182	18.727	18.03
184	18.756	19.06
186	18.790	18.57
188	18.823	19.09
192	18.890	18.41
194	18.927	19.90
196	18.971	18.58
198	19.019	19.20
202	19.096	17.80
212	19.174	17.91
224	19.267	18.22
236	19.497	19.55
248	19.687	19.30
259	19.877	20.74
272	20.087	18.60
284	20.298	21.33
288	20.391	21.52
293	20.691	20.76
296	20.830	20.49
299	20.974	23.17
304	21.205	23.66
308	21.389	22.20
313	21.593	23.81
316	21.715	22.91
324	22.071	22.29
328	22.246	22.28
332	22.418	21.71
336	22.575	22.62
341	22.784	21.68
344	22.909	23.23
348	23.109	21.93
352	23.654	22.35
356	24.209	22.95
359	24.605	22.29
364	25.297	21.40
368	25.834	20.97
372	26.412	22.36
376	26.985	18.75

Table A.11: GC528 IRD counts.

Depth, cm	Age, ka	>600 μm (grains/g)	>300 μm (grains/g)
2	1.11	0.00	0.17
3	1.1395	0.00	0.00
4	1.172	0.00	0.00
5	1.228	0.00	0.00
8	1.7865	0.00	0.00
9	1.958	0.00	0.00
10	2.103	0.00	0.00
11	2.2365	0.00	0.00
12	2.3585	0.00	0.00
13	2.462	0.00	0.00
15	2.7155	0.00	0.00
16	2.8285	0.00	0.00
17	2.9365	0.00	0.05
18	3.0385	0.00	0.00
19	3.17	0.00	0.00
20	3.2995	0.00	0.00
21	3.3945	0.00	0.05
22	3.515	0.00	0.04
23	3.6305	0.00	0.00
24	3.745	0.00	0.00
25	3.855	0.00	0.06
27	4.08	0.00	0.04
28	4.204	0.00	0.04
29	4.334	0.00	0.04
30	4.507	0.00	0.00
32	4.8065	0.00	0.00

Depth, cm	Age, ka	>600 μm (grains/g)	>300 μm (grains/g)
33	4.932	0.00	0.00
34	5.0525	0.00	0.14
35	5.1735	0.00	0.00
36	5.308	0.00	0.05
37	5.437	0.00	0.08
38	5.5675	0.00	0.07
39	5.6925	0.04	0.08
40	5.8175	0.00	0.17
41	5.987	0.05	0.27
42	6.1495	0.00	0.35
43	6.2745	0.00	0.04
44	6.4005	0.00	0.00
45	6.536	0.00	0.05
46	6.666	0.00	0.08
47	6.797	0.00	0.16
48	6.9355	0.00	0.32
50	7.346	0.00	0.04
52	7.843	0.06	1.23
53	8.084	0.00	0.77
54	8.3325	0.00	0.89
55	8.566	0.00	0.40
56	8.811	0.00	0.54
57	9.0415	0.06	0.93
58	9.299	0.00	1.02
59	9.509	0.00	0.33
60	9.6935	0.00	0.48
63	11.439	0.00	0.51
64	11.8895	0.00	0.23
65	12.346	0.00	0.55
66	12.749	0.00	0.63
67	12.843	0.12	1.18
68	12.899	0.00	1.43
69	12.953	0.00	0.86
70	13.007	0.14	5.76
72	13.111	0.06	4.73
73	13.142	0.21	2.17
74	13.16	0.04	2.51
75	13.177	0.00	2.75
76	13.194	0.11	5.79
77	13.21	0.05	5.29
78	13.237	0.30	6.31
79	13.264	0.21	9.78
80	13.288	0.27	6.76
81	13.31	0.13	5.14
82	13.339	0.00	3.09
83	13.369	0.00	2.40
84	13.394	0.05	0.67
85	13.418	0.00	0.80
86	13.443	0.00	1.36
87	13.469	0.08	1.65
88	13.501	0.12	3.80
89	13.542	0.08	4.04
90	13.571	0.00	1.11
92	13.628	0.09	7.18
93	13.658	0.09	5.36
94	13.685	0.28	9.99
95	13.713	0.13	4.91
96	13.741	0.42	7.07
97	13.7725	0.52	11.60
98	13.809	0.15	11.81
99	13.8325	0.38	7.67
100	13.8465	0.20	5.67
101	13.8605	0.21	9.09
102	13.873	0.32	5.83
103	13.8865	0.46	7.51
104	13.897	0.42	6.64
105	13.9075	0.40	8.94
106	13.9185	0.31	6.00
107	13.932	0.09	4.72
108	13.944	0.40	5.20
109	13.963	0.08	3.22
110	14.011	0.39	6.27
112	14.181	0.50	8.24
113	14.2625	0.38	8.13
114	14.3415	0.25	8.41
115	14.4075	0.38	10.55
116	14.4795	0.34	5.56
117	14.548	0.46	5.93
120	14.904	0.39	12.20
123	15.3885	0.32	7.52
124	15.528	0.88	12.96
125	15.607	0.23	11.45

Depth, cm	Age, ka	>600 μm (grains/g)	>300 μm (grains/g)
126	15.652	0.22	4.22
127	15.686	0.12	1.51
128	15.718	0.27	7.19
129	15.7535	0.87	8.08
130	15.789	0.80	11.24
133	15.872	0.22	5.66
134	15.903	0.27	4.96
135	15.932	0.26	7.31
136	15.9665	0.20	3.79
137	15.997	0.25	5.38
138	16.039	0.13	5.14
139	16.095	0.71	6.86
140	16.23	0.41	6.19
141	16.446	0.14	5.05
142	16.657	0.05	2.82
143	16.871	0.29	4.74
144	17.082	0.24	5.39
145	17.293	0.25	5.22
146	17.5015	0.27	3.48
147	17.7125	0.35	4.76
150	18.1825	0.28	9.97
151	18.206	0.27	4.49
153	18.251	0.19	5.54
154	18.271	0.42	8.05
155	18.291	0.56	11.45
156	18.3045	0.31	4.55
157	18.319	0.09	2.31
158	18.3355	0.19	3.43
159	18.354	0.00	5.20
160	18.366	0.31	3.70
161	18.382	0.00	2.22
162	18.4	0.05	2.81
163	18.417	0.23	4.53
164	18.434	0.28	4.55
165	18.4515	0.00	1.88
166	18.4665	0.14	3.02
167	18.482	0.09	2.19
168	18.4985	0.13	2.43
169	18.5165	0.11	1.63
170	18.535	0.14	2.89
172	18.5685	0.17	1.76
173	18.586	0.09	1.85
174	18.6	0.20	2.34
175	18.6165	0.17	3.55
177	18.6485	0.19	2.03
178	18.665	0.17	2.39
179	18.682	0.07	1.79
180	18.695	0.00	1.56
181	18.708	0.13	1.51
182	18.727	0.07	1.95
183	18.743	0.09	1.93
184	18.756	0.04	2.08
185	18.772	0.25	2.30
190	18.854	0.15	3.55
195	18.947	0.07	0.98
200	19.072	0.06	2.25
205	19.121	0.22	2.92
210	19.156	0.37	4.65
215	19.196	0.58	8.00
220	19.232	0.33	5.09
225	19.278	0.05	6.70
230	19.3665	0.95	26.74
235	19.4815	0.52	13.41
240	19.5585	0.26	10.92
245	19.6375	0.33	7.42
250	19.722	1.35	28.72
255	19.797	0.58	7.77
260	19.892	0.50	11.13
265	19.9735	0.48	13.08
270	20.0545	0.61	12.29
275	20.131	0.71	17.75
280	20.228	0.78	37.45
285	20.3195	2.71	60.75
290	20.5335	1.92	38.27
295	20.78	1.80	32.04
300	21.017	1.32	42.11
305	21.247	2.10	43.58
310	21.471	1.72	32.64
315	21.6725	3.10	40.15
320	21.899	2.43	56.70
325	22.1175	3.16	68.28
330	22.341	3.56	71.01

Depth, cm	Age, ka	>600 μm (grains/g)	>300 μm (grains/g)	Depth, cm	Age, ka	>600 μm (grains/g)	>300 μm (grains/g)
340	22.74	0.75	19.45	360	24.751	2.66	46.94
345	22.95	2.71	30.45	365	25.4385	2.57	40.23
350	23.3085	2.50	35.76	370	26.116	0.77	15.42
355	24.0895	4.10	52.12				

A.3.2 GC642

Table A.12: GC642 sortable silt data.

Depth, cm	Age, ka	$\overline{SS}$, μm	Depth, cm	Age, ka	$\overline{SS}$, μm
506	105.0	18.50	568	121.8	29.66
508	105.3	19.41	571	122.4	29.95
510	105.6	20.05	573	122.8	31.63
514	106.2	20.22	575	123.2	30.16
516	106.5	19.94	577	123.6	29.54
518	106.8	18.75	579	124.0	30.65
520	107.1	20.05	581	124.4	30.13
522	107.4	20.91	583	124.8	28.41
524	107.7	20.85	585	125.2	29.13
526	108.0	21.22	587	125.6	28.38
528	108.5	23.05	589	126.0	28.19
530	109.0	22.32	591	126.2	27.27
532	109.5	25.84	593	126.4	26.04
534	110.0	26.19	595	126.6	25.57
536	110.5	26.98	597	126.8	24.45
538	111.0	27.04	599	127.0	24.72
540	111.5	26.45	601	127.2	23.96
542	112.0	30.09	603	127.4	23.41
544	112.5	29.87	605	127.6	24.30
546	113.0	29.39	607	127.8	21.97
548	114.5	30.85	609	128.0	22.72
550	116.0	29.62	610	128.8	22.52
552	117.5	29.27	611	129.7	22.31
554	119.0	30.46	612	130.5	21.38
556	119.4	30.44	613	131.3	20.28
558	119.8	30.60	614	132.2	19.33
560	120.2	29.98	615	133.0	18.22
562	120.6	32.06	616	133.8	20.26
564	121.0	30.81	617	134.7	20.13
566	121.4	31.65	619	136.3	19.70

Depth, cm	Age, ka	$\overline{SS}$, μm
621	138.0	19.22
623	139.7	20.58
625	141.3	22.24
627	143.0	21.58
629	144.7	21.92
631	146.3	21.21
633	148.0	19.14

Table A.13: GC642 IRD counts.

Depth, cm	Age, ka	>600 μm, grains/g	>300 μm, grains/g	Depth, cm	Age, ka	>600 μm, grains/g	>300 μm, grains/g
478	100.19	1.04	4.83	540	111.50	1.58	25.65
480	100.54	0.48	1.78	542	112.00	0.32	9.92
482	100.88	0.16	1.14	544	112.50	0.41	6.05
484	101.22	0.18	2.66	546	113.00	0.11	4.04
486	101.57	0.16	0.92	548	114.50	0.00	0.96
488	101.91	0.05	0.20	550	116.00	0.38	10.22
490	102.25	0.00	0.39	552	117.50	0.39	5.87
492	102.60	0.10	4.48	554	119.00	0.23	5.18
494	102.94	0.21	5.14	556	119.40	0.00	0.26
496	103.28	0.04	0.75	558	119.80	0.31	1.71
498	103.63	0.09	1.59	560	120.20	0.00	1.14
500	103.97	0.08	0.90	562	120.60	0.00	1.02
502	104.31	0.00	0.79	564	121.00	0.05	1.79
504	104.66	0.05	0.65	566	121.40	0.00	1.43
506	105.00	0.00	0.81	568	121.80	0.03	1.23
508	105.30	0.00	1.10	571	122.40	0.28	2.03
510	105.60	0.00	1.38	573	122.80	0.14	1.60
512	105.90	0.00	1.30	575	123.20	0.23	2.52
514	106.20	0.35	3.86	577	123.60	0.00	0.96
516	106.50	1.01	8.13	579	124.00	0.00	1.26
518	106.80	0.17	3.22	581	124.40	0.05	2.28
520	107.10	0.44	9.61	583	124.80	0.09	2.40
522	107.40	0.98	26.35	585	125.20	0.14	3.52
524	107.70	0.57	17.15	587	125.60	0.00	3.65
526	108.00	0.77	13.56	589	126.00	0.44	4.36
528	108.50	2.08	40.72	591	126.20	0.13	5.43
530	109.00	2.34	33.04	593	126.40	0.12	5.16
532	109.50	1.75	25.24	595	126.60	0.11	3.72
534	110.00	1.35	28.17	597	126.80	0.37	4.07
536	110.50	2.42	36.60	599	127.00	0.26	7.05
538	111.00	2.39	35.05	601	127.20	0.29	11.36

Depth, cm	Age, ka	>600 μm, grains/g	>300 μm, grains/g
603	127.40	0.85	16.56
605	127.60	0.61	10.92
607	127.80	1.09	27.32
609	128.00	2.63	56.81
611	129.67	3.40	43.76
613	131.33	0.32	15.94
615	133.00	0.00	1.32
617	134.67	0.18	4.41
619	136.33	0.11	4.21
621	138.00	0.42	5.14
623	139.67	1.07	14.31
625	141.33	0.75	19.25
627	143.00	0.73	10.10
629	144.67	0.36	12.54
631	146.33	0.87	19.01
633	148.00	1.01	14.14
635	149.53	1.13	16.47
637	151.18	1.80	18.59

Depth, cm	Age, ka	>600 μm, grains/g	>300 μm, grains/g
641	154.47	1.35	28.26
643	156.12	1.16	33.84
645	157.76	1.35	23.29
647	159.41	0.96	25.90
649	161.06	1.90	28.12
651	162.71	2.08	27.17
653	164.35	0.80	19.94
655	166.00	0.92	15.78
657	167.41	0.92	17.45
659	168.83	1.19	17.22
661	170.24	0.90	11.92
663	171.66	0.15	12.47
665	173.07	0.32	13.67
668	175.20	0.67	20.34
670	176.61	0.86	37.08
672	178.02	1.10	35.25
674	179.44	1.88	46.79
676	180.85	2.38	54.95

A.3.3 TC290

Table A.14: TC290 Tiepoints for age model.

Depth, cm	Age, ka
3	0.44
31	9.40
53	13.42

Depth, cm	Age, ka
58	14.11
87	16.59
105	20.33

Table A.15: TC290 IRD and sortable silt data. N.B. IRD counts are the work of R.Pugh.

Depth, m	Age, ka	$\overline{SS}$, μm	>250 μm, grains/g
0.02	0.10	23.45	35.04
0.06	1.43	25.67	21.94
0.1	2.75	23.54	18.32
0.14	2.25	20.26	19.06
0.18	5.40	22.38	29.19
0.22	6.72	19.75	33.58
0.26	8.04	17.62	43.90
0.3	9.22		53.06
0.34	9.96	18.35	61.68
0.38	10.70		56.85

Depth, m	Age, ka	$\overline{SS}$, μm	>250 μm, grains/g
0.42	11.43	21.53	63.29
0.5	12.91	20.97	70.75
0.54	13.576	20.16	29.47
0.58	10.61	17.98	28.97
0.62	14.44	20.60	74.58
0.66	14.78	20.86	88.82
0.7	15.11	21.45	82.76
0.74	15.45	21.99	61.21
0.78	15.78	21.48	42.14
0.82	16.11	21.79	27.96

A.3.4 PC290

Table A.16: PC290 Tiepoints for age model.

Depth, cm	Age, ka	Depth, cm	Age, ka
3	26.80	133	47.15
19	27.82	159	49.17
21	28.49	233	55.87
29	31.06	305	64.04
37	31.93	362	70.41
103	43.55	396	76.00
115	44.94	468	103.13
127	46.53	534	133.49

Table A.17: PC290 IRD and sortable silt data. IRD counts are the work of R.Pugh.

Depth, m	Age, ka	$\overline{SS}$, μm	>250 μm, #/g	Depth, m	Age, ka	$\overline{SS}$, μm	>250 μm, #/g
5.02	118.9	20.62		5.62	140.3	19.93	54.95
5.06	120.8	19.14		5.66	141.3	20.01	36.56
5.1	122.7	19.48		5.7	142.3	22.08	59.80
5.14	124.5	19.36		5.74	143.3		36.58
5.18	126.4	19.76		5.78	144.3	21.72	47.67
5.22	128.3	20.07	15.26	5.82	145.2	20.90	14.07
5.26	130.1	19.85	22.49	5.86	146.2	21.69	31.32
5.3	132.0	21.22	31.22	5.9	147.2	19.573	31.88
5.34	133.4	20.70	60.92	5.94	148.2	19.32	28.68
5.38	134.4	21.75	77.28	5.98	149.2	20.86	31.05
5.42	135.4	21.61	94.56	6.02	150.2	19.65	35.79
5.46	136.4	20.13	79.82	6.06	151.1	20.10	20.487
5.5	137.4	21.28	112.63	6.1	152.1	19.17	13.32
5.54	138.4	20.78	118.25	6.14	153.1	18.83	21.43
5.58	139.3	20.67	84.13	6.18	154.1	20.40	16.86

A.3.5 PC078

Table A.18: PC078 Tiepoints for age model.

Depth, cm	Age, ka	Depth, cm	Age, ka	Depth, cm	Age, ka
3	0.5	160	27.5	371	55.7
63	14	170	31	441	63.7
85	16.6	178	31.9	532	75
101	19.6	241	43.5	606	103
111	23.7	271	47	670	133
113	24	297	49	1146	250

Table A.19: PC078 IRD and sortable silt data. IRD counts are the work of R.Pugh.

Depth, m	Age, ka	$\overline{SS}$, μm	>250 μm, grains/g	Depth, m	Age, ka	$\overline{SS}$, μm	>250 μm, grains/g
0.44	9.71	22.19	64.44	1.04	21.03	21.59	24.81
0.48	10.61	19.27	71.85	1.08	22.93	20.76	16.06
0.52	11.52	19.86	29.83	1.12	23.85	21.29	6.55
0.56	12.42	23.02	75.45	1.16	24.22	20.63	23.46
0.6	13.32	21.03	89.89	1.2	24.52	21.76	
0.64	14.12	21.14	83.42	1.24	24.82	20.91	
0.68	14.59	21.89	62.31	1.28	25.12	22.14	
0.72	15.06	21.10	43.11	1.32	25.41	21.18	23.26
0.76	15.54	21.09		1.36	25.71	21.46	
0.8	16.01	21.07	28.46	1.4	26.01	21.66	
0.84	16.48	21.60		1.44	26.31	21.71	60.70
0.88	17.16	22.35		1.48	26.61	23.39	10.51
0.92	17.91	21.71	57.73	1.52	26.90	21.92	
0.96	18.66	21.05	16.27	1.56	27.20	22.56	22.29
1.00	19.41	20.34	33.00	1.6	27.50	20.98	25.71

A.4 Chapter 5: Alkenone and LA-ICP-MS Data

Table A.20: GC528 alkenone data

Depth, cm	U^K_{37}	SST, °C	C_{37} conc., μg/g	ΣC_{37}: ΣC_{38}	Depth, cm	U^K_{37}	SST, °C	C_{37} conc., μg/g	ΣC_{37}: ΣC_{38}
0	0.21	3.99	0.90	3.29	50	0.31	7.34		2.88
2	0.32	7.53			52	0.35	8.47	0.44	0.36
5	0.36	8.88	2.78		53	0.37	9.36	0.68	1.26
8	0.30	6.89	2.65	1.28	54	0.37	9.32	0.66	1.38
10	0.25	5.31		3.73	55	0.25	5.39	0.48	1.73
13	0.30	6.95		1.21	56	0.36	8.81	0.85	1.36
20	0.35	8.60	0.32	1.60	59	0.34	8.31	0.92	1.54
27	0.32	7.50	4.44		60	0.26	5.64	0.34	3.73
29	0.30	6.79			61	0.28	6.24	0.45	1.96
30	0.29	6.43		3.14	62	0.27	6.05	0.36	1.99
32	0.30	6.81	1.59		63	0.25	5.19		1.83
37	0.52	14.30		0.12	64	0.17	2.44	1.44	1.54
40	0.29	6.49		3.08	66	0.27	5.85		1.08
42	0.30	6.81	2.01	1.36	67	0.14	1.70		1.30
47	0.40	10.16		0.63	68	0.18	3.00	1.27	1.26
48	0.30	6.99	0.41	2.84	69	0.15	1.89	3.38	1.75
50	0.28	6.17	1.98	1.30	70	0.24	4.88	0.42	1.94

Depth, cm	U^K_{37}	SST, °C	C_{37} conc., μg/g	ΣC_{37}: ΣC_{38}
70	0.21	4.06	1.03	1.62
74	0.21	3.75	1.93	1.30
80	0.27	5.81		4.32
82	0.22	4.27	0.77	
90	0.26	5.64	0.32	1.92
92	0.19	3.12	1.69	1.30
99	0.26	5.41	1.78	1.05
100	0.18	3.02	0.47	3.30
110	0.21	3.94	0.25	3.87
114	0.21	3.95	0.36	
117	0.13	1.29	0.38	1.33
120	0.17	2.42		
124	0.28	6.15	1.00	0.82
129	0.21	3.82		0.99
130	0.25	5.11	0.08	1.64
138	0.16	2.28	0.73	1.25
140	0.23	4.62	0.11	1.53
141	0.21	3.92	0.11	1.96
142	0.19	3.39	0.08	1.88
143	0.22	4.07	0.09	3.20
145	0.21	3.78		2.76
146	0.24	4.74	0.09	2.81
147	0.19	3.29	0.11	1.97
150	0.31	7.31	0.07	1.53
150	0.23	4.47	0.36	1.44
160	0.23	4.65	0.90	1.35
160	0.25	5.38		4.46
168	0.24	4.89	0.47	1.22
174	0.43	11.29	0.23	1.78
180	0.34	8.37	0.05	2.49
181	0.29	6.69		1.12
187	0.30	6.88		1.22
194	0.47	12.62	1.15	
200	0.41	10.53	0.17	
202	0.33	7.87		1.77
210	0.39	9.78	0.11	1.80
220	0.40	10.28		
230	0.27	6.02	0.07	3.76
230	0.27	6.02		3.76
232	0.34	8.35	0.19	
240	0.33	7.89	0.09	1.49
250	0.24	5.02		3.25
250	0.33	7.98	0.13	1.16
250	0.24	5.02		3.25
260	0.30	6.83	0.09	3.20
270	0.33	7.98	0.08	1.50
274	0.26	5.65		0.79
280	0.13	1.11		
286	0.20	3.66	0.90	
290	0.27	6.03	0.12	1.42
294			0.24	
300	0.16	2.39		
302	0.21	3.92	0.69	0.90
310	0.28	6.11	0.06	1.76
314	0.30	6.97	0.47	0.43
317	0.72	20.80		1.09
320	0.24	5.01	0.47	1.18
323	0.32	7.51	0.14	0.98
325	0.16	2.34		3.48
325	0.23	4.53		1.07
325	0.16	2.34		3.48
335	0.45	11.86		
345	0.05	-1.34	0.07	
355	0.05	-1.29		3.33
365	0.19	3.33		1.58
375	0.11	0.55	0.15	3.19
375	0.11	0.55		3.19
395	0.16	2.17		3.27
405	0.17	2.65	0.09	1.84

Table A.21: GC528 LA-ICP-MS data.

Depth, cm	Age, ka	# spots	B, ppm	Mg, ppm	Al,ppm	Mn, ppm	Fe, ppm	Cu, ppm	Zn, ppm	Sr, ppm
12	2.4	4	103.825	1.309	0.008	-0.002	0.862	0.122	0.121	1.596
12	2.4	4	115.675	1.134	0.033	0.004	0.898	0.138	0.330	1.513
12	2.4	4	113.250	0.696	0.014	0.004	0.954	0.072	0.142	1.544
12	2.4	4	150.725	1.420	0.016	0.009	1.060	0.062	0.061	1.531
12	2.4	3	126.533	0.631	0.013	0.002	1.039	0.047	0.029	1.513
12	2.4	4	118.225	0.882	0.034	0.006	0.989	0.036	0.174	1.492
12	2.4	4	130.975	0.748	0.008	0.002	0.907	0.070	0.201	1.452
12	2.4	4	101.425	0.643	0.011	0.005	0.825	0.003	0.012	1.475
12	2.4	4	92.050	0.541	0.003	-0.002	0.677	0.014	0.027	1.457
12	2.4	3	80.533	1.095	0.016	0.004	0.641	0.032	0.053	1.249
12	2.4	4	82.525	0.963	0.014	0.006	0.675	0.170	0.108	1.235
12	2.4	4	70.775	0.593	0.019	0.007	0.579	0.058	0.087	1.171
49	7.1	1	0.088	1.117	0.031	0.013	0.943	0.055	0.087	1.593
49	7.1	2	0.103	0.894	0.082	0.002	0.909	0.046	0.033	1.510
49	7.1	1	0.117	0.871	0.036	0.015	1.113	0.059	0.057	1.714
49	7.1	3	0.080	0.733	0.019	0.003	0.936	0.017	0.019	1.466
49	7.1	4	0.080	0.672	0.074	0.000	0.904	0.010	0.008	1.632
49	7.1	1	0.095	1.082	0.035	0.003	0.923	0.034	0.025	1.598
49	7.1	3	0.080	0.787	0.063	-0.003	0.891	0.011	0.019	1.487
64	11.9	1	0.109	0.708	0.060	-0.011	0.906	0.022	0.017	1.487
64	11.9	2	0.095	0.488	0.033	0.002	0.906	0.017	0.010	1.651
64	11.9	3	0.102	0.503	0.009	0.003	0.832	0.002	0.002	1.536
64	11.9	2	0.092	0.856	0.024	0.001	0.880	0.016	0.008	1.611
64	11.9	1	0.095	0.374	0.006	-0.007	0.853	0.005	0.006	1.567
64	11.9	1	0.072	0.529	0.010	0.009	0.848	0.006	0.008	1.570
64	11.9	2	0.089	0.782	0.014	0.001	0.835	0.011	0.006	1.569
64	11.9	2	0.081	0.823	0.005	0.007	0.834	0.005	0.003	1.540
64	11.9	2	0.083	0.420	0.025	-0.001	0.863	0.008	0.009	1.590
64	11.9	1	0.074	0.612	0.031	-0.010	0.904	0.007	0.005	1.717
64	11.9	2	0.071	0.799	0.010	0.009	0.846	0.004	0.007	1.584
64	11.9	2	0.079	0.794	0.026	-0.004	0.830	0.003	0.003	1.702
68	12.9	4	0.114	0.736	0.014	0.008	0.906	0.008	0.004	1.629
68	12.9	3	0.086	0.683	0.012	-0.002	0.999	0.008	0.007	1.636
68	12.9	2	0.095	0.807	0.023	-0.001	0.915	0.015	0.004	1.463
68	12.9	1	0.107	0.647	0.059	-0.003	0.928	0.013	0.018	1.538
68	12.9	1	0.082	0.466	0.044	0.002	0.802	0.006	0.016	1.660
68	12.9	1	0.095	0.741	0.010	0.012	0.848	0.006	0.011	1.594
92	13.6	2	0.089	0.578	0.101	0.014	0.884	0.018	0.018	1.741
92	13.6	1	0.101	0.909	0.106	0.006	1.007	0.011	0.015	1.536
92	13.6	2	0.100	0.739	0.026	0.014	0.829	0.013	0.010	1.740
92	13.6	2	0.109	0.433	0.015	-0.002	0.884	0.009	0.003	1.423
119	14.7	5	86.040	0.604	0.119	0.026	0.861	0.029	0.026	1.695
119	14.7	3	69.867	0.639	0.015	0.016	0.685	0.012	0.122	1.201
119	14.7	4	0.068	0.594	0.021	0.003	0.850	0.002	0.002	1.141
119	14.7	5	88.933	0.568	0.101	0.025	0.809	0.015	0.011	1.765
119	14.7	3	0.094	0.674	0.013	0.002	1.115	0.010	0.008	0.781
119	14.7	4	73.625	0.991	0.085	0.010	0.827	0.004	0.006	1.897

Depth, cm	Age, ka	# spots	B, ppm	Mg, ppm	Al,ppm	Mn, ppm	Fe, ppm	Cu, ppm	Zn, ppm	Sr, ppm
119	14.7	3	59.780	0.723	0.019	0.003	0.622	0.005	0.069	1.106
119	14.7	3	0.092	0.535	0.022	-0.003	0.944	0.002	0.003	0.583
119	14.7	3	64.233	0.550	0.056	0.001	0.789	0.008	0.003	2.021
119	14.7	4	71.025	0.757	0.194	0.018	0.705	0.015	0.015	1.221
119	14.7	3	0.109	0.738	0.008	0.004	1.160	0.005	0.004	0.377
119	14.7	1	77.300	0.884	0.458	0.019	0.870	0.077	0.053	1.833
119	14.7	2	54.750	0.576	0.102	0.005	0.647	0.009	0.019	1.216
119	14.7	4	0.088	0.497	0.016	0.003	1.364	0.004	0.005	0.282
119	14.7	2	95.850	0.757	0.060	0.005	0.864	0.062	0.054	1.823
119	14.7	3	89.800	0.653	0.067	0.032	0.953	0.027	0.038	1.532
119	14.7	4	0.084	0.473	0.003	-0.009	0.819	0.002	0.002	0.203
119	14.7	4	104.700	1.212	0.097	0.014	3.471	0.040	0.032	1.795
119	14.7	9	74.330	0.474	0.066	0.004	0.824	0.016	0.008	1.240
119	14.7	2	0.100	0.965	0.012	0.010	1.019	0.003	0.007	0.140
119	14.7	1	84.700	0.913	0.039	0.034	1.036	0.057	0.042	1.915
119	14.7	9	79.311	0.648	0.142	0.007	2.792	0.016	0.013	1.481
119	14.7	3	0.113	1.167	0.030	-0.001	1.448	0.010	0.011	0.100
119	14.7	2	93.350	1.049	0.179	0.005	0.961	0.170	0.092	1.828
119	14.7	4	71.250	0.497	0.312	0.000	0.837	0.035	0.033	1.504
119	14.7	2	125.350	0.906	0.049	0.035	1.573	0.069	0.055	1.597
124	15.5	1	0.110	0.651	0.021	0.009	0.804	0.011	0.008	1.707
124	15.5	1	0.128	0.553	0.105	0.004	1.057	0.058	0.048	1.816
124	15.5	1	0.123	1.050	0.165	-0.011	1.600	0.103	0.067	1.706
134	15.9	1	0.105	0.799	0.016	0.001	0.812	0.025	0.024	1.637
134	15.9	1	0.086	0.729	0.009	0.009	0.780	0.004	0.007	1.763
134	15.9	1	0.090	0.974	0.018	0.015	0.797	0.005	0.035	1.778
144	17.1	3	0.104	0.854	0.066	0.016	0.917	0.004	0.006	1.610
144	17.1	4	0.083	0.917	0.013	0.010	0.848	0.007	0.009	1.638
144	17.1	4	0.084	0.776	0.005	0.007	0.823	0.001	0.001	1.720
144	17.1	4	0.078	0.692	0.068	0.001	1.027	0.009	0.011	1.668
144	17.1	2	0.081	0.549	0.005	0.013	0.765	0.002	0.003	1.609
144	17.1	1	0.101	1.211	0.004	0.010	0.797	0.002	0.004	1.651
144	17.1	2	0.086	0.457	0.022	0.012	1.681	0.003	0.005	1.657
144	17.1	1	0.073	0.660	0.024	-0.002	0.778	0.001	0.002	1.654
144	17.1	2	0.114	0.632	0.097	-0.010	0.822	0.003	0.006	1.697
178	18.7	4	0.082	0.538	0.217	0.014	0.810	0.015	0.016	1.498
178	18.7	2	0.097	0.686	0.064	0.026	0.831	0.020	0.008	1.768
178	18.7	4	0.096	0.414	0.029	0.016	0.825	0.009	0.007	1.632
178	18.7	2	0.115	0.368	0.075	0.015	0.828	0.001	0.005	1.736
178	18.7	3	0.093	0.571	0.005	0.003	0.753	0.002	0.010	1.666
178	18.7	2	0.099	0.363	0.003	-0.002	0.738	0.001	0.003	1.858
178	18.7	3	0.097	0.422	0.027	0.017	0.779	0.005	0.016	1.755
178	18.7	4	0.099	0.714	0.017	0.008	1.472	0.014	0.030	1.636
178	18.7	1	0.089	0.290	0.016	-0.003	0.911	0.003	0.003	1.674
178	18.7	4	0.062	0.372	0.038	-0.003	0.760	0.002	0.002	1.686
178	18.7	1	0.123	0.421	0.029	0.020	0.776	0.005	0.007	1.765
178	18.7	3	0.120	0.399	0.011	0.007	0.755	0.003	0.004	1.685

Depth, cm	Age, ka	# spots	B, ppm	Mg, ppm	Al,ppm	Mn, ppm	Fe, ppm	Cu, ppm	Zn, ppm	Sr, ppm
178	18.7	1	0.082	0.699	0.049	0.006	0.852	0.002	0.003	1.720
178	18.7	1	0.081	0.492	0.006	0.014	0.739	0.001	0.003	1.832
178	18.7	2	0.110	0.483	0.054	0.004	0.774	0.004	0.008	1.679
178	18.7	1	0.083	0.494	0.005	0.015	1.840	0.004	0.006	1.678
178	18.7	2	0.095	0.427	0.003	0.012	0.868	0.004	0.003	1.723
199	19.1	4	0.071	0.670	0.009	0.003	1.099	0.003	0.002	1.563
199	19.1	4	0.090	0.477	0.126	0.022	0.903	0.021	0.014	1.594
199	19.1	1	0.068	0.427	0.201	0.002	1.877	0.018	0.024	1.659
199	19.1	4	0.082	0.404	0.030	0.000	0.845	0.012	0.004	1.645
199	19.1	2	0.083	0.237	0.009	0.008	1.588	0.001	0.001	1.742
199	19.1	4	0.087	0.515	0.018	0.006	1.596	0.005	0.002	1.677
199	19.1	3	0.091	0.318	0.017	-0.006	1.521	0.003	0.002	1.622
199	19.1	3	0.064	0.409	0.021	0.014	3.608	0.010	0.005	1.560
206	19.1	2	0.092	0.507	0.065	0.017	0.995	0.016	0.013	1.611
206	19.1	2	0.076	0.512	0.031	0.013	0.989	0.011	0.009	1.764
206	19.1	2	0.091	0.857	0.130	0.011	1.019	0.008	0.010	1.718
206	19.1	1	0.084	0.699	0.924	0.005	1.162	0.019	0.013	1.474
206	19.1	1	0.094	0.736	0.144	0.008	1.006	0.011	0.017	1.631
206	19.1	2	0.104	0.595	0.430	0.003	1.050	0.014	0.009	1.695
206	19.1	2	0.099	0.318	0.029	-0.003	0.929	0.006	0.005	1.696
206	19.1	3	0.091	0.481	0.098	0.014	0.958	0.007	0.006	1.610
207	19.1	3	0.089	0.362	0.008	0.009	1.672	0.013	0.012	1.611
207	19.1	4	0.067	0.748	0.014	0.002	1.004	0.003	0.006	1.514
208	19.1	1	0.082	0.596	0.021	0.003	1.039	0.025	0.009	1.601
208	19.1	1	0.091	0.296	0.113	-0.005	1.040	0.007	0.009	1.589
208	19.1	3	0.088	0.513	0.029	0.003	1.011	0.021	0.021	1.488
208	19.1	1	0.066	0.379	0.208	-0.005	1.090	0.008	0.007	1.817
208	19.1	3	0.073	0.491	0.013	0.003	0.971	0.003	0.003	1.594
236	19.5	3	0.096	0.633	0.071	0.008	0.763	0.006	0.004	1.655
237	19.5	1	0.100	0.936	0.023	0.011	0.754	0.011	0.005	1.863
237	19.5	1	0.083	0.708	0.030	0.004	0.800	0.006	0.006	1.574
238	19.5	3	0.078	0.988	0.010	-0.001	0.747	0.001	0.001	1.638
238	19.5	1	0.093	0.370	0.082	-0.002	0.780	0.009	0.015	1.720
239	19.5	4	0.085	0.722	0.064	0.005	0.761	0.002	0.003	1.568
239	19.5	3	0.097	0.638	0.029	0.002	0.791	0.002	0.006	1.665
239	19.5	1	0.082	0.798	0.047	0.004	0.785	0.008	0.010	1.713
284	20.3	3	0.098	0.653	0.093	0.006	0.761	0.004	0.002	1.642
284	20.3	2	0.065	0.385	0.054	0.003	0.962	0.006	0.002	1.654
284	20.3	2	0.082	0.583	0.005	-0.004	0.747	0.000	0.000	1.536
284	20.3	1	0.120	0.333	0.061	0.013	0.748	0.002	0.002	1.859

Table A.22: GC528 Seawater $\delta^{18}O$ collected on JR299: CTD119

Depth, mbsl	$\delta^{18}O$, ‰VSMOW2	repeat	Depth, mbsl	$\delta^{18}O$, ‰VSMOW2	repeat
10	-0.04		350	+0.01	
50	-0.05	-0.04	350	-0.03	
100	-0.08		400	-0.01	
100	-0.01		400	+0.01	-0.03
150	-0.07		450	-0.04	
150	-0.01		450	-0.03	
200	-0.04		500	-0.05	
200	-0.01	-0.02	500	-0.04	
250	-0.04		550	-0.02	
250	-0.03		550	-0.01	
300	+0.01		590	+0.01	
300	-0.02		590	-0.03	

A.5 Chapter 6: Benthic Foraminifera Assemblage Data (Main Species)

A.5.1 GC528

Table A.23: GC528 Benthic Foraminifera Assemblage (Main Species). Uvi = *Uvigerina bifurcata*; Ang = *Angulogerina earlandi*; Fus = *Fursenkoina fusiformis*; Bul = *Bulimina aculeata*; Nut = *Nuttallides umbonifera*; Cras = *Cassidulina crassa*; Cari = *Cassidulina carinata*; Mel = *Melonis barleeanum*; Or = *Oridorsalis umbonatus*; N.pul = *Nonionella pulchella*; N.aur = *Nonionella auris*; Pull = *Pullenia bulloides*; Ala = *Alabaminella weddellensis*; Ep = *Epistominella exigua*; Cib = *Cibicidoides sp.*; Bol = *Bolivina sp.*; Pyr = *Pyrgo sp.*; Glo = *Globobulimina sp.*.

Depth, cm	Real Counts	Total	Uvi	Ang	Fur	Bul	Nut	Cras	Cari	Mel	Or	N. pul	N.aur	Pul	Ala	Ep	Cib	Bol	Pyr	Glo
1	335	20244	150	1152	0	0	0	2304	1680	880	112	16	704	208	112	9472	48	1152	16	0
4	722	35228	132	1088	64	0	0	1696	8256	1536	256	128	896	752	0	10880	656	6096	0	16
8	506	27624	68	960	112	0	0	3616	3024	592	272	224	1136	128	144	12240	416	1424	0	0
12	322	61787	81	704	32	0	0	10368	1920	3136	128	32	1792	192	1600	30848	384	6080	0	0
16	577	32958	60	1168	16	0	0	3488	4304	1152	320	48	2240	176	176	15072	320	1360	32	0
21	578	74937	20	960	64	0	0	9440	3168	832	256	160	6240	352	704	35680	1728	9312	0	32
24	707	44293	64	2208	16	0	0	2192	5712	1200	144	48	2304	224	592	21728	528	3056	0	0
28	413	83613	10	4768	32	0	0	9536	8576	5824	64	128	5312	256	1280	37376	832	2784	32	32
32	640	38413	27	1584	0	0	0	1232	4960	1488	272	32	2656	464	448	19824	208	2016	0	16
34	441	41175	39	1568	32	0	0	2592	8736	1184	160	96	2080	832	3136	17120	416	992	32	0
36	654	32000	32	1024	96	0	0	1328	4480	1392	272	48	2224	464	608	14880	160	1792	0	0
38	719	39178	23	1440	0	0	0	1376	5312	1232	368	0	1232	304	880	22816	112	1392	0	32
41	742	44234	90	2560	320	0	0	1904	6976	1552	208	16	2592	576	352	22336	336	2112	0	32
42	1050	33957	58	1096	368	0	0	816	5928	904	232	8	2184	352	992	16392	576	1992	8	24
44	1066	13260	74	296	20	0	0	148	2044	396	112	8	676	168	492	7236	396	224	0	4
46	1163	24364	185	1112	232	0	0	488	5416	904	144	72	1480	288	592	10560	368	1496	0	0
48	721	17238	81	720	160	0	0	120	3896	352	104	40	1896	184	656	7456	240	424	0	16
52	285	4790	14	184	40	0	0	160	1776	224	40	0	168	144	240	1384	24	144	0	0
54	545	16092	63	176	0	0	0	512	6792	592	64	0	200	240	672	5952	240	88	0	0
56	447	10634	54	192	8	0	0	16	5312	344	72	24	360	224	136	2800	248	248	0	0
58	530	7901	83	192	56	0	0	72	3856	448	120	16	208	104	112	2256	24	112	0	8
62	232	2104	120	48	44	0	0	0	708	60	4	4	28	4	0	812	4	124	0	0
64	359	5580	152	76	244	0	0	160	1128	292	32	12	184	28	8	2528	16	264	0	4
66	583	3079	202	26	124	0	0	266	804	106	16	2	80	52	0	1052	2	248	0	2

Depth, cm	Real Counts	Total	Uvi	Ang	Fur	Bul	Nut	Cras	Cari	Mel	Or	N. pul	N.aur	Pul	Ala	Ep	Cib	Bol	Pyr	Glo
68	452	1479	210	72	42	0	0	60	542	68	8	8	46	4	0	330	2	0	8	0
72	471	604	328	5	19	0	1	1	95	15	9	0	4	2	2	84	2	0	5	0
74	506	614	497	5	18	0	0	0	13	1	0	0	0	1	0	37	0	0	0	0
76	588	1311	1078	28	48	0	2	0	8	6	0	22	10	0	0	28	0	2	0	0
78	508	1240	950	8	60	0	0	4	2	8	0	24	0	2	0	102	0	0	0	0
81	279	2438	872	32	264	0	4	408	4	40	0	12	96	0	0	536	4	4	12	0
82	456	2175	1564	40	52	0	4	0	80	16	0	36	32	4	0	200	0	0	36	0
84	343	7432	188	272	160	0	0	240	2168	112	8	40	88	0	8	3104	152	0	576	0
86	792	1584	416	27	138	0	0	112	405	63	10	10	143	5	0	180	2	0	10	0
88	433	728	346	7	77	0	0	12	3	4	0	2	21	1	0	173	1	0	0	0
92	438	1204	716	14	26	0	6	88	0	8	0	6	14	8	0	236	0	0	0	0
94	82	733	516	16	64	0	0	8	8	0	0	8	8	0	0	24	0	0	0	0
96	218	4200	1124	128	544	0	0	336	0	176	0	96	200	0	0	1320	16	0	0	0
98	193	1744	1196	104	96	0	0	80	0	24	0	40	0	0	0	40	0	0	0	0
102	134	1212	876	64	32	0	8	0	0	0	0	64	0	0	0	64	0	0	0	0
104	337	1905	916	108	316	0	16	12	0	112	0	120	16	0	0	116	4	0	80	0
106	387	3688	736	152	312	0	0	76	80	72	4	104	316	0	0	1388	16	0	140	0
108	372	1332	522	34	308	0	2	6	0	22	2	64	56	0	0	196	2	0	0	0
111	785	1310	515	54	200	0	5	68	0	20	0	44	73	2	0	183	4	0	2	0
114	190	332	130	5	86	0	0	18	0	11	0	5	30	0	0	28	0	0	0	0
116	128	564	53	0	290	0	0	56	0	0	0	0	88	0	0	23	0	0	1	0
118	142	341	49	0	194	0	0	19	0	5	0	1	11	0	0	38	0	0	0	0
124	66	186	38	0	121	0	1	9	0	3	0	0	4	0	0	0	0	0	0	0
126	123	485	49	4	321	0	4	36	0	0	0	1	49	0	0	0	0	0	0	0

Depth, cm	Real Counts	Total	Uvi	Ang	Fur	Bul	Nut	Cras	Cari	Mel	Or	N. pul	N.aur	Pul	Ala	Ep	Cib	Bol	Pyr	Glo
128	78	223	18	0	154	0	0	23	8	1	0	0	1	0	0	0	0	0	0	0
131	24	61	20	0	25	0	0	2	0	0	0	0	4	0	0	0	0	0	0	0
134	63	160	23	0	91	0	0	23	0	4	0	1	12	0	0	0	0	0	0	0
136	90	238	26	0	123	0	0	74	0	0	0	0	7	0	0	0	0	0	0	0
138	392	649	270	8	190	0	3	58	1	9	0	2	37	0	0	40	0	0	0	0
141	257	456	45	0	301	0	1	19	1	52	0	1	12	0	0	0	0	0	0	0
142	569	942	261	4	414	0	0	64	1	26	0	8	116	0	0	2	0	0	1	0
144	313	601	100	3	307	0	0	20	2	11	0	4	49	0	0	63	4	0	1	0
146	2683	5063	85	201	1958	0	3	144	106	134	6	57	248	6	1	1659	42	0	222	0
148	739	1067	65	0	876	0	0	29	0	8	0	0	23	0	0	0	0	0	0	0
152	148	233	81	0	114	0	0	17	0	3	0	3	0	0	0	0	0	0	0	0
154	442	703	170	0	462	0	0	19	0	13	0	0	10	1	0	0	0	0	0	0
156	612	1061	120	0	851	0	0	24	0	5	0	1	13	0	0	0	0	0	0	0
158	785	1268	138	0	1036	0	0	4	0	20	0	1	4	0	0	0	0	0	0	0
161	467	837	84	0	610	0	0	49	0	10	0	1	35	0	0	0	0	0	0	0
162	869	1453	135	0	893	0	3	76	0	26	0	23	206	0	0	30	0	0	0	0
164	359	730	102	0	555	0	1	9	0	3	0	0	23	0	0	0	0	0	0	0
166	11	25	5	0	18	0	0	0	0	0	0	0	1	0	0	0	0	0	0	0
168	789	1528	73	0	1194	0	0	62	0	10	0	0	123	0	0	0	0	0	0	0
171	35	73	29	0	35	0	0	0	0	1	0	0	0	0	0	0	0	0	0	0
174	285	499	109	0	305	0	0	10	0	3	0	0	44	0	0	0	0	0	0	0
176	129	176	82	0	64	0	0	6	0	6	0	0	9	0	0	0	0	0	0	0
178	5	20	6	0	12	0	0	0	0	0	0	0	0	0	0	0	0	0	0	0
181	196	226	91	0	100	0	1	0	0	7	0	1	12	0	0	0	0	0	0	0

Depth, cm	Real Counts	Total	Uvi	Ang	Fur	Bul	Nut	Cras	Cari	Mel	Or	N. pul	N.aur	Pul	Ala	Ep	Cib	Bol	Pyr	Glo
182	522	661	138	0	434	0	1	24	0	9	0	0	27	0	0	0	0	0	0	0
184	81	107	92	0	2	0	0	1	0	1	0	0	2	0	0	0	0	0	0	0
186	364	596	70	0	465	0	0	17	0	5	0	0	3	0	0	0	0	0	0	0
188	2	2	0	0	2	0	0	0	0	0	0	0	0	0	0	0	0	0	0	0
192	7	11	6	0	2	0	0	1	0	0	0	0	1	0	0	0	0	0	0	0
194	3	10	1	0	1	0	0	0	0	0	0	0	0	0	0	0	0	0	0	0
196	6	18	5	0	10	0	0	0	0	0	0	0	1	0	0	0	0	0	0	0
198	224	357	78	0	250	0	0	0	0	2	0	0	3	0	0	0	0	0	0	0
202	530	1265	49	0	1000	0	0	40	0	4	0	29	72	0	0	0	0	0	0	0
212	304	555	146	0	379	0	0	0	0	0	0	0	1	0	0	0	0	0	0	0
224	180	369	108	0	243	0	0	0	0	0	0	0	0	0	0	0	0	0	0	0
236	186	631	57	0	459	0	0	24	0	4	0	1	34	0	0	0	0	0	20	0
248	370	515	194	0	274	0	1	4	0	3	0	0	8	0	0	0	0	0	0	0
259	688	1400	317	0	845	0	0	102	0	4	0	1	64	0	0	0	0	0	0	0
272	742	1211	209	0	760	0	3	109	0	28	0	1	47	0	0	0	0	0	0	0
284	1026	2170	268	0	1492	0	0	93	0	29	0	1	182	0	0	0	0	0	0	0
288	231	605	161	0	395	0	0	0	0	7	0	0	1	0	0	0	0	0	0	0
293	394	1118	322	0	676	0	2	10	0	28	0	0	20	0	0	0	0	0	0	0
296	735	1312	303	0	797	0	0	57	0	25	0	1	59	0	0	0	0	0	0	0
299	723	1696	233	0	1158	0	0	104	0	18	0	0	95	0	0	0	0	0	0	0
304	242	439	117	0	268	0	5	2	0	21	0	0	0	0	0	0	0	0	0	0
308	153	181	102	0	45	0	1	2	0	16	0	0	1	0	0	0	0	0	0	0
313	161	441	73	0	318	0	2	4	0	11	0	0	1	0	0	0	0	0	0	0
316	198	362	60	0	110	0	1	64	0	13	0	2	94	0	0	0	0	0	0	0

Depth, cm	Real Counts	Total	Uvi	Ang	Fur	Bul	Nut	Cras	Cari	Mel	Or	N. pul	N.aur	Pul	Ala	Ep	Cib	Bol	Pyr	Glo
321	282	482	49	0	292	1	1	52	0	8	0	3	49	0	0	0	0	0	0	0
324	125	226	22	0	162	0	0	8	0	3	0	2	16	0	0	0	0	0	0	0
328	105	334	56	0	239	0	2	9	0	7	0	0	1	0	0	0	0	0	0	0
332	141	278	51	0	179	0	2	6	0	13	0	0	18	0	0	0	0	0	0	0
336	35	51	30	0	16	0	0	0	0	1	0	0	0	0	0	0	0	0	0	0
341	38	112	22	0	56	0	3	0	0	2	0	0	21	0	0	0	0	0	0	0
344	83	104	32	0	53	0	3	5	0	2	0	0	1	0	0	0	0	0	0	0
348	228	417	94	0	113	0	6	55	0	73	0	0	55	0	0	0	0	0	0	0
352	41	85	11	0	5	0	0	60	0	3	0	0	0	0	0	0	0	1	0	0
356	79	172	13	0	132	0	0	10	0	3	0	0	1	0	0	0	0	0	0	0
359	66	136	26	0	17	1	0	74	0	13	0	0	0	0	0	0	0	0	0	0
364	123	181	55	0	89	0	1	16	0	5	0	0	2	0	0	0	0	0	0	0
368	118	145	53	0	41	3	1	25	0	11	0	0	1	0	1	0	0	0	0	0
372	111	137	52	0	5	24	0	5	0	8	0	0	0	0	0	0	0	0	0	0
376	116	184	66	0	46	24	2	13	0	11	0	0	0	0	0	0	0	0	0	0
379	222	238	98	0	20	61	2	18	0	24	0	0	0	0	0	0	0	0	0	0
384	173	211	91	0	35	60	1	1	0	11	0	0	0	0	0	0	0	0	0	0
392	120	126	71	0	11	25	2	3	0	0	0	1	0	0	0	1	0	0	0	0
401	174	166	101	1	5	49	2	0	0	1	0	0	0	0	0	0	0	0	0	0
413	478	565	213	0	39	208	4	1	0	64	0	0	2	2	0	1	0	1	1	0
418	173	196	96	0	20	59	0	0	0	9	0	0	0	0	0	0	0	0	0	0
423	300	347	140	0	48	96	1	4	0	35	0	0	3	1	0	0	0	0	0	0
429	328	409	90	0	137	103	1	4	0	19	0	1	20	0	0	0	3	0	0	0
441	178	316	45	0	159	65	0	0	0	16	0	3	15	0	0	0	1	0	0	0

Depth, cm	Real Counts	Total	Uvi	Ang	Fur	Bul	Nut	Cras	Cari	Mel	Or	N. pul	N.aur	Pul	Ala	Ep	Cib	Bol	Pyr	Glo
446	176	183	44	1	4	119	0	1	0	4	0	0	1	0	0	0	0	0	0	0
459	361	418	55	0	56	237	2	2	0	38	0	0	1	4	0	0	0	0	0	0
479	0	0	0	0	0	0	0	0	0	0	0	0	0	0	0	0	0	0	0	0
503	30	31	17	0	0	12	0	0	0	0	0	0	0	0	0	0	0	0	0	0
516	0	0	0	0	0	0	0	0	0	0	0	0	0	0	0	0	0	0	0	0
521	0	0	0	0	0	0	0	0	0	0	0	0	0	0	0	0	0	0	0	0
532	2	2	2	0	0	0	0	0	0	0	0	0	0	0	0	0	0	0	0	0
539	1	1	1	0	0	0	0	0	0	0	0	0	0	0	0	0	0	0	0	0
546	0	0	0	0	0	0	0	0	0	0	0	0	0	0	0	0	0	0	0	0
556	10	10	8	0	0	2	0	0	0	0	0	0	0	0	0	0	0	0	0	0
566	12	13	11	0	0	1	0	0	0	0	0	0	0	0	0	0	0	0	0	0
572	0	0	0	0	0	0	0	0	0	0	0	0	0	0	0	0	0	0	0	0
581	0	0	0	0	0	0	0	0	0	0	0	0	0	0	0	0	0	0	0	0
592	6	6	6	0	0	0	0	0	0	0	0	0	0	0	0	0	0	0	0	0
601	22	22	9	0	0	13	0	0	0	0	0	0	0	0	0	0	0	0	0	0
608	267	277	214	0	0	41	1	0	0	0	0	0	0	1	0	0	0	0	0	0
616	99	103	91	0	0	8	0	0	0	0	0	0	0	0	0	0	0	0	0	0
624	241	250	210	0	0	22	0	0	0	0	0	0	0	0	0	0	0	0	0	0
633	237	246	159	0	0	71	0	0	0	2	0	0	0	0	0	0	0	0	0	0
641	141	147	126	0	0	14	0	0	1	0	0	0	0	0	0	0	0	0	0	0
648	396	464	153	0	63	209	0	0	0	0	0	2	0	0	0	0	0	0	0	0

A.5.2 GC642

Table A.24: GC642 Benthic Foraminifera Assemblage (Main Species). Uvi = *Uvigerina bifurcata*; Ang = *Angulogerina earlandi*; Fus = *Fursenkoina fusiformis*; Bul = *Bulimina aculeata*; Nut = *Nuttallides umbonifera*; Cras = *Cassidulina crassa*; Cari = *Cassidulina carinata*; Mel = *Melonis barleeanum*; Or = *Oridorsalis umbonatus*; N.pul = *Nonionella pulchella*; N.aur = *Nonionella auris*; Pull = *Pullenia bulloides*; Ala = *Alabaminella weddellensis*; Ep = *Epistominella exigua*; Cib = *Cibicidoides sp.*; Bol = *Bolivina sp.*; Pyr = *Pyrgo sp.*; Glo = *Globobulimina sp.*.

Depth, cm	Real Counts	Total	Uvi	Ang	Fur	Bul	Nut	Cras	Cari	Mel	Or	N. pul	N.aur	Pul	Ala	Ep	Cib	Bol	Pyr	Glo
506	278	374	147	0	12	155	0	0	1	21	0	0	10	2	0	0	0	0	0	0
508	524	638	297	0	36	240	0	20	0	11	0	0	0	0	0	0	0	0	1	0
510	540	680	231	0	61	334	0	0	0	14	0	0	11	0	0	0	0	0	3	0
512	522	610	280	0	5	278	0	0	0	13	0	3	0	0	0	0	0	0	0	0
514	373	480	259	0	46	149	0	0	0	0	0	1	0	0	0	0	0	0	0	0
516	271	306	180	0	0	122	0	0	0	0	0	0	0	0	0	0	0	0	0	0
518	100	134	98	0	0	32	0	0	0	0	0	0	0	0	0	0	0	0	0	0
520	162	198	95	0	0	95	0	0	0	2	0	0	0	0	0	0	0	0	0	0
522	369	487	187	0	1	291	0	1	0	3	0	0	0	0	0	0	0	0	0	0
524	21	39	32	0	0	5	0	0	0	0	0	0	0	0	0	0	0	0	0	0
526	56	75	45	0	0	29	0	0	0	0	0	0	0	0	0	0	0	0	0	0
528	72	106	81	0	0	10	0	0	4	1	0	1	1	0	0	1	0	0	0	0
530	28	48	43	0	0	3	0	0	0	0	0	0	0	0	0	0	0	0	0	0
532	128	649	221	4	24	344	0	0	4	8	0	0	0	0	0	44	0	0	0	0
534	344	3084	332	96	476	452	0	436	260	132	0	4	208	0	0	408	80	0	180	0
536	272	3645	717	128	160	672	0	688	328	376	0	0	120	8	0	240	80	0	16	0
538	200	2235	547	32	32	952	0	168	32	120	0	0	0	8	0	176	0	0	160	0
540	248	4899	411	104	248	424	0	1032	672	320	0	0	88	24	0	352	336	0	184	0
542	565	8045	1197	192	272	2104	0	984	984	360	0	0	416	0	0	1176	16	0	0	0
544	505	6159	1511	32	216	1824	0	520	256	504	0	0	48	16	0	1152	8	0	0	0
546	442	10127	2207	128	352	3008	0	1392	544	336	0	0	320	16	0	1056	0	0	496	0
548	372	20878	1214	912	656	1968	0	3904	2160	1568	0	0	784	48	0	3664	976	0	1296	0
550	482	29630	638	1024	704	848	0	5072	3200	1472	0	32	5072	16	0	4720	16	16	3968	0
552	870	33542	726	1328	864	1160	8	6592	2680	496	0	24	5320	32	0	5384	648	8	2112	0

Depth, cm	Real Counts	Total	Uvi	Ang	Fur	Bul	Nut	Cras	Cari	Mel	Or	N. pul	N.aur	Pul	Ala	Ep	Cib	Bol	Pyr	Glo
554	710	54444	380	2768	784	848	0	11872	6384	3616	0	128	8336	48	48	8896	1344	0	5504	16
556	498	65818	442	4288	128	800	0	18560	5280	2720	0	0	6560	160	672	12800	1376	0	960	0
558	653	95709	189	5440	1440	192	0	17440	11520	1984	0	128	18848	128	0	17088	1440	0	4544	32
560	594	75571	51	3520	64	256	0	11392	6464	2240	0	96	14496	0	0	18080	192	32	6144	0
562	1142	65113	153	4272	656	368	0	8672	10304	2208	0	80	10832	0	368	7488	1008	96	4288	0
564	588	80836	4	5440	704	0	0	11136	8992	736	0	96	8896	0	736	18144	96	0	8352	32
566	653	87170	34	3904	96	32	0	13216	11840	2336	0	96	10880	0	1408	16640	896	0	9280	96
568	700	80769	1	5408	736	0	0	8672	9024	2304	0	160	22592	0	128	11040	2080	0	6368	0
571	548	95968	0	4672	32	0	0	18432	14048	1056	0	128	16672	64	0	13216	1472	0	10400	64
573	545	36257	1	2208	0	0	0	2080	11008	672	0	96	6080	0	224	5696	736	32	3744	64
575	393	54528	0	1760	672	64	0	10112	8992	1120	0	64	3616	32	32	12832	1344	0	6880	32
577	442	59904	0	1888	0	0	0	10080	6368	224	0	0	7552	160	768	14784	832	0	4672	0
579	489	81312	0	3520	0	0	0	7584	7072	1696	0	704	15136	96	64	18720	2720	0	11904	0
581	557	55264	0	4064	320	0	0	9952	7872	640	0	352	6848	192	960	11712	1088	0	5408	0
583	649	101409	1	3680	1152	0	0	10528	14400	192	32	832	17184	0	448	23872	480	0	12992	0
585	1862	30856	0	2640	496	0	0	1608	9152	272	0	208	5208	8	32	2392	224	8	3552	16
587	603	49248	64	3104	384	0	0	2304	12032	960	0	0	8544	32	64	9728	320	0	4832	0
589	439	28864	0	1056	128	32	256	640	8256	800	0	416	2144	160	704	8960	288	0	1664	0
591	486	32160	32	2144	128	0	0	2144	9696	704	0	32	2944	32	416	7200	192	0	2336	0
593	402	32962	34	1312	192	0	0	1024	6240	448	0	288	3840	0	1280	11584	32	0	1728	0
595	715	33427	131	1328	688	0	0	1472	5504	576	0	480	6416	16	224	10272	432	0	2400	0
597	524	18176	16	784	288	0	0	640	3664	272	0	160	2912	0	208	5152	64	0	1424	0
599	334	10576	80	720	192	0	0	688	2912	176	0	224	1264	0	128	1968	0	0	912	0
601	528	19846	22	1600	160	0	0	576	4400	640	0	400	1760	0	176	6832	16	0	1424	0

Depth, cm	Real Counts	Total	Uvi	Ang	Fur	Bul	Nut	Cras	Cari	Mel	Or	N. pul	N.aur	Pul	Ala	Ep	Cib	Bol	Pyr	Glo
603	1001	21326	14	1776	96	0	0	1120	4736	272	0	216	2968	0	96	5664	40	0	1768	0
605	871	18620	36	832	224	0	0	320	3896	240	0	264	3264	72	176	5248	112	0	1472	8
607	611	16631	199	1552	192	0	0	304	5744	592	0	320	1120	0	96	4496	16	0	704	0
609	2429	10735	217	1030	84	0	0	162	6042	293	0	248	274	2	0	1691	18	0	328	4
611	838	21277	365	1392	112	0	0	672	8832	336	0	768	1136	128	176	5648	144	0	912	0
613	1732	4099	110	128	168	0	0	137	1054	63	0	103	101	2	5	1797	189	1	99	0
615	62	124	9	6	1	0	0	3	27	5.5	0	4	0	0	0	55	5.5	0	5.5	0
617	0	0	0	0	0	0	0	0	0	0	0	0	0	0	0	0	0	0	0	0
619	2	11	0	6	0	0	0	0	0	0	0	0	0	0	0	0	0	0	5.5	0
621	11	21	14	0	0	0	0	0	0	0	0	0	0	0	0	0	0	0	0	0
623	0	0	0	0	0	0	0	0	0	0	0	0	0	0	0	0	0	0	0	0
625	16	35	34	0	0	0	0	0	0	0	0	0	0	0	0	0	0	0	0	0
627	192	219	212	0	0	0	2	2	0	1	0	0	0	0	0	0	0	0	0	0
629	26	51	50	0	0	0	0	1	0	0	0	0	0	0	0	0	0	0	0	0
631	145	184	180	0	0	0	0	0	0	0	0	0	0	0	0	0	1	0	0	0
633	32	52	51	0	0	0	0	0	0	0	0	0	0	0	0	0	0	0	0	0